学位論文

A Few Tens au Scale Physical and Chemical Structures around Young Low-Mass Protostars

(数10 auスケールで見た若い低質量原始星天体の物理的·化学的構造)

平成29年6月博士 (理学) 申請

東京大学大学院理学系研究科
物理学専攻

大屋 瑶子

Abstract

Thorough understanding of the star/planet formation and the associated chemical evolution is an important target for astrophysics and astrochemistry. Although radio and infrared observations have recently enhanced our understandings of the protostellar formation process, it is still controversial *when and how disk structures are formed around newly-born protostars*, and *how molecules of parent molecular clouds are delivered into the disks*. To answer these questions, we conducted physical and chemical analyses of disk forming regions. This thesis describes the observational studies with Atacama Large Millimeter/submillimeter Array (ALMA) at a few 10 au scale resolution. Specifically, the following five young low-mass protostellar sources in the Class 0 and I stages were observed: L1527, IRAS 15398–3359, IRAS 16293–2422 Source A, Source B, and L483.

Rotational spectral lines of various molecular species were detected toward the above protostellar sources with ALMA. We found that the kinematic structure of the flattened envelope at a few 100 au scale was well explained by a simple ballistic model. In this model ('infalling-rotating envelope model'), the gas cannot fall inward of a certain radius due to the energy and angular momentum conservation. This radius is called as the 'centrifugal barrier'. In this thesis, the common occurrence of the infalling-rotating envelope and its centrifugal barrier is demonstrated for the five sources. A high-velocity component was also detected inside the centrifugal barrier. We attributed this component to the disk structure. Thus, the disk structures seem to have already been formed even at the earliest stage (Class 0) of the protostellar evolution.

We also investigated the outflow components in L1527, IRAS 15398–3359, and L483. Since the infalling-rotating envelope, the centrifugal barrier, the disk component, and the outflow components are thought to be related to one another through the angular momentum of the gas, their comprehensive understandings are essential to star formation studies. The physical parameters (the protostellar mass, the radius of the centrifugal barrier, and the inclination angle) are indeed evaluated with the aid of the infalling-rotating envelope model, the Keplerian disk model, and the parabolic outflow model, and mutual relations of the components are discussed.

We also analyzed the chemical composition of the gas in the above five sources. It is well known that the chemical composition of the protostellar envelopes shows significant diversity at a few 1000 au scale. In this thesis, we found that the chemical diversity was indeed delivered from the envelope into the disk. Moreover, we also found the drastic chemical changes across the centrifugal barrier, whose radius is typically a few 10 au. Three physical components of the disk forming regions (the infalling-rotating envelope, the centrifugal barrier, and the disk component) were traced by particular molecules. These new findings allow us the 'chemical diagnostics' of the disk forming regions. The chemical changes across the centrifugal barrier are also of particular importance in astrochemistry

of protoplanetary disks, because they are expected to determine the initial condition of the chemical evolution toward planet formation.

These results provide us with important clues to general understandings of the physical mechanism and the chemical diversity in the disk formation.

Contents

Chapter 1

Introduction

It has been established that the Universe consists of dark energy, dark matter, and baryons (Hinshaw et al., 2013). Although the mass of baryons is only 4.6% of the total mass of the Universe, they form rich structures in the Universe from large scales (clusters of galaxies and galaxies) to small scales (stars and planets). Among such hierarchical structure, stars are the most fundamental physical elements in the Universe. They also play important roles in chemical evolution of the Universe through nucleosyntheses. All said and done, they harbor planets where the life can emerge. Thus, detailed understanding of star formation is a central issue for astrophysics and astrochemistry. This thesis describes a part of such efforts, focusing on a relation between physical and chemical processes of the star and planetary system formation.

1.1 Formation of Low-Mass (Solar-type) Stars

Stars are born through gravitational collapse of dense parts of interstellar clouds, called molecular clouds. In the Milky Way galaxy, the total mass of molecular clouds is roughly 10^9 $M_\odot$, from which stars are continuously formed. The star-formation rate of molecular clouds in the solar neighborhood is 1.6 $M_\odot$ Myr^{-1} pc^{-2} (Evans et al., 2009), although it largely depends on molecular clouds.

In star formation studies, stars are roughly classified into two categories. Stars with a mass less than 8 $M_\odot$ are called as *'low-mass stars'* (or *'Solar-type stars'*), while ones with a higher mass are called as *'high-mass stars'*. This is because the time scale of star formation is much different between them. The timescale from the stellar birth to the main sequence is 10^{7-8} yr for low-mass stars, while it is as short as 10^5 yr for high-mass stars. High-mass stars often reach the main sequence before their parent cores are completely dissipated. Hence, the formation of high-mass stars heavily affects the environment of parent molecular clouds, and this fact results in a complexity of their formation process. The high-mass star formation study itself is an important and interesting subject. However, their observational studies often encounter various difficulties, because they are mostly distant from us. Although a rapid progress has been made by high angular-resolution observations for these years, the unified picture of high-mass star formation has not been established yet.

As for low-mass stars, especially isolated ones, their formation processes have extensively been studied both theoretically and observationally (e.g., Hayashi, 1961; Stahler et

al., 1980; Shu et al., 1987; Benson & Myers, 1989; Onishi et al., 1996; André et al., 2010; Hartmann et al., 2016). Since planetary systems are potentially formed around low-mass stars, detailed understandings of their formation processes are essential to understanding the origin of the Solar system. So far, the following scenario is suggested as the formation of low-mass stars:

(1) Starless core

Before the birth of a protostar, parent molecular clouds are called as *'starless cores'*. While the gas collapses due to self-gravity, the temperature of the core is stably kept low ($\sim$10 K) due to the radiative cooling (the isothermal collapse). Since the gas is usually sustained by the turbulence and the magnetic fields, the timescale of the starless-core stage is reported to be about $(0.5 \pm 0.3) \times 10^6$ yr, which is slightly longer than the free-fall time of the gas with the H_2 density of 10^{-4} cm^{-3} (Evans et al., 2009).

(2) Protostar

The central density of a starless core increases as the core collapses. When the central H_2 density exceeds 10^{11} cm^{-3}, the thermal radiation from dust grains is absorbed by the gas before it escapes from of the core; namely, the core becomes *'optically thick'* for dust emission. This results in a low cooling efficiency, and thus the temperature in the central part of the core starts to rise. This optically thick core is called as *'first core'* (Larson, 1969). Within 100 yr or so, the temperature of the core reaches 1500 K, and then the thermal dissociation of H_2 to 2H starts. Since the thermal dissociation of H_2 absorbs substantial energy, the gravitational collapse of the core is accelerated (*'second collapse'*). After this stage, the core is called as *'second core'*, which is recognized as the birth of the protostar.

After the protostellar birth, the gas continues to accrete onto the protostar, and the protostar grows. The protostar shines by releasing the gravitational energy of the accreting gas (*'main accretion phase'*). Generally, the physical structure of the gas is no more spherically symmetric due to the angular momentum of the accreting gas, and the gas forms a flat envelope and a protostellar disk around the protostar. At this moment, a bipolar outflow perpendicular to the disk/envelope system also blows out from the protostar (e.g., Bachiller, 1996). It is generally thought that outflows are launched by the interaction between the gas motion and the magnetic field (e.g., Machida & Hosokawa, 2013). They are thought to play an important role in extracting the angular momentum from the accreting gas. An outflow phenomenologically consists of an ionized jet and a molecular flow in its inner and outer parts, respectively. The velocity of an outflowing gas reaches as high as $(10 - 100)$ km s^{-1}. At this evolutionary stage, the gas simultaneously shows an infall motion in the envelope and an outflowing motion.

(3) T Tauri star

The envelope gas is dispersed by the outflow, and then the accretion of the gas onto the protostar gets settled (*'T Tauri star'*). At this evolutionary stage, the star shrinks quasi-statically so that the temperature in the central part rises. The heat generated inside the star is transported to its surface by convection (*'Hayashi phase'*;

Hayashi, 1961). When the temperature of the central part of the star becomes enough high, the heat is transported by radiation (*'Henyey track'*; Henyey et al., 1955). Then, T Tauri stars finally reach the main sequence in $(10^7 - 10^8)$ yr. Since the envelope gas is almost dissipated around a T Tauri star, the star is surrounded by only a protoplanetary disk, which is a parent of a planetary system. At the first phase of T Tauri stars (*'classical T Tauri stars'*), a small amount of the gas is still accreting onto the star through the protoplanetary disk, and it causes episodic phenomena, such as UV and X-ray flares (e.g., Feigelson & Montmerle, 1999). At the later phase of T Tauri stars, such phenomena due to the gas accretion scarcely occur, and the H_α line emission caused by the accretion is weakened (*'weak-line T Tauri stars'*).

For stars before they reach the main sequence (*'pre-main sequence stars'*), their radiation spectra in the infrared region (*'Spectral energy distribution'*; SED) are commonly used to classify their evolutionary stages phenomenologically (Lada & Wilking, 1984). Generally, the stellar evolutionary stages are classified into the stages called as *'Class I–III'*. The typical SEDs for these stages are shown in Figure 1.1. Class I, II, and III correspond to the evolutionary stages of the protostar, the classical T Tauri star, and the weak-line T Tauri star, respectively. Stars in earlier phases than Class I are called as Class 0 (Andre et al., 1993). In these stages, the SED changes depending on which component in the source emits dominantly. In the Class 0 stage, the emitting source is a thick envelope gas at a low temperature which surrounds the protostar. It shows the black body radiation with its intensity peak in the far infrared region. Emission from the protostar is almost absorbed by the envelope, and its energy is reprocessed as far infrared emission. A Class I source is also surrounded by the envelope gas, and the radiation in the near infrared region is obscured and its peak is in the mid-infrared region. A Class II source shows the radiation from the stellar photosphere as well as that from the protoplanetary disk, and the radiation in the near infrared region is dominant. The SED of a Class III source is almost dominated by the black body radiation from the stellar photosphere in the near infrared region with a little excess in the infrared and UV regions. Since the SED is affected by various factors, such as the inclination angle of the protostellar/protoplanetary disk and the possible companion, this classification, especially that of Class 0 and I, has some uncertainty. Because of this reason, the bolometric temperature of sources is often employed for the classification; the bolometric temperature $T_{\rm bol}$ of an observed continuum spectrum is defined as the temperature of a black body having the same mean frequency as the observed spectrum (Myers & Ladd, 1993). Sources with the bolometric temperature less than 70 K are classified as Class 0, while ones with the temperature higher than 70 K are as Class I. In these classification of the evolutionary stages, the outflows blow during the stages from Class 0 to Class I. Protostellar disks are thought to be formed in the stages from Class 0 to Class I, while protoplanetary disks are in the stages from Class II to Class III. During the Class II and III stages, planetary systems are thought to be formed in protoplanetary disks. The life time scales for the starless-core, Class 0, I, II, and III stages are roughly 10^5, 10^4, 10^5, 10^6, and 10^7 yr, respectively (Figure 1.1; Bachiller, 1996).

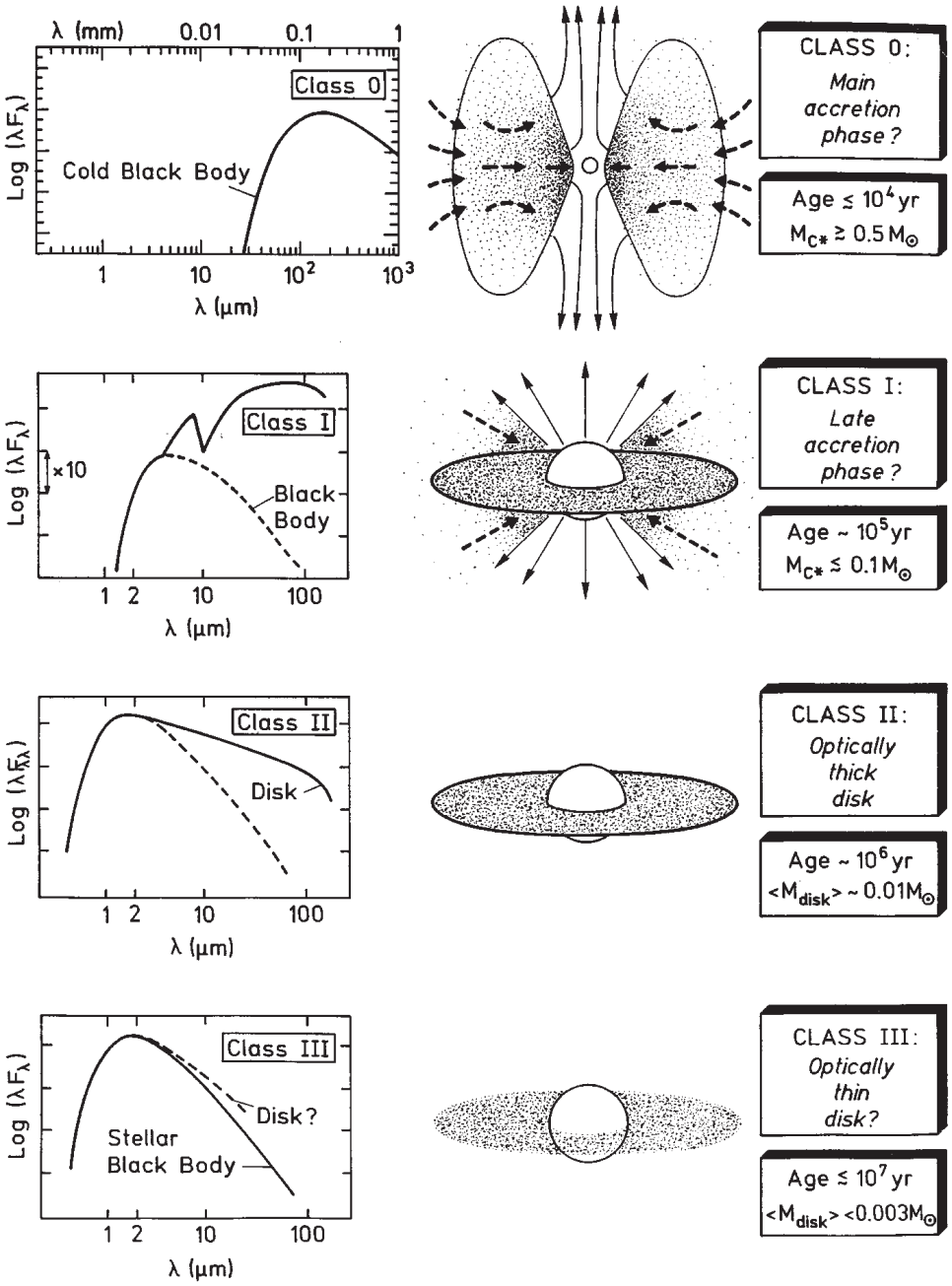

Figure 1.1: Spectral energy distribution of a source at each evolution stage. Taken from Bachiller (1996).

1.2 Radio Astronomy

Radio wave is the electromagnetic wave, whose wavelength is longer than those of visible and infrared radiation. The boundary between the radio wave and the (far) infrared radiation is arbitary, which is often set at 100 μm (3 THz). The dawn of the radio astronomy was broken by Jansky in 1931, who detected a radio wave ($\lambda = 14.6$ m) from the Galactic Center (Jansky, 1933). This is emission of a huge plasma gas in interstellar medium. Reber (1940) observed the Milky Way with a hand-made parabola antenna, and mapped the distribution of the radio continuum emission ($\lambda = 1.85$ m). Then, Hey (1946) observed the Solar flare in radio wave, which is an explosive event on the Solar photosphere, producing a high temperature plasma gas and relativistic charged particles.

Radio observations have drastically been developed by making use of the development of the technologies of a microwave radar and communications during the World War II. Ewen & Purcell (1951) and Muller & Oort (1951) discovered the 21-cm line of atomic hydrogen. In 1960s, Penzias and Wilson detected the cosmic microwave background emission, providing a definitive proof of the big-bang theory. New types of celestial objects, such as quasars and pulsers, were also found by radio observations. From the late 1960s to the early 1970s, spectral lines (mostly rotational spectral lines) of various molecular species, such as NH_3, H_2O, H_2CO, and CO, were found in the radio wave region (Cheung et al., 1968, 1969; Snyder et al., 1969; Wilson et al., 1970), and moreover, *'interstellar molecular clouds'* were recognized as a dense and cold part of interstellar clouds, which harbor various molecular species. Since interstellar molecular clouds are the birthplaces of stars and planetary systems, they have been extensively studied as an important target for the radio astronomy. At the same time, detection of various interstellar molecules opened a new interdisciplinary field, *'astrochemistry'*.

Radio observations have several advantages in studies of star formation:

(1) Radio waves go through interstellar clouds with less attenuation due to the scattering and absorption by gas and dust than the electromagnetic wave at shorter wavelengths. Thus we can see through the central part of interstellar clouds, where protostars and protostellar disks are being formed. Moreover, the earth atmosphere is transparent in some frequency ranges of radio waves. These frequency ranges are called as *'radio window'* or *'atmospheric window'*. Hence, the radio waves in the windows can be observed by ground-based radio telescopes.

(2) Radio-wave photons have low energy, and can be emitted by cold matter. The black body radiation at a temperature from 10 to 50 K has its intensity peak in the millimeter/submillimeter region. The temperature of molecular clouds, which are the birthplaces of protostars, is typically as low as 10 K. Hence, their structures, including the protostellar envelope and disk system, can be traced by radio observations.

(3) The radio region contains various molecular lines. Rotational spectra of various molecular species, not only the basic species such as CO and CS but also more complex species such as $HCOOCH_3$ (methyl formate) and $(CH_3)_2O$ (dimethyl ether) fall in the radio-wave region, particularly in the millimeter and submillimeter wave

regions. Thus, radio observations tell us what kinds of molecules are contained in the source and how much (Section 1.3).

On the other hand, radio astronomy has an apparent weakness: the angular resolution of radio telescopes is generally much poorer than those of visible and infrared telescopes with the same diameter (D). A diffraction-limited angular resolution of a telescope is proportional to $\frac{\lambda}{D}$, where λ is the wavelength. Thus, a radio telescope ($\lambda \sim 1$ mm) require a larger dish by 2000 times with respect to a visible telescope ($\lambda \sim 500$ nm) to achieve the same diffraction-limited angular resolution. However, the available size as a fully steerable dish is at most 100 m. Hence, radio astronomy overcomes this weakness by using the technique of the aperture synthesis, which is described in Chapter 2.

1.3 Astrochemistry in Star-Forming Region

Astrochemistry was initiated in the early 1970s thanks to the birth of millimeter-wave astronomy. Since then, breakthroughs in astrochemistry have always been triggered by new observational technologies. In this section, the progress of astrochemistry in star-forming regions is outlined in relation to technological developments.

1.3.1 1980s: Astrochemistry in High- and Low-mass Star-Forming Region

Chemistry of star-forming regions was first studied for high-mass star-forming regions. This is simply because they have very bright emission of various molecular species. Therefore, their chemical compositions can readily be studied. Orion KL (Keinmann-Low object in Orion) is one of the best studied source in astrochemistry. It is known as the nearest high-mass star-forming region and the richest source in molecular emission (437 pc; Hirota et al., 2007). In the early era of radio astronomy, the chemical composition of Orion KL was extensively studied by spectral line survey observations (e.g. Johansson et al., 1984; Sutton et al., 1985; Blake et al., 1987; Turner, 1989) with the millimeter-wave telescopes (Onsala 20 m telescope, NRAO 12 m telescope, Owens Valley 10.4 m telescope). Later, the line survey of Orion KL has been expanded to higher frequencies (Schilke et al., 1997; Beuther et al., 2005; Tercero et al., 2010). The most characteristic chemical feature of Orion KL is the existence of various saturated complex organic molecules (COMs), such as $(CH_3)_2O$, $HCOOCH_3$, and C_2H_5CN. These species mostly resides in the hot and dense part near the protostar. Sulfur-containing molecules (SO and SO_2) and non-volatile molecules (SiO, SiS, and PN) are also found there. Chemical differentiation at a small spatial scale within Orion KL was inferred by the different spectral line shapes among molecules (e.g. Blake et al., 1987). This was indeed confirmed by interferometric observations (e.g. Plambeck & Wright, 1987; Masson & Mundy, 1988; Wilson et al., 1989). The N-bearing molecules are concentrated around *'hot core'* close to the high-mass protostar source I, while the O-bearing molecules are distributed in a *'compact ridge'*, which is a bit apart from the hot core. Observations toward high-mass protostellar sources have been extensively conducted to study its chemical composition itself and to search for new interstellar molecules.

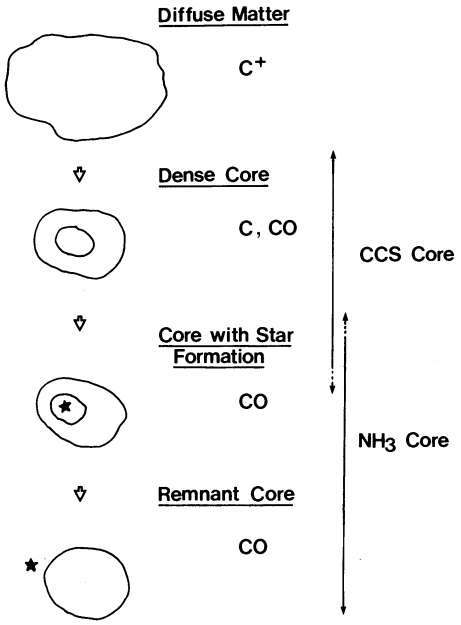

Figure 1.2: Schematic illustration of the chemical evolution of a contracting cloud. Taken from Suzuki et al. (1992).

In the 1980s, a number of low-mass protostars were identified in dense cores by the Infrared Astronomical Satellite (IRAS) (e.g. Beichman et al., 1986; Benson & Myers, 1989). However, chemical compositions of low-mass star-forming regions were relatively less studied in comparison with those of high-mass star-forming regions in those days. Since the molecular emission in low-mass star-forming regions is generally weaker than that in high-mass star-forming regions, less attention was paid for low-mass star-forming regions in astrochemistry. Some survey observations of only a few representative molecules, such as NH_3, CS, CCS, and HC_3N (e.g. Benson & Myers, 1989; Zhou et al., 1989; Suzuki et al., 1992), were conducted toward low-mass protostellar sources. A systematic chemical difference was found between starless cores and star-forming cores (Suzuki et al., 1992). However, this is a chemical evolutionary effect, and is not ascribed to the chemical composition in the vicinity of protostar (Figure 1.2).

1.3.2 1990s: Chemical Composition at a 10^3 au Scale

In the 1990s, the sensitivity of the radio telescope was much improved by using the superconducting heterodyne mixers, and the submillimeter-wave observations became possible. Thanks to these technological progresses, a pioneering study in astrochemistry of low-mass star-forming regions was conducted by Blake et al. (1994) and van Dishoeck et al. (1995). They carried out spectral line surveys in the millimeter/submillimeter-wave regions toward a low-mass protostellar source IRAS 16293–2422 in Ophiuchus ($137 - 147$ pc; Ortiz-León et al., 2017) with spatial resolutions of $\sim 10^3$ au. They found that sulfur-containing molecules, including SO, SO_2, CS, and H_2CS, are abundant in this source. The emission of SO and SO_2 was thought to come from the hot and dense region near

the protostar. Detection of high-excitation lines of CH_3OH clearly reveals the association of a 'hot core' like region in this source. However, the spectral lines of COMs, such as $HCOOCH_3$, $(CH_3)_2O$, and C_2H_5CN, were not detected in their observation, probably because of insufficient sensitivity. The existence of such a hot region was also inferred by the single-dish observations of H_2CO and CH_3OH toward this source and other low-mass protostellar sources (e.g. Ceccarelli et al., 1998; Schöier et al., 2002). With the aid of the simplified model considering the abundance jump in a hot region around the protostar, the size of the hot region was estimated to be as small as a few tens of au, although it was not able to be resolved by single-dish radio observations.

1.3.3 2000s: Chemical Diversity at a $10^2 - 10^3$ au Scale

The existence of the hot and dense region in IRAS 16293–2422 was confirmed in the 2000s. Cazaux et al. (2003) detected various spectral lines of COMs, including $(CH_3)_2O$, $HCOOCH_3$, and C_2H_5CN, toward this source, and demonstrated the occurrence of a hot-core like chemistry even in a low-mass protostellar source. This discovery was made possible by development of sensitive receivers, whose noise temperature is close the quantum limit ($h\nu/k$). Such a hot and dense region around a low-mass protostar was called as *'hot corino'*, named after its resemblance to the hot core in the high-mass star-forming region case with a much smaller scale. Indeed, interferometric studies of IRAS 16293–2422 show that those COMs exist in compact regions associated with the two components of the binary systems. It is thought that COMs are evaporated from grain mantle in the hot ($T \sim 100$ K) region around the protostar. Since then, some low-mass protostellar sources are also recognized to harbor a hot corino around their protostars (e.g. Serpens SMM1, SMM4, NGC1333 IRAS 2A, IRAS 4A, and IRAS 4B; Öberg et al., 2011; Bottinelli et al., 2004b; Sakai et al., 2006; Maury et al., 2014). The complex molecules detected toward hot corinos are thought to be related to the pre-solar organic materials found in meteorites, and thus, the discovery of hot corinos are of particular interest not only in astrochemistry but also in planetary science.

On the other hand, a low-mass protostellar source with a completely different chemical composition from IRAS 16293–2422 was found by Sakai et al. (2008a). They found that carbon-chain and related molecules, such as C_4H and c-C_3H_2, are abundant in a warm and dense region in the low-mass protostellar core L1527 in Taurus (137 pc; Torres et al., 2007). Furthermore, they also detected some negatively charged carbon-chain molecules, such as C_6H^- and C_4H^- (Sakai et al., 2007, 2008b). In contrast to the IRAS 16293–2422 case, the spectral lines of $HCOOCH_3$ are not detected toward this source, and the CH_3OH lines are much weaker. The chemical characteristics found in L1527 is called as *'warm carbon-chain chemistry'* (WCCC; Sakai et al., 2009a; Sakai & Yamamoto, 2013). It is proposed that CH_4, which is an important constituent of grain mantle, is evaporated in a warm ($T \sim 30$ K) and dense region around the protostar, triggering efficient formation of various carbon-chain chemistry. Sakai et al. (2009a) successively found another low-mass protostellar core having similar chemical characteristics to L1527, IRAS 15398–3359. The discovery of the WCCC sources established the chemical diversity in low-mass protostellar sources.

Since planetary systems are formed around low-mass stars, the chemical composition in low-mass star-forming regions, including its diversity, is essential to understanding the

chemical evolution from molecular clouds to planetary systems.

1.3.4 2010s: ALMA Era at $10 - 10^2$ au Scale

With the advent of Atacama Large Millimeter/submillimeter Array (ALMA), astrochemistry in low-mass star-forming regions have extensively been advanced. ALMA has allowed us to study thermal emission of less abundant molecules at a subarcsecond resolution. One of the most notable studies conducted with ALMA is the discovery of the centrifugal barrier of an infalling-rotating envelope around the protostar in the WCCC source L1527 (Figure 1.3; Sakai et al., 2014a). They found that the CCH emission in the envelope gas abruptly disappears at the distance of 100 au from the protostar. Before the ALMA era, kinematic structures of the gas around protostars have often been interpreted as the Keplerian motion, where the gas is rotationally supported, without careful considerations. Although the infall motion in L1527 was inferred in the analysis of the CO isotopologue lines at a resolution of ∼1000 au (e.g., Ohashi et al., 1997), its detailed characterization was difficult because of the limited resolution and sensitivity. With ALMA, the kinematic structure traced by CCH in L1527 was confirmed to have infall motion, and it was simply explained by the ballistic motion. In the infalling-rotating envelope, the gas cannot fall inward of a certain radius, because of the energy and angular momentum conservation. This position corresponds to the 'perihelion', and is called as *'centrifugal barrier'*. Sakai et al. (2014a) characterized the physical parameters of its infalling-rotating envelope at a 100 au scale, and identified its centrifugal barrier. They also reported a drastic chemical change across the centrifugal barrier in L1527 (Sakai et al., 2014a,b). The CCH and c-C_3H_2 lines trace the infalling-rotating envelope, while the SO line selectively highlights the centrifugal barrier. Since the radius of the centrifugal barrier (100 au) corresponds to the typical size of a protoplanetary disk system, such a chemical differentiation around the centrifugal barrier is an important clue to understand what kinds of molecules are delivered into the disk component. We are now going into the era of observations at the disk-forming region scale with ALMA.

1.4 Motivation for This Research

The formation process of low-mass (Solar-type) stars and their planetary systems is classified into the following three stages: (1) the contraction of the interstellar molecular cloud and the birth of the protostar inside it; (2) the formation of the protostellar/protoplanetary disk around the protostar; (3) the formation of the planetary system in the disk. As described above, radio and infrared observations have greatly enhanced our understandings of the first and the last stages of the formation process recently. However, the formation process of the protostellar/protoplanetary disk and the associated material evolution are still unknown. Therefore, understanding the formation processes of rotationally-supported disks around young low-mass protostars is an important target for star formation studies. Rotationally-supported disks are usually found around low-mass Class I protostars (e.g. Hogerheijde, 2001; Takakuwa et al., 2012; Yen et al., 2014), and a few observational evidences of disks associated with the Class 0 stage have also been reported (e.g. Tobin et al., 2012; Yen et al., 2013, 2017; Murillo et al., 2013; Ohashi et

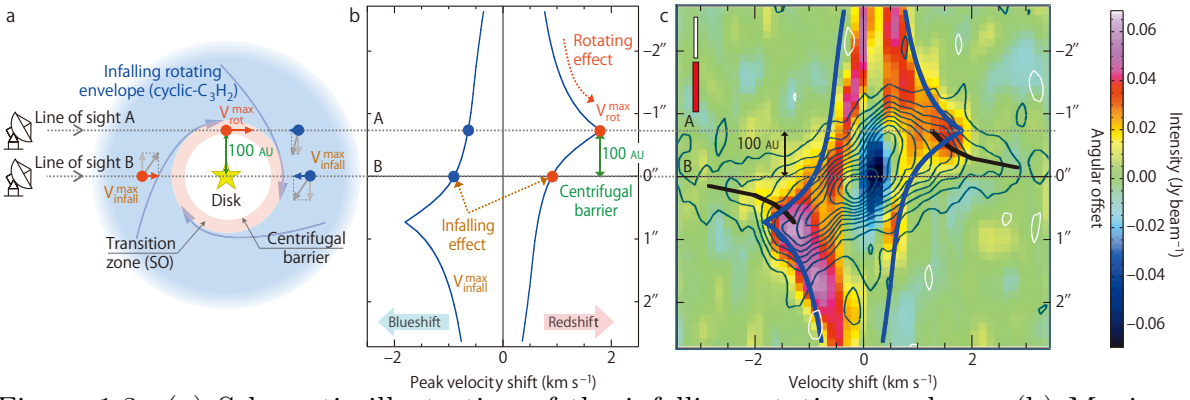

Figure 1.3: (a) Schematic illustration of the infalling-rotating envelope. (b) Maximum velocity-shifts calculated with the model for the edge-on configuration. (c) Position-velocity diagrams of c-C_3H_2 (color) and SO (contours) along the mid-plane of the disk/envelope system in L1527. Blue and black lines represent the maximum velocity-shifts of the infalling-rotating and Keplerian motion, respectively, calculated by using the models explained in Chapter 3. Taken from Sakai et al. (2014a).

al., 2014). Hence, it seems likely that the disk structure is formed in an early stage of protostellar evolution.

The rotation velocity of the Keplerian motion is proportional to $r^{-0.5}$, where r denotes the radius from the protostar. On the other hand, the rotation velocity of the infalling-rotating motion conserving the angular momentum shows r^{-1} dependence. Based on these relations, the disk radius is evaluated as the knee point of the radial dependence of the velocity centroid (e.g., Figure 1.4; Ohashi et al., 2014). However, it should be noted that the evaluation of the disk radius may suffer from the complex structure of the disk/envelope system, if it is not spatially resolved.

Disk formation processes are deeply related to angular momentum of the infalling gas of the envelope. In these early phases of protostellar evolution, energetic outflows blow from protostars, which means that accretion and ejection of mass are occurring at the same time (e.g. Bachiller, 1996). Outflows are thought to play an important role in extracting angular momentum of the infalling gas (e.g. Shu et al., 1994a,b; Tomisaka, 2002; Hartmann, 2009a; Machida & Hosokawa, 2013). Hence, both disk formation and outflow launching are related to angular momentum, and understanding one of the two would help understanding the other.

The existence of the centrifugal barrier of the infalling-rotating envelope and the associated drastic chemical change mentioned above were totally unexpected in star-formation studies and astrochemical studies, and their discovery opened a new door toward understanding physical and chemical processes in disk formation and outflow-launching. I started my PhD work just after the discovery of the centrifugal barrier in L1527.

For better understandings of the observed kinematic structure of the infalling-rotating envelope in L1527, I constructed a simplified three dimensional model assuming the ballistic motion of the gas, and simulated the position-velocity (PV) diagram shown in Figure 1.3. As demonstrated later in Chapter 3, the model successfully reproduce the kinematic structure of the infalling-rotating envelope. From this result, it is confirmed that CCH and c-C_3H_2 preferentially exist in the infalling-rotating envelope. With the aid of this model,

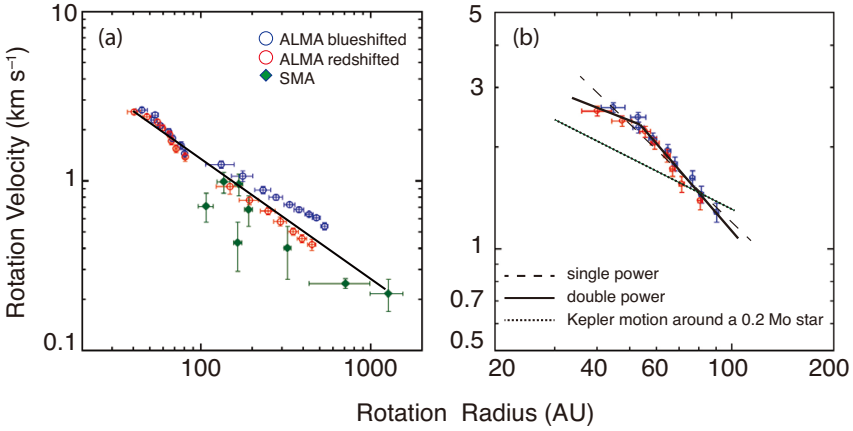

Figure 1.4: Radial dependence of the rotation velocity traced by the $C^{18}O$ line. (a) Blue and red marks represent the data points at the blue- and red-shifted velocities, respectively. Green marks represent the data points observed with SMA (Yen et al., 2013) for comparison. (b) Blow-up of panel (a), where only the data points within the radius of 100 au are shown. The dashed and solid lines represent the least-square fitting with single and two power laws, respectively. The dotted line represents the radial dependence of the Keplerian velocity with the protostellar mass of 0.2 $M_\odot$. Taken from Ohashi et al. (2014).

the protostellar mass and the radius of the centrifugal barrier of L1527 are evaluated to be 0.18 $M_\odot$ and 100 au, respectively. This exercise gave me a strong impression that the model, despite simplified one, can be a powerful tool to extract the physical parameters of the infalling-rotating envelope.

Although the basic concept of the centrifugal barrier had been reported for L1527 by Sakai et al. (2014a), important new questions related to the centrifugal barrier were raised to be addressed. Several of them are:

(1) Is the centrifugal barrier of the infalling-rotating envelope a common occurrence in low-mass protostellar sources?

(2) What is a role of the centrifugal barrier in star formation? How is the disk structure formed inside the centrifugal barrier? Is there any relation between the centrifugal barrier and the outflow launching?

(3) How does the magnetic field affect the centrifugal barrier and the disk formation processes?

(4) What a chemical change occurs at the centrifugal barrier? Is the chemical change different between the WCCC sources and the hot corino sources?

(5) What is the chemical heritage passed from the infalling-rotating envelope to the disk component?

(6) Are there molecular lines that can selectively trace specific physical components (i.e., the infalling-rotating envelope, the centrifugal barrier, and the disk component) for the chemical diagnostics?

To answer these questions, observations of various low-mass protostellar sources other than L1527 are indispensable. In astrophysical and astrochemical studies, we cannot artificially control the environments of the target source unlike the laboratory experiments. It is also impossible to trace the evolution of the target source, because the time scale of the astrophysical and astrochemical phenomena is always quite longer than the lifetime of human beings. Instead, we can investigate the environmental effect and the evolutionary effect by observing a number of sources. Such an approach is standard in astrophysics and astrochemistry. With this in mind, we observationally investigated the physical and chemical structures of five low-mass protostellar sources at a few 10 au scale by using ALMA, as the initial step toward statistical studies. The sources studied in this thesis are listed in Table 1.1. The list involves two WCCC sources (L1527 and IRAS 15398–3359), two hot corino sources (IRAS 16293–2422 Source A and Source B), and one intermediate (mixed) character source (L483). They are all representative low-mass protostellar sources in the Solar neighborhood. By analyzing the observational results with the aid of the kinematic model, the physical and chemical processes occurring in disk formation will be investigated in various protostellar sources. This is the principal aim of this thesis. It will contribute to bridging the missing link in the low-mass star formation process mentioned above.

1.5 Outline of This Thesis

This thesis consists of 11 chapters. After this introductory section (Chapter 1), the mechanisms of an interferometers and the principle of an aperture synthesis are described (Chapter 2). Chapter 3 deals with the kinematic models of the infalling-rotating envelope, the Keplerian disk, and the outflow. In addition to the details of the models, some examples of the model simulations are presented. Chapters 4–8 presents the observational results and analyses for the individual protostellar sources listed in Table 1.1. The overall discussions based on the observational results are given in Chapters 9 and 10 for chemical and physical implications, respectively. Finally, Chapter 11 concludes the thesis with a few future prospects.

Table 1.1: Target Sources Studied in This Thesis.

Source Name	Distance (pc)	Luminosity ($L_\odot$)	Chemistry
L1527	137[a]	1.7[b]	WCCC[c]
IRAS 15398–3359	155[d]	1.8[e]	WCCC[f]
IRAS 16293–2422 Source A	137 – 147[g]	22[h]	hot corino[i]
IRAS 16293–2422 Source B	137 – 147[g]	22[h]	hot corino[i]
L483	200[j]	13[k]	Intermediate[l]

Taken from [a]Torres et al. (2007), [b]Green et al. (2013), [c]e.g., Sakai et al. (2008a), [d]Lombardi et al. (2008), [e]Jørgensen et al. (2013), [f]Sakai et al. (2009a) [g]Ortiz-León et al. (2017), [h]Crimier et al. (2010) assuming d of 120 pc (Knude & Hog, 1998), [i]e.g., Schöier et al. (2002), Cazaux et al. (2003), [j]Jørgensen et al. (2002) and Rice et al. (2006), [k]Shirley et al. (2000), [l]Chapter 8

Chapter 2

ALMA Observation

In this thesis, we utilized the data observed with Atacama Large Millimeter/submillimeter Array (ALMA) to study physical and chemical structures of low-mass protostellar sources. This chapter describes a principle of an aperture synthesis with an interferometer and the basic features of ALMA.

2.1 Principles of Interferometers

ALMA employs a technique of the aperture synthesis, mixing signals from a cluster of antennas, to obtain a radiation source image at a high angular resolution. This technique derives the image of the source from the the difference of the phase between the signals detected by different antennas. Ryle established the technique, and received a Noble Prize for this technique conjointly with Hewish for the other contribution.

2.1.1 Coordinate System

Here, $\vec{s}$ is defined as a unit vector with the direction from the earth to the radiation source. The origin is taken at the center of the radiation source on the plane of the sky. l and m axes are defined along the east-west and south-north direction, respectively, through the origin on the plane of the sky (Figure 2.1). Hereafter, the radiation source is assumed to be distributed within a compact region where $|l|$ and $|m|$ can be assumed to be infinitesimal, and thus the curvature of the plane of the sky is ignored. The vector from one antenna to the other is called as a *'baseline vector'*. Thus a cluster of n antennas has $n\,(n-1)$ baseline vectors. For two antennas with a baseline vector $\vec{D}$, the radiation from the source is detected by them with a mutual time delay (τ_g) of $\frac{1}{c}\left(\vec{D}\cdot\vec{s}\right)$, where c denotes the speed of light. Here, τ_g is called as a *'geometrical delay'* (Figure 2.2).

2.1.2 Correlation Function and Cross Power Spectrum

If the radiation from the source is monochromatic, which is represented as $E\,(t) = E_0 \exp\,(2\pi i \nu_0 t)$, the signals detected by two antennas are represented as:

$$\tilde{E}_1(t) = a_1 E\,(t)\,, \quad \tilde{E}_2(t) = a_2 E\,(t-\tau_g)\,, \tag{2.1}$$

where a_i is the complex gain of the antenna i. When a correction of the delay (τ_i) is applied to the antenna 1, the correlation function of the two signals as a function of a delay time τ is represented as:

$$\begin{aligned} C(\tau) &= \lim_{T\to\infty}\frac{1}{T}\int_{-T/2}^{T/2}\tilde{E}_1(t-\tau_i)\tilde{E}_2^*(t-\tau)dt \\ &= \lim_{T\to\infty}\frac{1}{T}\int_{-T/2}^{T/2}a_1a_2^*|E_0|^2\exp(2\pi i\nu_0((t-\tau_i)-(t-\tau_g-\tau)))dt \\ &= a_1a_2^*|E_0|^2\exp(2\pi i\nu_0(\tau+\tau_g-\tau_i)). \end{aligned} \tag{2.2}$$

$C(\tau)$ is the output data from the interferometer, and the cross power spectrum ($\hat{C}(\nu)$) is obtained by its Fourier transformation as:

$$\begin{aligned} \hat{C}(\nu) &= \int_{-\infty}^{\infty}C(\tau)\exp(-2\pi i\nu\tau)d\tau \\ &= a_1a_2^*|E_0|^2\delta(\nu_0-\nu)\exp(2\pi i\nu_0(\tau_g-\tau_i)). \end{aligned} \tag{2.3}$$

When τ_i is correctly taken to be τ_g, the phase of $\hat{C}(\nu)$ ($2\pi i\nu_0(\tau_g-\tau_i)$) equals to 0. Hence, the cross power spectrum for a monochromatic radiation at a frequency of ν_0 has a non-zero value only for ν of ν_0.

The radiation from the source is not always monochromatic. Even in this case, we can approximate it as the quasi-monochromatic radiation represented as:

$$\begin{aligned} E(t) &= \int_{-\infty}^{\infty}\hat{E}(\nu)\exp(2\pi i\nu t)\,d\nu \\ &= a_m(t)\exp(2\pi i\nu_0 t), \end{aligned} \tag{2.4}$$

where $a_m(t)$ denotes the time dependent amplitude of the radiation. Here, the correlation

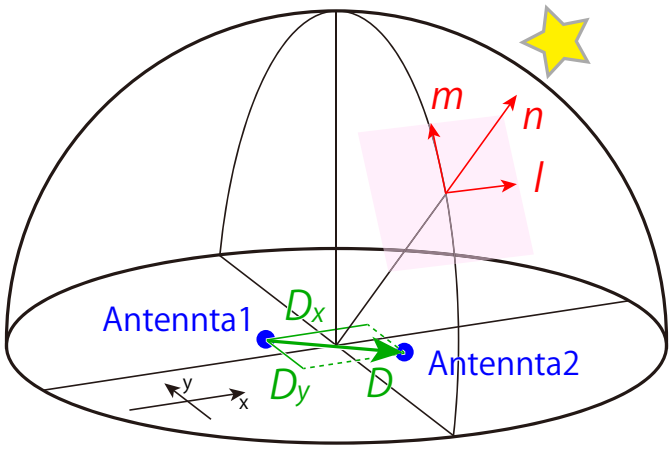

Figure 2.1: Coordinate system of the plane of the sky and a baseline vector.

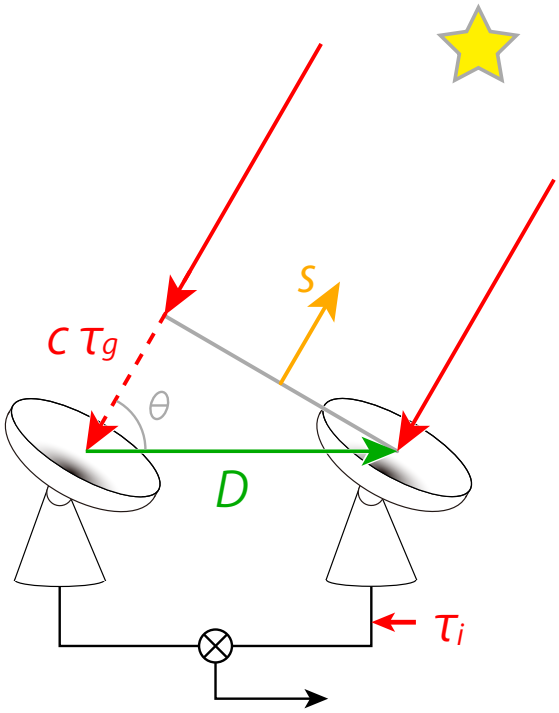

Figure 2.2: Geometrical delay for two antennas.

function (2.2) is rewritten as:

$$\begin{aligned} C(\tau) &= \lim_{T\to\infty}\frac{1}{T}\int_{-T/2}^{T/2}\tilde{E}_1(t-\tau_i)\tilde{E}_2^*(t-\tau)dt \\ &= \lim_{T\to\infty}\frac{1}{T}\int_{-T/2}^{T/2}a_1a_2^*a_m(t-\tau_i)a_m^*(t-\tau_g-\tau_i)\exp(2\pi i\nu_0(\tau+\tau_g-\tau_i))dt \\ &= a_1a_2^* < a_m(t)a_m^*(t) >_T \exp(2\pi i\nu_0(\tau+\tau_g-\tau_i)). \end{aligned} \tag{2.5}$$

Here, the temporal variation of $a_m(t)$ is assumed to be sufficiently longer than $(\tau+\tau_g-\tau_i)$, so that $\lim_{T\to\infty}\frac{1}{T}\int_{-T/2}^{T/2}a_m(t-\tau_i)a_m^*(t-\tau_g-\tau_i)dt$ can be approximated to be the time-averaged power spectrum of the radiation $< a_m(t)a_m^*(t) >_T$ $(= |E_0|^2)$. Then, the cross power spectrum is obtained as:

$$\begin{aligned} \hat{C}(\nu) &= \int_{-\infty}^{\infty}C(\tau)\exp(-2\pi i\nu\tau)d\tau \\ &= a_1a_2^* < a_m(t)a_m^*(t) >_T \delta(\nu_0-\nu)\exp(2\pi i\nu_0(\tau_g-\tau_i)). \end{aligned} \tag{2.6}$$

Again, the phase of $\hat{C}(\nu)$ equals to 0 when τ_i is correctly taken to be τ_g. This, we can treat the radiation as if it were monochromatic.

2.1.3 Visibility

For simplicity, we first consider one-dimensional distribution of the sources on the l axis. We expand the result to the two-dimensional distribution later. With an angular offset of Δl for the position of the radiation source, the phase of $\hat{C}(\nu)$ ($\phi = 2\pi\nu(\tau_g - \tau_i)$) changes by $\Delta\phi$. $\Delta\phi$ is represented as:

$$\begin{aligned}\Delta\phi &= \frac{\partial\phi}{\partial l}\Delta l \\ &= 2\pi\nu\frac{\partial\tau_g}{\partial l}\Delta l \\ &= \frac{2\pi\nu}{c}\frac{\partial}{\partial l}(\vec{D}\cdot\vec{s})\Delta l \\ &= \frac{2\pi}{\lambda}D\cos\theta\Delta l, \end{aligned} \tag{2.7}$$

where θ denotes the angle between the baseline vector ($\vec{D}$) and the direction from the earth to the source center ($\vec{s}(\Delta l = 0)$). Here, $\dfrac{D\cos\theta}{\lambda}$ ($\equiv u$) is called as a *'fringe frequency'*. Thus, Δl is represented by using the relation as: $\Delta\phi = 2\pi u\Delta l$.

We denote the radiation spectra of two radiation sources at l_1 and l_2 as $\hat{E}_1(\nu)$ and $\hat{E}_2(\nu)$, respectively. Then, the intensity distribution on the plane of the sky is represented as $I(\nu, l) = |\hat{E}_1(\nu)|^2\delta(l - l_1) + |\hat{E}_2(\nu)|^2\delta(l - l_2)$. For simplicity, the geometrical delay (τ_g) is assumed to be completely canceled out by its correction (τ_i) for the radiation from the origin ($l = 0$). Then, the phases of the cross power spectra from the radiation source at l_1 and l_2 are represented as:

$$\phi_1 = 2\pi\nu\tau_{g1} = 2\pi u l_1, \quad \phi_2 = 2\pi\nu\tau_{g2} = 2\pi u l_2, \tag{2.8}$$

respectively. Here, τ_{gi} denotes the difference between the geometrical delays for the radiation from the source at the origin and that at l_i. If the radiation from the two sources does not interfere with each other (quasi-monochromatic radiation; Born & Wolf, 1959), their correlation function and cross power spectrum are obtained as the sum of contributions from each radiation source. They are represented as follows:

$$\begin{aligned} C(\tau) &= a_1 a_2^* \int_{-\infty}^{\infty} d\nu \ \left[|\hat{E}_1(\nu)|^2\exp(2\pi i\nu(\tau + \tau_{g1})) + |\hat{E}_2(\nu)|^2\exp(2\pi i\nu(\tau + \tau_{g2}))\right] \\ &= a_1 a_2^* \int_{-\infty}^{\infty} d\nu \ \left[|\hat{E}_1(\nu)|^2\exp(2\pi i u l_1) + |\hat{E}_2(\nu)|^2\exp(2\pi i u l_2)\right]\exp(2\pi i\nu\tau), \end{aligned} \tag{2.9}$$

$$\begin{aligned} \hat{C}(\nu) &= \int_{-\infty}^{\infty} d\tau \ C(\tau)\exp(-2\pi i\nu\tau) \\ &= a_1 a_2^* \int_{-\infty}^{\infty} d\tau \int_{-\infty}^{\infty} d\nu' \ \left[|\hat{E}_1(\nu')|^2\exp(2\pi i\nu'\tau_{g1}) + |\hat{E}_2(\nu')|^2\exp(2\pi i\nu'\tau_{g2})\right] \\ &\quad \times \exp(2\pi i(\nu' - \nu)\tau) \\ &= a_1 a_2^* \left(|\hat{E}_1(\nu)|^2\exp(2\pi i u l_1) + |\hat{E}_2(\nu)|^2\exp(2\pi i u l_2)\right). \end{aligned} \tag{2.10}$$

As for the case with more radiation sources, the intensity distribution is represented as: $I(\nu, l) = \sum_k |\hat{E}_k(\nu)|^2\delta(l - l_k)$. The cross power spectrum is then obtained as:

$\hat{C}(\nu) = a_1 a_2^* \sum_k |\hat{E}_k(\nu)|^2 \exp(2\pi i u l_k)$. For a continuous source distribution, the cross power spectrum is represented by an integral as:

$$\begin{aligned}\hat{C}(\nu) &= a_1 a_2^* \int_{\text{source}} dl\ |\hat{E}(\nu, l)|^2 \exp(2\pi i u l) \\ &= a_1 a_2^* \int_{\text{source}} dl\ I(\nu, l) \exp(2\pi i u l). \end{aligned} \tag{2.11}$$

Here, $\hat{C}(\nu)$ can be regarded as a function of the fringe frequency (u), which is denoted as $V(\nu, u)$. $V(\nu, u)$ is called as a *'complex visibility'*. When the intensity distribution $I(\nu, l)$ equals 0 outside the radiation source, it is represented as

$$V(\nu, u) = a_1 a_2^* \int_{-\infty}^{\infty} dl\ I(\nu, l) \exp(2\pi i u l) \tag{2.12}$$

by extending the integral area to all l. Here, $V(\nu, u)$ is the Fourier transform function of $I(\nu, l)$ with respect to u and l. Hence, once the visibility data $V(\nu, u)$ at a specific frequency (ν) is obtained by observations for every fringe frequency (u), the intensity distribution of the radiation source $I(\nu, l)$ at the frequency (ν) is derived from the visibility data by applying Fourier transformation to it. An interferometer is a device to observe $V\left(\nu, u = \dfrac{D\cos\theta}{\lambda}\right)$ for every baseline vector $\vec{D}$ of each pair of two antennas.

2.2 ALMA

ALMA (Figure 2.3) is the largest radio interferometer working in the millimeter- and submillimeter-wave regions, which is located at the high altitude (5000 m) site (Llano de Chajnantor) of the Atacama desert of northern Chile. It was constructed by the trilateral international partnership among East Asia (including Japan), North America, and Europe. The construction was started in 2002, and the early science operation was started with the limited number of the array antennas in September 2011. Finally, the inauguration of ALMA was declared in March 2012. ALMA is now being operated by the Joint ALMA observatory, which is funded by ESO, AUI/NRAO, and NAOJ.

2.2.1 ALMA Site

Llano de Chajnantor is an excellent site for millimeter- and submillimeter interferometry. This site is very dry over the whole year. This is essential, because the submillimter-wave are strongly absorbed by the water vapor contained in the atmosphere. At this site, the precipitable water vapor (pwv) is often below 0.5 mm, which allows us to conduct good observations even at the frequency from 400 GHz to 1000 GHz. Moreover, the site is reasonably flat over a large area, and hence, the large array of antennas can be extended with the maximum baseline length of 18.5 km. Such a long-baseline configuration enables us to achieve a very high angular resolution of $0''.01$ at the wavelength of 1 mm (300 GHz). This angular resolution is higher by about ten times than that of Subaru Telescope of $0''.2$ ($\lambda = 2.15\mu$m).

Figure 2.3: Atacama Large Millimeter/submillimeter Array (ALMA)

2.2.2 Antennas

ALMA consists of 54 antennas with a diameter of 12 m and 12 antennas with a diameter of 7 m. Thus the total number of antennas is currently 66. The 12 m and 7 m antennas have a surface accuracy better than 25 μm and 20 μm (ALMA Partnership, 2017), which is much smaller than the wavelength of the highest frequency (0.2 mm). The highly accurate surface ensures a high aperture efficiency. Fifty 12-m antennas compose the main array (or the 12 m array). The main array is used for observations at various angular resolution. The array configuration is changed little by little (almost monthly) by moving some antennas from the stations to the others. Thus the configuration is extended from the most compact configuration to the most extended configuration for about a half year, and then back to the most compact configuration for another half year. This allows the observers to choose the best angular resolution needed their observations. Four 12-m antennas (the total power array) and 12 7-m antennas constitute Atacama Compact Array (ACA) or Morita Array. Since the baseline length between neighboring antennas can be relatively short (7 m in principle) in comparison with that between the 12 m antennas (12 m in principle), the low spatial frequency component can be recovered by the ACA system. Furthermore, the total power array provides the visibility data for the zero baseline spacing.

2.2.3 Receivers

ALMA covers all the atmospheric windows from 30 GHz to 950 GHz. For this purpose, 10 receiver bands (Band 1 to 10) are defined as listed in Table 2.1, and a high-sensitivity receiver is prepared for each receiver band. The receiver bands cover the atmospheric transmission windows (Figure 2.4). At this moment, Band 1 and Band 2 have not been com-

missioned yet, and Band 5 is now being installed. All the receivers except for Band 1 make use of the superconducting mixers called SIS (superconductor-insulator-superconductor) mixers whose receiver temperature is a few times the quantum noise ($h\nu/k$). All the receivers equip two mixer systems sensitive to the orthogonal linear polarization signals. Moreover, the 2 sideband (2SB) mixer is employed except for the higher frequency bands (Band 9 and 10), where the upper sideband (USB) and the lower sideband (LSB) signals are separated in the mixer and are observed simultaneously. These state-of-the art technologies realizes very high sensitivity of ALMA in combination with the good observing condition of the site. Roughly speaking, the sensitivity for point sources are higher than those of the other single-dish telescopes and interferometers by two orders of magnitude.

Table 2.1: Frequency Ranges of ALMA Bands[a]

ALMA Band	Frequency Range (GHz)
1	31 – 45
2	67 – 90
3	84 – 116
4	125 – 163
5	162 – 211
6	211 – 275
7	275 – 373
8	385 – 500
9	602 – 720
10	787 – 950

[a] Taken from ALMA website (http://www.almaobservatory.org/en/about-alma/how-does-alma-work/technology/front-end).

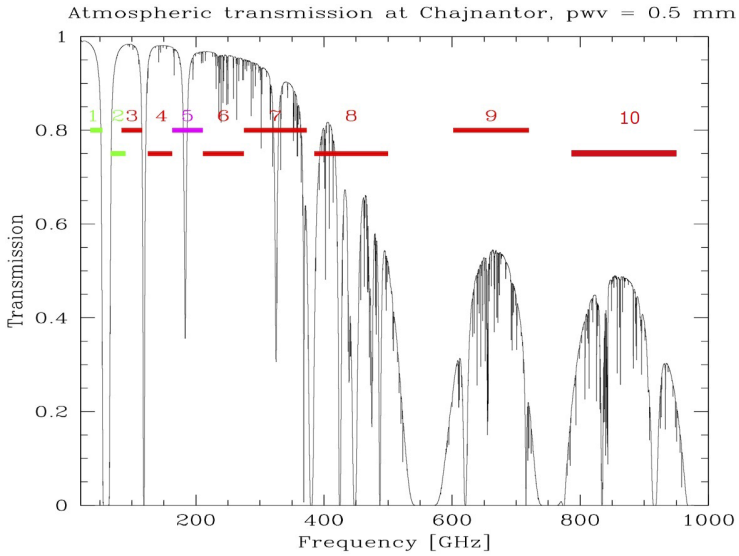

Figure 2.4: The ALMA receiver bands and the zenith atmospheric transparency plot at the Array Operation Site for 0.5 mm of Precipitable Water Vapor (PWV). Taken from ALMA Partnership (2017).

2.2.4 Backends

ALMA has a strong bank of backend correlators. The correlators for the main array can be used in the various modes with different frequency resolutions and total bandwidths. They are summarized in Table 2.2. For the continuum observation or the observation of broad spectral lines (e.g. external galaxies), the mode with a lower spectral resolution and a wide bandwidth is useful to maximize the sensitivity. On the other hand, the high resolution mode is employed to study the kinematic structure of the source in detail. It is also useful for line identification in a congested spectrum. The correlator setup is quite flexible. One can set two sub-bands each in USB and LSB, and four chunks of the correlator each in sub-bands. Hence, 16 frequency ranges can be observed simultaneously in total. This is very powerful for astrochemical studies, because various molecular lines can be observed at once under the identical observation condition.

The high frequency resolution is also powerful for astrophysical studies, because it allow us to know the velocity of the molecular gas. If the molecule is moving at a certain velocity, the line frequency of the molecule shifts from its rest frequency by the Doppler effect. The doppler shifted frequency (f') is represented as:

$$f' = \frac{c}{c+v} f, \tag{2.13}$$

where c denotes the speed of light, v the velocity of the molecule along the line of sight, and f the rest frequency of the molecule. In this study, v is sufficiently smaller than c, and thus f' can be approximated by $\left(1 - \frac{v}{c}\right) f$. The ALMA correlator can resolve even the fine change in f due to the Doppler effect. The velocity resolution with the rest frequency f of 100 GHz is also summarized in Table 2.2. The velocity resolution better than the sound speed of the molecular-cloud gas ($\sim$0.2 km s^{-1}) can readily be achieved.

Table 2.2: Frequency Resolutions and Total Bandwidths of ALMA Correlators[a]

Total Bandwidth (MHz)	Number of Channels	Frequency Resolution (kHz)	Velocity Resolution at 100 GHz (km s^{-1})
2000	128	15625	46.84
1875	3840	488	1.46
936	3840	244	0.73
469	3840	122	0.37
234	3840	61	0.18
117	3840	30.5	0.09
58.6	3840	15.3	0.05

[a] The total bandwidths, number of channels, and frequency resolutions are taken from (ALMA Partnership, 2017).

2.3 Observations with Interferometers

2.3.1 Calibration

The output data from an interferometer (*'observed complex visibility function'*) suffer from amplitude variations and phase delays due to the array hardware as well as the atmospheric absorption and scintillation. Thus, calibrations are required to obtain the true visibility function, which is physically related to the angular and spectral distribution of the target source, from the raw observed data. Here, the major calibrations required for interferometers are briefly described.

Phase Calibration

The phase calibration is the calibration for the phase of the visibility function. The phase of the visibility function, which contains the information of the position of the radiation source distribution, suffers from the atmosphere delay over each antenna and the instrumental delay in the array. In order to eliminate these effects, the phase calibration is performed toward a well-known calibrator source every several minutes (e.g. 8 minutes in the ALMA observations in Chapter 6) during the observation. A phase calibrator source should be close to the science target, and its position, spectrum, and flux density should accurately be known. In order to determine the phase center accurately, the angular size of the phase calibrator has to be sufficiently small in comparison with the beam size of the observation. Thus quasars are often used as the phase calibrator because their true visibility function can be modeled. The phase calibrator sources used in this study are listed in Table 2.3. If the target source is enough bright, the phase calibration can be done with the target source itself. This procedure is called as *'self-calibration'*. We applied the self-calibration to the analyses for IRAS 16293–2422 Source B and L483 (Chapters 7 and 8).

In addition, a water vapor radiometer (WVR) is used for the short-term fluctuation of the phase delay due to the atmosphere. Since the delay is caused by the water vapor, it is related to the precipitable water vapor (pwv). The delay can be corrected by measuring the temporal fluctuation of the pwv by WVR equipped on each antenna. This method, which is automatically done in the observation, allows us to achieve the high angular-resolution performance of ALMA.

Bandpass Calibration

The frequency response of the interferometer is corrected by the bandpass calibration. The bandpass calibration is performed with a bright calibrator source, which has a known radio spectral index without spectral features. Some bright quasars are typically used as a bandpass calibrator. The frequency response is almost stable over many hours, and nearly independent of the sky position of the radio source. Thus, the bandpass calibration is performed only the start or end of the observation, or additionally a few times during the observation. The bandpass calibrations typically takes a half or one hour. However, if the observation for other calibrations is performed toward a sufficiently bright source, it can be also used for the bandpass calibration. The bandpass calibrator sources used in this study are listed in Table 2.3.

Gain and Flux Density Calibrations

The absolute flux density of the target source is obtained by applying the gain calibration and the flux density calibration. The relative amplitude between the phase calibrator and the target source is determined by the gain calibration. The scale from the observed amplitude to the absolute flux density is usually obtained by observations toward a Solar System object. The flux density of the flux calibrator is monitored by the ALMA observatory and its recent value is accurately known. The observations toward flux calibrator should be performed in each phase calibration. However, if the antenna gains are sufficiently stable, the observation for the flux calibration is performed only once at the start of the observation in order to scale the absolute flux of the phase calibrator. Then the absolute flux of the target source can be derived from the relative amplitude to the phase calibrator. For the ALMA Cycle 5 observation, the flux density model accuracy is 3-15% at Band 3-9 for the Solar System objects. The flux calibrator sources used in this study are listed in Table 2.3.

2.3.2 Observed Intensity Distribution

In the actual observational studies, the visibility data (2.12) is two-dimensional, and is represented as $V(\nu; u, v)$. Here, the fringe frequencies u and v are represented as:

$$u = \frac{D_x \cos\theta}{\lambda}, \quad v = \frac{D_y \cos\phi}{\lambda}, \tag{2.14}$$

where θ and ϕ are the components of the apparent angle between the baseline vector ($\vec{D}$) and the direction from the earth to the source center ($\vec{s}$) projected onto the (l, n)- and (m, n)-plane, respectively. D_x and D_y denote the component of $\vec{D}$ along the x- and y-axis. The intensity distribution of the radiation source on the plane of the sky $I(\nu; l, m)$ is obtained by applying two dimensional Fourier transformation to $V(\nu; u, v)$ for u and v. Practically, the number of antennas of an interferometer is limited, so that $V(\nu; u, v)$ is observed only for a limited number of the (u, v) values, and the data for the remaining (u, v) values are missing. Hence, the observed data $\tilde{V}(\nu; u, v)$ can be regarded as the product of the real visibility data $V(\nu; u, v)$ and a two dimensional function $U(u, v)$. $U(u, v)$ is called as the *'(u, v)-coverage'*. It has a non-zero value for (u, v) corresponding to a certain baseline vector in an interferometer, while it equals 0 for the other (u, v) without the observed visibility data. Since the array of the antennas rotates relative to the target source due to the earth rotation, each pair of two antennas draws a part of

Table 2.3: Calibrator Sources Used in This Study

Chapter	Science Target	Phase Calibrator	Bandpass Calibrator	Flux Calibrator
4	L1527	J0510+180	J0423–013	Callisto
5	IRAS 15398–3359	J1517–243	J1256–057, J1924–292	Mars, Titan
6, 7	IRAS 16293–2422	J1625–2527	J1427–4206	Titan
8	L483	J1733–1304	J1733–1304	Titan

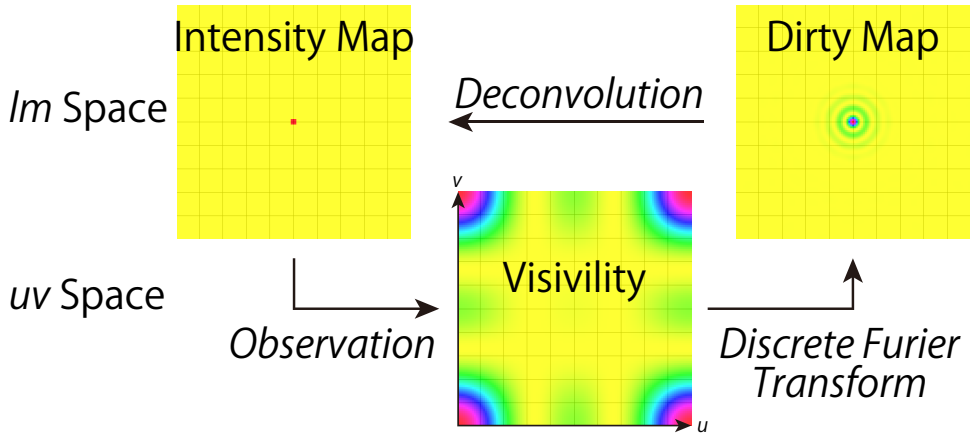

Figure 2.5: Relations between the maps of the real intensity distribution, the observed visibility data, and the observed intensity distribution.

a conic section in the (u, v)-plane. This effect can be used for a better coverage of the (u, v)-plane.

The image of the intensity distribution $\tilde{I}(\nu; l, m)$ is obtained by Fourier transformation of the observed visibility data $\tilde{V}(\nu; u, v)$. $\tilde{I}(\nu; l, m)$ does not reproduce the real intensity distribution $I(\nu; l, m)$ perfectly, as shown in Figure 2.5, due to an imperfect (u, v)-coverage of the visibility data. The fringe frequency (u, v) is related to the spatial frequency component in $I(\nu; l, m)$. The values of $V(\nu; u, v)$ for a set of small values of (u, v) correspond to the low spatial frequency component of $I(\nu; l, m)$, or an extended component, while those for a set of large values of (u, v) do the high frequency component, or a compact component. Hence, the integrated value of the observed intensity $\left(\int dldm\ \tilde{I}(\nu; l, m) \right)$ is generally lower than that of the real intensity $\left(\int dldm\ I(\nu; l, m) \right)$, and their difference is called as *'missing flux'*. Specifically, if the visibility data with (u, v) close to the origin is missing, extended components of the radiation source is not reproduced. It is called as *'resolving out'*. We define the Fourier-transformed function of $U(u, v)$ as $B(l, m)$. Since $\tilde{I}(\nu; l, m)$ is the Fourier-transformed function of the product of $V(\nu; u, v)$ and $U(u, v)$, it is represented as the convolution of $I(\nu; l, m)$ with $B(l, m)$:

$$\begin{aligned} \tilde{I}(\nu; l, m) &= \int dudv\ V(\nu; u, v) \cdot U(u, v) \exp(-2\pi i(ul + vm)) \\ &= I(\nu; l, m) * *B(l, m). \end{aligned} \tag{2.15}$$

Here, $B(l, m)$ is called as *'synthesized beam'*. If $U(u, v)$ is unity for all (u, v) values, $B(l, m)$ is represented as $\delta(l)\delta(m)$. In reality, $U(u, v)$ takes non-zero values only for the observed (u, v) values, and $B(l, m)$ has a width inversely proportional to the maximum u and v values. If the visibility data with the large (u, v) values are missing, compact components of the radiation source are not reproduced. Thus, the longest baseline (the largest (u, v) value) determines the angular resolution of the interferometer.

2.3.3 CLEAN Method

$\tilde{I}(\nu; l, m)$ obtained with using the equation (2.15) is called as *'dirty map'*. It is the convolution function of the real intensity distribution $I(\nu; l, m)$ with the synthesized beam $B(l, m)$ as shown in Figure 2.5. A dirty map suffers from a spurious wavy distributions on the real intensity distribution, which is called as a *'side lobe'*. In order to reproduce the image of the observed intensity distribution closer to the real one, a *'deconvolution'* procedure, which is an operation to eliminate the effect of the synthesized beam from the image, is usually performed the analysis of interferometer data. Since the real $V(\nu; u, v)$ for missing (u, v) is unknown, the image obtained by the deconvolution is not unique due to this uncertainty. In this study, the *'CLEAN'* method is employed to obtain an appropriate image.

CLEAN is a method of the deconvolution suggested by Högbom (1974), and is commonly used in radio interferometry. In the CLEAN method, the intensity distribution of the radiation source is modeled by a set of point sources. A point source is supposed at the intensity peak in a dirty map, and its convolved image with the synthesized beam (or *'dirty beam'*) is calculated. The convolved image, including its side lobe, is subtracted from the dirty image, and thus the effect of the spurious component is reduced. This operation is repeated specified times or until the peak intensity in the residual image becomes lower than a specified value. After that, the residual image has distributions, side lobe, and noise, which are expected to be much weaker than the modeled image. Then, the modeled image, which is a set of point sources, is convolved with an ideal beam function (or *'CLEAN beam'*), and is added together with the residual image to estimate the real intensity distribution $I(\nu; l, m)$. In the process, the Gaussian beam with the same FWHM (full width at half maximum) as that of the synthesized beam $B(l, m)$ is commonly employed as the CLEAN beam. Figure 2.6(a) shows examples of the dirty map and the image obtained after applying the CLEAN method. These are the distribution of H_2CO $(5_{1,5} - 4_{1,4})$ observed toward the low-mass Class 0 protostellar source IRAS 15398–3359with ALMA (Chapter 5). Twenty-five antennas were used in these observations. These images are derived from the observed visibility data with a (u, v) coverage shown in Figure 2.6(b). Figure 2.6(c) is the *'point spread function'*, which is the convolved image of a point source with the dirty beam.

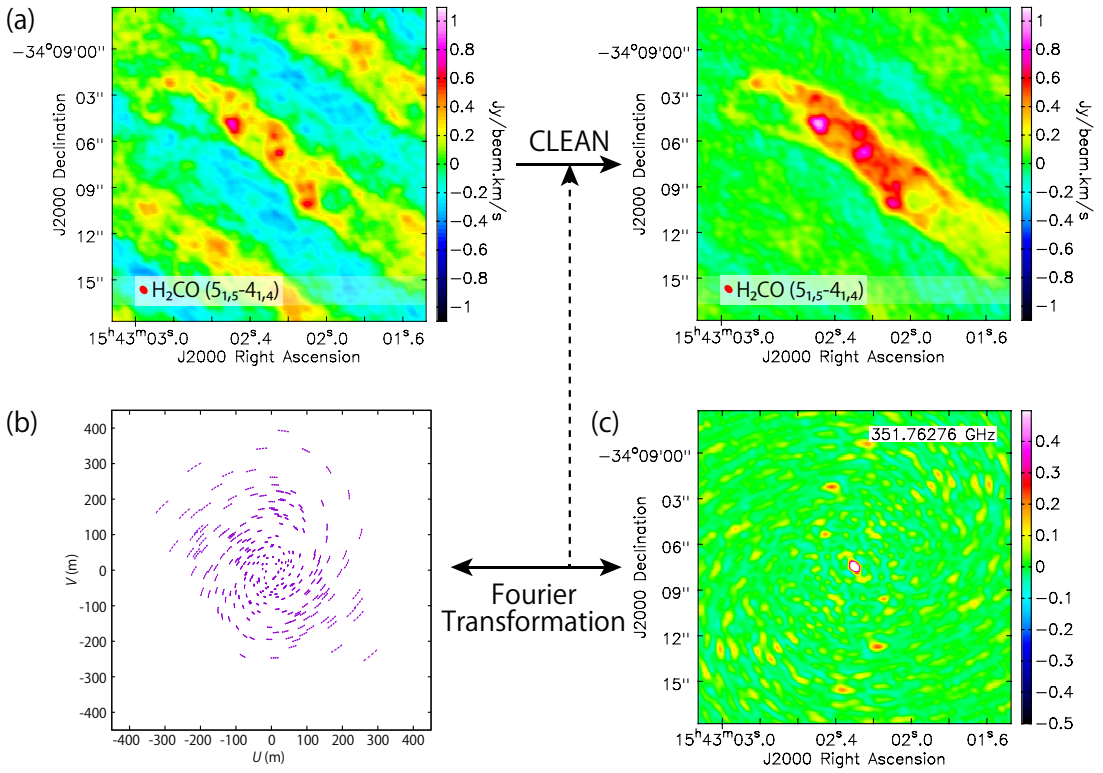

Figure 2.6: (a) Dirty map and the CLEANed image of the H_2CO $(5_{1,5} - 4_{1,4})$ line toward IRAS 15398–3359 observed with ALMA. (b) (u, v)-coverage of this observation. (c) Point spread function of this observation, which corresponds to the dirty map observed toward a ideal point source with the intensity of unity. These panels show the case for the frequency (∼351.763 GHz) almost correspond to the doppler-shifted frequency by the systemic velocity of the source (∼5 km s^{-1}).

Chapter 3

Model Calculation

In this thesis, we investigate the high angular resolution observations toward five low-mass protostellar sources with ALMA (Table 1.1). The observational results are discussed in Chapters 4–8. For each source, we characterize the physical structure of the gas with the aid of some simple physical models. For the envelope components around the protostar, we prepare an infalling-rotating envelope model (Oya et al., 2014). We also employ the Keplerian disk model for the disk components. We calculate the three dimensional velocity field in a disk/envelope system, and project it on to the plane of the sky to compare it with the observed kinematic structure of the gas. The model results are convolved with the intrinsic line width and the Gaussian beam for fair comparison with the observations. As for the outflow components, we employ a standard parabolic model (Lee et al., 2000). We here describe the details of the above models. We also present some representative examples of the model results, demonstrating their dependences of the kinematic structure on the physical parameters.

3.1 Introduction

As shown in Chapters 4–8, we detect the disk and envelope components associated to the protostar and the bipolar outflow launched in the vicinity of the protostar. These components are heavily contaminated with one another, and thus their disentanglement is essential to investigate the geometrical and kinematic structure around the protostar. For this purpose, we employ simple models of an envelope, a disk, and an outflow to calculate their kinematic structure, and use it to disentangle the contaminated components obtained by the observations. Moreover, the models are useful to evaluate physical parameters, such as the protostellar mass, the specific angular momentum of the gas, and the inclination angle of the disk/envelope system.

It is generally thought that the mid-plane of the disk/envelope system and the outflow axis are almost perpendicular to each other. We can thus constrain their configuration if one of them is characterized. In Chapters 4–8, we therefore start with characterization of the component detected more clearly in each source. For instance, the disk/envelope system is more clearly delineated than the outflow component in L1527 (Chapter 4), while the outflow is more clearly delineated in IRAS 15398–3359 (Chapter 5).

3.2 Infalling-Rotating Envelope Model

3.2.1 Configuration of the Infalling-Rotating Envelope Model

We made a ballistic model of an infalling-rotating envelope (Oya et al., 2014). The basic concept of this model is introduced to explain the kinematic structure of the infalling-rotating envelope of L1527 (Sakai et al., 2014a). Here, it is improved to consider the velocity field in the three dimensional space with the convolution by the beam size and the velocity resolution.

Figure 3.1 shows the schematic illustration of the 'infalling-rotating envelope' model. In this model, the gas is simply assumed to be falling and rotating under the gravity of the central protostar. The motion of the gas is approximated by the particle motion, ignoring effects of gas pressure, magnetic field, self gravity, and so on. Because of the energy and angular momentum conservation, the gas cannot fall inward of a certain radius, or the 'perihelion'. This position is called as 'centrifugal barrier'. The radius of the centrifugal barrier ($r_{\rm CB}$) is represented as:

$$r_{\rm CB} = \frac{j^2}{2GM}, \tag{3.1}$$

where G is the gravitational constant, M is the protostellar mass, and j is the specific angular momentum of the gas. It is the radius at which all the kinetic energy is converted to the rotational energy. It is a half of the centrifugal radius ($r_{\rm CR}$), where the gravitational force and the centrifugal force balance each other out:

$$\begin{aligned} r_{\rm CR} &= \frac{j^2}{GM} \\ &= 2r_{\rm CB}. \end{aligned} \tag{3.2}$$

The rotation and infall velocities ($v_{\rm rot}$ and $v_{\rm fall}$) of the gas at the distance of r to the protostar are represented as follows:

$$\begin{aligned} v_{\rm rot} &= \frac{j}{r} \\ &= \frac{1}{r}\sqrt{2GMr_{\rm CB}}, \end{aligned} \tag{3.3}$$

$$\begin{aligned} v_{\rm fall} &= \sqrt{\frac{2GM}{r} - v_{\rm rot}^2} \\ &= \frac{1}{r}\sqrt{2GM\left(r - r_{\rm CB}\right)}. \end{aligned} \tag{3.4}$$

Thus, the velocity field is determined by M and $r_{\rm CB}$. The inclination angle (i) of the disk/envelope system also affects the apparent velocity along the line of sight. At the centrifugal barrier, $v_{\rm fall}$ equals to 0, and $v_{\rm rot}$ takes its maximum value. On the other hand, $v_{\rm fall}$ takes its maximum value at the centrifugal barrier. The values of $v_{\rm rot}$ and $v_{\rm fall}$ as a function of the radius from the protostar are plotted in Figure 3.2.

In this model, the distribution of the gas is assumed to have a power-law. The power-law of $r^{-1.5}$ corresponds to the density profile of an infalling cloud (e.g. Shu, 1977; Ohashi

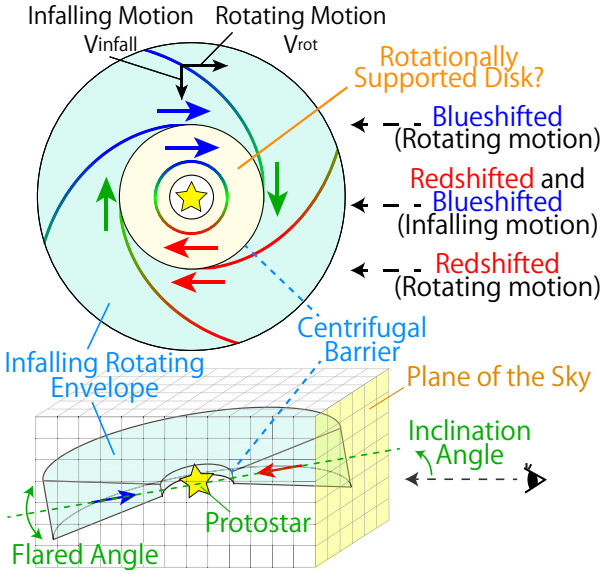

Figure 3.1: Schematic illustration of the infalling-rotating envelope model. The space and the velocity field are sectioned into meshes.

et al., 1997; Harvey et al., 2003). Optically thin condition is also assumed, where the intensity of the line emission is proportional to the column density along the line of sight. Namely, excitation effects and radiative transfer effects are not considered. These assumptions are rather arbitrary in this study, because our main interest in the model analysis is on the velocity field of the gas around the protostar.

The spectral line is assumed to have an intrinsic Gaussian profile with a certain line width, and the emission is convolved with a Gaussian beam with a certain full width at half maximum (FWHM) (Figure 3.3). The intrinsic line width and the beam size are employed depending on each source. The mesh sizes are also appropriately chosen for each source.

Figure 3.4 shows an example of the results of the infalling-rotating envelope model. Its physical parameters are summarized in the caption. Figure 3.4(a) shows the integrated intensity map. The envelope is assumed to have an edge-on configuration extended along the east-west axis, where the left- and right-hand sides correspond to east and west, respectively. The integrated intensity relative to its peak value in the panel is shown in color scale. The protostar with a mass (M) of 0.1 $M_{\odot}$ exists at the central position in Figure 3.4(a). The distance to the source from the Sun (d) is set to be 100 pc, where $1''$ corresponds to 100 au. The envelope has an outer radius (R) of 500 au, outside which there is no molecule. The radius of the centrifugal barrier is 100 au, and the molecular density is zero inside the centrifugal barrier. The integrated intensity is highest around the centrifugal barrier.

Figure 3.4(b) shows the position-velocity (PV) map along the blue arrow shown in Figure 3.4(a). The angular offset of $0''$ corresponds to the protostellar position. The vertical axis represents the line-of-sight velocity of the molecules relative to the systemic velocity of the source. In Figure 3.4(b), a spin-up feature can be seen along the east-west axis; the rotation velocity of the molecules increases as approaching to the protostar till

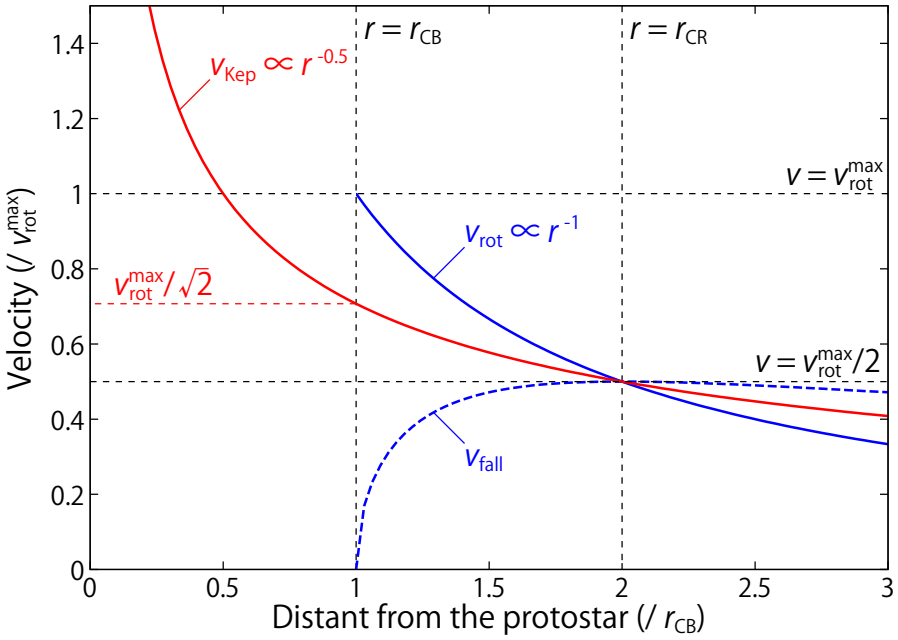

Figure 3.2: The velocity of the gas in the infalling-rotating envelope and Keplerian disk model as a function of the distance from the protostar. The horizontal axis represents the distance from the protostar (r) normalized by the radius of the centrifugal barrier ($r_{\rm CB}$), and the vertical axis represents the velocity (v) normalized by the rotation velocity of the infalling-rotating envelope model at the centrifugal barrier ($v_{\rm rot}^{\rm max}$). The blue solid and dashed lines represent the rotation ($v_{\rm rot}$) and infall ($v_{\rm fall}$) velocities of the infalling-rotating envelope model. $v_{\rm fall}$ equals 0 at the centrifugal barrier ($r = r_{\rm CB}$), and $v_{\rm rot}$ takes its maximum value there. On the other hand, $v_{\rm fall}$ takes the maximum value at the centrifugal radius ($r_{\rm CR}$= 2 $r_{\rm CB}$). The red solid line represents the Keplerian velocity ($v_{\rm Kep}$). All of $v_{\rm rot}$, $v_{\rm fall}$, and $v_{\rm Kep}$ take the same value ($v = v_{\rm rot}^{\rm max}/2$) at the centrifugal radius ($r_{\rm CR}$).

the centrifugal barrier. The velocity takes its maximum and minimum values around the centrifugal barrier, where the velocity is positive (red-shifted) and negative (blue-shifted) in the eastern and western sides of the protostar, respectively. Toward the protostellar position, only a velocity shift due to the infall motion can be seen. The infall motion can also be confirmed as the counter velocity component (Figure 3.4b).

3.2.2 Infalling-Rotating Envelope Model with Various Physical Parameters

In this study, we evaluate physical parameters of low-mass protostellar sources by comparing the observed kinematic structure of the gas and the infalling-rotating envelope model. For this purpose, we here show how sensitive to the physical parameters the model results are for some cases.

The infalling-rotating envelope model has three major physical parameters; M, $r_{\rm CB}$, and i. The apparent distribution of the line emission projected onto the plane of the sky

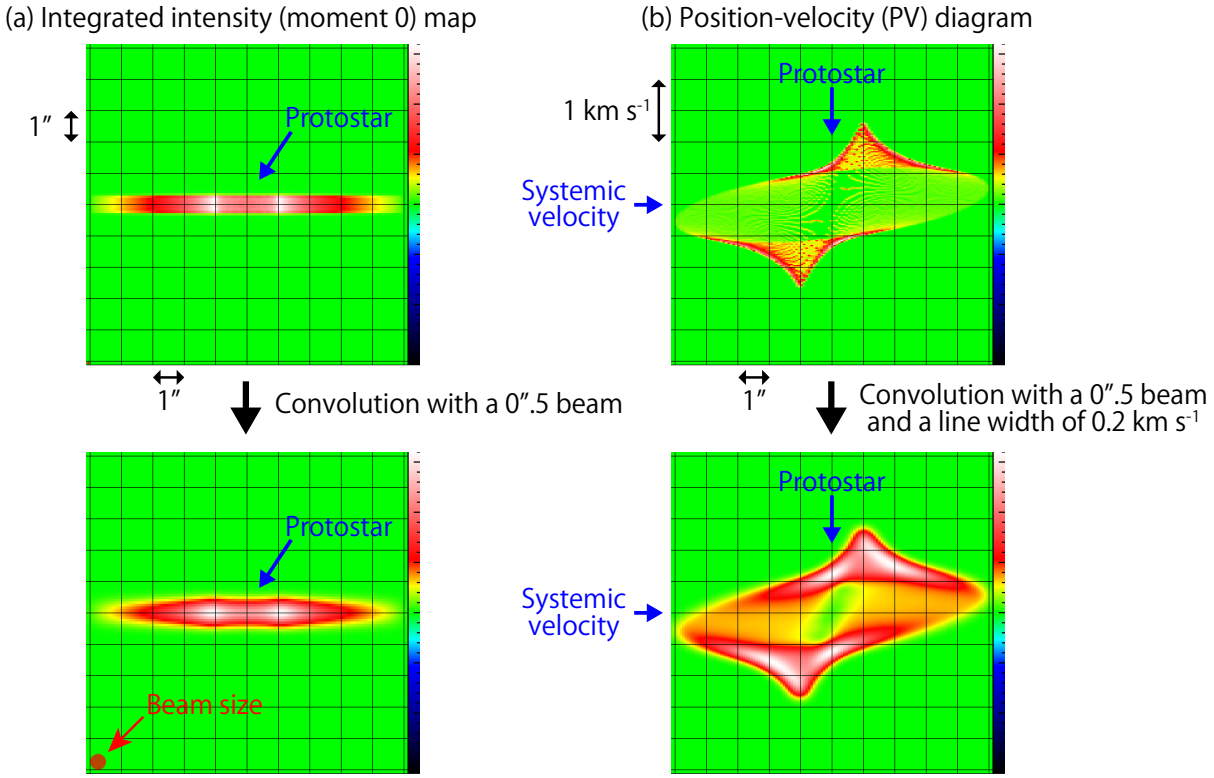

Figure 3.3: Effects of the convolution of the line emission with an intrinsic Gaussian profile (FWHM = 0.2 km s^{-1}) and a Gaussian beam (0.″5 × 0.″5) in the infalling-rotating envelope model. The color scales represent the intensity of the line emission. Panels (a) and (b) show the integrated intensity map and the position velocity (PV) map along the disk/envelope system, respectively. In these models, the inclination angle (i) of 90° (an edge-on configuration) is employed for simplicity.

is determined by $r_{\rm CB}$ and i. Figure 3.5 shows the integrated intensity maps for various sets of $r_{\rm CB}$ and i. Here, i of 0 and 90° corresponds to face-on and edge-on configurations, respectively. The FWHM value of the Gaussian beam (angular resolution) is 0.″5 (50 au). The other physical parameters are summarized in the caption of Figure 3.5. With the edge-on configuration (i = 90°), the integrated intensity maps show a flattened feature. The maps with $r_{\rm CB}$ of 10 and 30 au shows single-peaked distributions, Their centrifugal barriers seem to be almost unresolved with the beam of 0.″5. On the other hand, the maps with $r_{\rm CB}$ of 100 and 300 au shows double-peaked distributions. The peak positions seem to correspond to the positions of their centrifugal barriers; namely, their centrifugal barriers are spatially resolved with the beam. At i of 60° (nearly edge-on), the hole of the distribution is clearly seen in the panels for $r_{\rm CB}$ of 100 and 300 au. Although the model for $r_{\rm CB}$ of 30 au does not show a clear double-peaked distribution at i of 60°, it shows an intensity dip toward the protostar at i of 30° (nearly face-on). With the face-on configuration (i = 0°), the distributions show completely circlic or ring-like structures. The intensities have their maximum value around the centrifugal barriers.

The velocity field of the gas is determined by M, $r_{\rm CB}$, and i. For easy comparison with observations, we calculate the velocity along the line of sight ($v_{\rm shift}$) in each mesh. Figure

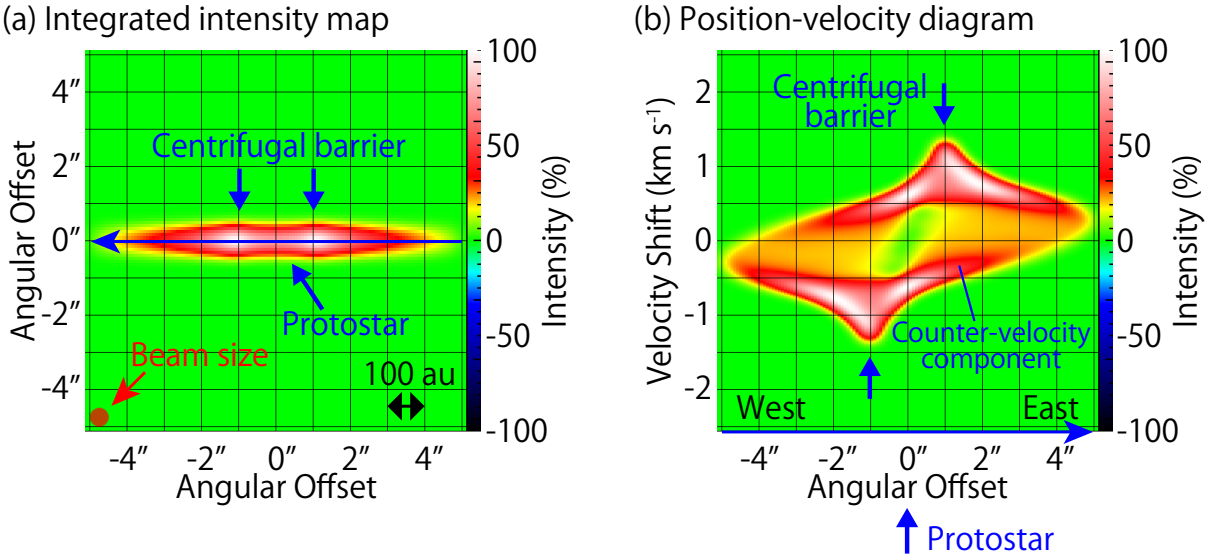

Figure 3.4: The results of the infalling-rotating envelope model. Panels (a) and (b) show its integrated intensity map and position-velocity diagram, respectively. The position axis in panel (b) is taken along the blue horizontal arrow shown in panel (a), along which the mid-plane of the envelope is extended. The physical parameters of the model is as follows; the distance to the source from the Sun (d) of 100 pc, the protostellar mass (M) of 0.1 $M_{\odot}$, the radius of the centrifugal barrier ($r_{\rm CB}$) of 100 au, the inclination angle of the disk/envelope system (i) of 0° (0° for a face-on configuration), and the outer radius of the envelope (R) of 500 au. The scale height of the envelope is assumed to be 50 au independent of the radius. The mesh size for the calculation is 0.″08 (8 au), and $128 \times 128 \times 128$ meshes are applied to cover the cubic space of $10.''24 \times 10.''24 \times 10.''24$ ($1024 \times 1024 \times 1024$ au^3). The mesh size for the velocity axis is 0.02 km s^{-1}, and 256 meshes are applied to cover the velocity range from -2.56 km s^{-1} to 2.56 km s^{-1}. The intensity is convolved with the intrinsic line width of 0.2 km s^{-1} and the beam of $0.''5 \times 0.''5$.

3.6 shows the moment 1 maps with the various sets of $r_{\rm CB}$ and i. The FWHM value of the Gaussian beam is 0.″5 (50 au). The other physical parameters are summarized in its caption. The color map represents the average velocity shift weighted by the intensity ($\bar{v}$). It is calculated by using the following equation:

$$\bar{v} = \frac{\int vI(v)dv}{\int I(v)dv}, \tag{3.5}$$

where $I(v)$ denotes the intensity at the velocity v at the position. The denominator in the equation (3.5) corresponds to the integrated intensity at the position. Thus, the averaged velocity at a position having an infinitesimal integrated intensity have no sense. Hence, the data at the positions with integrated intensities smaller than the 1% relative to the peak integrated intensity are dropped in Figure 3.6, and they are shown in white in the moment 1 maps. With the edge-on configuration ($i = 90°$), the averaged velocity in the eastern and western side of the protostar is blue- and red-shifted, respectively. These

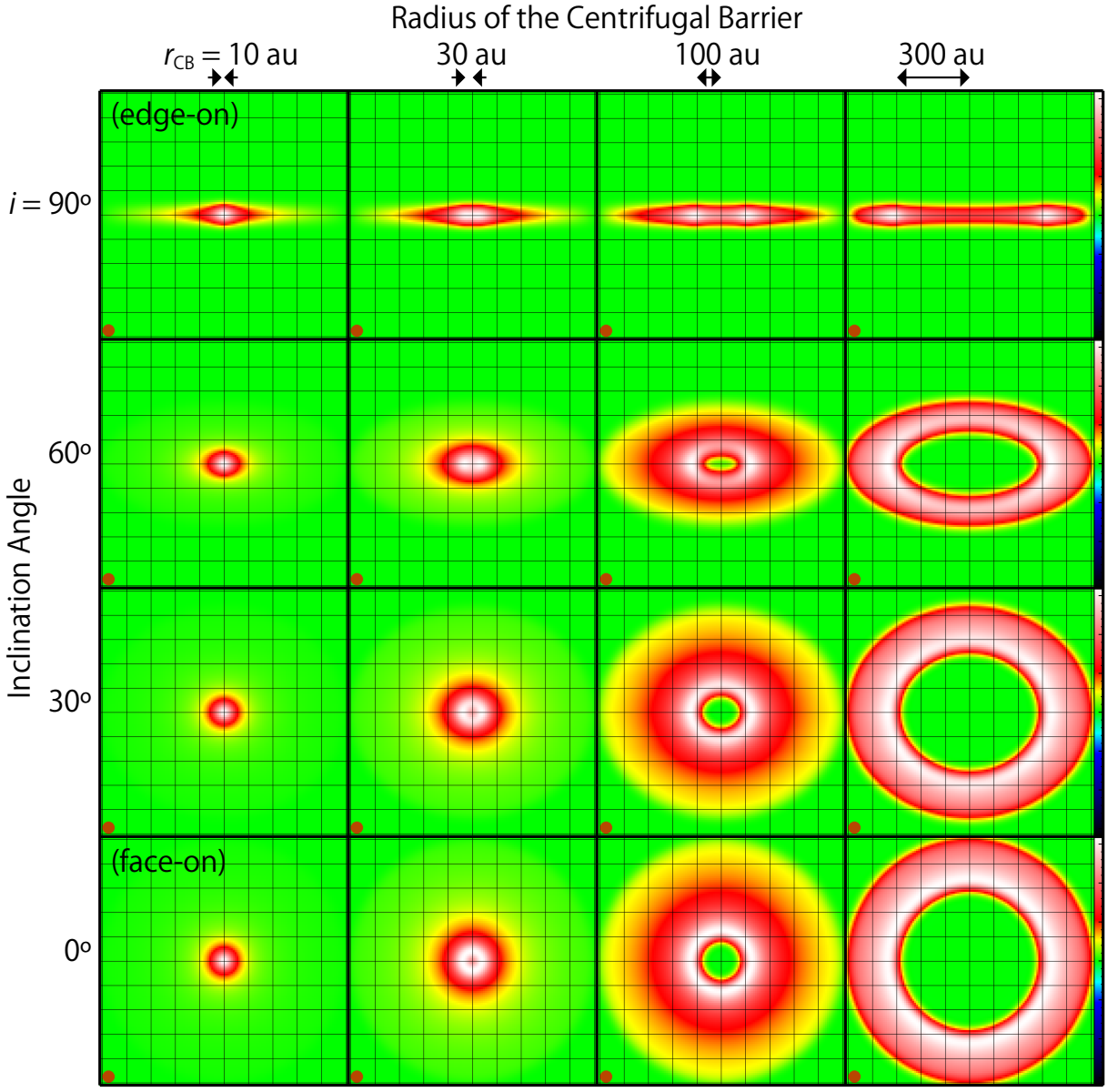

Figure 3.5: Integrated intensity (moment 0) maps of the infalling-rotating envelope model with various sets of the radius of the centrifugal barrier ($r_{\rm CB}$) and the inclination angle of the disk/envelope system (i). The other physical parameters for the models are set as follows; the distance from the Sun $d = 100$ pc, the protostellar mass $M = 0.1\ M_{\odot}$, and the outer radius of the envelope $R = 500$ au. The FWHM values of the intrinsic line width and the Gaussian beam are set to be 0.2 km s^{-1} and $0\farcs5$, respectively. The uniform scale height of the envelope of 50 au is assumed. The mesh sizes are set to be $0\farcs08$ and 0.01 km s^{-1}.

velocity shifts represent the rotation motion around the protostar. The maximum velocity shift is seen around the centrifugal barrier. The velocity does not show any gradient along the north-south axis.

On the other hand, velocity gradients along the north-south axis are seen in the

panels for i of 30° and 60°. These velocity gradients are due to the infall motion. In these models, the southern side of the envelopes face to us, and thus the line emission is red-shifted in the northern side of the protostar, where the molecules are in front of the protostar. In these panels, the velocity fields show skewed features; the most blue- and red-shifted components are seen in the southwestern and northeastern sides of the protostar, respectively, where the projected velocity components of the rotation and infall motions have the same direction along the line of sight. With the face-on configuration ($i = 0°$), the velocity shift is completely symmetric to the mid-plane of the envelope, and thus the average velocity is zero everywhere. The value of $v_{\rm shift}$ is proportional to M as shown in the equations (3.3, 3.4). Thus, M does not affect the moment 1 map in appearance.

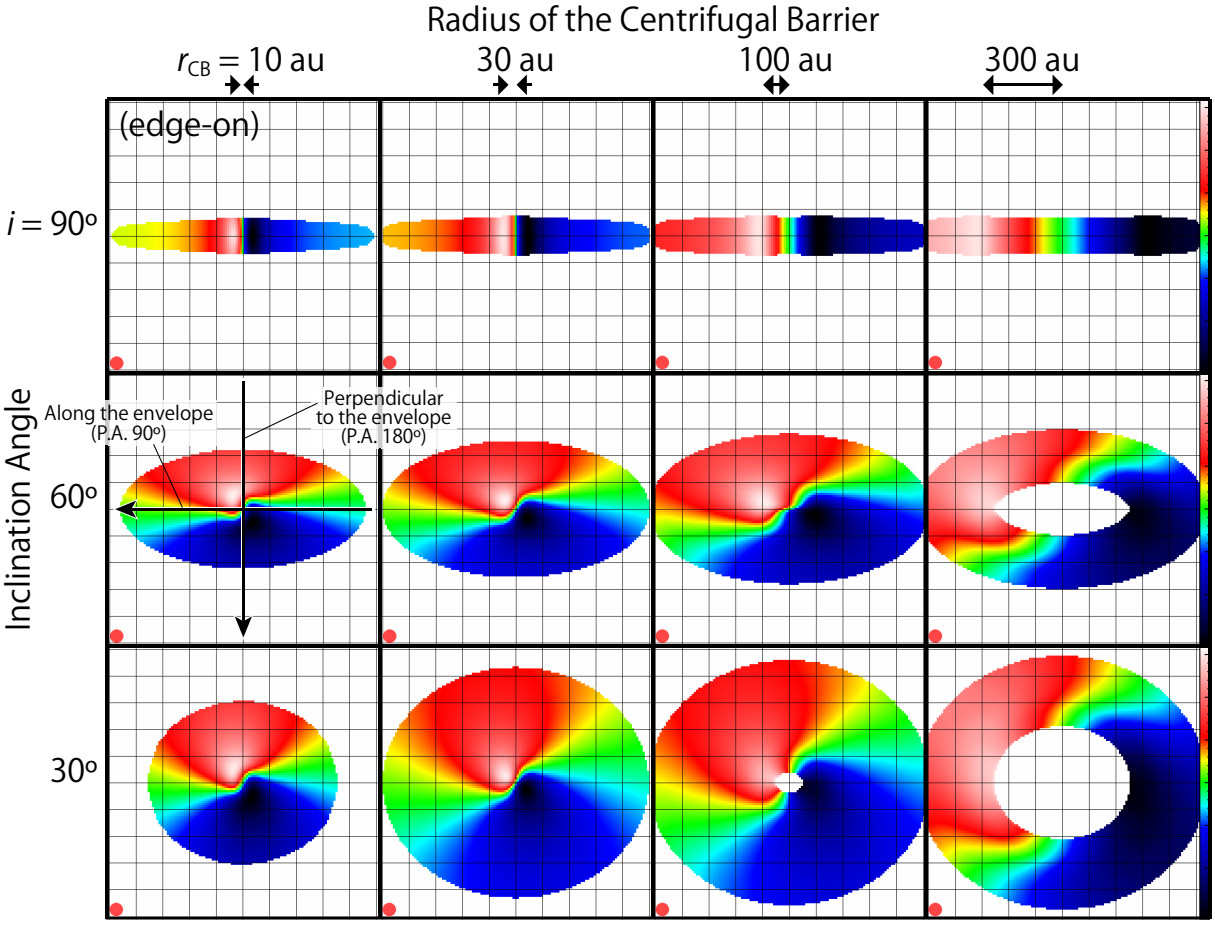

Figure 3.6: Maps of the velocity field (moment 1 maps) of the infalling-rotating envelope model with various sets of $r_{\rm CB}$ and i. The other physical parameters are set to be as the same as those in Figure 3.5. The color scale represents the averaged velocity-shift (equation 3.5). The color maps are shown only at the positions where the integrated intensity (Figure 3.5) is larger than 1% of the peak integrated intensity. Thus, the data at the positions showing a weaker integrated intensity than this criteria are shown in white. The black arrows in the panel with $r_{\rm CB}$ of 10 au and i of 60° represent the directions along which the PV diagrams in Figures 3.7–3.9 are prepared.

Figure 3.7 shows the position-velocity (PV) diagrams along the arrows shown in Figure 3.6. The position axes are taken along the direction, where the mid-plane of the envelopes are extended (Figure 3.6). In Figure 3.7, $r_{\rm CB}$ and i are varied to show how sensitive to these physical parameters the model results are. The FWHM value of the Gaussian beam is $0\farcs5$ (50 au). The other physical parameters are summarized in the caption. With the edge-on configuration ($i = 90°$), the spin-up feature toward the centrifugal barrier is seen with all $r_{\rm CB}$. The maximum velocity-shift seen at the centrifugal barrier is larger for a smaller $r_{\rm CB}$. Although the centrifugal barriers are not spatially resolved in the integrated intensity maps for $r_{\rm CB}$ of 10 and 30 au (Figure 3.5), a velocity gradient is visible between the positions of the centrifugal barriers in their PV diagrams. The infall motion can be confirmed as the counter velocity components. The velocity shifts toward the protostellar position also reflect the infall motion. With i of 30° and 60°, the counter velocity components are not seen for $r_{\rm CB}$ of 100 and 300 au, while they can be seen with $r_{\rm CB}$ of 10 and 30 au. The infall gas in the models with $r_{\rm CB}$ of 100 and 300 au are distant from the protostellar position in the plane of the sky. Therefore, these components are almost outside the beam, and do not have effective contributions in these PV diagrams. With the face-on configuration ($i = 0°$), a velocity gradient due to the rotation motion cannot be seen regardless of $r_{\rm CB}$. Although the PV diagrams with $r_{\rm CB}$ of 10 au is not smooth like those for larger $r_{\rm CB}$, this feature does not have any kinematical meaning, but is due to an artificial effect of the insufficient size of the mesh.

Figure 3.8 shows the model results of PV diagrams prepared along various position angles (P.A.) at various i. The position angles are taken for every 30°. The P.A.s of '90°' and '180°' represent the direction along which the mid-plane of the envelope is extended and one perpendicular to it, respectively. The FWHM value of the Gaussian beam is $0\farcs5$ (50 au). The other physical parameters are summarized in the caption. With the edge-on configuration ($i = 90°$), the distributions look concentrated around the protostar in the PV diagrams with the P.A. of $120° - 240°$. A slight velocity gradient can be seen for these P.A.s, except for the P.A. of 180° (the direction perpendicular to the envelope). The velocity shift in the diagram with the P.A. of 180° is due to the infall motion, and it is smaller than that of the rotation motion at the centrifugal barrier. At i of 30° and 60°, the velocity structure changes from P.A. to P.A.. The value of the velocity shift is determined by the complex combination of the rotation and infall motions. As shown in Figure 3.6, the rotation and infall motions cancel each other in the northwestern and southeastern sides of the protostar, while they strengthen each other in the northeastern and southwestern sides. Because of this, the absolute values of the velocity shift tend to be higher in the diagrams with the P.A. of 210° and 240°, where the position axis is along the northeast-southwest direction, than those with the P.A. of 120° and 150°, where the position axis is along the northwest-southeast direction. With the face-on configuration (i of 0°), no velocity gradient can be seen regardless of the P.A..

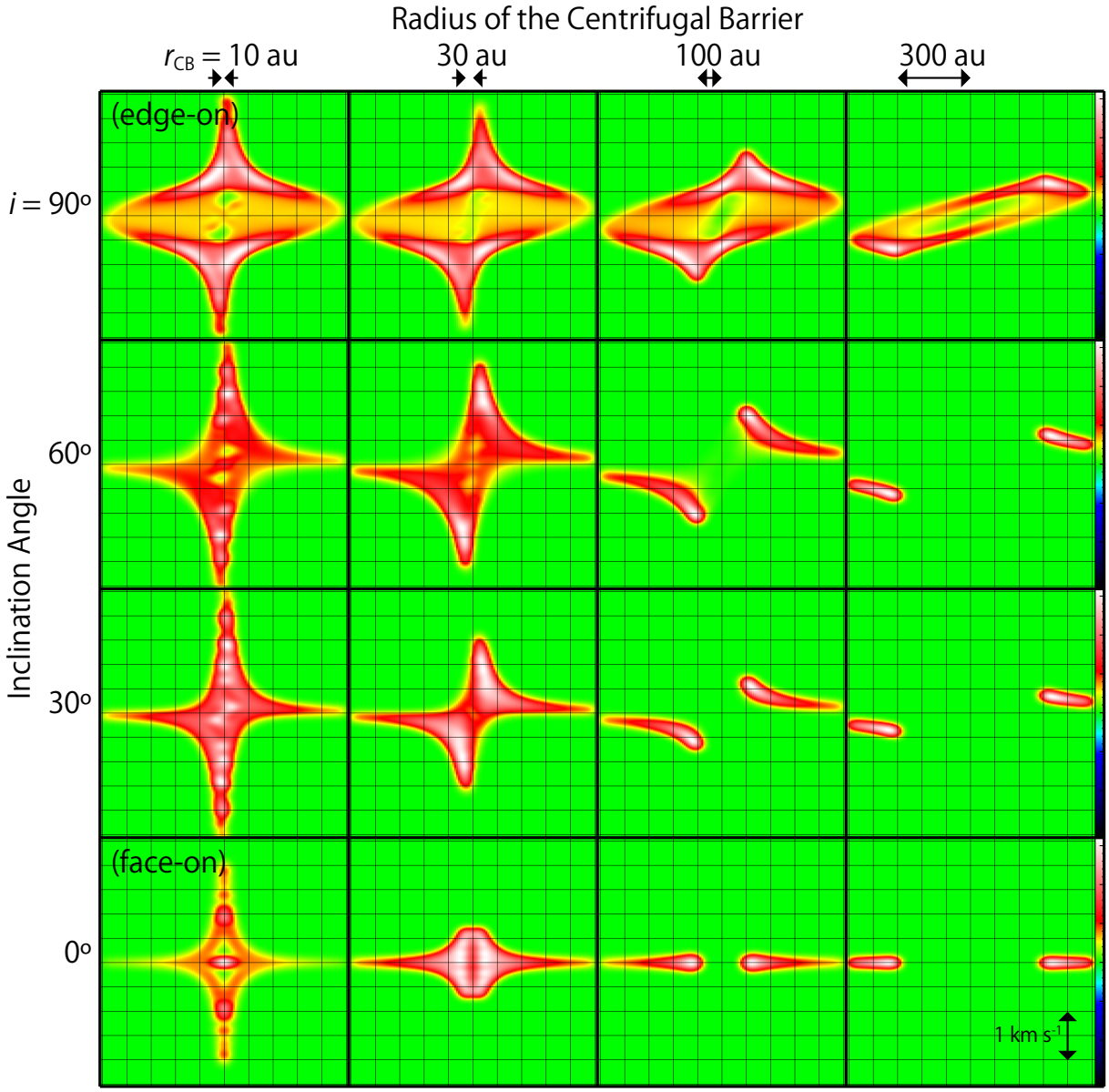

Figure 3.7: PV diagrams of the infalling-rotating envelope model with various sets of $r_{\rm CB}$ and i. Their position axis is along the arrow (P.A. of 90°) shown in Figure 3.6. It is the direction along which the disk/envelope system is extended. The other physical parameters are set to be as the same as those in Figure 3.5.

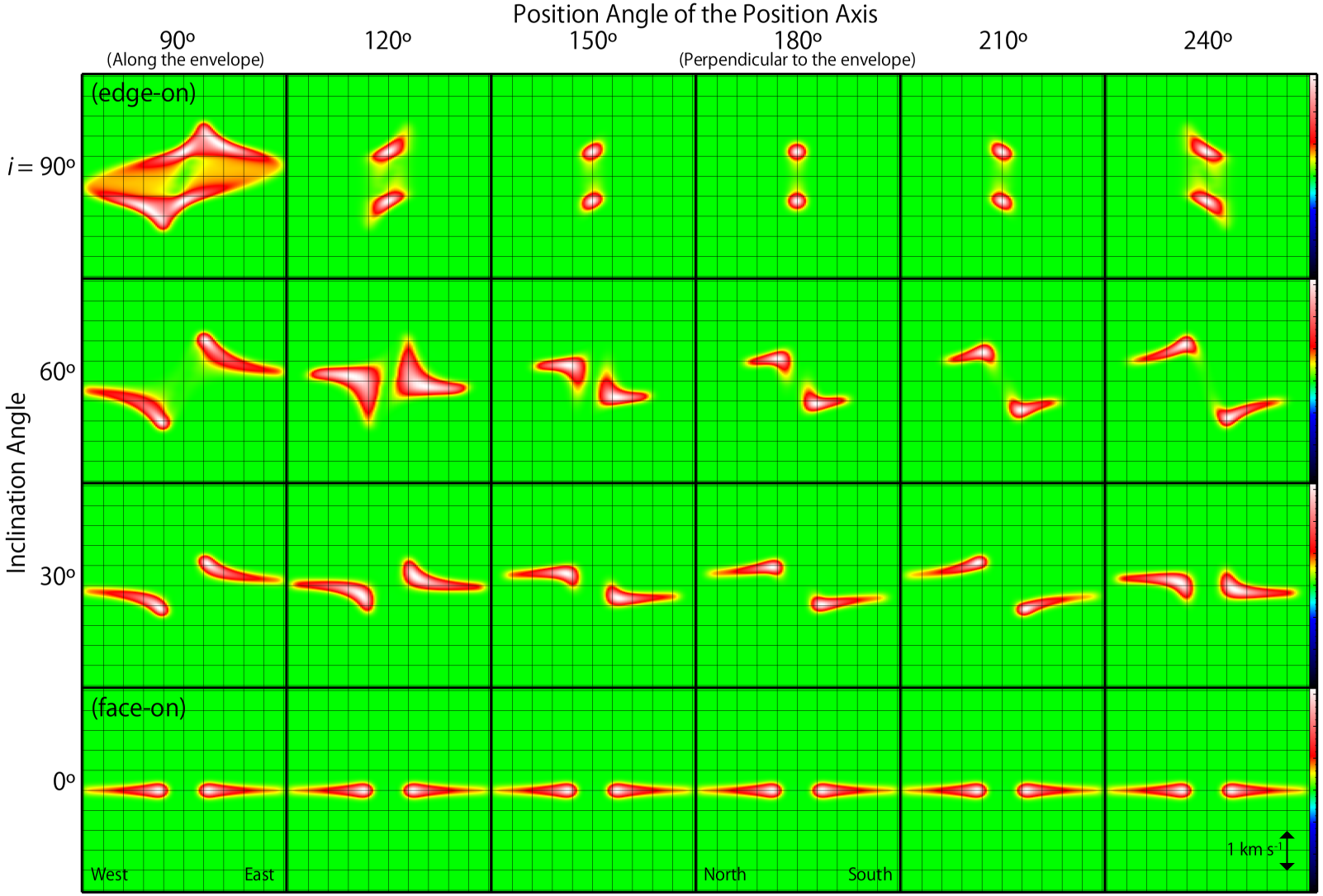

Figure 3.8: PV diagrams of the infalling-rotating envelope model with various i, where the physical parameters are as follows; M = 0.1 $M_{\odot}$, $r_{\rm CB}$ = 100 au, and R = 500 au. The position axes are taken for every 30° from the envelope direction (P.A. 90°).

In Figure 3.9, the effects of the other physical parameters, such as the protostellar mass (M), the outer radius of the envelope (R), and its scale height, are examined. Although the absolute velocity shift is larger for larger M, the essential feature of the PV diagrams is not largely affected by M. With a smaller R, the spin-up feature and the counter velocity components are less clear, although the velocity gradient between the centrifugal barrier s can be seen. The scale height of the envelope (H) does not seriously affect the appearance of the PV diagrams with a P.A. of 90° (along the mid-plane extension). With the edge-on configuration, the scale height affects the distribution along the direction perpendicular to the mid-plane extension.

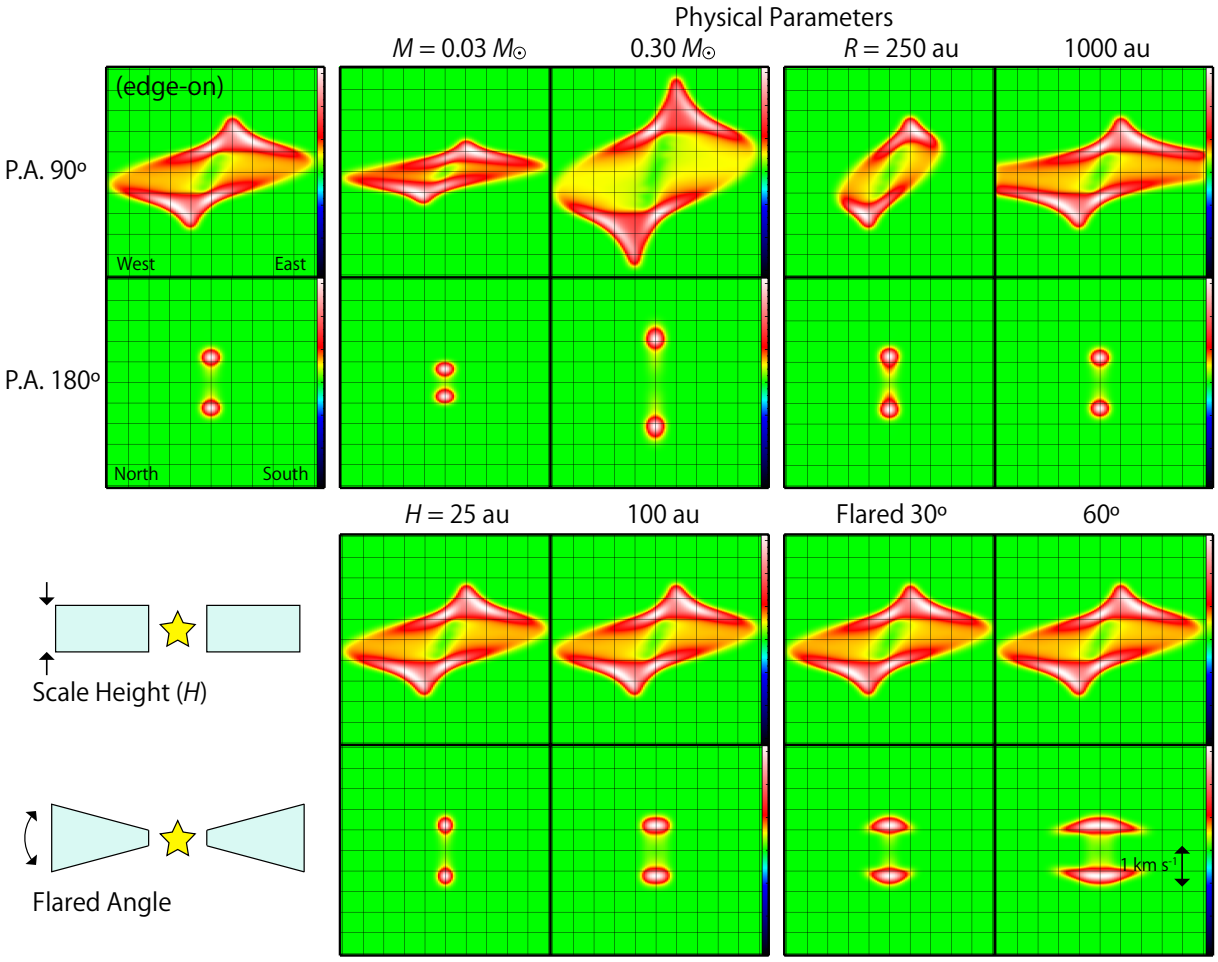

Figure 3.9: PV diagrams of the infalling-rotating envelope model, whose position axes are along the arrows (P.A. 90° and 180°) shown in Figure 3.6. The left upper panels show the results of the fiducial model with the following physical parameters; $M = 0.1\ M_{\odot}$, $r_{\rm CB} = 100$ au, $i = 90°$ (edge-on), $R = 500$ au, and H of 50 au independent of the radius. In the other panels, one of the following physical parameters is changed; the protostellar mass M (0.03 and 0.3 $M_{\odot}$), the outer radius of the envelope R (250 and 1000 au), and the scale height of the envelope H (25 and 100 au). The scale height is assumed to be independent of the radius, or assumed to increase as the radius ('flared') with the flare angle of 30° and 60°.

Figure 3.10 shows how the appearance of the model results changes with a large beam size ($5''$). The centrifugal barrier ($r_{\rm CB} = 100$ au) is not spatially resolved enough with the beam (500 au). The velocity gradient due to the rotation motion is recognized for the cases at i of $30^\circ - 90^\circ$. Although the counter velocity components cannot be seen with i of 30° and 60° with a beam of $0''.5 \times 0''.5$ in Figure 3.7, they are seen in Figure 3.10. Since the beam is larger than the apparent distance of the centrifugal barrier in these models, the emission of the infalling gas contributes to the PV diagram. A similar effect due to the large beam is also seen in the PV diagrams along the direction perpendicular to the envelope; the rotating gas at the centrifugal barrier contributes to these diagrams, and hence, the maximum velocity-shift is as high as the maximum rotation velocity at the centrifugal barrier. In these diagrams, disentanglement of the rotation and infall motion is difficult. In the observational studies, it also makes difficult to find position angle of the envelope component. Higher angular-resolution observations are always essential.

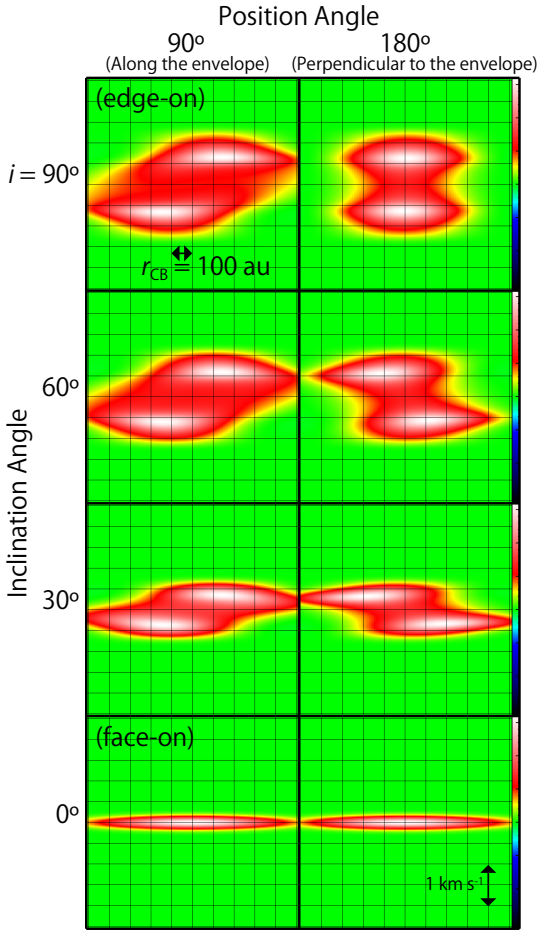

Figure 3.10: PV diagrams of the infalling-rotating envelope model with various set of i and the position angle, where the other physical parameters are as follows; $M = 0.1\ M_\odot$, $r_{\rm CB} = 100$ au, $R = 500$ au, and $H = 50$ au. The position angles of the line along which the position-velocity diagram is prepared are along the mid-plane of the envelope and perpendicular to it in the left and right panels, respectively. The intensity is convolved with the Gaussian beam of $5'' \times 5''$.

3.3 Keplerian Model

In Chapters 6 and 8, we also employ the Keplerian disk model to simulate the disk component. The velocity of the gas at the radius r from the protostar are represented as:

$$v_{\rm Kep} = \sqrt{\frac{GM}{r}}, \quad v_{\rm fall} = 0. \tag{3.6}$$

As shown in Figure 3.2, the Keplerian velocity takes the half value of $v_{\rm rot}$ in the above infalling-rotating envelope model at the centrifugal barrier ($r = r_{\rm CB}$), while it equals to $v_{\rm rot}$ in the infalling-rotating envelope model at the centrifugal radius ($r = 2r_{\rm CB}$).

Figure 3.11 shows the integrated intensity map (moment 0 map), velocity field (moment 1 map), and PV diagrams of the Keplerian model. In these models, the protostellar mass and the outer radius of the Keplerian disk are assumed to be 0.1 $M_\odot$ and 1000 au, respectively. The constant scale height of 50 au is assumed. The FWHM value of the Gaussian beam is $0\farcs5$ (50 au).

In the integrated intensity (moment 0) maps, the distributions seem to be compact and concentrated around the protostar. Since the density of the gas is assumed to be proportional to $r^{-1.5}$, the contributions from the vicinity of the protostar are dominant. In the maps of the velocity field (moment 1 maps), the rotation motion is clearly shown. No skewed feature is seen in the moment 1 maps. In the PV diagrams along the envelope (P.A. of 90°), the spin-up feature can be confirmed, except for the model with a face-on configuration. No counter velocity component which is seen in the infalling-rotating envelope model is seen in the Keplerian model, because there is no infall motion. In the PV diagrams along the direction perpendicular to the envelope (P.A. of 180°), no velocity gradient is seen regardless of i. High velocity components seen in the panels for i of 30° and 60° in Figure 3.11(d) are the contamination of the rotation motion near the protostar due to the finite beam size.

3.4 Outflow Model

In addition to the disk/envelope system, we investigate the kinematic structure of outflow cavities. We employ the standard model of an outflow cavity from Lee et al. (2000) to analyze the observed geometrical and kinematical structures of the outflow. This is just a morphological model. This parabolic model is widely applied to various low-mass and high-mass protostellar sources (e.g. Arce et al., 2013; Beuther et al., 2004; Lumbreras & Zapata, 2014; Takahashi & Ho, 2012; Takahashi et al., 2013; Yeh et al., 2008; Zapata et al., 2014).

In this model, the outflow cavity is assumed to have a parabolic shape and its velocity is proportional to the distance to the protostar. The shape of the outflow cavity wall and the velocity of the gas on the cavity wall are represented as follows:

$$z = CR^2, \quad v_R = v_0\frac{R}{R_0}, \quad v_z = v_0\frac{z}{z_0}, \tag{3.7}$$

where the z axis is taken along the outflow axis with an origin at the protostar, and R denotes the radial size of the outflow cavity perpendicular to z-axis. R_0 and z_0 are

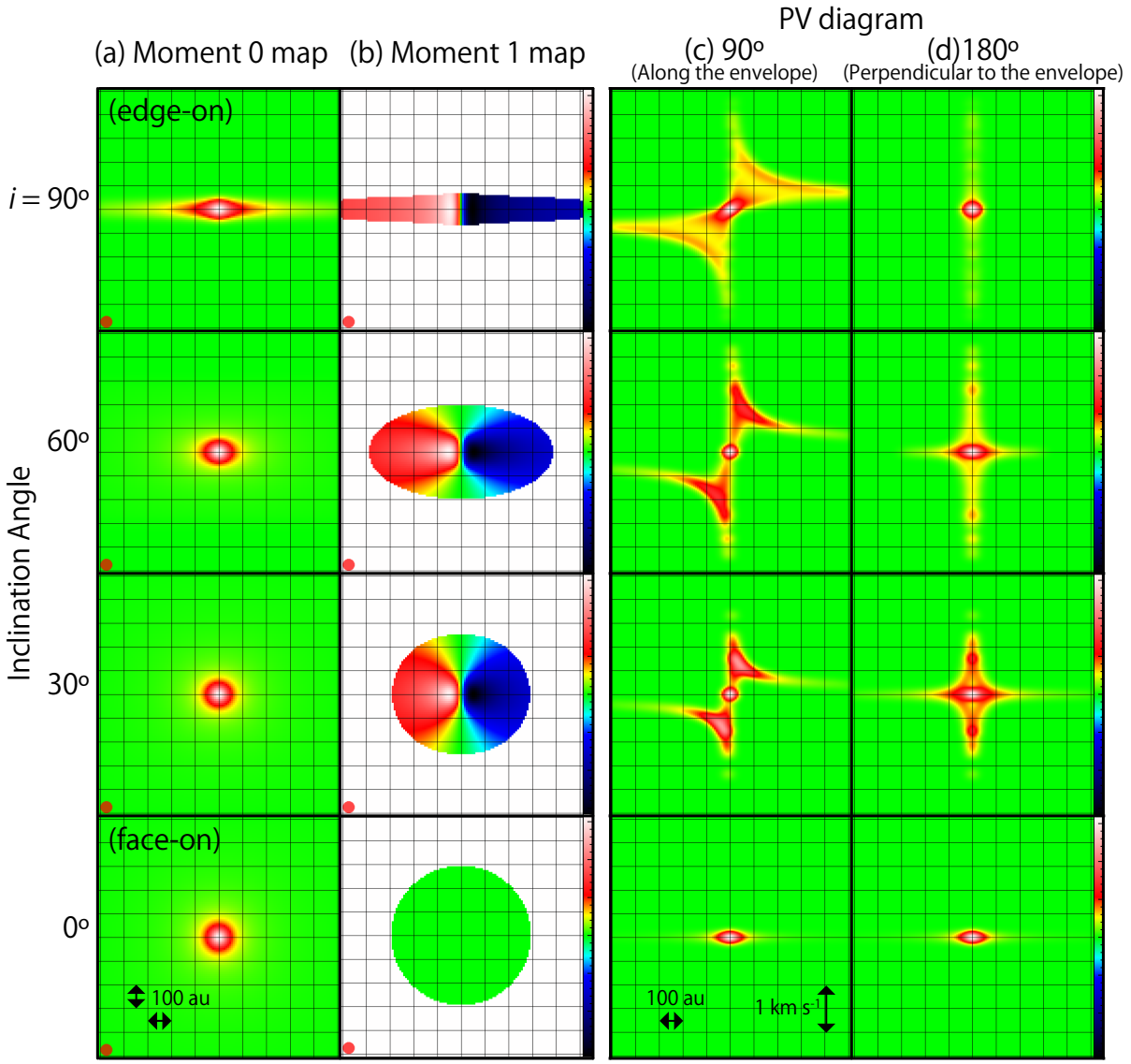

Figure 3.11: (a) Integrated intensity map, (b) map of the velocity field, and (c) PV diagrams of the Keplerian model. The position axes in panels (c) and (d) are as the same as those in Figure 3.10. The physical parameters are as follows; $M = 0.1\ M_{\odot}$, $R = 500$ au, and $H = 50$ au. The intrinsic line width and the beam size are 0.2 km s^{-1} and $0''.5$, respectively, which are the same as those in Figures 3.5–3.9.

normalization constants, and both are set to be 1 au. C and v_0 are free parameters. Thus, the outflow cavity wall has a parabolic shape in this model, and it is linearly accelerated as the distance from the protostar along the outflow axis (z) and that from the outflow axis (R). In this model, the distribution of the gas is artificially assumed to be uniform for all data points, where the mass of the outflowing gas is not conserved along z-axis. Optically thin condition is also assumed, where the intensity of the line emission is proportional to the column density along the line of sight. These simplified assumptions are employed in this study, because our main interest in the model analysis is on the

velocity profile. Since the extended component would be resolved-out, it is difficult to derive accurate density profile from the observations with the interferometer. Therefore, we do not consider the emissivity in the outflow analysis.

Figure 3.12 shows the schematic illustration of this model. Figure 3.13 shows how sensitive to the physical parameters the model results are in their integrated intensity map (moment 0 map), the map of the velocity field (moment 1 map), and the PV diagrams. In these models, the outflow axes are assumed to be along the north-south axis. The two outflow lobes blow in parallel to the plane of the sky with i of 90°, while they are nearly pole-on for the case at i of 30°. In each PV diagram, two parabolic features are seen. One parabolic feature corresponds to one outflow lobe. With smaller C, the parabolic features show larger opening angles. For the case at i of 90°, the gas on the outflow cavity wall shows both a red- and blue-shifted velocity at one position. These are the contributions from two positions on the cavity wall in front of and behind the outflow axis. These velocity shifts have the same absolute value. With i of 30° and 60°, the symmetric axis of the parabolic feature is red- and blue-shifted in the northern and southern sides of the protostar, respectively. Thus they can be called as the 'red-shifted lobe' or 'blue-shifted lobe'. The sign of the velocity shift is determined by the combination of the inclination angle and the curvature of the lobes. As a result, there are some parts showing a counter velocity shift to the symmetric axis. Some parts of a lobe can appear in the counter side to the outflow axis with respect to the protostellar position. It can be confirmed as a parabolic feature which crosses the protostellar position in the PV diagram.

3.5 Physical Parameters of the Models

In the models described in Sections 3.2–3.4, there are some key free parameters while some physical parameters are fixed. They are summarized in Table 3.1.

3.6 Examples of the Model Analysis

3.6.1 The L1527 Case

The infalling-rotating envelope model explained in Section 3.2 was first applied for L1527 (Sakai et al., 2014b). L1527 is a low-mass protostellar core in Taurus (d = 137 pc; Torres et al., 2007). The details of L1527 are described in Chapter 4.

Sakai et al. (2014b) reported the high angular-resolution observations toward L1527 with ALMA. Figure 3.14(a) shows the integrated intensity maps of CCH and c-C_3H_2 toward L1527. The envelope component is seen to be extended along the north-south axis. Figure 3.14(b) shows the position-velocity (PV) diagram of CCH along the north-south axis centered at the protostellar position represented by the white cross in Figure 3.14(a). The velocity of the gas is red- and blue-shifted at the northern and southern sides of the protostar, respectively. A clear spin-up feature is seen in the PV diagram; the velocity shift increases as approaching to the protostar. The CCH emission abruptly disappears at the distance of 100 au from the protostar. There are also seen the components with the inverse velocity of the spin-up feature (*'counter-velocity component'*). The results of the infalling-rotating envelope model are represented as blue contours in Figure 3.14(b).

Table 3.1: Free and Fixed Physical Parameters in the Models

Physical Parameter	Free or Fixed
Infalling-Rotating Envelope Model	
Distance (d)	Fixed (See Table 1.1)
Protostellar mass (M)	Free
Inclination angle (i)	Fixed (The value from references or derived from the outflow analysis)
Radius of the centrifugal barrier ($r_{\rm CB}$)	Free
Outer radius (R)	Free
Scale height of the envelope	Fixed (Uniformed or proportional to the distance from the protostar)
Beam size	Fixed based on the observations
Intrinsic linewidth	Fixed
Emissivity[a]	Fixed ($\propto r^{-1.5}$)
Mesh size	Fixed
Keplerian Model	
Distance (d)	Fixed (See Table 1.1)
Protostellar mass (M)	Fixed (The value derived from the envelope analysis)
Inclination angle (i)	Fixed (The same value in the envelope analysis)
Outer radius of the disk (R)	Fixed to be $r_{\rm CB}$
Beam size	Fixed based on the observations
Intrinsic linewidth	Fixed
Emissivity[a]	Fixed ($\propto r^{-1.5}$)
Mesh size	Fixed
Outflow Model	
Distance (d)	Fixed (See Table 1.1)
Inclination angle (i)	Free (0° for a face-on configuration)
Curvature (C)	Free
Velocity (v_0)	Free
Beam size	Fixed based on the observations
Intrinsic linewidth	Fixed
Emissivity[b]	Fixed to be uniform
Mesh size	Fixed

[a] In reality, the intensity of the line emission from each data point is determined by the combination of several physical conditions; e.g. the H_2 density ($n(H_2)$), the abundance ratio of the molecule to H_2 ($f(X)$), the gas temperature. In this model, the intensity is simply assumed to be proportional to the column density, where $n(H_2)$ is assumed to be proportional to $r^{-1.5}$ (an infalling envelope; e.g. Shu, 1977; Ohashi et al., 1997; Harvey et al., 2003), $f(X)$ is constant, and the temperature does not affect the emissivity.

[b] In the outflow model, the density of the molecule is simply assumed to be constant for all data points, because only the velocity structure is focused on in this study.

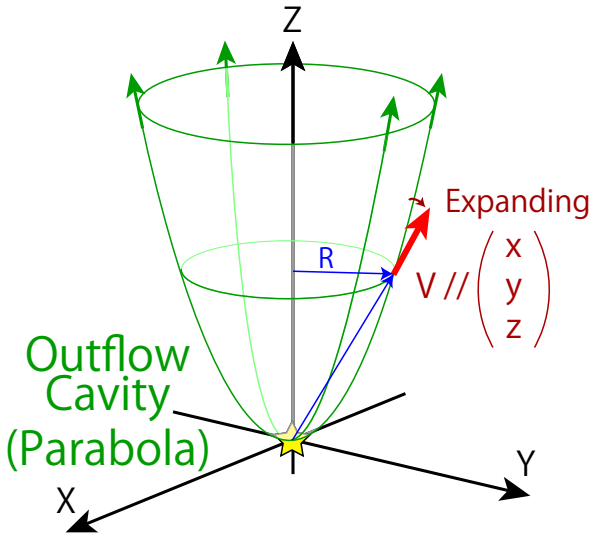

Figure 3.12: Schematic illustration of the parabolic outflow model.

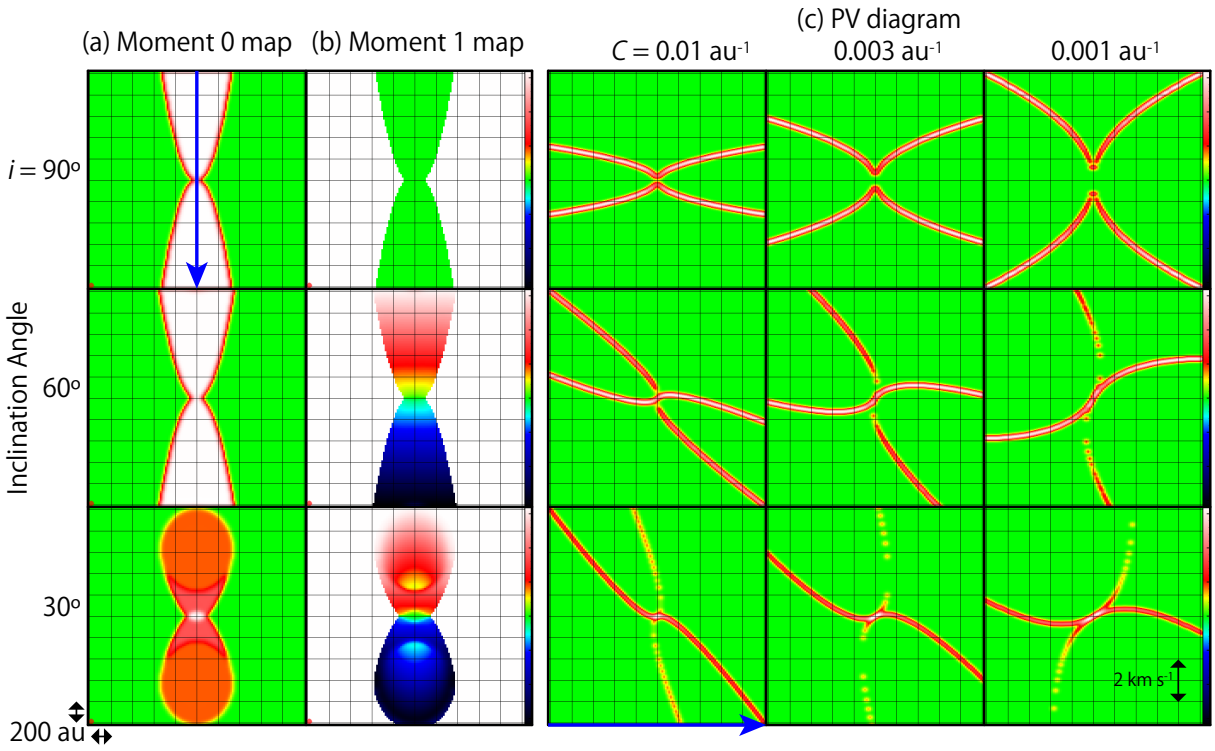

Figure 3.13: (a) Integrated intensity maps and (b) maps of the velocity field of the outflow model with various i. The parameters of the curvature (C) and the velocity (v_0) are fixed to be 0.01 au^{-1} and 0.5 km s^{-1}. (c) PV diagrams of the outflow model along the outflow axis with various i and the curvature C (au^{-1}). The position axis is along the blue arrow shown in panel (a) for i of 90°. The parameter of the velocity (v_0) is fixed to be 0.5 km s^{-1}, where the velocity is 0.5 km s^{-1} at the distance of 1 au from the protostar.

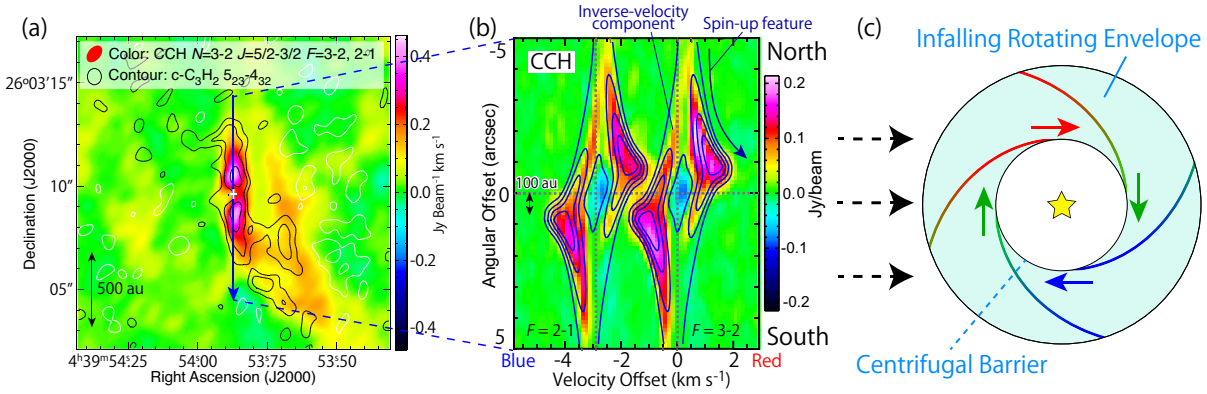

Figure 3.14: (a) Integrated intensity maps of the CCH ($N = 3-2, J = 5/2-3/2, F = 3-2$ and $2-1$; color) and c-C_3H_2 ($5_{23} - 4_{32}$; contours) lines. Contours levels are -6, -3, 3, 6, and 12 σ, where σ is 6.5 mJy beam^{-1} km s^{-1}. White contours represent a negative intensity. The white cross represents the position of the 0.8 mm continuum peak. (b) Position-velocity diagram of the CCH line prepared along the blue arrow shown in panel (a), along which the mid-plane of the disk/envelope system is extended. The hyperfine component ($F = 2 - 1$) is seen with the velocity offset of -2.8 km s^{-1}, and the same structure is repeated twice. Blue contours represent the results of the infalling-rotating envelope model. The physical parameters for the model are as follows; the protostellar mass $M = 0.18\ M_\odot$, the radius of the centrifugal barrier $r_{\rm CB} = 100$ au, and the inclination angle $i = 85°$ (0° for a face-on configuration). Contour levels are every 20% of the peak intensity. (c) Schematic illustration of the infalling-rotating envelope model. Panels (a) and (b) are taken from Sakai et al. (2014b).

The physical parameters for the infalling-rotating envelope model are as follows; the protostellar mass is 0.18 $M_\odot$, the radius of the centrifugal barrier is 100 au, and the inclination angle of the disk/envelope system is 85° (0° for a face-on configuration). The model results well reproduce the observed kinematic structures of the CCH lines, including the counter-velocity component.

3.6.2 The TMC-1A Case

Another example is the TMC-1A case. This source is located in the Heiles Cloud 2 ($d = 137$ pc; Torres et al., 2007), which harbors the low-mass Class I protostar IRAS 04365+2535. It shows the chemical characteristic of WCCC similar to L1527 (Sakai et al., 2008a). Sakai et al. (2016) conducted high angular-resolution observations of the CS ($J = 5 - 4$) and SO ($J_N = 7_6 - 6_5$) lines toward this source with ALMA (Figure 3.15). The kinematic structure in the vicinity of the protostar can be explained by the above infalling-rotating envelope model (Figure 3.15b), where the physical parameters are M of 0.25 $M_\odot$ and $r_{\rm CB}$ of 50 au. Figures 3.15 show the PV diagrams of CS and SO prepared along the envelope direction and the line perpendicular to it. Although some parts of the molecular distributions seem to be missing due to the asymmetric gas distribution, the results of the infalling-rotating envelope model shown in white contours reasonably explain the kinematic structures. Thus, the infalling-rotating envelope model is expected

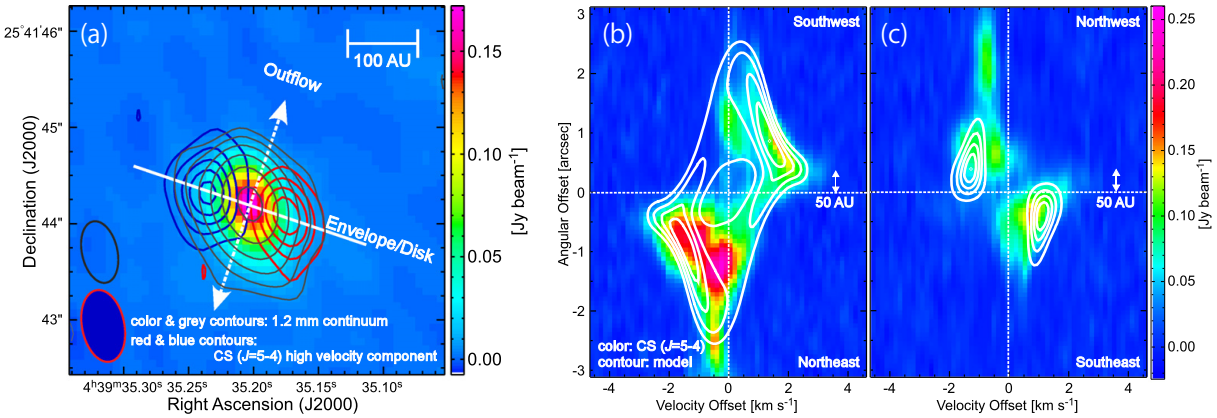

Figure 3.15: (a) 1.2 mm continuum map (color, gray contours) and the integrated intensity maps of the high velocity components of CS ($J = 5 - 4$; red and blue contours) in TMC-1A. (b, c) PV diagrams of CS ($J = 5 - 4$) along the envelope direction (b) and the line perpendicular to it (c). The position axes are represented by the white line and arrow in panel (a). Taken from (Sakai et al., 2016).

to be a powerful tool to examine the essential kinematics in the disk forming region.

3.6.3 Some Caveats for the Model

As demonstrated in the L1527 case (Figure 3.14), we investigate the observed kinematic structures by comparing it with the physical models. The infalling-rotating envelope model is a quite simplified one as described in Section 3.2.1: the model does not consider any excitation effects, radiative transfer effects, and abundance variations of molecules. However, in reality, some parts of the envelope gas can be optically thick, and the distribution itself can be asymmetric around the protostar. Thus, it is not fruitful to make a fine tuning of the model so as to better match with the observed intensity. We therefore focus on the fundamental characteristics of the kinematic structure in this thesis. Hence, we conduct model simulations with a wide range of physical parameters, and basically evaluate the suitable values of the parameters by eye. In model analyses, chi-squared tests are often employed to derive reliable values for the model parameters. However, we do not conduct chi-squared tests for the infalling-rotating envelope model in this thesis, considering the overwhelming systematic errors caused by the simplified assumptions described above.

Chapter 4

L1527

Sub-arcsecond resolution images of the rotational line emissions of CS and c-C_3H_2 obtained toward the low-mass protostar IRAS 04368+2557 in L1527 with the Atacama Large Millimeter/submillimeter Array are investigated to constrain the orientation of the outflow/envelope system. The distribution of CS consists of an envelope component extending from north to south and a faint butterfly-shaped outflow component. The kinematic structure of the envelope is well reproduced by a simple ballistic model of an infalling-rotating envelope. Although the envelope has a nearly edge-on configuration, the inclination angle of the rotation axis from the plane of the sky is found to be 85°, where we find that the western side of the envelope faces the observer. This configuration is opposite to the direction of the large-scale ($\sim 10^4$ au) outflow suggested previously from the ^{12}CO ($J = 3 - 2$) observation, and to the morphology of infrared reflection near the protostar ($\sim$ 200 au). The latter discrepancy could originate from high extinction by the outflow cavity of the western side, or these discrepancies may indicate that the outflow axis is not parallel to the rotation axis of the envelope. Position-velocity diagrams show the accelerated outflow cavity wall, and its kinematic structure in the 2000 au scale is explained by a standard parabolic model with the inclination angle derived from the analysis of the envelope. The different orientation of the outflow between the small and large scale implies a possibility of precession of the outflow axis.

4.1 Introduction

As demonstrated in Chapter 3, we have found that the kinematic structure of the envelope in a low-mass Class 0/I protostellar core L1527 is well reproduced by a simple model assuming the ballistic motion. We further investigate its kinematic structure in this chapter. As well as the envelope component, we look into the structure of the outflow cavity wall in this source, because they are expected to be deeply related with each other.

IRAS 04368+2557 in L1527 (d = 137 pc; Torres et al., 2007) is a representative Class 0/I low-mass protostar, whose bolometric luminosity is 1.7 $L_\odot$ (Green et al., 2013). It is also known as a prototypical warm carbon-chain chemistry (WCCC) source (Sakai et al., 2008a, 2010; Sakai & Yamamoto, 2013). This source has a flattened infalling envelope with an edge-on configuration extending from north to south. Ohashi et al. (1997) and Yen et al. (2013) reported the infall motion of the envelope gas conserving angular momentum

This chapter has been published in Oya et al., 2015, ApJ, 812, 59

based on interferometer observations. On the other hand, the existence of a Keplerian disk was suggested by Tobin et al. (2012) and Ohashi et al. (2014) by observations of the ^{13}CO and ^{18}CO ($J = 2-1$) lines, respectively. Recently, Sakai et al. (2014a,b) presented a clear infalling-rotating motion in its envelope at a resolution of 0.″6 with ALMA. With the aid of a simple ballistic model, they identified the centrifugal barrier of the infalling gas at a radius of 100 au; the observed kinematic structure was well reproduced by this simple model. Moreover, they discovered a drastic change in chemical compositions across the centrifugal barrier (Sakai et al., 2014b). Carbon-chain molecules and CS mainly reside in the infalling envelope outside the centrifugal barrier, whereas SO and probably CH_3OH are enhanced at the centrifugal barrier and may survive inside it at least partly. Such a chemical change at the centrifugal barrier had not been anticipated before.

In this source, molecular outflows from the protostar are extended toward the east-west direction which is almost perpendicular to the flattened envelope (i.e. almost on the plane of the sky). Hogerheijde et al. (1998) delineated the outflow extending over 2′ ($\sim 2 \times 10^4$ au) scale by observations of the ^{12}CO ($J = 3-2$) line with the James Clerk Maxwell Telescope (JCMT), as shown in Figure 4.1(a). The blue-shifted and red-shifted components are strong in the eastern side and western side of the protostar, respectively. As for a smaller scale, Tobin et al. (2008, 2010) conducted L' band imaging of this source with the Gemini North telescope and the 3.6 μm band with the Infrared Array Camera (IRAC) on the *Spitzer* Space Telescope (Figure 4.1b). They reported that the outflow cavity has a butterfly shape at the ($10^3 - 10^4$) au scale. The outflow cavity on the eastern side of the protostar is brighter than that on the western side, and hence they suggest that the eastern cavity would point to us. If so, it corresponds to the blue-shifted lobe. This result is consistent with the orientation of the larger scale outflow observed with the ^{12}CO line emission mentioned above. The protostellar-core model has so far been discussed by assuming this orientation of the outflow.

Based on the ALMA data analysis of the envelope, we have fortuitously found that the direction of the outflow/envelope system in this source is opposite to that just described above. In this chapter, we report the determination of the inclination angle and morphological properties of the outflow.

4.2 Results

We used the ALMA Cycle 0 data (#2011.0.00604S) reported by Sakai et al. (2014a). The observed lines are shown in Table 4.1. The primary beam (HPBW) is 24.″5. The synthesized beam size is 0.″8 × 0.″7 (P.A. = −6°) for the CS ($J = 5-4$) and c-C_3H_2 ($5_{2,3} - 4_{3,2}$) lines.

4.2.1 Overall Distribution

Figure 4.2 shows the moment 0 map of the CS ($J = 5-4$) line. The envelope component extends almost along the north-south axis, as reported in other lines (Sakai et al., 2014a,b). Although the emission of the outer part is heavily resolved out, a part of the butterfly-shaped outflow cavity wall (Tobin et al., 2010) can be seen mainly on the western side of the protostar in addition to the envelope component. The high-density gas traced by the

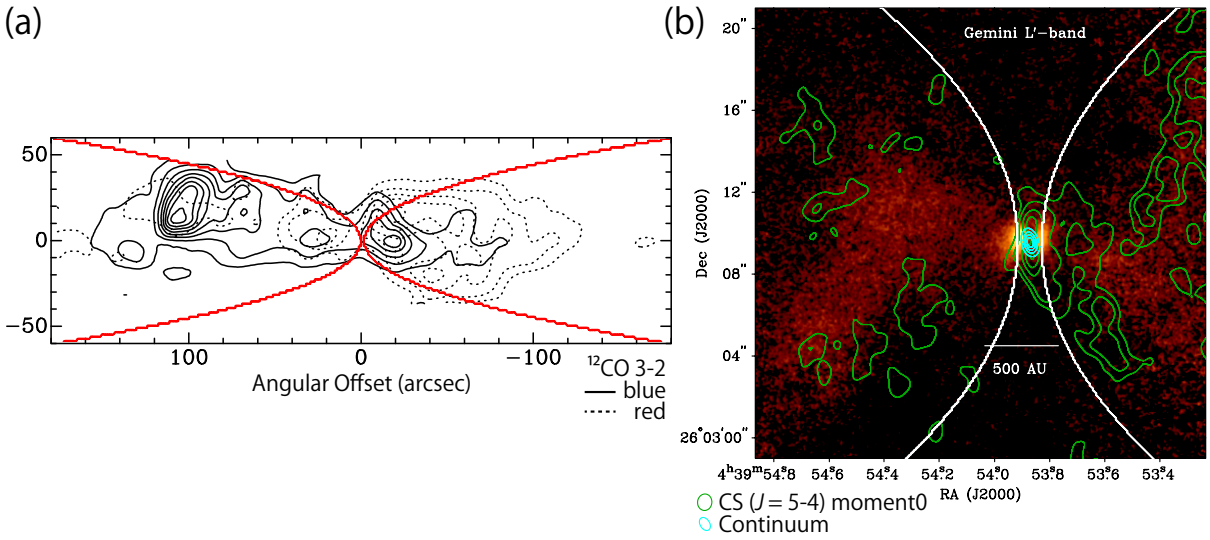

Figure 4.1: (a) ^{12}CO map (black contours) by MacLeod et al. (1994) (Hogerheijde et al., 1998). The FWHM beam size is 11″ and the contours are drawn at the 3σ level. (b) L' band observation (color) by Tobin et al. (2010), the moment 0 map of CS ($J = 5-4$; green contours) and the 1.3 mm continuum map (light blue contours). Contours for CS are 3, 6, 12, 18, and 24σ, where the rms level is 9 mJy beam^{-1} km s^{-1}. Contours for the continuum are every 20% of the peak intensity, which is 308 mJy beam^{-1}. Red lines in the panel (a) and white lines in the panel (b) represent the best-fit model of the outflow (Section 4.2.3), where the parameters are; $i = +85°$, $C_{\rm as} = 0.05$ arcsec^{-1} and $v_{\rm as} = 0.10$ km s^{-1}, and the origins of the lobes have an offset of 0.″62 from the protostellar position Tobin et al. (2010).

CS ($J = 5 - 4$) line is distributed asymmetrically around the protostar.

Figure 4.3 shows the position-velocity (PV) diagram along the outflow axis. Envelope components are concentrated at the protostellar position, while outflow components are extended along the east-west axis from the protostar. The outflow seems to be accelerated as the distance from the protostar. Although blue-shifted components are prominent on the western side of the protostar, the velocity shifts of the outflow are almost symmetrical to the protostellar position. It is therefore obvious that the outflow axis is close to the plane of the sky, as reported previously (Tobin et al., 2008, 2010). Unfortunately, it is difficult to derive the inclination angle accurately from the kinematic structure of the outflow, because the outflow components are faint and heavily resolved out. Hence, we first investigate the envelope components to discuss the geometry of the outflow/envelope system.

4.2.2 Envelope

The kinematic structure of the protostellar envelope of L1527 observed in the c-C_3H_2, CCH, and CS emission is well reproduced with a model of an infalling-rotating envelope (Sakai et al., 2014a,b). Details of this model are described in Chapter 3. In this model, the particles cannot fall inward of a certain radius because of conservation of angular

Table 4.1: Parameters of the Observed Line[a]

Molecule	Transition	Frequency (GHz)	E_u (K)	$S\mu^{2}$[b] (D^2)
CS	$J = 5 - 4$	244.9355565	35	19.17
c-C_3H_2	$5_{2,3} - 4_{3,2}$	249.0543680	41	76.32

[a] Taken from CDMS (Müller et al., 2005).
[b] Nuclear spin degeneracy is not included.

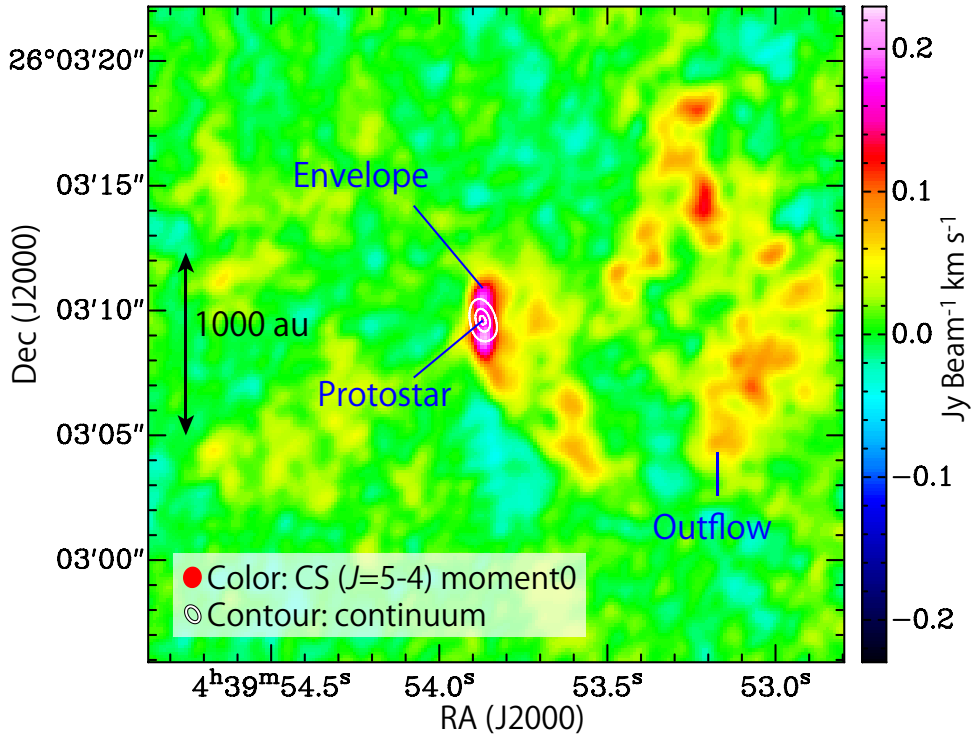

Figure 4.2: Integrated intensity (moment 0) map of CS ($J = 5-4$; $v = (3.1-8.7)$ km s^{-1}; color) and the 1.3 mm continuum map (white contours). Contour levels for the continuum are 30, 150, and 270σ, where the rms level is 1 mJy beam^{-1}.

momentum and energy, and this radius defines the centrifugal barrier. In this ballistic model, the velocity field of the particle motion is characterized by the protostellar mass and the radius of the centrifugal barrier. The PV diagram of the model prepared along the envelope reflects only the absolute value of its inclination angle, and it does not reflect the direction of its inclination from the plane of the sky. Hence, (Sakai et al., 2014b) (Chapter 3) did not consider the direction of the inclination with respect to the edge-on configuration ($i = 90°$) in the analysis of the PV diagram. Therefore, we here examine the PV diagrams of the CS ($J = 5 - 4$) and c-C_3H_2 ($5_{2,3} - 4_{3,2}$) lines prepared along various lines passing through the protostellar position to investigate the direction of the inclination of the envelope.

Figures 4.4 and 4.5 show the PV diagrams of the CS ($J = 5 - 4$) line along the six

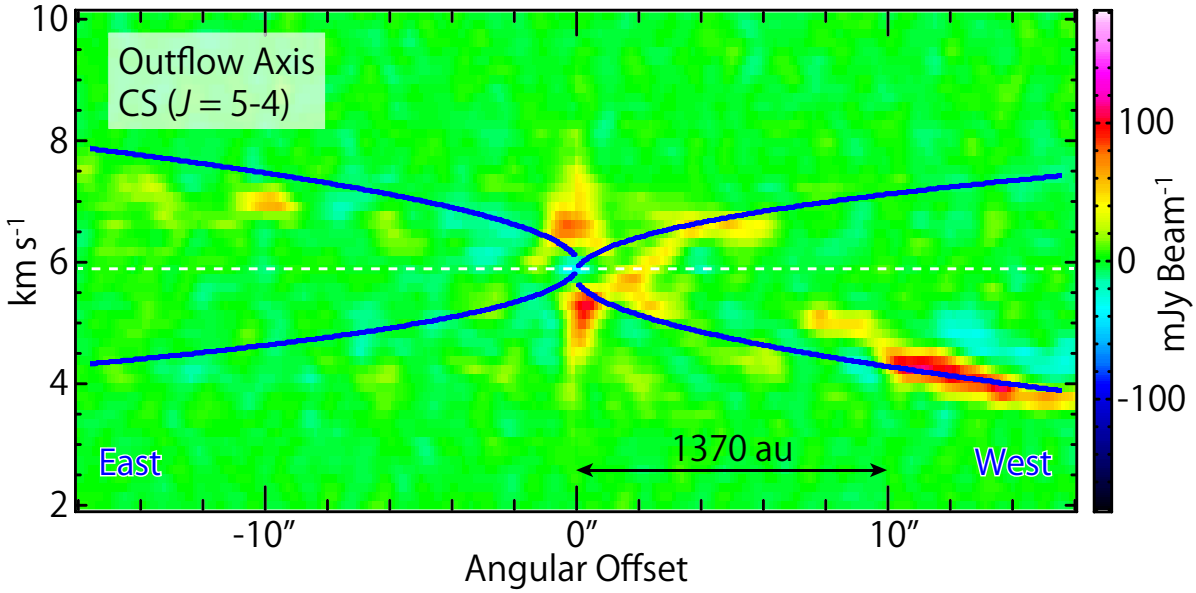

Figure 4.3: PV diagram of CS ($J = 5 - 4$; color) along the outflow axis. The blue lines represent the result of the outflow model (Section 4.2.3) with the parameters of $i = +85°$, $C_{\rm as} = 0.05$ arcsec^{-1} and $v_{\rm as} = 0.10$ km s^{-1}, where no offset of the origin of the outflow from the protostar is assumed in this figure.

lines shown in Figure 4.6(a) for the inclination angle (i) of 85° and 95°, respectively, which correspond to the cases shown in Figures 4.6(b) and (c), respectively. It should be noted that Tobin et al. (2013) assumed an inclination angle of 95° (Figure 4.6c). The other physical parameters assumed in the model are described in Appendix of this chapter. The emission of CS ($J = 5 - 4$) at the centrifugal barrier is more enhanced than in the outer part of the envelope in comparison with the c-C_3H_2 ($5_{2,3} - 4_{3,2}$) case (Sakai et al., 2014a). Moreover, the red-shifted components are slightly weaker than the blue-shifted components, and the systemic velocity components are self-absorbed. Nevertheless, the kinematic structure along the envelope (P.A. "180°") is well explained by the above model assuming the either direction of the inclination ($i = 85°$ or 95°; Sakai et al., 2014b). Note that resolved-out components are negligible, because we focus on the compact distribution around the protostar for the envelope analyasis.

However, it is evident that the model with the inclination angle of 85° well reproduces the PV diagrams along all the lines (Figure 4.4), whereas the model with the inclination angle of 95° does not (Figure 4.5). In particular, the PV diagrams labeled as "240°", "270°", "300°" in Figures 4.4 and 4.5, which reflect the infall motion rather than the rotation motion, seem to be reproduced better by the model with the inclination angle of 85° (Figure 4.4) than that with the inclination angle of 95° (Figure 4.5). For instance, the observed PV diagram along the "270°" line shows two peaks; one at the eastern side of the protostar with the red-shifted velocity and the other at the western side with the blue-shifted velocity. In the model with the inclination angle of 85°, the peaks appear

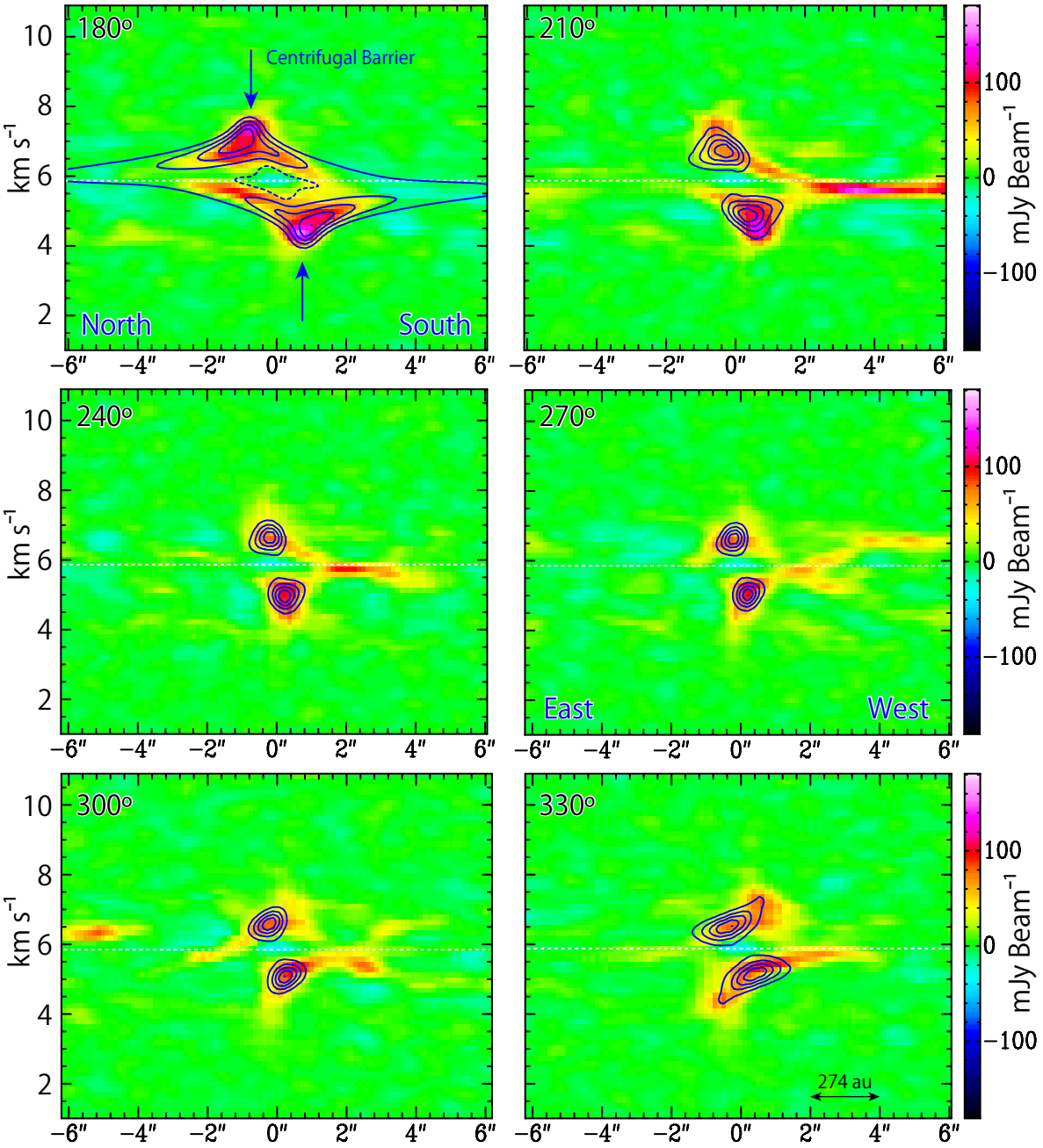

Figure 4.4: PV diagrams of CS ($J = 5 - 4$; color) along the lines shown in Figure 4.6(a). The label in the left upper corner ("180°", "210°", "240°", "270°", "330°", and "330°") represents the position angle of the position axis in each panel. The blue contours represent the infalling-rotating envelope model with the inclination angle of 85° (Figure 4.6b). Contour levels are every 20 % of the peak intensity in each panel. The dashed contour around the central position in the panel "180°" represents the dip toward the center.

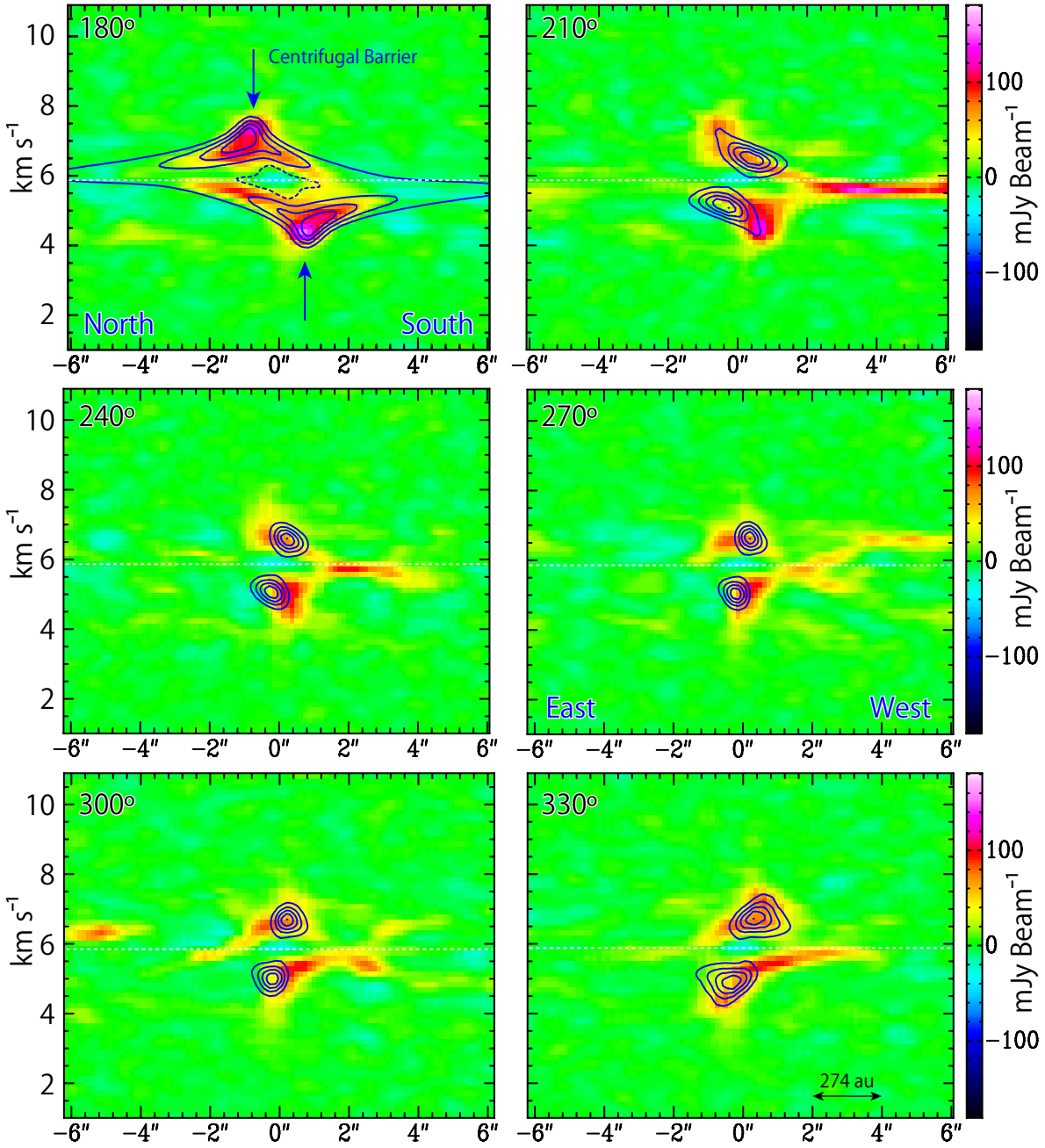

Figure 4.5: PV diagrams of CS ($J = 5 - 4$; color) along the lines shown in Figure 4.6(a). The blue contours represent the infalling-rotating envelope model with the inclination angle of 95° (Figure 4.6c). Contour levels are every 20 % of the peak intensity in each panel. The dashed contour around the central position in the panel "180°" represents the dip toward the center.

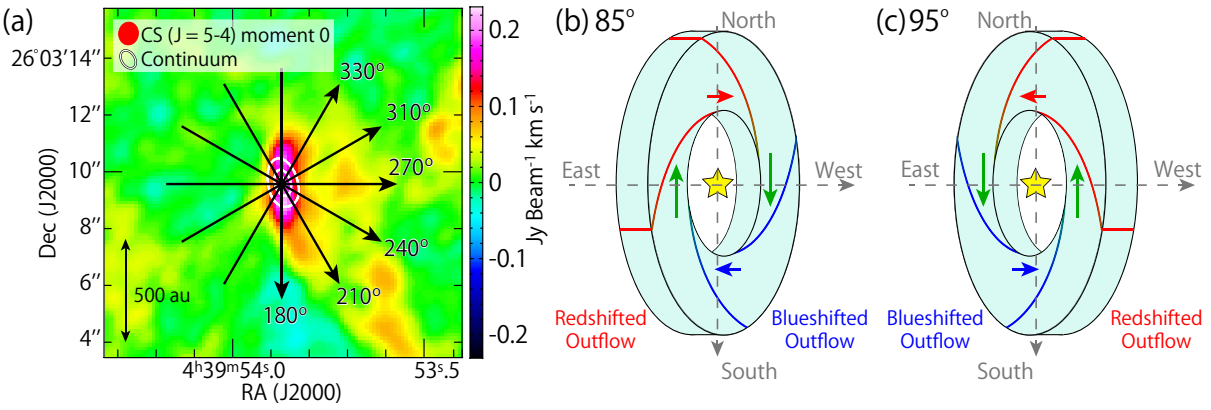

Figure 4.6: (a) A blow-up of the central part of the moment 0 map of CS ($J = 5-4$; color) and the continuum map (white contours) shown in Figure 4.2. Contours for continuum are as the same as in Figure 4.2. The black arrows represent the lines along which the PV diagrams in Figures 4.4, 4.5 and 4.7 are prepared. (b) Schematic illustration of the envelope model with the inclination angle of 85°. (c) Schematic illustration of the envelope model with the inclination angle of 95°.

as the observational trend mentioned above. In the model with the inclination angle of 95°, the two peaks, on the other hand, appear in the opposite way; one at the eastern side with the blue-shifted velocity, and the other at the western side with the red-shifted velocity. Hence, the inclination angle of 85° better explains the observation.

We calculated the root-mean-square (rms) of the difference between the observed and simulated PV diagrams in order to evaluate the goodness of the fit more quantitatively. However, this attempt was not very successful. Our model is a simplified one involving many assumptions described in Appendix of this chapter in order to explore just the basic physical and kinematic structure of the envelope. Hence, we have to note that the rms of the difference suffers from systematic errors due to these assumptions, as described in Chapter 3. Nevertheless, the rms of the difference for the PV diagram along the "270°" line is 0.022 Jy beam^{-1} for the model with the inclination angle of 95°, which is confirmed to be larger than that for the model with the inclination angle of 85° (0.018 Jy beam^{-1}).

We also attempted to optimize the inclination angle from the fit of the PV diagrams. For this purpose, we conducted simulations for the other inclination angles, as shown in Appendix of this chapter. Since the fit is not perfect due to the simplicity of the model, the statistical argument based on the rms of the difference is almost meaningless, as mentioned above. Nevertheless, we found that the inclination angle from 80° to 85° reasonably reproduces the observation. More safely, it is constrained to be larger than 75°. In addition, we can firmly conclude that the inclination angle is less than 90°; the positions and the velocities of the two peaks mentioned above are not consistent with the observations, if the opposite direction, where the eastern lobe points to us, are employed for the model. Tobin et al. (2008) reported that the morphology of the L' band image cannot be explained, if the disk is inclined by much smaller than 80°. Hence, our estimation of the inclination angle is consistent with theirs except for the direction of the inclination. In the following discussion, we employ the inclination angle of 85°.

The inclination angle less than 90° means that the envelope in front of the protostar appears in the eastern side of the protostar, and the outflow axis in the western side of the protostar points to us (Figure 4.6b). This direction is opposite to that reported previously (Hogerheijde et al., 1998; Tobin et al., 2010). However, it is consistent with the moment 1 map of SO ($J_N = 7_8 - 6_7$) reported by Sakai et al. (2014a). It shows a slightly skewed feature, where the red-shifted component slightly extends from the northern part to the eastern part due to the rotation and infall motion, and the blue-shifted component slightly extends from the southern part to the western part. This indicates that the eastern part and the western part of the envelope are in front of and behind the protostar, respectively (Figure 4.6b). This configuration is consistent with our interpretation.

Figure 4.7 shows the PV diagrams of c-C_3H_2 ($5_{2,3} - 4_{3,2}$) along the six lines passing through the protostellar position (Figure 4.6a). Although the red-shifted components are weaker than the blue-shifted components and the systemic velocity components are self-absorbed as in the case of CS, these diagrams of c-C_3H_2 seem to be well reproduced by the model with the inclination angle of 85°, as represented by the blue contours. Because c-C_3H_2 preferentially exists in the envelope (Sakai et al., 2014b), the CS emission which is not seen in the c-C_3H_2 emission would trace the outflow component.

4.2.3 Outflow

On the basis of the kinematics of the envelope, we constrained the inclination angle of the envelope. Then we investigate the outflow structure seen in Figure 4.3, assuming that the outflow axis is perpendicular to the mid-plane of the infalling-rotating envelope. We employ a standard model of the outflow structure for the analysis (Lee et al., 2000; Oya et al., 2014). In this model, the shape of the outflow cavity wall and the velocity field on the wall are approximated by the following formulae (Lee et al., 2000):

$$z = C_{\rm as} R^2, \quad v_R = v_{\rm as} \frac{R}{R_0}, \quad v_z = v_{\rm as} \frac{z}{z_0}, \tag{4.1}$$

where the z axis is taken along the outflow axis with an origin at the protostar, and R denotes the radial size of the cavity perpendicular to z-axis. R_0 and z_0 are normalization constants, and both are set to be $1''$ (Oya et al., 2014). $C_{\rm as}$ and $v_{\rm as}$ are free parameters. Note that these parameters correspond to $(c \times D)$ and $(v_0 \times D)$ in the outflow model described in Chapter 3, where D denotes the distance of the source from the Sun (See also Chapter 10). Thus, the wall of the outflow cavity is assumed to have a parabolic shape, and it is assumed to be linearly accelerated as the distance from the outflow axis and the protostar. Such a parabolic model is widely applied to various low-mass and high-mass protostellar sources (e.g. Beuther et al., 2004; Yeh et al., 2008; Takahashi & Ho, 2012; Takahashi et al., 2013; Arce et al., 2013; Lumbreras & Zapata, 2014; Zapata et al., 2014). In this model, the intensity of the emission is assumed to be proportional to the column density, where the molecular density is simply assumed to be constant. Although these assumptions are not realistic, it does not matter the following analysis, where we only focus on the velocity structure but not on the intensity profile.

The blue lines shown in Figure 4.3 represent the best-fit result by eye, where the inclination angle is fixed to 85°, which is derived from the kinematic structure in the envelope (Section 4.2.2). The parameters are; $C_{\rm as} = 0.05$ arcsec^{-1} and $v_{\rm as} = 0.10$ km s^{-1}. The

accelerated outflow component in the western side of the protostar seems to be explained by this parameter. However, the velocity structure in the vicinity of the protostar is not well reproduced. This result suggests that the origin of the parabolic shape has a certain offset from the protostellar position, as pointed out by Tobin et al. (2008).

We therefore adopt the offset ($0\farcs62 \sim 85$ au) of the outflow origin reported by Tobin et al. (2010) in the outflow model. The upper left panel in Figure 4.8 shows the moment 0 map of CS ($J = 5 - 4$), whereas the other panels in Figure 4.8 are the PV diagrams along the gray arrows shown in the upper left panel. The blue lines in the PV diagrams represent the best model with the inclination angle of 85°, where $C_{\rm as} = 0.05$ arcsec^{-1}

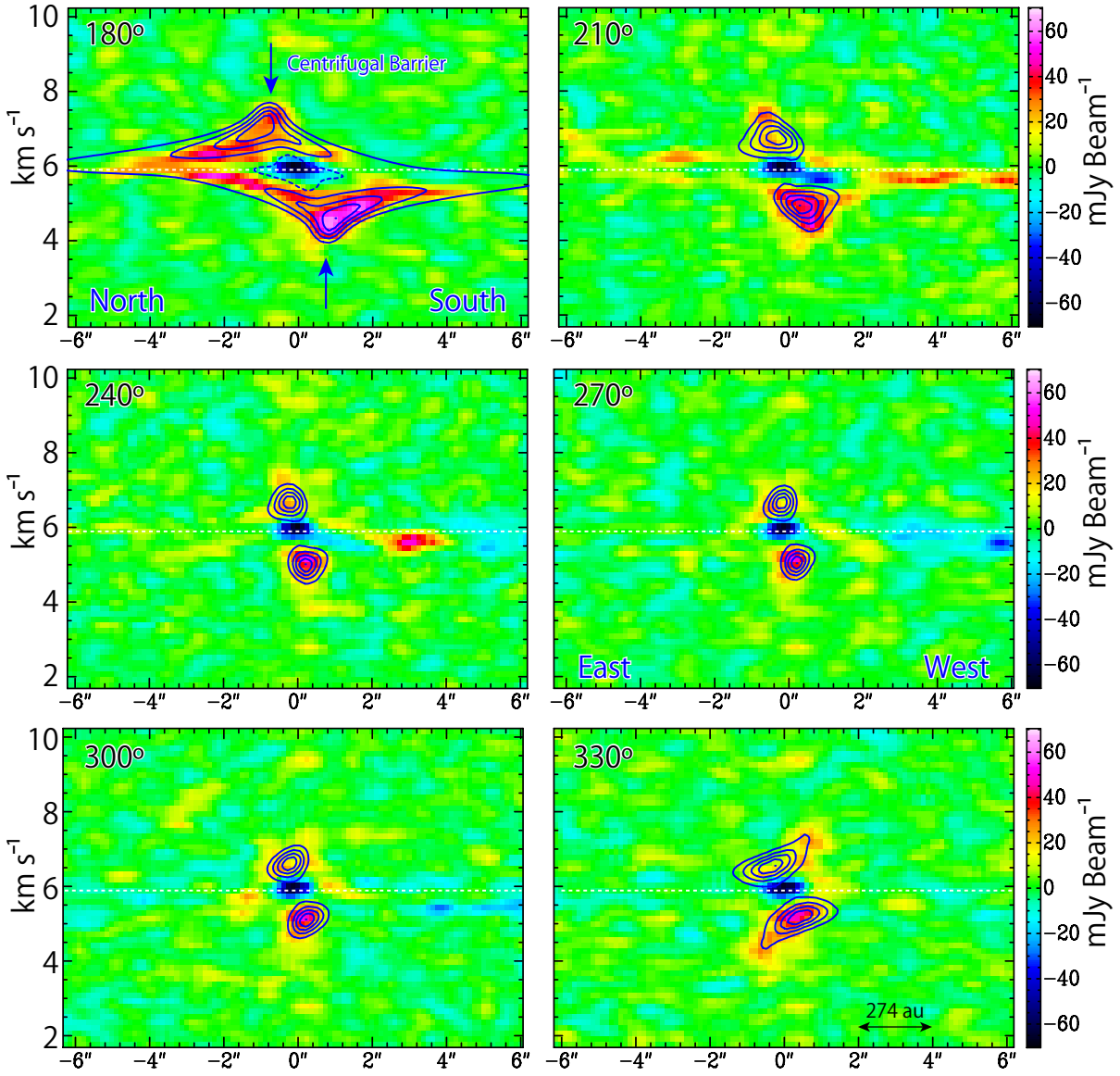

Figure 4.7: PV diagrams of c-C_3H_2 ($5_{2,3}-4_{3,2}$; color) along the lines shown in Figure 4.6(a). The blue contours represent the infalling-rotating envelope model with the inclination angle of 85°. Contours levels are every 20% of the peak intensity. The dashed contour around the central position in the panel "180°" represents the dip toward the center.

and $v_{\rm as} = 0.10$ km s^{-1}. When the inclination angle is lower than 70° or higher than 95°, the model does not reproduce the observations well with any values of $C_{\rm as}$ and $v_{\rm as}$. This constraint is consistent with that derived from the kinematic structure of the envelope (Section 4.2.2). The red lines in Figure 4.1(a), the white lines in Figure 4.1(b), and the blue lines in the upper left panel in Figure 4.8 represent the best model with the inclination angle of 85°. Although the parameters for the model are derived from the kinematic structure of the outflow/envelope system, the model seems to explain the spatial extent of the outflow in the vicinity of the protostar. The maximum velocity shifts from the systemic velocity (5.9 km s^{-1}; Sakai et al., 2010) along the line of sight for the eastern and western lobe in Figure 4.1(a) are reported to be 6.9 and 9.6 km s^{-1}, respectively, from the ^{12}CO ($J = 3 - 2$) observation (Hogerheijde et al., 1998). In the above model, the maximum velocity shift for the two lobes is 8.2 km s^{-1} at the distance of 200″ from the protostar. Then, the physical parameters for the model appear to be roughly consistent with the larger-scale observation, even though they are derived from the kinematic structure in the spatial scale of a few tens of arcsecond.

Figure 4.9 shows the PV diagrams of the outflow along the lines perpendicular to the outflow axis shown in the upper left panel in Figure 4.8. The blue lines represent the best model, which seems to reproduce the basic features. When the outflow axis is almost parallel to the plane of the sky, PV diagrams across the outflow axis show an elliptic feature, as seen in the IRAS 15398–3359 case (Chapter 5). A part of such an elliptic feature is indeed seen in the PV diagrams.

It should be noted that the kinematic and geometric structure might be different between the eastern and western lobes, because the simple model cannot perfectly explain the distribution (for instance, the PV diagrams in Figure 4.8). This may originate from different distributions of ambient gas between the two sides. However, a detailed discussion on this issue is outside the scope of this thesis, since the CS ($J = 5 - 4$) distributions in the outflow are faint and heavily resolved out.

4.3 Discussion

4.3.1 Direction of the outflow

We evaluated the inclination angle of the infalling-rotating envelope with its direction by use of a simple ballistic model. If the outflow axis is perpendicular to the mid-plane of the envelope, the direction of the inclination contradicts previous reports (Hogerheijde et al., 1998; Tobin et al., 2008, 2010). Here, we discuss this contradiction.

Tobin et al. (2008, 2010) assumed a configuration in which the eastern part of the envelope faces the observer (Figure 4.6c), because the infrared (L' band) reflection by the cavity wall of the outflow in the vicinity of the protostar is brighter in the eastern part. The contradiction can originate from the following two reasons.

The first possibility is the extinction by inhomogeneous gas distribution around the protostar. Green contours in Figure 4.1(b) represent the moment 0 map of the CS ($J = 5 - 4$) emission. In the southwestern side of the protostar, a ridge structure is extended along the western outflow-cavity, where the CS ($J = 5 - 4$) emission is bright. In this ridge, the emission in the L' band is relatively weak. This indicates that the dense gas

on the near side of the outflow cavity obscures the scattered light in the L' band. In fact, the upper right panel in Figure 4.9 shows that the bright CS emission of this ridge is slightly blue-shifted, which indicates that this component is in front of the outflow axis. We evaluated the CS column density to be $(1-2)\times10^{13}$ cm^{-2} toward the western position offset from the protostar by 0.″7, which is the FWHM of the synthesized beam along the east-west axis. This value was derived by using the RADEX code (van der Tak et al., 2007), where the H_2 density and the kinetic temperature were assumed to be

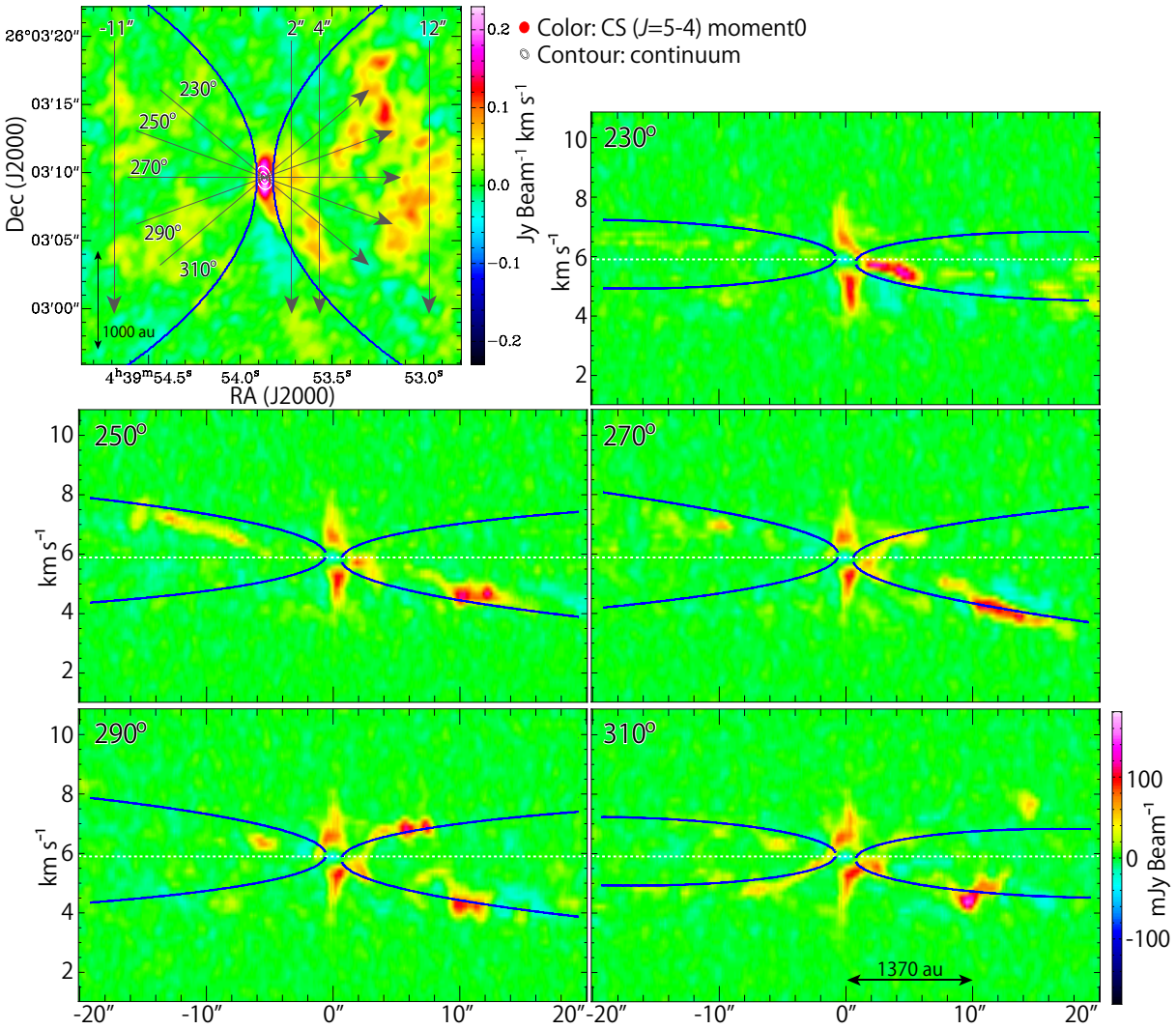

Figure 4.8: Integrated intensity (moment 0) map (upper left panel) and PV diagrams of CS ($J = 5-4$). The moment 0 map of CS is the same as in Figure 4.2. White contours in the moment 0 map represent the continuum map, whose contour levels are as the same as those in Figure 4.2. PV diagrams are prepared along the gray arrows passing through the protostellar position shown in the moment 0 map. The blue lines represent the result of the best-fit outflow model, where the parameters are as follows; $i = 85°$, $C_{\rm as} = 0.05$ arcsec^{-1}, $v_{\rm as} = 0.10$ km s^{-1}, and the origins of the lobes have an offset of 0.″62 from the protostellar position (Tobin et al., 2010).

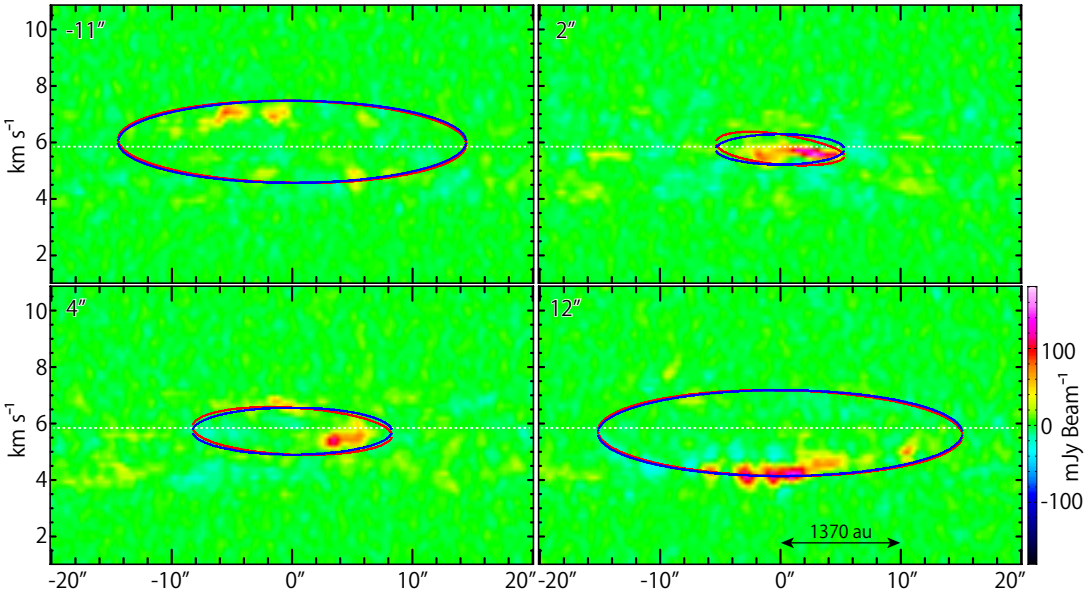

Figure 4.9: PV diagrams of CS ($J = 5-4$; color) across the outflow axis, where the position axes are shown in the upper left panel in Figure 4.8. The blue lines represent the result of the best-fit outflow model, where the parameters are; $i = 85°$, $C_{\rm as} = 0.05$ arcsec^{-1} and $v_{\rm as} = 0.10$ km s^{-1}, and the origins of the lobes have an offset of $0\farcs62$ from the protostellar position (Tobin et al. 2010). The red lines represent another outflow model, where arotation motion of the outflow cavity wall is taken into account (See Section 4.3.2), although they are almost overlapped with the blue lines.

$(10^6 - 10^7)$ cm^{-3} and 30 K, respectively (Sakai et al., 2014a,b). The H_2 column density is then roughly estimated to be $(1-2) \times 10^{22}$ cm^{-2} by using a CS fractional abundance relative to H_2 of 10^{-9}, which is a typical value for protostellar cores (e.g. van Dishoeck et al., 1995; Watanabe et al., 2012). This H_2 column density corresponds to an L' band extinction of about $(0.5-1)$ mag.

Since the observed CS emission is heavily resolved out and mainly traces dense gas ($> 10^6$ cm^{-3}), the L' band extinction estimated above could be the lower limit. If the emission in the L' band is weakened by the outflow cavity wall, the brightness on the two sides of the protostar depends on the distribution of matter in the outflow cavity, and the brightness asymmetry cannot constrain the direction of the inclination. Velusamy et al. (2014) recently reported that the *Spitzer* 3.6 μm HiRes deconvolved image shows the brightness asymmetry of the outflow cavity in the vicinity of the protostar which is opposite to that reported by Tobin et al. (2008, 2010). The result by Velusamy et al. (2014) seems consistent with the configuration which we found in this analysis (Figure 4.6b). Thus, the observations of the morphology of the cavity reflection seem inconsistent with each other. Hence, the configuration of the outflow/envelope system derived from the kinematics of the infalling-rotating envelope is more reliable than that from the morphology.

The second possibility solving the contradiction is that the outflow axis is not perpendicular to the mid-plane of the envelope. This may be possible due to some asymmetry of the protostellar system such as binarity, although the binarity in this source is contro-

versial (Loinard et al., 2002). In recent studies of exoplanets, it is reported that the spin axis of the central star is not always parallel to the orbital axes of planets (e.g. Xue et al., 2014). Although the scattering among planets are considered as an important cause, the angular momentum of the central star and the disk could have different axes. This is an important issue for exo-planet studies. In this relation, exploring this possibility would be very interesting.

According to Hogerheijde et al. (1998), the outflow seen in the ^{12}CO ($J = 3 - 2$) line is mainly blue-shifted and red-shifted in the eastern and western side of the protostar, respectively, in a large scale of $\sim 100''$, although the counter velocity components are seen in both lobes. If the direction of the small-scale outflow is different from that of the large-scale one, it may imply that the outflow is precessing. The dynamical time scales for the eastern and western lobe are reported to be 1.5×10^4 and 9.0×10^3 yr, respectively, which are not corrected for inclination (Hogerheijde et al., 1998). Note that the dynamical time scales are rough estimates based on the apparent maximum velocity shifts and the lengths of the lobes. Here, it should be stressed that the velocity along the line of sight ($v_{\rm LOS}$) almost consists of the velocity component perpendicular to the outflow axis, which represents an expanding motion of the cavity wall, because of the almost edge-on geometry. Hence, the velocity along the outflow axis can hardly be estimated by $v_{\rm LOS}/\cos i$, where i is the inclination angle of the outflow axis (0° for the pole-on geometry). When the apparent distance from the protostar on the plane of the sky is $100''$, the distance from the protostar along the outflow axis (z) is also $\sim 100''$ with the inclination angle of 85°. The line of sight and each outflow cavity wall have two intersections, which have different line-of-sight velocities ($v_{\rm LOS}$). In the red-shifted lobe, the velocity along the outflow axis (v_z) and the expanding velocity (v_r) at the distance projected on the plane of the sky of $100''$ from the protostar are calculated to be $(v_z, v_r) = (9.6\ {\rm km\ s^{-1}}, 4.4\ {\rm km\ s^{-1}})$ and $(v_z, v_r) = (10.4\ {\rm km\ s^{-1}}, 4.6\ {\rm km\ s^{-1}})$ for the intersection in front of the outflow axis and that behind the outflow axis, respectively. Hence, the velocities along the line-of-sight ($v_{\rm LOS}$) are calculated to be -3.5 and $5.4\ {\rm km\ s^{-1}}$. In the blue-shifted lobe, the velocity along the outflow axis and the expanding velocity are the same as those in the red-shifted lobe, while the velocity shifts from the systemic velocity along the line-of-sight ($v_{\rm LOS}$) have the opposite sign. Then, the age of the lobe at the distance of $100''$ from the protostar is estimated to be $t = z/v_z \sim 6.5 \times 10^3$ yr. Assuming that the inclination angle is 85° in the $10''$ scale and 95° in the $100''$ scale, we speculate a precession of 10° in $\sim 6.5 \times 10^3$ yr. Here, we assume that there was no other precession event in between. This is comparable to the case of L1157, where a precession of 6° is observed with a period of $\sim 4 \times 10^3$ yr (Gueth et al., 1996).

An alternative possibility is that emission of the outflow cavity is not homogeneous, and the blue-shifted and red-shifted emissions are dominant in the large scale eastern and western lobes, respectively, by accident. This situation could happen because the outflow is blowing almost along the plane of the sky.

4.3.2 Angular momentum

In the model of the infalling-rotating envelope, it is assumed that the gas cannot fall inward of the centrifugal barrier due to the angular momentum conservation (Chapter 3). However, Sakai et al. (2014b) pointed out that H_2CO possibly resides inside the centrifugal

barrier. If so, the gas has to lose its angular momentum to fall beyond the centrifugal barrier. The outflow is a candidate mechanism extracting the angular momentum from the envelope gas (e.g. Tomisaka, 2002; Machida & Hosokawa, 2013). Hence, it is interesting to explore the possibility of outflow rotation. In fact, rotation of outflow and jet is suggested for various protostellar sources (Codella et al., 2007; Coffey et al., 2007; Lee et al., 2007, 2008, 2009; Launhardt et al., 2009; Zapata et al., 2010; Choi et al., 2011; Pech et al., 2012; Hara et al., 2013). Rotation is mostly observed for a collimated jet, while rotation of a well spread outflow like the L1527 outflow is not very evident (B59#11; Hara et al., 2013).

As shown in Figure 4.9, the velocity field on the outflow cavity wall is almost symmetric to the outflow axis. Arotation motion is hardly seen in the outflow cavity wall. If the angular momentum in the envelope were extracted by the outflow, the northern edge and the southern edge of the outflow should be more red-shifted and blue-shifted than the model, respectively. The red lines in Figure 4.9 represent another outflow model, where therotation motion of the outflow cavity wall is taken into account by a simple model. In this rotating outflow model, it is assumed that the specific angular momentum on the outflow cavity wall is conserved (Launhardt et al., 2009), and the launching point of the outflow is at the centrifugal barrier. The specific angular momentum of the outflow in this model is roughly approximated to be the same as that of the envelope gas, which is determined by the protostellar mass and the radius of the centrifugal barrier (Section 4.2.2). Then therotation motion on the outflow cavity wall is represented by the radial size R of the outflow cavity perpendicular to the outflow-axis as:

$$v_{\rm rot} = \frac{\sqrt{2GMr_{\rm CB}}}{R}, \tag{4.2}$$

where $r_{\rm CB}$ denotes the radius of the centrifugal barrier in the infalling-rotating envelope, M denotes the protostellar mass, and G is the gravitational constant. Therotation motion on the outflow cavity wall would be large near the launching point of the outflow (small R; the upper right panel in Figure 4.9), and decrease as the distance from the protostar (large R; the bottom right panel in Figure 4.9). This would be a reason why the rotation motion has been found in the well collimated jets. Figure 4.9 shows that the results of the two models are almost overlapped with each other. Therefore, it is essential to investigate the launching point of the outflow at a higher spatial resolution.

In this chapter, we investigated the kinematic structure of the outflow in L1527 with the aid of the kinematic structure of the envelope. Recently, spatial resolution in millimeter/submillimeter-wave observations has become much higher with ALMA than before, and hence, it will be possible to unveil the small-scale structure of the envelope, especially in the vicinity of the centrifugal barrier. In addition to the envelope, we here stress that the outflow can be investigated from observations focused on a narrow region around the protostar by use of the outflow model. Outflow morphology in a large scale is often affected by interactions with the ambient gas, and elimination of this effect is indispensable for characterization of outflows, as discussed by Velusamy et al. (2014). Hence, observations of outflows in the vicinity of the protostar will be an important technique in the further outflow studies, as demonstrated in this chapter. Moreover, such high-resolution observations will delineate both the inner structure of the envelope and

the launching point of the outflow, which would be related to each other in forming the rotationally-supported disks.

Appendix: Envelope model with various inclination angles

Figure 4.10 shows the PV diagrams of CS ($J = 5 - 4$; color) along the two lines passing through the protostellar position shown in Figure 4.6; one is perpendicular to the outflow axis ("180°") and the other is parallel to it ("270°"). The blue contours represent the infalling-rotating envelope models with various inclination angles. In these models, the protostellar mass and the radius of the centrifugal barrier are assumed to be 0.18 $M_\odot$ and 100 au, respectively, which are derived by Sakai et al. (2014a). The outer radius of the envelope is fixed to be 1000 au, which well reproduces the PV diagram of CCH (Chapter 3; Sakai et al., 2014b). The emission is convolved with a Gaussian beam with FWHM of $0''.5 \times 0''.5$ and the intrinsic line width of 0.5 km s^{-1}. In this model, the intensity of the emission is simply assumed to be proportional to the column density, where the molecular density is assumed to be proportional to $r^{-1.5}$. The effects of the optical depth, the excitation, and the temperature gradient are not taken into account. The gas kinetic temperature is reported to be $(30 - 60)$ K for the infalling-rotating envelope component and the centrifugal barrier (Sakai et al., 2014a,b). With the assumption of the optically thin condition and the constant molecular abundance, the intensity is proportional to $\frac{1}{U(T)} \exp\left(-\frac{E_\mathrm{u}}{kT}\right)$, where T denotes the gas temperature, $U(T)$ the partition function of the upper state, E_u the upper state energy, and k the Boltzmann constant. With the upper energy of the CS line ($J = 5 - 4$) of 35 K, $\frac{1}{U(T)} \exp\left(-\frac{E_\mathrm{u}}{kT}\right)$ is calculated to be 0.012 and 0.011 with T of 30 and 60 K, respectively. Thus, the temperature gradient does not seriously affect the intensity profile in the infalling-rotating envelope.

The optically thin condition for the velocity components outside the systemic velocity (5.9 km s^{-1}; Sakai et al., 2010) can be justified for the CS line, because the optical depth toward the centrifugal barrier estimated by the LVG analysis is 0.1 for the H_2 density range form 3×10^6 to 3×10^7 cm^{-3} and the temperature range from 30 to 60 K. Although the CS line is heavily self-absorbed at the systemic velocity, we do not consider this component in comparison with the models.

Panels for the inclination angles of 85° and 95° in Figure 4.10 are the same as the corresponding panels in Figures 4.4 and 4.5, respectively. As discussed in Section 4.2.2, the PV diagram along the line perpendicular to the outflow axis (i.e. along the envelope; "180°") reflects the absolute value of the inclination angle regardless of the directions of the inclination with respect to the edge-on configuration ($i = 90°$). On the other hand, the PV diagram along the outflow axis ("270°") reflects the infall motion of the envelope more significantly, and is sensitive to the direction of the inclination.

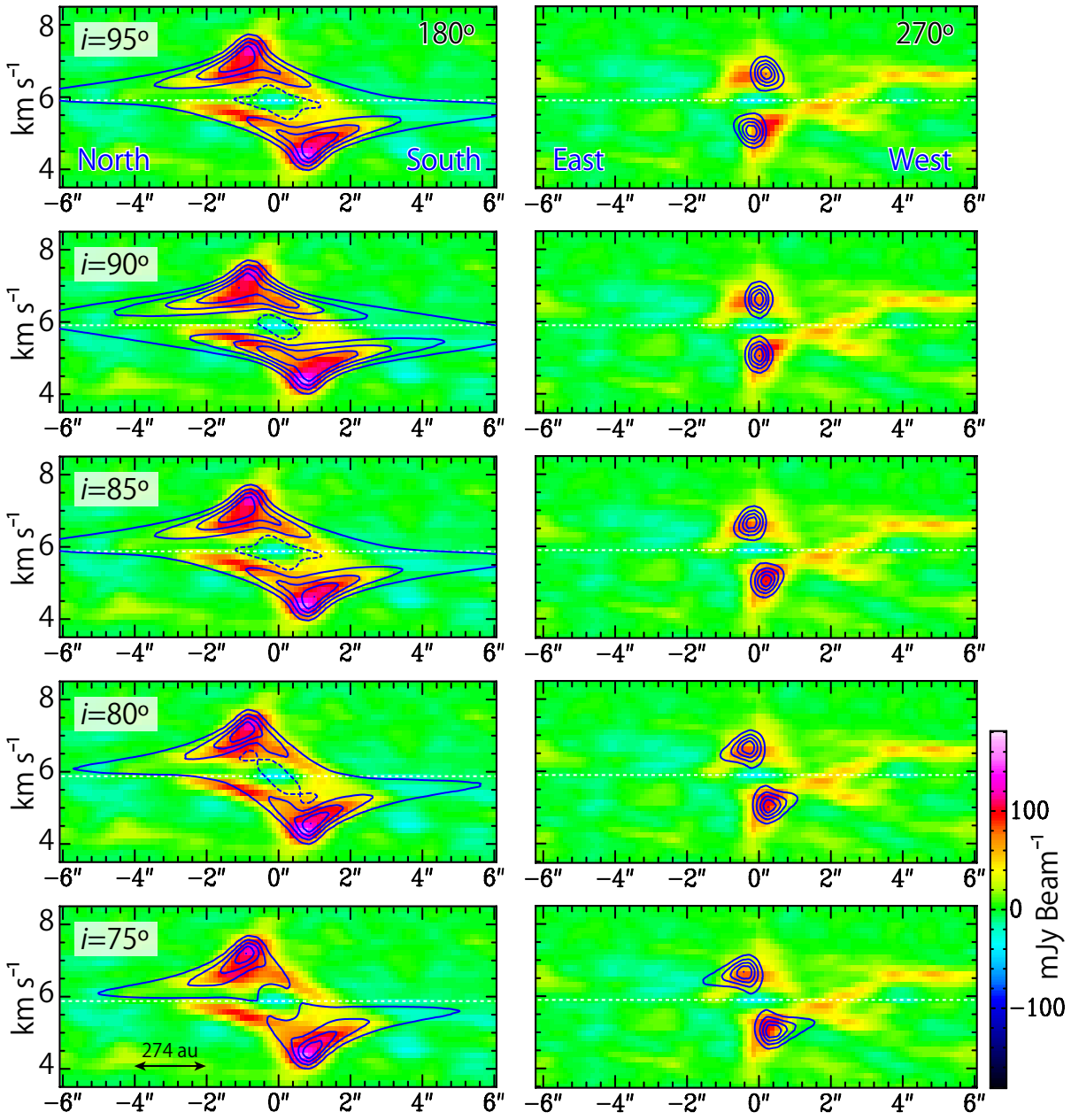

Figure 4.10: PV diagrams of CS ($J = 5 - 4$; color) along the lines shown in Figure 4.6(a). The blue contours in the two diagrams in each row represent the infalling-rotating envelope model with the inclination angle of 95° (Figure 4.6c), 90° (edge-on), 85° (Figure 4.6b), 80°, or 75°. Contour levels are every 20% of the peak intensity in each model. The dashed contours around the central position in the panels in the left column, except for the panel for i of 75°, represent the dip toward the center. The panels for the inclination angles of 85° and 95° are the same as those in Figures 4.4 and 4.5, respectively.

Chapter 5

IRAS 15398–3359

Sub-arcsecond (0.″5) images of the H_2CO and CCH line emission have been obtained in the 0.8 mm band toward the low-mass protostar IRAS 15398–3359 in the Lupus 1 cloud as one of the Cycle 0 projects of the Atacama Large Millimeter/Submillimeter Array. We have detected a compact component concentrated in the vicinity of the protostar and a well-collimated outflow cavity extending along the northeast-southwest axis. The inclination angle of the outflow is found to be about 70°, or nearly edge-on, based on the kinematic structure of the outflow cavity. This is in contrast to previous suggestions of a more pole-on geometry. The centrally concentrated component is interpreted by use of a model of the infalling-rotating envelope with the estimated inclination angle, and the protostellar mass is estimated to be less than 0.09 $M_\odot$. Higher spatial resolution data are needed to infer the presence of a rotationally-supported disk for this source, hinted at by a weak high-velocity H_2CO emission associated with the protostar.

5.1 Introduction

In L1527, we have demonstrated that the kinematic structures of the infalling-rotating envelope and the outflow cavity wall are explained by the simple models. Especially, the discovery of the centrifugal barrier in an infalling-rotating envelope and the chemical change across the centrifugal barrier provide us with a completely new insight in disk formation study. It is now required to confirm whether such kinematic and chemical structures are common in low-mass protostellar sources. In this chapter, we conduct a similar analysis in another WCCC source IRAS 15398–3359. While we have analyzed the structure of the outflow in L1527 based on the analysis of its envelope, we here make use of the clear outflow components in IRAS 15398–3359 to investigate the envelope structure.

As mentioned in Chapter 4, it is still unknown when and how disks are formed in the star formation process. This is because disks are generally difficult to identify in Class 0 sources due to the overwhelming emission from protostellar envelopes and outflows. Even absence of such a disk down to 45 au is claimed for the Class 0 protostar NGC 1333 IRAS 2A (Brinch et al., 2009; Maret et al., 2014). Furthermore, the disk structure in Class 0 sources is expected to be small, and high spatial resolution and high sensitivity observations are essential.

This chapter has been published in Oya et al., 2014, ApJ, 795, 152

IRAS 15398–3359 is a low-mass Class 0 protostar in the Lupus 1 molecular cloud at a distance of 155 pc (Lombardi et al., 2008). A molecular outflow was detected by single-dish observations of CO emission (Tachihara et al., 1996; van Kempen et al., 2009). Based on the relatively large overlap between the red- and blue-shifted lobes of the outflow (CO $J = 3 - 2$) observed with the James Clerk Maxwell Telescope ($\theta_{\rm HPBW} \sim 15''$), the outflow was thought to have a pole-on geometry (van Kempen et al., 2009). Mardones et al. (1997) observed H_2CO and CS lines toward this source to search for a sign of an infall motion without success. On the other hand, Kristensen et al. (2012) reported the presence of an inverse P-Cygni profile of the H_2O ($1_{1,0} - 1_{0,1}$) at 557 GHz, indicating an infall motion of the envelope on a scale of about 10^4 au. Jørgensen et al. (2013) detected a ring structure of the $H^{13}CO^+$ ($J = 4 - 3$) emission at a (150 − 200) au scale. They proposed that the ring structure is caused by the destruction of HCO^+ through reactions with H_2O that is evaporated by the enhanced luminosity due to a recent accretion burst.

IRAS 15398–3359 also shows peculiar chemical features in other ways. Various carbon-chain molecules such as CCH, C_4H, and CH_3CCH are detected in the vicinity of the protostar, which is characteristic of so-called warm carbon-chain chemistry (WCCC) sources (Sakai et al., 2008a, 2009a; Sakai & Yamamoto, 2013). As demonstrated in Chapters 3 and 4, the kinematic structure of the envelope in another WCCC source, L1527, is well reproduced by the infalling-rotating envelope model. Since both L1527 and IRAS 15398–3359 are WCCC sources, it is interesting to investigate whether the envelope of IRAS 15398–3359 has a similar structure. To explore when and how a rotationally-supported disk is formed around a protostar, a deep insight into the structure of the envelope of Class 0 protostars is important. With these motivations, we conducted ALMA observations toward IRAS 15398–3359 in several molecular lines.

5.2 Observations

Observations of IRAS 15398–3359 were carried out with ALMA in Cycle 0 operations on 2012 December 31. Spectral lines of H_2CO and CCH were observed with the Band 7 receiver at frequencies of 349 − 352 GHz, and 364 GHz. The spectral line parameters are listed in Table 5.1. Twenty-five antennas were used in the observations, where the baseline length ranged from 13 to 338 m. The field center of the observations was (α_{2000}, δ_{2000}) = ($15^{\rm h}43^{\rm m}02\overset{\rm s}{.}3$, $-34°09'07\overset{''}{.}5$). The typical system temperature was 120 − 300 K. The backend correlator was tuned to a resolution of 122 kHz and a bandwidth of 469 MHz, which corresponds to the velocity resolution of 0.1 km s^{-1} at 366 GHz. J1517–243 was used for phase calibration every 12 minutes. The bandpass calibration was carried out on J1256–057 for the H_2CO lines and on J1924–292 for the CCH lines, whereas the absolute flux density scale was derived from Mars and Titan, respectively. The data calibration was performed in the antenna-based manner and uncertainties are less than 10%. Images were obtained by using the CLEAN algorithm. The continuum image was prepared by averaging line-free channels and the line maps were obtained after subtracting the continuum directly from the visibilities. The primary beam (half-power beam width) is $17''$. The total on-source time was 27 minutes for the H_2CO lines and 21 minutes for the CCH lines. The synthesized-beam size is $0\overset{''}{.}57 \times 0\overset{''}{.}42$ (P.A. = 49°) for the continuum image and $0\overset{''}{.}60 \times 0\overset{''}{.}44$ (P.A. = 46°) for the H_2CO image. The rms noise levels for the continuum

Table 5.1: Observed Line Parameters[a]

Transition	Frequency (GHz)	$E_u k^{-1}$ (K)	$S\mu^{2b}$ (D^2)
H_2CO			
$5_{0,5} - 4_{0,4}$	362.7360480	52	27.168
$5_{1,5} - 4_{1,4}$	351.7686450	62	26.096
$5_{2,4} - 4_{2,3}$	363.9458940	100	22.834
CCH			
$N = 4 - 3, J = 7/2 - 5/2, F = 3 - 2$	349.4006712	42	1.6942
$N = 4 - 3, J = 7/2 - 5/2, F = 4 - 3$	349.3992756	42	2.2712

[a] Taken from CDMS Müller et al. (2005).
[b] Nuclear spin degeneracy is not included.

and the H_2CO emission are 0.001 and 0.01 Jy beam^{-1}, respectively. The continuum peak is at: $(\alpha_{2000}, \delta_{2000}) = (15^h43^m02\overset{s}{.}24, -34°09'06\overset{''}{.}7)$. The CCH data were combined with those taken in another observing program (2011.0.00628.S; PI: Jes Jørgensen) carried out with $15 - 16$ antennas. The signal-to-noise ratio (S/N) was improved from 13.7 to 24.5 with this combination. The synthesized beam of the combined CCH image is $0\overset{''}{.}70 \times 0\overset{''}{.}46$ (P.A. = 72°), and the rms noise level is 0.015 Jy beam^{-1}. We also detected the CH_3OH line in these observations (Jørgensen et al., 2013). We did not observe any other significant line features in the observed frequency range.

5.3 Results

5.3.1 Overall Distribution of H_2CO and CCH

Figure 5.1(a) shows the moment 0 (integrated intensity) map of the H_2CO ($5_{1,5} - 4_{1,4}$) line. The most prominent feature is a well-collimated outflow extending symmetrically from the protostar along a northeast-southwest axis. The outflow has a very straight-wall structure, as in the case of the HH46 outflow (Arce et al., 2013). The northeastern lobe of the outflow is red-shifted, while the southwestern lobe is blue-shifted, as shown in the moment 1 (velocity field) map (Figure 5.1b). In these observations, the emission extending over $12''$ scale or larger is not reliable due to the lack of short baselines. Although the size of the outflow looks compact (about $8''$ for each lobe), the emission of the outer part may be resolved out or may be weak due to insufficient excitation conditions. The apparent width of the outflow is $4''$ at a distance of $8''$ from the protostar. Figure 5.1(c) shows the moment 0 map of a high-excitation line of H_2CO ($5_{2,4} - 4_{2,3}$). The emitting region of the H_2CO ($5_{2,4} - 4_{2,3}$) line is essentially similar to that of the H_2CO ($5_{1,5} - 4_{1,4}$) line, although the S/N ratio of the former is rather poor. In these maps, a bright knot ('Clump A' in Figure 5.1a) can be seen in the red-shifted lobe, which could be a shocked region caused by an impact of the outflow with dense clumps in a surrounding cloud.

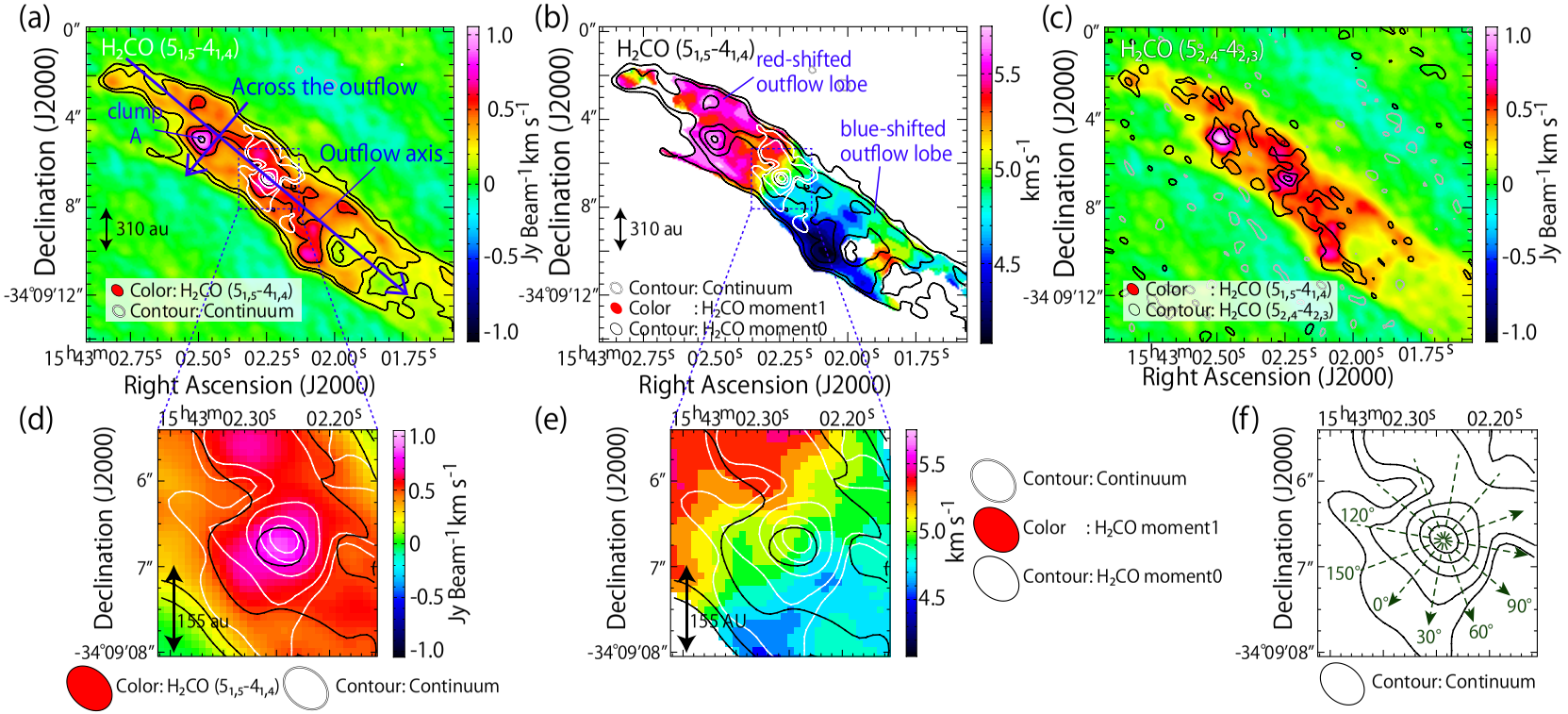

Figure 5.1: (a) Moment 0 (integrated intensity) map of the H_2CO ($5_{1,5} - 4_{1,4}$; color, black contours) line. White contours represent the 0.8 mm continuum emission. The blue arrows represent the lines along which the PV diagrams of Figures 5.5(a) and (b) are prepared. (b) Moment 1 map (velocity field) of the H_2CO ($5_{1,5} - 4_{1,4}$) line. The black and white contours are the same as those in panel (a). (c) Moment 0 map of the H_2CO ($5_{2,4} - 4_{2,3}$; contours) line superposed on that of the H_2CO ($5_{1,5} - 4_{1,4}$; color) line . A few bright spots can be seen in both maps. (d) A blow-up of the central part of panel (a). The black and white contours are the same as those in panel (a). (e) A blow-up of the central part of panel (b). The black and white contours are the same as those in panel (a). (f) A blow-up of the central part of the 0.8 mm continuum map. The black dashed arrows represent the lines along which the PV diagrams of Figures 5.7, 5.9, and 5.10 are prepared. The arrow labeled as "0°" has the position angle (P.A.) of 140°, and others are taken for P.A. of every 30°.

In addition to the outflow feature, a centrally concentrated component with a single-peaked distribution can also be recognized, as shown in a blow-up of the central part of Figure 5.1(a) (Figure 5.1d). A blow-up of the moment 1 map is also shown in Figure 5.1(e). The approximate extent of the central component is estimated to be about 2″ in diameter based on the intensity distribution along the line perpendicular to the outflow (Figure 5.2), which corresponds to 310 au. Figure 5.3 shows the spectral line profiles of the H_2CO and CCH lines toward the protostellar position averaged over the synthesized beam. The line width of the H_2CO line is as narrow as 2 km s^{-1} even toward the protostellar position. By using the RADEX program (van der Tak et al., 2007) to fit the intensity of the two temperature sensitive lines of para-H_2CO ($5_{0,5} - 4_{0,4}$, $5_{2,4} - 4_{2,3}$), the column density of H_2CO and the kinetic temperature toward the protostar are estimated to be 3×10^{13} cm^{-2} and $36 - 38$ K on the assumption that H_2 density is $(1 \times 10^7 - 1 \times 10^8)$ cm^{-3} and the line width is 1.8 km s^{-1}. In addition, the ortho/para ratio is estimated to be 2.8 with the intensity of an ortho-H_2CO line ($5_{1,5} - 4_{1,4}$). The optical depths for these lines are 0.27 ($5_{0,5} - 4_{0,4}$), 0.06 ($5_{2,4} - 4_{2,3}$), 0.53 ($5_{1,5} - 4_{1,4}$), respectively, therefore the lines are not opaque.

Figure 5.4(a) shows the moment 0 map of CCH ($N = 4{-}3$, $J = 7/2{-}5/2$, $F = 4{-}3$ and $3{-}2$), while Figure 5.4(b) is a blow-up of its central part. The outflow cavity is prominent and the centrally concentrated component can also be seen. The emitting region of the CCH line around the protostar is more extended along the southeast-northwest axis than that of the H_2CO line. It seems to have a slight dip toward the protostellar position as shown in the intensity profile along the line perpendicular to the outflow axis (Figure 5.2). This feature of CCH is consistent with that reported by Jørgensen et al. (2013). Although the spectrum of CCH at the protostellar position is complicated because of the two hyperfine components (Figure 5.3), the line width of each hyperfine component of CCH is 2 km s^{-1} or less, as in the case of H_2CO.

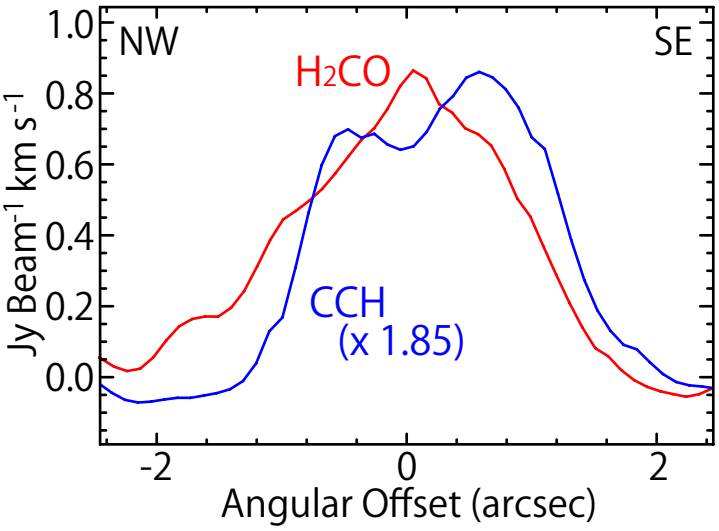

Figure 5.2: Intensity profiles of the H_2CO ($5_{1,5} - 4_{1,4}$) and CCH (F_2) lines along the line perpendicular to the outflow axis ("0°" shown in Figure 5.1f).

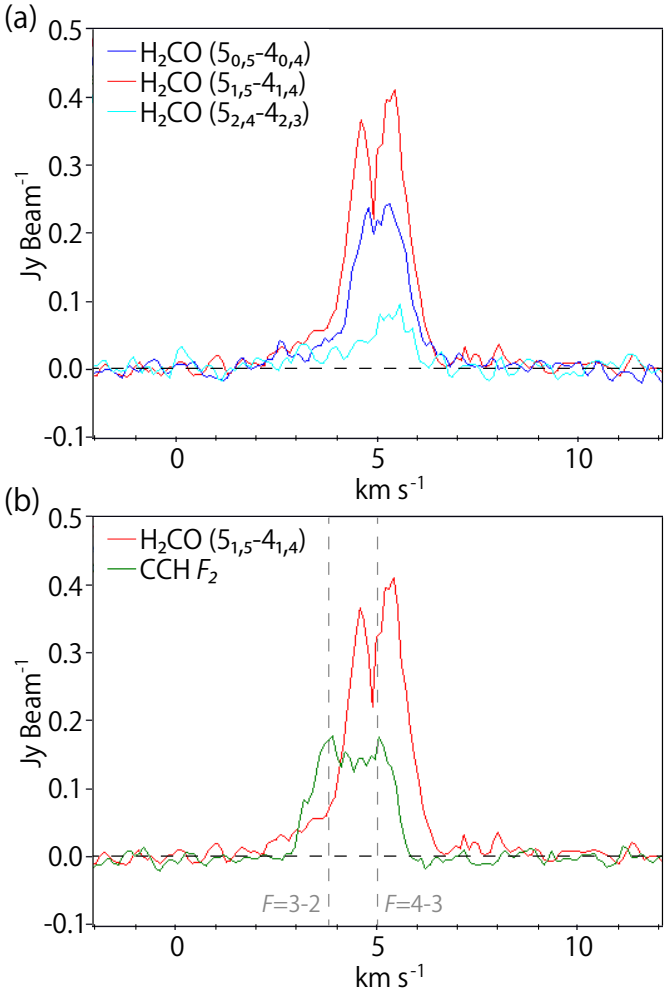

Figure 5.3: Spectra of the H_2CO ($5_{0,5} - 4_{0,4}$, $5_{1,5} - 4_{1,4}$ and $5_{2,4} - 4_{2,3}$) and CCH ($N = 4 - 3, J = 7/2 - 5/2, F = 4 - 3$ and $3 - 2$) lines toward the protostellar position. Two vertical dashed lines in panel (b) represent the systemic velocities for the two hyperfine components of CCH.

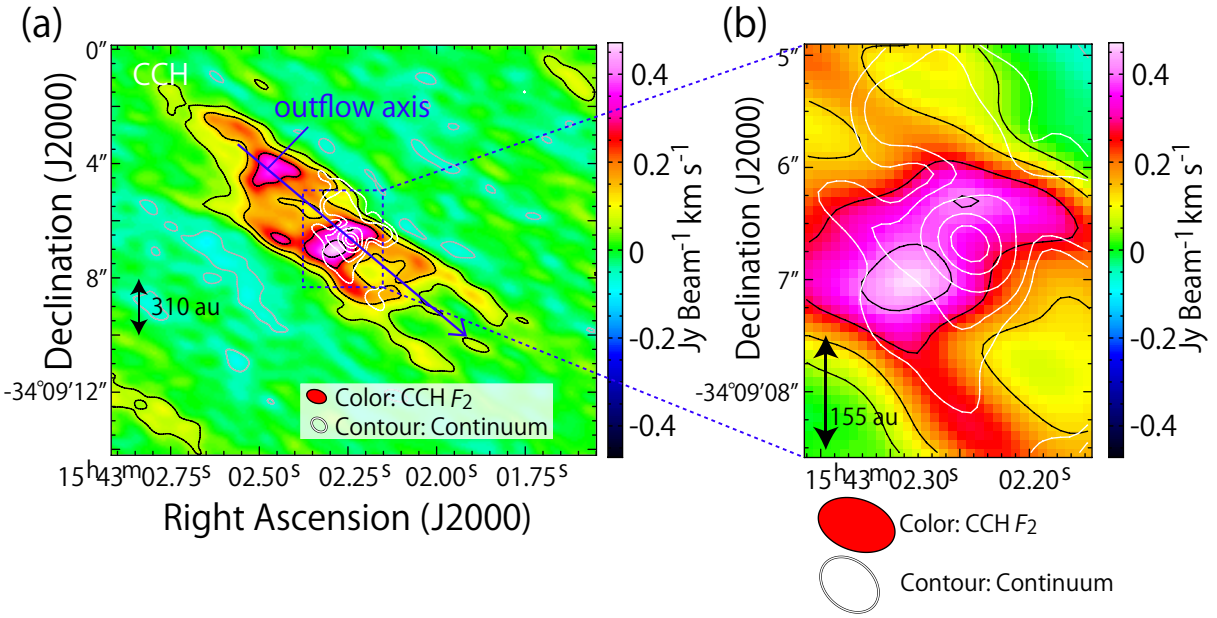

Figure 5.4: (a) Moment 0 map of the CCH ($N = 4 - 3, J = 7/2 - 5/2, F = 4 - 3$ and $3 - 2$; F_2; color, black contour) line. White contours represent the 0.8 mm continuum distribution, which is the same as those in Figure 5.1(a). The blue arrow represents the line along which the PV diagram of Figure 5.6 is prepared. (b) A blow-up of the central part of panel (a). The black and white contours are the same as those in panel (a).

5.3.2 Outflow

We first analyze the outflow feature observed in the H_2CO ($5_{1,5} - 4_{1,4}$) line. Figure 5.5(a) shows the position-velocity (PV) diagram of the H_2CO ($5_{1,5} - 4_{1,4}$) line emission along the outflow axis through the protostellar position shown in Figure 5.1(a). The outflow has a red-shifted component extending to the northeast from the protostar and a blue-shifted component extending to the southwest from the protostar. Since the red- and blue-shifted lobes of the outflow show little overlap with each other around the protostar, the outflow axis seems to be close to the plane of the sky, indicating that the disk/envelope geometry is almost edge-on. The highest velocity at a certain distance to the protostar linearly increases as a function of the distance, as often observed for outflow cavities (e.g. Lee et al., 2000; Arce et al., 2013). The intense knot in the red-shifted component corresponds to Clump A in Figure 5.1(a). In addition to the high-velocity component, another velocity component can be seen around the systemic velocity ($\sim$ 5 km s^{-1}; Sakai et al., 2009a). This component is slightly blue-shifted on the northeastern side of the protostar and red-shifted on the southwestern side of the protostar, which is the reverse case compared to the high-velocity component.

Figure 5.5(b) is the PV diagram of the H_2CO ($5_{1,5} - 4_{1,4}$) line along the line perpendicular to the outflow axis in the red-shifted lobe shown in Figure 5.1(a). The PV diagram shows an elliptic feature with a knot-like distribution at the higher-velocity range. This knot-like structure corresponds to Clump A in Figure 5.1(a). The gas in the cavity wall seems to be expanding.

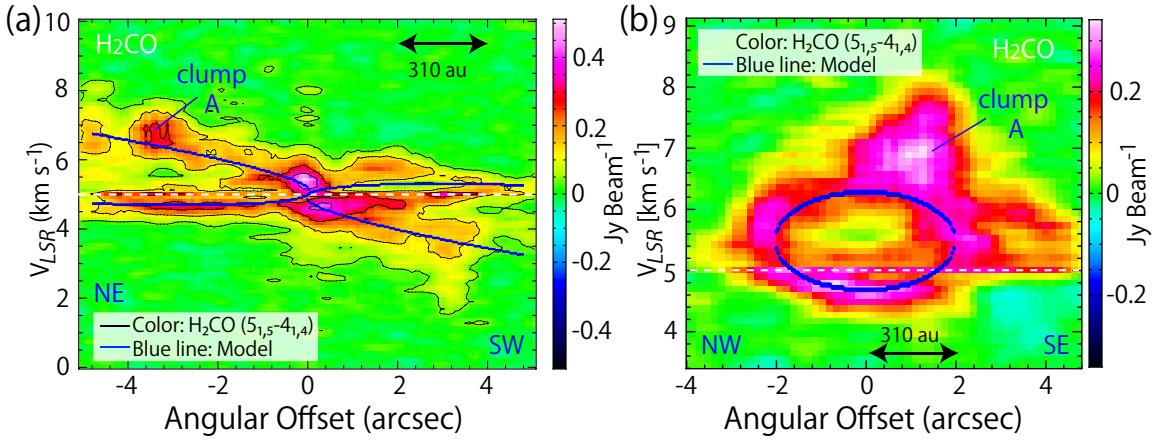

Figure 5.5: PV diagrams of the H_2CO ($5_{1,5} - 4_{1,4}$) line (a) along the outflow axis and (b) across the outflow axis shown in Figure 5.1(a). The blue lines show the best outflow model with an inclination angle of 70°. The white horizontal dashed lines represent the systemic velocity.

We employ the standard model of an outflow cavity from Lee et al. (2000) to analyze the observed geometrical and kinematical structures of the outflow, which is employed for the outflow analysis in L1527 (Chapter 4). In this model, the outflow cavity is assumed to have a parabolic shape and its velocity is proportional to the distance to the protostar:

$$z = C_{\rm as} R^2, \quad v_R = v_{\rm as} \frac{R}{R_0}, \quad v_z = v_{\rm as} \frac{z}{z_0} \tag{5.1}$$

where z denotes the distance to the protostar along the outflow axis, and R the radial size of the cavity perpendicular to z. R_0 and z_0 are both normalization constants, and are set to be $1''$. $C_{\rm as}$ and $v_{\rm as}$ are free parameters. In this model, the intensity of the emission is assumed to be proportional to the column density, where the molecular density is simply assumed to be constant. These assumptions may not be realistic. However, they do not matter the following analysis, because we only focus on the velocity structure but not on the intensity profile. The best results are obtained with an inclination angle of 70° (0° for a face-on configuration), as represented by the blue lines in Figure 5.5. When the inclination angle is less than 60° or higher than 80°, the model does not reproduce the observations well with any values of $C_{\rm as}$ and $v_{\rm as}$. Hence, the inclination angle is determined to be $70° \pm 10°$, where the quoted error is the estimated limit of error based on the above analysis. The derived parameters are; $C_{\rm as} = 0.8$ arcsec^{-1} and $v_{\rm as} = 0.38$ km s^{-1} for an inclination angle of 70°. As mentioned in Section 5.1, van Kempen et al. (2009) reported an inclination angle of 15° (nearly face-on). This discrepancy seems to originate from the limited spatial resolution of their data. Another possibility is that the outflow direction at a small scale is different from that on larger scales (e.g., Mizuno et al., 1990; Yıldız et al., 2012; Sakai et al., 2012; Kristensen et al., 2013), as discussed in the analysis of L1527 (Chapter 4). On the other hand, recent Atacama Pathfinder EXperiment observations of CO ($J = 6-5$) indicate an inclination angle of 70° (Yıldız et al., 2015), which is consistent with our result.

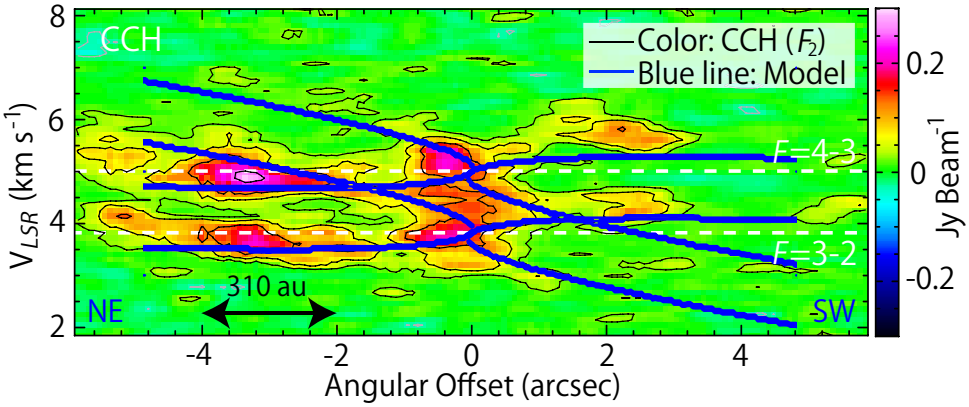

Figure 5.6: PV diagram of the CCH (F_2) line along the outflow axis shown in Figure 5.4(a). The blue lines show the outflow model with an inclination angle of 70° which is the best model for the H_2CO case. The white dashed lines represent the systemic velocities for the two hyperfine components of CCH.

Figure 5.6 shows the PV diagram of the CCH (F_2) line along the outflow axis through the protostellar position. The PV diagram is complicated, because the two hyperfine components are blended with a separation of only 1.2 km s^{-1}. In comparison with the H_2CO case, the low-velocity component close to the systemic velocity is relatively bright in comparison with the high-velocity component. This means that the CCH emission from the outflow part primarily traces the compressed ambient gas around the outflow cavity rather than the entrained outflowing gas. CCH may be formed by gas-phase reactions in dense photodissociation region layers (e.g., Sternberg & Dalgarno, 1995; Jansen et al., 1995a,b).

5.3.3 Protostellar Envelope

As shown in Figures 5.1(d) and 5.4(b), there is a centrally concentrated component in the H_2CO and CCH emission. The distributions of $C^{34}S$, $C^{17}O$, and CH_3OH also have such a component (Jørgensen et al., 2013). Here, we investigate the kinematic structure of this component. A blow-up of the moment 1 map of the H_2CO line (Figure 5.1e) is dominated by the overwhelming outflow motion. However, a slightly skewed feature around the continuum peak is marginally recognized. In order to reveal the motion near the protostar more carefully, we prepared PV diagrams.

Figures 5.7(a) and (b) show the PV diagrams of the H_2CO ($5_{1,5} - 4_{1,4}$) line along the two lines centered at the protostellar position shown in Figure 5.1(f). Figure 5.7(a) is along the axis perpendicular to the outflow axis, which is shown by a dashed arrow labeled as "0°" in Figure 5.1(f). Figure 5.7(b) is along the outflow axis, which is shown by a dashed arrow labeled as "90°" in Figure 5.1(f). In Figure 5.7(a), we can see a marginal trend that the intensity peaks in the red-shifted and the blue-shifted velocity ranges are in the southeastern and northwestern sides of the protostellar position, respectively, although a rotation signature is not obvious in the centrally concentrated component. On the other hand, two intensity peaks are seen in Figure 5.7(b), one of which is red-shifted

in the northeastern side of the protostellar position and the other is blue-shifted in the southwestern side. This systematic velocity gradient in Figure 5.7(b) is the same case of that in the outflow, but the modest velocity gradient in the vicinity of the protostar is difficult to attribute to the outflow, according to our outflow model represented by the blue lines. Based on the outflow direction and its inclination angle, the outflow-envelope structure of this source is expected to be like a schematic illustration shown in the upper panel of Figure 5.8. Therefore, the velocity gradient could be a signature of an infall motion in the envelope rather than outflow.

An infalling/rotating signature is not clearly seen in the PV diagrams for CCH (F_2) (Figures 5.7c, d), in contrast to the L1527 case (Chapters 3, 4; Sakai et al., 2014a,b). In L1527, whose protostellar mass and inclination angle are derived to be 0.18 $M_\odot$ and 85°, respectively, the velocity shift from the systemic velocity observed for the CCH line is 1.8 km s^{-1} at a radius of 100 au from the protostar. On the other hand, the velocity shifts from the systemic velocity are as small as 1 km s^{-1} and 0.7 km s^{-1} for the H_2CO and CCH lines, respectively, in IRAS 15398–3359 (Figure 5.7), despite its nearly edge-on configuration (70°). Although IRAS 15398–3359 is similar to L1527 in its large-scale ($\sim$ a few 1000 au) chemical composition (Sakai et al., 2009a), the infalling/rotating motion is not very clear.

In these observations, we resolve the structure down to 78 au (0.″5) around the protostar. Nevertheless the observed line width is quite narrow. This means that the Doppler shift due to infalling/rotating motions around the protostar should be small. In principle, the small velocity-shift could be explained if the dense gas were not associated with the protostar, that is, if it were mostly present in the outflow. However, this possibility seems unlikely because the outflow motion cannot well explain the velocity gradient traced by the H_2CO line (Figure 5.7b), as mentioned above. Hence, the small velocity-shift likely implies a low protostellar mass. The upper limit of the protostellar mass is roughly estimated from the maximum velocity shifts from the systemic velocity. Under the energy conservation law, the protostellar mass M can be represented in terms of the infall velocity ($v_{\rm infall}$) and the rotation velocity ($v_{\rm rotation}$) at the distance r from the protostar as:

$$M = \frac{r}{2G}\left(v_{\rm infall}^2 + v_{\rm rotation}^2\right). \tag{5.2}$$

By use of this relation, the protostellar mass can roughly be estimated to be smaller than 0.09 $M_\odot$ with a maximum velocity of less than 1 km s^{-1} at 0.″5 (78 au) from the protostar. Here, we assume as a robust case that the infall velocity and the rotating velocity are both the observed maximum value of 1 km s^{-1} in Figure 5.7(a). In the case of no rotation (free fall), the upper limit of the protostellar mass is estimated to be about 0.04 $M_\odot$.

5.3.4 Comparison with an Envelope Model

In the case of L1527, which has similar chemical characteristics to IRAS 15398–3359, a ballistic model of the infalling-rotating envelope shown in Figure 5.8 was applied to analyze the observational results for the c-C_3H_2 and CCH lines as demonstrated in Chapters 3 and 4. In spite of such a simple model, the basic features of the PV diagrams of c-C_3H_2 and CCH in L1527 are well reproduced. Therefore, it is worth applying the same model to the kinematic structure traced by the H_2CO and CCH lines in IRAS 15398–3359. In

L1527, CCH resides only in the infalling-rotating envelope. Hence, it is preferable to apply the infalling-rotating envelope model for the CCH line. However, the PV diagrams of CCH in IRAS 15398–3359 are complex due to the hyperfine structure, and their S/Ns are insufficient for critical comparison. In contrast, the emission of H_2CO ($5_{1,5} - 4_{1,4}$) is bright enough in IRAS 15398–3359. Although H_2CO seems to present in the inner disk-like structure as well as the infalling-rotating envelope in L1527, the contribution of the envelope is significant (Sakai et al., 2014b). Hence, we compare the model results

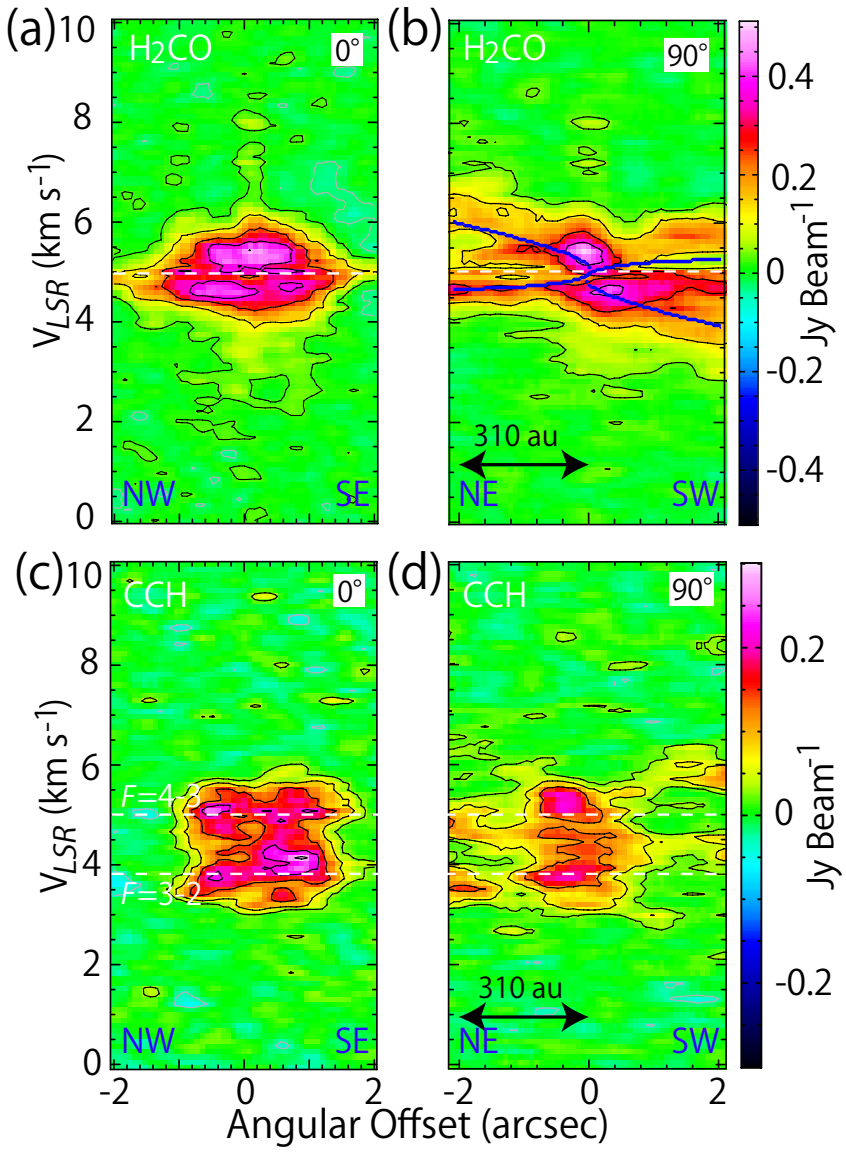

Figure 5.7: PV diagrams of the H_2CO ($5_{1,5} - 4_{1,4}$) (a, b) and CCH (F_2) (c, d) line. Panels (a) and (c) are prepared along the line perpendicular to the outflow axis, while panels (b) and (d) along the outflow axis, as shown in Figure 5.1(f) (the black dashed arrows labeled as "0°" and "90°", respectively). Panels (b) and (d) are the blow-ups of the central parts of Figures 5.5(a) and 5.6, respectively. The blue lines in panel (b) show the outflow model.

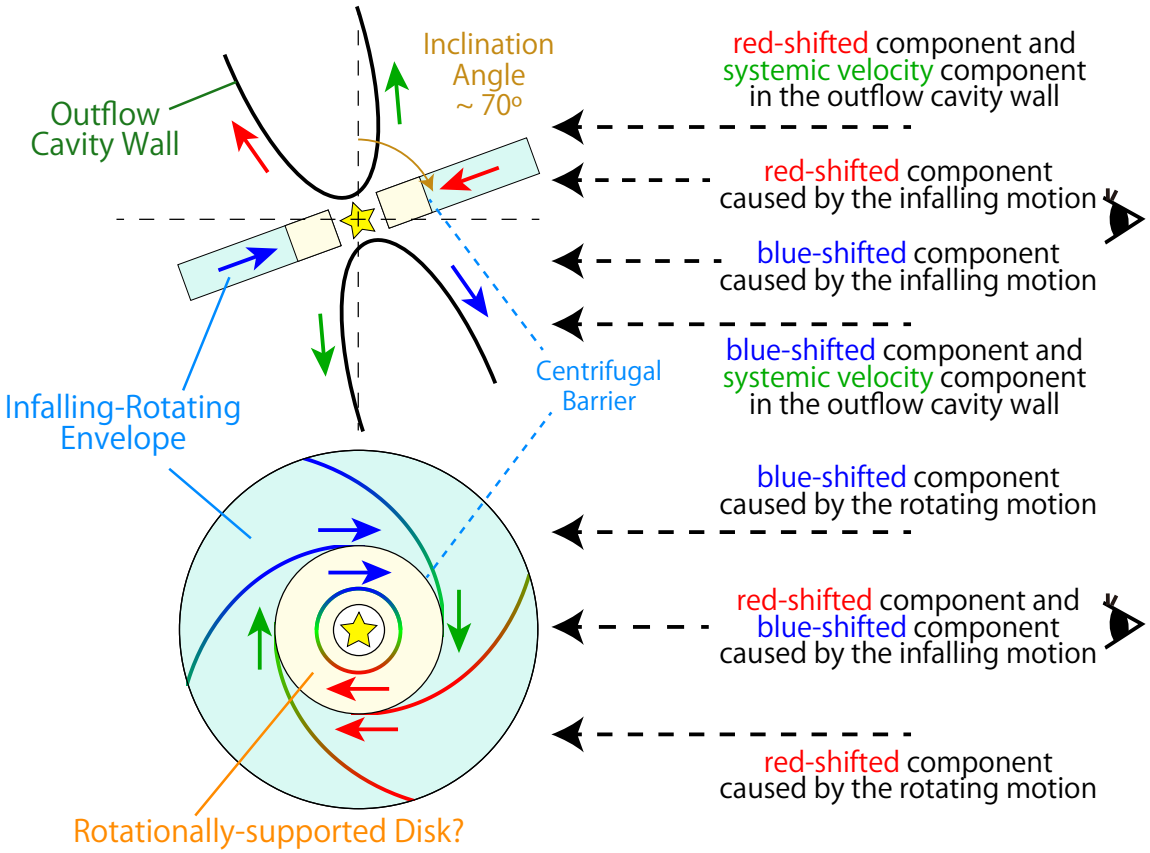

Figure 5.8: Schematic illustrations of the outflow/envelope system. An observer sits on the right hand side. The black dashed arrows represent the lines of sight. The disk/envelope geometry is almost edge-on with an inclination angle of 70°.

with the H_2CO ($5_{1,5} - 4_{1,4}$) line in IRAS 15398–3359.

Figure 5.9 shows the PV diagrams of the H_2CO ($5_{1,5} - 4_{1,4}$) line along the envelope direction. The blue contours represent the results of the infalling-rotating envelope model. In this model, the intensity is simply assumed to be proportional to the column density, and the molecular density is assumed to be proportional to $r^{-1.5}$. The assumption of the optically thin condition seems to be reasonable, because the optical depth is evaluated to be less than 0.3 (Section 5.3.1). The excitation effect and the effect of the temperature gradient are not taken into account, neither. However, these simplifications may not affect the following analysis, because we here only focus on the velocity structure but not on the intensity profile. Unlike the L1527 case, we cannot determine the radius of the centrifugal barrier from the PV diagram because of absence of an obvious rotation signature. Nevertheless, we can roughly estimate its upper limit from the CCH distribution. If CCH is present only in the infalling-rotating envelope as in the case of L1527 and the radius of the centrifugal barrier is larger than the synthesized beam ($0''.5$; 78 au), a hole in the CCH distribution toward the protostellar position should be resolved. Although an intensity dip toward the center is marginally seen in the CCH distribution (Figure 5.2), it is not well resolved in the present observation. Hence, we set the upper limit of the centrifugal radius to 80 au. We simulated the PV diagram for various sets of the protostellar mass and the radius of the centrifugal barrier under this constraint, as shown in Figure 5.9. The models with a protostellar mass of 0.02 $M_\odot$ and a radius of the centrifugal barrier of $0 - 30$ au are chosen as the best simulations among the 20 models shown in Figure 5.9 by eye. The mass is consistent with the upper limit estimated in Section 5.3.3. Thus, the low protostellar mass can be confirmed with this simulation. We also simulated the PV diagrams along the different directions through the protostellar position shown in Figure 5.4 (the six dashed arrows labeled as "0°", "30°", "60°", "90°", "120°", "150°") for certain values of the protostellar mass (0.02 $M_\odot$) and the centrifugal barrier (30 au) as an example (Figure 5.10). The trends of a velocity gradient around the protostar are reproduced by the model.

5.4 Discussion

The low protostellar mass of IRAS 15398–3359 (< 0.09 $M_\odot$) is essentially derived from the narrow line width in the inner envelope ($r < 80$ au) which has an almost edge-on configuration. The above mass estimation may suffer from the uncertainty of the inclination angle of the disk/envelope system. If the inclination angle is larger (nearer to the face-on configuration), the mass evaluated by the model becomes larger. However, the upper limit of the protostellar mass does not change significantly, even if an inclination angle of 60° is employed.

By use of the dynamical timescale of the extended outflow ($1 - 2 \times 10^3$ yr for each lobe; Yıldız et al., 2015) and the upper limit of the protostellar mass (< 0.09 $M_\odot$) obtained in this study, the average accretion rate is calculated to be less than 9.0×10^{-5} $M_\odot$ yr^{-1}. The dynamical timescale of the outflow can be regarded as the lower limit, because the older part of the outflow may not be detected. Hence, the above accretion rate is regarded as the upper limit. Nevertheless, this estimation is roughly consistent with the typical accretion rate for low-mass protostars of ($10^{-5} - 10^{-6}$) $M_\odot$ yr^{-1} (e.g., Hartmann et al., 1997), and

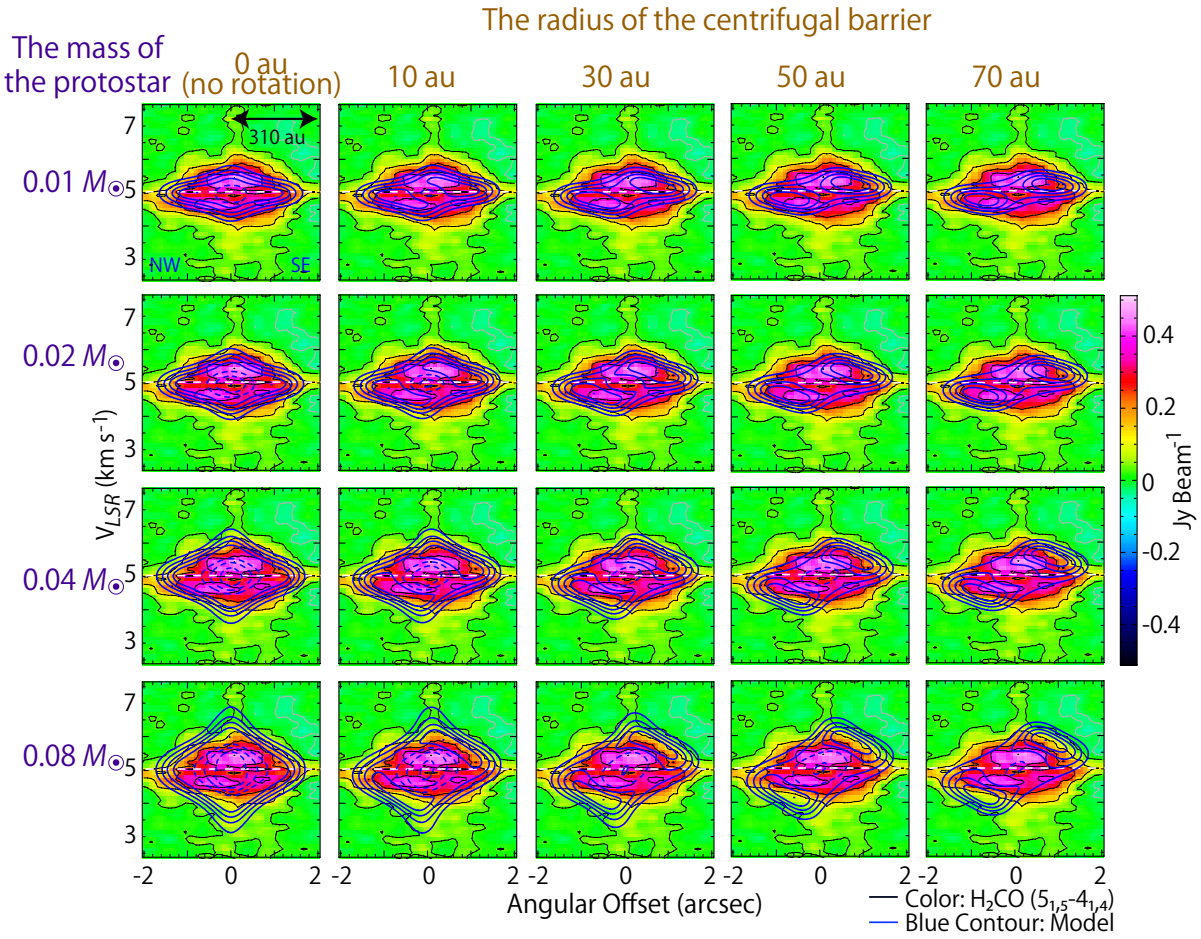

Figure 5.9: PV diagrams of the H_2CO ($5_{1,5} - 4_{1,4}$) line along the line perpendicular to the outflow axis ("0°") shown in Figure 5.1(f). The blue contours represent 16 model simulations of the infalling-rotating envelope with an inclination angle of 70°. The model parameters are the protostellar mass and the radius of the centrifugal barrier (see Chapter 3). The contour levels are every 20% of each peak intensity. The dashed contours around the central position represent the dip toward the center.

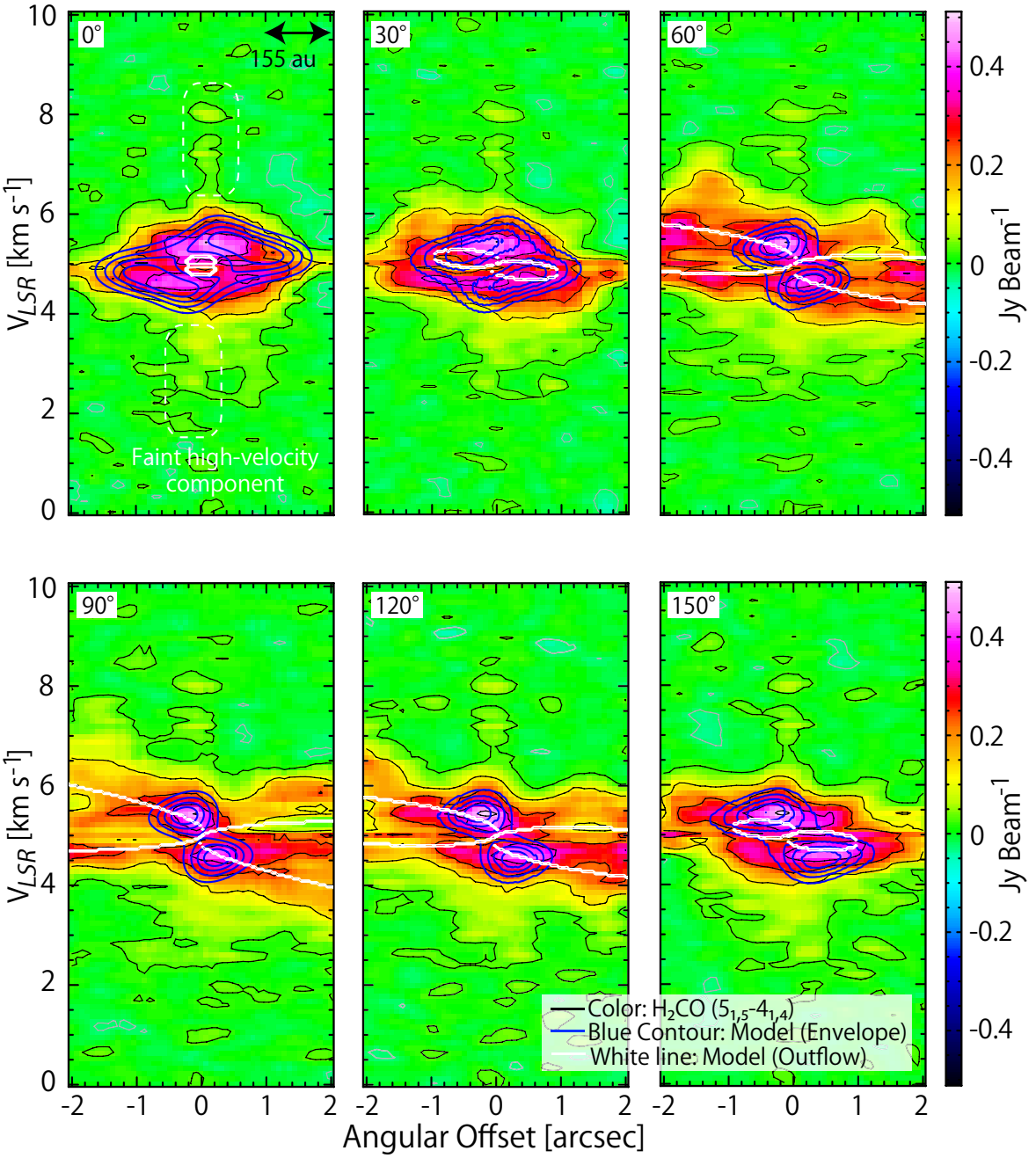

Figure 5.10: PV diagrams of the H_2CO ($5_{1,5} - 4_{1,4}$) line along the six lines shown in Figure 5.1(f). The blue contours represent the infalling-rotating envelope model. The parameters for the model are; $i = 70°$, $M = 0.02\ M_\odot$, and $r_{\rm CB} = 30$ au, where $r_{\rm CB}$ is the radius of the centrifugal barrier. The contour levels are every 20% of each peak intensity. The white lines show the outflow model.

may be higher than that for another WCCC source L1527 (10^{-6} $M_\odot$ yr^{-1}; Ohashi et al., 1997). By use of the mass and the dynamical timescale of the outflow reported by van Kempen et al. (2009), the mass outflow rate is calculated to be 6.3×10^{-6} $M_\odot$ yr^{-1} and 2.2×10^{-6} $M_\odot$ yr^{-1} for the red- and blue-shifted lobes, respectively. These values correspond to 1.7×10^{-5} $M_\odot$ yr^{-1} and 6.0×10^{-6} $M_\odot$ yr^{-1}, when an inclination angle of 70° is employed. Hence, the mass accretion rate and the mass outflow rate are roughly comparable to each other.

On the other hand, the mass accretion rate can be estimated with using the following equation (Palla & Stahler, 1991):

$$\dot{M} = \frac{LR_{\rm star}}{GM}, \tag{5.3}$$

where the L is the luminosity and the $R_{\rm star}$ the radius of the protostar. With the obtained upper limit of M (0.09 $M_\odot$), the mass accretion rate $\dot{M}$ is estimated to be larger than 1.6×10^{-6} $M_\odot$ yr^{-1} with L of 1.8 $L_\odot$ (Jørgensen et al., 2013) and $R_{\rm star}$ of 2.5 $R_\odot$ (e.g., Palla, 1999; Baraffe & Chabrier, 2010). This lower limit is consistent with the above-mentioned upper limit (9.0×10^{-5} $M_\odot$ yr^{-1}). In spite of the episodic accretion suggested by Jørgensen et al. (2013), the average mass accretion rate is not so different from the canonical value ($10^{-5} - 10^{-6}$ $M_\odot$ yr^{-1}).

On the other hand, the upper limit of the protostar/envelope mass ratio is evaluated to be 0.18 from the upper limit of the protostellar mass of 0.09 $M_\odot$ and an envelope mass of 0.5 $M_\odot$ (Kristensen et al., 2012). The ratio is 0.04, if the mass of 0.02 $M_\odot$ is employed. Hence, the ratio seems smaller than that in L1527 (0.2; Tobin et al., 2012). This implies that the protostar is in the infant stage and is still growing. Since the specific angular momentum brought into the inner region is smaller at the earlier stage of the protostellar evolution, it seems likely that the rotation signature is not so evident as in the L1527 case.

The H_2CO distribution has a centrally concentrated component with a single-peaked distribution, whereas the CCH distribution is more flattened (Figure 5.2). Therefore, the H_2CO line traces the inner region in comparison with the CCH line. This trend is also seen in the observations of L1527 (Sakai et al., 2014b). It should be noted that Figure 5.10 shows a faint high-velocity component of H_2CO ($v_{\rm lsr} < 4$ km s^{-1} or $v_{\rm lsr} > 6$ km s^{-1}) toward the protostellar position. If this component really represents the contribution of a rotationally-supported disk, it suggests that a disk structure is already formed at such an early stage of the low-mass star formation. If the upper limit of the protostellar mass of 0.09 $M_\odot$ is employed, H_2CO may be present even at ~ 10 au, according to its maximum velocity shift (~ 3 km s^{-1}). We here stress that extensive studies of the disk structure in Class 0 sources have now become possible with ALMA and that a chemical approach will be of help to such studies. Our result reveals that the disk/envelope structure can be observed with various molecular lines. Hence, the chemical evolution can be investigated even in the disk-forming stage.

Chapter 6

IRAS 16293–2422 Source A

We have analyzed rotational spectral line emission of OCS, CH_3OH, $HCOOCH_3$, and H_2CS observed toward the low-mass Class 0 protostellar source IRAS 16293–2422 Source A at a sub-arcsecond resolution ($\sim 0\farcs6 \times 0\farcs5$) with ALMA. Significant chemical differentiation is found at a 50 au scale. The OCS line is found to well trace the infalling-rotating envelope in this source. On the other hand, the CH_3OH and $HCOOCH_3$ distributions are found to be concentrated around the inner part of the infalling-rotating envelope. With a simple ballistic model of the infalling-rotating envelope, the protostellar mass and the radius of the centrifugal barrier are evaluated from the OCS data to be from 0.5 to 1.0 $M_\odot$ and from 40 to 60 au, respectively, assuming the inclination angle of the disk/envelope system to be 60° (0° for a face-on configuration). Although the protostellar mass is correlated with the inclination angle, the radius of the centrifugal barrier is not. This is the first indication of the centrifugal barrier of the infalling-rotating envelope in a hot corino source. CH_3OH and $HCOOCH_3$ may be liberated from ice mantles due to weak accretion shocks around the centrifugal barrier, and/or due to protostellar heating. The H_2CS emission seems to come from the disk component inside the centrifugal barrier in addition to the envelope component. The centrifugal barrier plays a central role not only in the formation of a rotationally-supported disk but also in the chemical evolution from the envelope to the protoplanetary disk.

6.1 Introduction

In previous Chapters, we have demonstrated the analyses of the kinematic structures of the infalling-rotating envelope and the outflow in the two sources L1527 and IRAS 15398–3359. Both of them show the chemical characteristics of warm carbon-chain chemistry (WCCC), and their envelope components are traced by unsaturated carbon-chain and related molecules. In principle, the physics in the infalling-rotating envelope model itself does not depend on the chemistry of the source. Here, we thus move on to another source with a chemical characteristics quite different from the above sources in this chapter: a hot corino, IRAS 16293–2422 Source A. We examine the applicability of the infalling-rotating envelope model to this source regardless of the chemical characteristics.

IRAS 16293–2422 is a well-known Class 0 protostar in Ophiuchus ($d = 120$ pc; Knude & Hog, 1998), whose molecular gas distribution and dynamics, outflows, and chemical

This chapter has been published in Oya et al., 2016, ApJ, 824, 88

composition have been extensively studied (e.g., Wootten, 1989; Mizuno et al., 1990; Mundy et al., 1990, 1992; Blake et al., 1994; van Dishoeck et al., 1995; Looney et al., 2000; Ceccarelli et al., 2000a,b,c; Schöier et al., 2002; Cazaux et al., 2003; Bottinelli et al., 2004a; Takakuwa et al., 2007b; Yeh et al., 2008; Caux et al., 2011; Jørgensen et al., 2011). While L1527 is rich in unsaturated carbon-chain molecules, IRAS 16293–2422 is rich in saturated complex organic molecules (COMs) such as $HCOOCH_3$ and $(CH_3)_2O$ in the vicinity of the protostars (Schöier et al., 2002; Cazaux et al., 2003; Bottinelli et al., 2004a; Kuan et al., 2004; Pineda et al., 2012). This characteristic chemical composition is known as hot corino chemistry (Ceccarelli, 2004; Bottinelli et al., 2004a). Because of the proximity to the Sun and relatively bright emission of COMs, this source has been subject to extensive astrochemical studies. IRAS 16293–2422 consists of Source A and Source B, which are separated by $5''$ (Chandler et al., 2005). The protostellar masses of Source A and Source B are reported to be $\sim 1\ M_\odot$ and $< 0.1\ M_\odot$, respectively, and it is suggested that Source B rotates around Source A (Bottinelli et al., 2004a; Caux et al., 2011). Since Source B has a disk/envelope component with a face-on configuration, its rotation motion can scarcely be detected (Pineda et al., 2012; Zapata et al., 2013). Inverse P-Cygni profiles are instead reported for the COM lines toward Source B, indicating that COMs are in the gas falling to the protostar. On the other hand, Source A shows a rotation signature (Pineda et al., 2012). Favre et al. (2014) recently reported the observation of $C^{34}S$ ($J = 7 - 6$) with SMA and eSMA at a resolution of $0\farcs46 \times 0\farcs29$, and revealed a clear spin-up feature toward the protostar. They discussed two possibilities to explain the origin of the rotation motion; a Keplerian disk and an infalling-rotating envelope. Since CS line is found to trace the infalling-rotating envelope in L1527 (Chapter 4), it is likely that the rotation signature found by Favre et al. (2014) is due to the infalling-rotating envelope around IRAS 16293–2422 Source A. In this chapter, we have analyzed ALMA archival data of other molecular species to examine whether the centrifugal barrier of the infalling-rotating envelope can be identified in this source.

6.2 Data

The archival data of IRAS 16293–2422 observed in the ALMA Cycle 1 operation are used in this chapter. We analyzed the spectral lines listed in Table 6.1. Images were obtained by using the CLEAN algorithm. The details of the observations are described in Appendix of this chapter. The continuum image was prepared by averaging line-free channels, and the line maps were obtained after subtracting the continuum component directly from the visibilities. The synthesized-beam sizes for the continuum and the spectral lines are listed in Table 6.1. The rms noise levels for the 1.2 mm continuum, OCS, CH_3OH, $HCOOCH_3$, and H_2CS maps are 2.0, 2.0, 4.0, 1.8, and 2.0 mJy beam^{-1}, respectively, for a channel width of 122 kHz. The coordinates of Source A are derived from a two-dimensional Gaussian-fit at the continuum peak: $(\alpha_{2000}, \delta_{2000}) = (16^{\rm h}32^{\rm m}22\fs8713 \pm 0\fs0012, -24°28'36\farcs5023 \pm 0\farcs0111)$. In this chapter, we focus only on Source A to examine its kinematic structure, because the rotation signature is seen in Source A but not in Source B as mentioned in Section 6.1. We also discuss on the Source B case in the following chapter.

Table 6.1: Parameters of the Observed Lines

Molecule	Transition	Frequency (GHz)	E_u (K)	$S\mu^2$ (Debye^2)[a]	Synthesized Beam
OCS[b]	$J = 19 - 18$	231.0609934	111	9.72	$0\farcs65 \times 0\farcs51$ (P.A. $85\fdg29$)
CH_3OH[b]	$11_{0,11} - 10_{1,10}$; A^+	250.5069800	153	10.6	$0\farcs60 \times 0\farcs47$ (P.A. $80\fdg34$)
$HCOOCH_3$[c]	$19_{9,10} - 19_{8,11}$; E	232.5972780	166	4.10	$0\farcs64 \times 0\farcs51$ (P.A. $85\fdg78$)
H_2CS[b]	$7_{0,7} - 6_{0,6}$	240.2668724	46	19.0	$0\farcs53 \times 0\farcs46$ (P.A. $73\fdg48$)
H_2CS[b]	$7_{2,5} - 6_{2,4}$	240.5490662	99	17.5	$0\farcs53 \times 0\farcs46$ (P.A. $73\fdg66$)
H_2CS[b]	$7_{4,4} - 6_{4,3}$, $7_{4,3} - 6_{4,2}$	240.3321897	257	12.8, 12.8	$0\farcs53 \times 0\farcs46$ (P.A. $73\fdg57$)

[a] Nuclear spin degeneracy is not included.
[b] Taken from CDMS (Müller et al., 2005).
[c] Taken from JPL (Pickett et al., 1998).

6.3 Line intensity Distribution

The ALMA archival data of IRAS 16293–2422 (Cycle 1) contain a number of spectral lines of various molecules including COMs. In order to trace the infalling-rotating envelope suggested by the $C^{34}S$ line observed with SMA and eSMA (Favre et al., 2014), we focused on the molecular line whose distribution is the most extended. We found that the OCS line ($J = 19 - 18$) is the best for this purpose. Figure 6.1(a) shows the moment 0 map of OCS. The two-dimensional Gaussian-fitted size of the OCS line intensity distribution deconvolved by the beam is $(1\farcs665 \pm 0\farcs017) \times (1\farcs351 \pm 0\farcs015)$ (P.A. $21\fdg2 \pm 2\fdg2$) in FWHM (full width at half maximum). This size is almost comparable to that of $C^{34}S$ reported by Favre et al. (2014), whose deconvolved size is estimated to be $1\farcs6$ by using the SMA/eSMA archival data. Hence, it is most likely that OCS also traces the infalling-rotating envelope. This prediction will be verified by the analysis of its velocity structure in the following sections. It should be noted that the peak of the $C^{34}S$ distribution is offset by $0\farcs52$ from the dust continuum peak (submillimeter continuum source Aa reported by Chandler et al., 2005), while such an offset is smaller in OCS ($0\farcs14$) than in $C^{34}S$. In contrast, the CH_3OH ($11_{0,11} - 10_{1,10}$; A^+) and $HCOOCH_3$ ($19_{9,10} - 19_{8,11}$; E) distributions, whose moment 0 maps are shown in Figures 6.1(b) and 6.1(c), respectively, are more compact and more centrally concentrated than OCS and $C^{34}S$. Figures 6.1(d–f) show the moment 0 maps of the three lines of H_2CS ($7_{0,7} - 6_{0,6}$; $7_{2,5} - 6_{2,4}$; $7_{4,4} - 6_{4,3}/7_{4,3} - 6_{4,2}$). They are also concentrated around the protostar. The two-dimensional Gaussian-fitted sizes of the CH_3OH, $HCOOCH_3$, and H_2CS ($7_{0,7} - 6_{0,6}$) intensitiy distributions deconvolved by the beam are $(1\farcs042 \pm 0\farcs018) \times (0\farcs862 \pm 0\farcs016)$ (P.A. $46\fdg4 \pm 4\fdg5$), $(0\farcs728 \pm 0\farcs023) \times (0\farcs371 \pm 0\farcs020)$ (P.A. $58\fdg5 \pm 2\fdg5$), and $(0\farcs876 \pm 0\farcs011) \times (0\farcs572 \pm 0\farcs007)$ (P.A. $79\fdg3 \pm 1\fdg1$) in FWHM, respectively.

6.4 Velocity Structure

6.4.1 OCS

Figure 6.2(a) shows the moment 1 map of OCS. It reveals a rotation signature around the protostar Source A; a clear velocity gradient is found in the northeast-southwest direction, which is consistent with that previously found by Takakuwa et al. (2007b), Rao et al. (2009), Pineda et al. (2012), and Favre et al. (2014). Here, we employ 3.8 km s^{-1} as the systemic velocity of Source A, judging from the range of the systemic velocity in the previous reports ($3.6 - 3.9$ km s^{-1}; Takakuwa et al., 2007b; Bottinelli et al., 2004a; Favre et al., 2014). In order to define the position angle (P.A.) of the disk/envelope system, we investigated the peak positions of the distributions of the most red-shifted emission ($v_{\rm lsr} = 10.4 - 10.7$ km s^{-1}) and the most blue-shifted emission ($v_{\rm lsr} = -2.8 - -3.1$ km s^{-1}) of OCS. These two components have peaks with slight offsets from the continuum peak position, and the continuum and the OCS emission peaks are well on a common line. The position angle of the disk/envelope system is thus determined to be $65^\circ \pm 10^\circ$, as shown in Figure 6.1(a). Then, the position angle of the rotation axis (i.e., outflow direction) is $155^\circ \pm 10^\circ$, being consistent with the previous report (P.A. 144°; Favre et al., 2014).

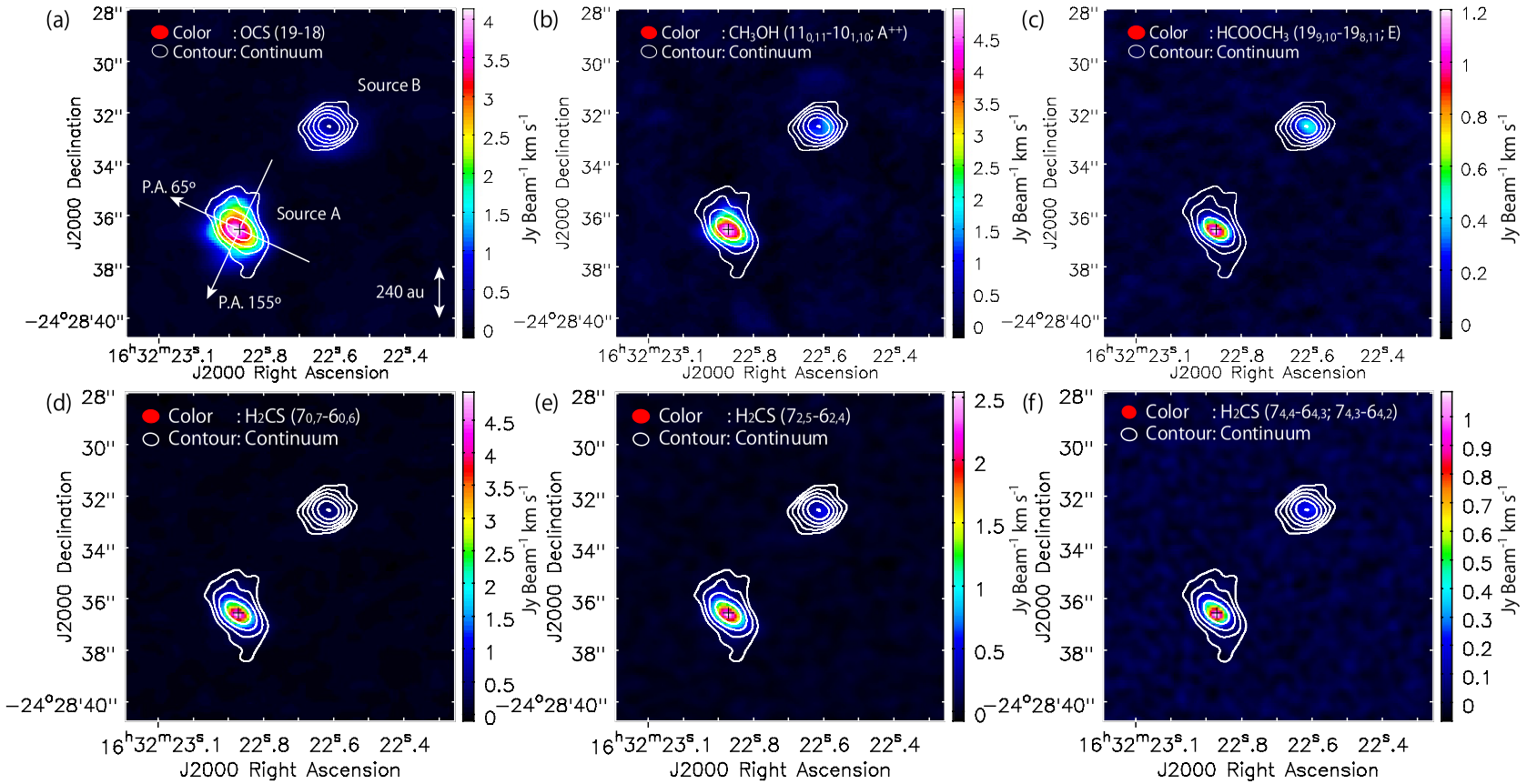

Figure 6.1: Moment 0 maps (integrated intensity maps) of OCS (a), CH_3OH (b), $HCOOCH_3$ (c), and H_2CS (d–f) (color). The integrated velocity ranges are from −6.1 to 14.0, from −5.9 to 14.1, from −11.2 to 18.8, from −7.3 to 20.9, from −7.3 to 20.9, and from −13.2 to 11.2 km s^{-1} for panels (a), (b), (c), (d), (e), and (f), respectively. White contours represent the continuum emission at 1.2 mm. The contour levels for the continuum are 10, 20, 40, 80, 160, and 320σ, where the rms noise level is 2 mJy beam^{-1}. White arrows in panel (a) represent the envelope direction (P.A. 65°) and the outflow direction (P.A. 155°) along which the PV diagrams in Figures 6.3 and 6.5–6.13 are prepared. The position of Source A is represented by black crosses: (α_{2000}, δ_{2000}) = ($16^h32^m22^s.8713$, $-24°28'36''.5023$).

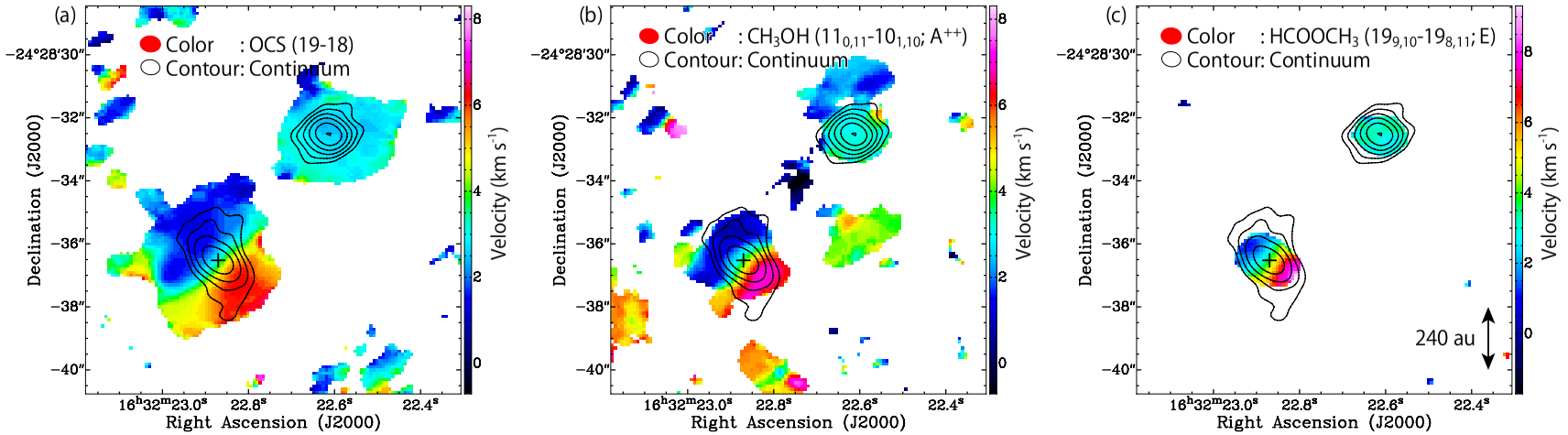

Figure 6.2: Moment 1 maps of OCS (a), CH_3OH (b), and $HCOOCH_3$ (c) (color). Black contours represent the continuum at 1.2 mm, which are the same as the white contours in Figure 6.1. The position of Source A is represented by black crosses.

Figures 6.3(a) and 6.3(b) show the position-velocity (PV) diagrams of OCS, where the position axes in panels (a) and (b) are along the disk/envelope direction (referred to hereafter as envelope direction) and the direction perpendicular to it (referred to hereafter as outflow direction), respectively, as shown in Figure 6.1(a). The PV diagram of OCS along the envelope direction (Figure 6.3a) shows a clear spin-up feature toward the protostar. The PV diagram of OCS along the outflow direction (Figure 6.3b) shows a significant velocity gradient. Since the OCS emission is concentrated around the protostar, the contribution of outflows is unlikely. This velocity gradient most likely represents an infall motion of the rotating envelope in the vicinity of the protostar. Such a velocity gradient along the outflow direction is similar to that of the infall motion observed for CS in L1527 (Chapter 4). Hence, the rotation motion traced by OCS is not Keplerian, but the gas is falling and rotating at a scale of 400 au in diameter. This situation is schematically illustrated in Figure 6.4 (right).

6.4.2 CH_3OH and $HCOOCH_3$

Figure 6.2(b) depicts the moment 1 map of CH_3OH, which clearly shows a velocity gradient around the protostar. The PV diagram of CH_3OH along the envelope direction (Figure 6.3c) also supports the rotation signature, as in the case of OCS. However, the distribution is more concentrated near the protostar than that of OCS (Figure 6.3a), as mentioned in Section 6.3. The PV diagram of CH_3OH along the outflow direction (Figure 6.3d) shows little velocity gradient unlike the OCS case (Figure 6.3b), suggesting less infall motion. This also suggests that the distribution is rather concentrated around a more inner part of the infalling-rotating envelope than that of OCS, because the infall velocity vanishes when approaching the centrifugal barrier of the infalling-rotating envelope (Chapter 3). In the PV diagram of CH_3OH along the envelope direction (Figure 6.3c), the intensity peaks seem to appear at the $+0''.5$ and $-0''.5$ positions with the blue-shifted and red-shifted velocity, respectively. This feature can be explained if the emitting region of CH_3OH mainly exists in a ring-like structure with an apparent radius of about $0''.5$ in the innermost part of the infalling-rotating envelope.

Figure 6.2(c) shows the moment 1 map of $HCOOCH_3$, while Figures 6.3(e) and 6.3(f) are the PV diagrams of $HCOOCH_3$ along the envelope and outflow directions, respectively. The velocity structure of the $HCOOCH_3$ line is essentially similar to that of CH_3OH, and is more concentrated around the protostar. Although the PV diagram of CH_3OH along the envelope direction (Figure 6.3c) reveals a slight extension toward the southwestern side, such a feature is absent in $HCOOCH_3$ (Figure 6.3e). No velocity gradient along the outflow direction is seen (Figure 6.3f), suggesting that the $HCOOCH_3$ emission mainly comes from the gas without infall motion. This feature is similar to the case seen in SO toward L1527 and TMC-1A (Sakai et al., 2014a,b, 2016).

6.4.3 H_2CS

Figures 6.3(g) and 6.3(h) show the PV diagrams of H_2CS ($7_{0,7} - 6_{0,6}$) along the envelope and outflow directions. Figure 6.5 also shows them in contours superposed on those of OCS, CH_3OH, and $HCOOCH_3$ in color. In the moment 0 maps (Figures 6.1d–f), the distribution of the H_2CS emission looks concentrated around the protostar as in

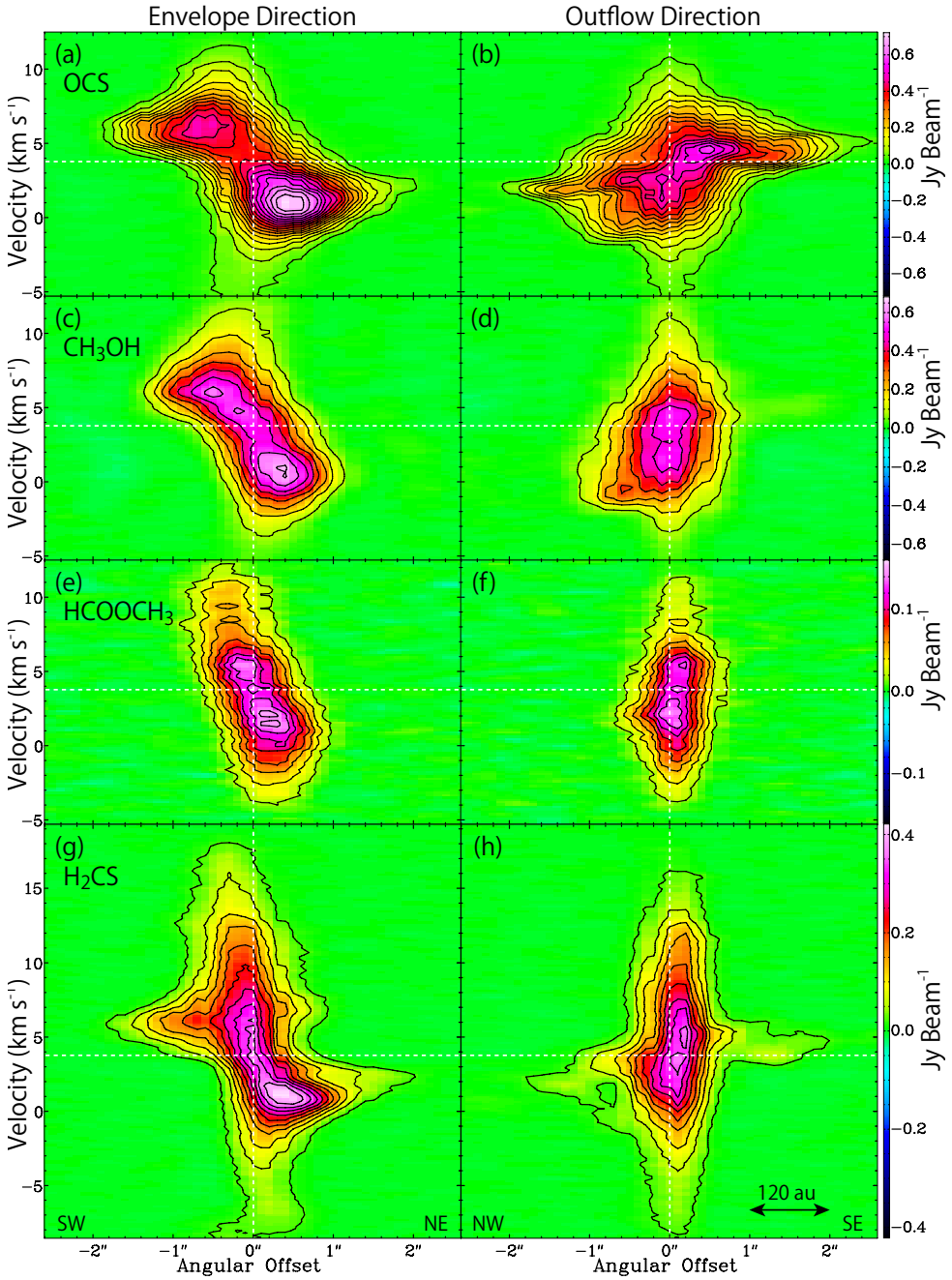

Figure 6.3: PV diagrams of OCS (a, b), CH_3OH (c, d), $HCOOCH_3$ (e, f) and H_2CS ($7_{0,7} - 6_{0,6}$; g, h) along the envelope direction (P.A. 65°) and the outflow direction (P.A. 155°) shown in Figure 6.1(a). The first contour levels are at 20σ, 20σ, 10σ, and 10σ and the level steps are 20σ, 20σ, 10σ, and 20σ for OCS, CH_3OH, $HCOOCH_3$, and H_2CS, where the rms noise levels are 2.0, 4.0, 1.8, and 2.0 mJy beam^{-1}, respectively.

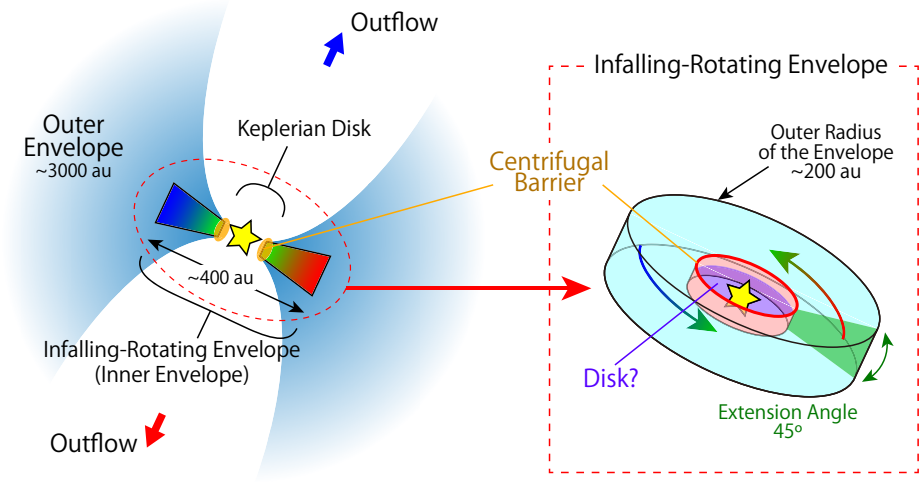

Figure 6.4: Schematic illustration of the gas components around Source A. The outer envelope part represented by light blue regions in the left figure is resolved out in these observations. The kinematic structure in the inner envelope component, which is assumed to be cylindrical around the protostar, is analyzed with our infalling-rotating envelope model in Section 6.5. The Keplerian disk component, which is the most inner part in the figure and is inside the centrifugal barrier of the infalling-rotating envelope, is traced by H_2CS (Figures 6.3g, h). Its kinematic structure is discussed in Section 6.5.3.

the case of CH_3OH and $HCOOCH_3$ (Figures 6.1b, c). However, the PV diagrams of H_2CS are much different from those of these two molecules (Figure 6.5). First, the PV diagrams of H_2CS contain broader velocity components near the protostar. For instance, the maximum velocity-shift from the systemic velocity (3.8 km s^{-1}) is as large as 14 km s^{-1}, which is about twice the corresponding velocity shift ($\sim$7 km s^{-1}) seen in the OCS line (Figures 6.5a, b). The broad-velocity components seen in H_2CS may trace the Keplerian disk component in the vicinity of the protostar. In addition, weak emission from the envelope component is also visible in the PV diagram of H_2CS along the envelope direction unlike the CH_3OH and $HCOOCH_3$ cases (Figures 6.5c, e), which is very similar to the distribution of OCS, as shown in Figure 6.5(a). Hence, H_2CS seems to reside in all the regions from the infalling-rotating envelope to the disk component inside it. Such a behavior of H_2CS is similar to that seen in H_2CO toward L1527 (Sakai et al., 2014b); H_2CO resides in all the regions from the envelope to the disk component in L1527.

6.5 Infalling-Rotating Envelope Model

As described above, the different molecules allow us to trace different parts of the gas around the protostar in IRAS 16293–2422 Source A. In this section, we analyze their distributions and kinematic structures by using a simple physical model (Chapter 3). Although the envelope gas of IRAS 16293–2422 is reported to extend on a 3000 au scale and to have a spherical configuration (Ceccarelli et al., 2000a), we here focus on the small

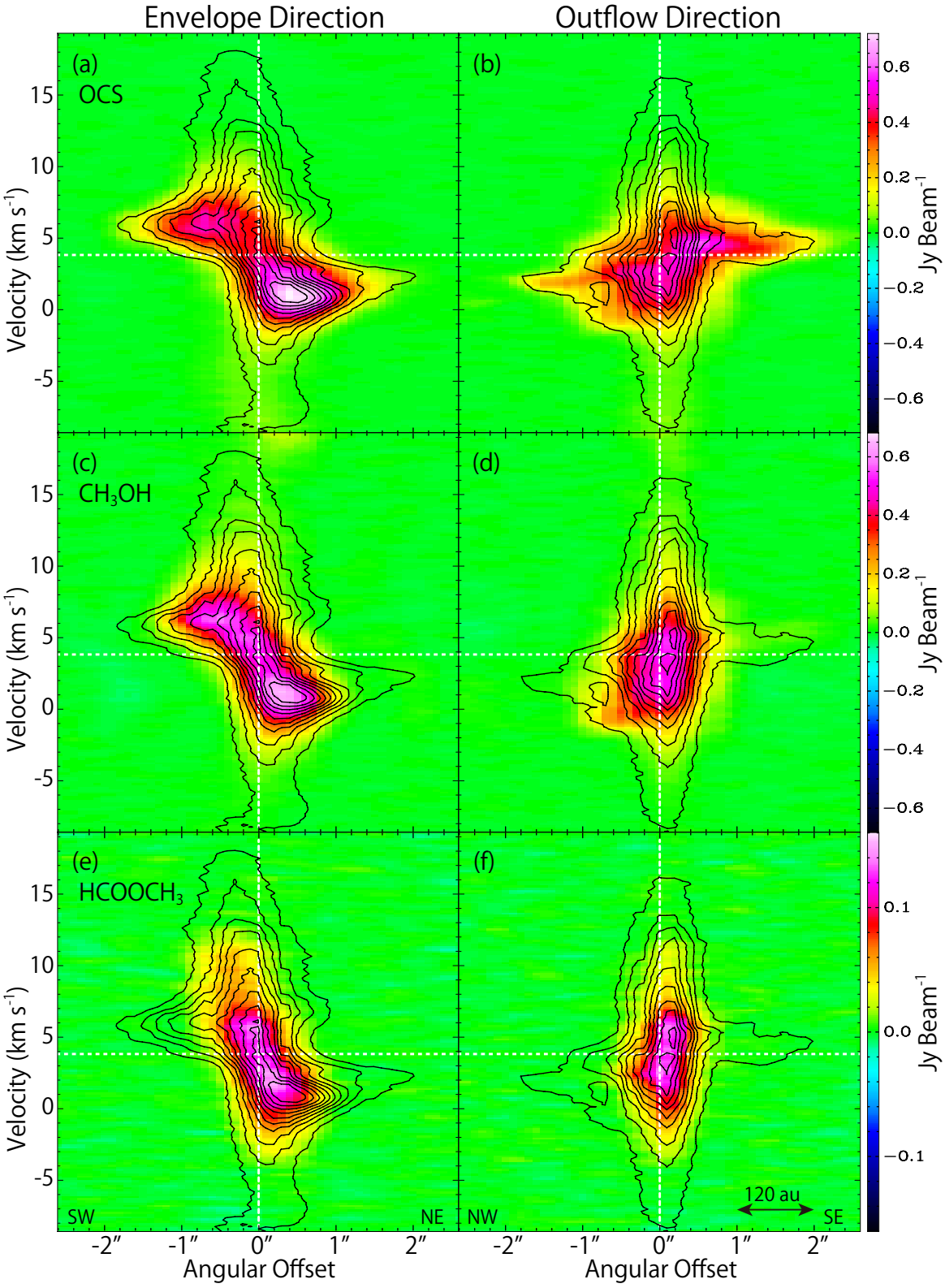

Figure 6.5: PV diagrams of OCS, CH_3OH, $HCOOCH_3$ (color) and H_2CS ($7_{0,7}-6_{0,6}$; black contours) along the envelope direction (P.A. 65°) and the outflow direction (P.A. 155°). The contour levels for H_2CS are every 20σ from 10σ, where the rms noise level is 2.0 mJy beam^{-1}.

scale ($\sim$ 400 au) structure showing the rotation motion of the inner envelope and the disk around the protostar, as illustrated in Figure 6.4. The spherical outer envelope component is resolved out in these observations, as shown in the moment 0 maps (Figure 6.1). Hence, we assume a cylindrical model to examine the compact and flattened structure in the vicinity of the protostar.

6.5.1 OCS

The velocity structure of the OCS line (Figures 6.3a, 6.3b) suggests the existence of an infalling-rotating envelope around the dust continuum peak. Hence, we analyze it with a simple model of an infalling-rotating envelope (Chapter 3), which has been applied to L1527, IRAS 15398–3359, and TMC-1A (Chapters 4, 5; Sakai et al., 2016). The velocity field in the infalling-rotating envelope can be determined by the two parameters; the radius of the centrifugal barrier ($r_{\rm CB}$) and the protostellar mass (M). The model includes additional parameters to account for the observed PV diagrams; the inclination angle of the disk/envelope system, the extending angle of the scale height of the envelope, and its outer radius (R), as shown in Figure 6.4. Note that the outer radius does not mean the size of the envelope, but the size of the distribution of molecular emission. The model images are convolved by the synthesized beam of ($0\farcs65 \times 0\farcs51$; P.A. $85\fdg29$) for the OCS line (Table 6.1) and the intrinsic line width of 1 km s^{-1}. This intrinsic line width is assumed by considering the possible turbulent motions in the inner envelope.

We conducted simulations of the PV diagrams of OCS with a wide range of parameters. As an example, simulations of the PV diagram along the envelope direction with various sets of the protostellar mass and the radius of the centrifugal barrier are shown in Figure 6.6, while those along the outflow direction in Figure 6.7. These figures show how sensitive to the protostellar mass and the radius of the centrifugal barrier the simulated PV diagrams are. By judging from the goodness of the simultaneous fit for the two directions (Figures 6.6 and 6.7) by eye, a protostellar mass of 0.75 $M_\odot$ and a radius of the centrifugal barrier of 50 au reasonably reproduce the PV diagrams, with the assumptions of an inclination angle of 60° (90° for the edge-on configuration) and the distance of 120 pc (Knude & Hog, 1998). To verify this result, we calculated the root mean square (rms) of the residuals (Table 6.2), and the rms value is confirmed to be almost the lowest for the above parameters. We note that the rms values of the residuals in Table 6.2 themselves do not have a statistical meaning, because we employ a simple model concentrating on the velocity structure of the envelope and do not consider abundance variation, asymmetrical distribution of molecules, optical depth effects, and so on. Systematic errors caused by these assumptions would overwhelm the statistical noise, which makes the chi-square analysis difficult (see also Chapter 4). Nevertheless, it should be stressed that even such a simple model can reasonably explain the basic velocity structure observed in the OCS line. Further comparisons were made by considering the other model parameters including the inclination angle, which allowed us to finally constrain the model parameters. As a result, the radius of the centrifugal barrier lies in the range from 40 au to 60 au. The outer radius of the OCS distribution is derived to be 180 au. The results of the simulation for the PV diagrams of OCS along the envelope and outflow directions for the inclination angle of 60° are shown in Figures 6.8(a) and 6.8(b).

It is important to note that the protostellar mass is highly correlated with the incli-

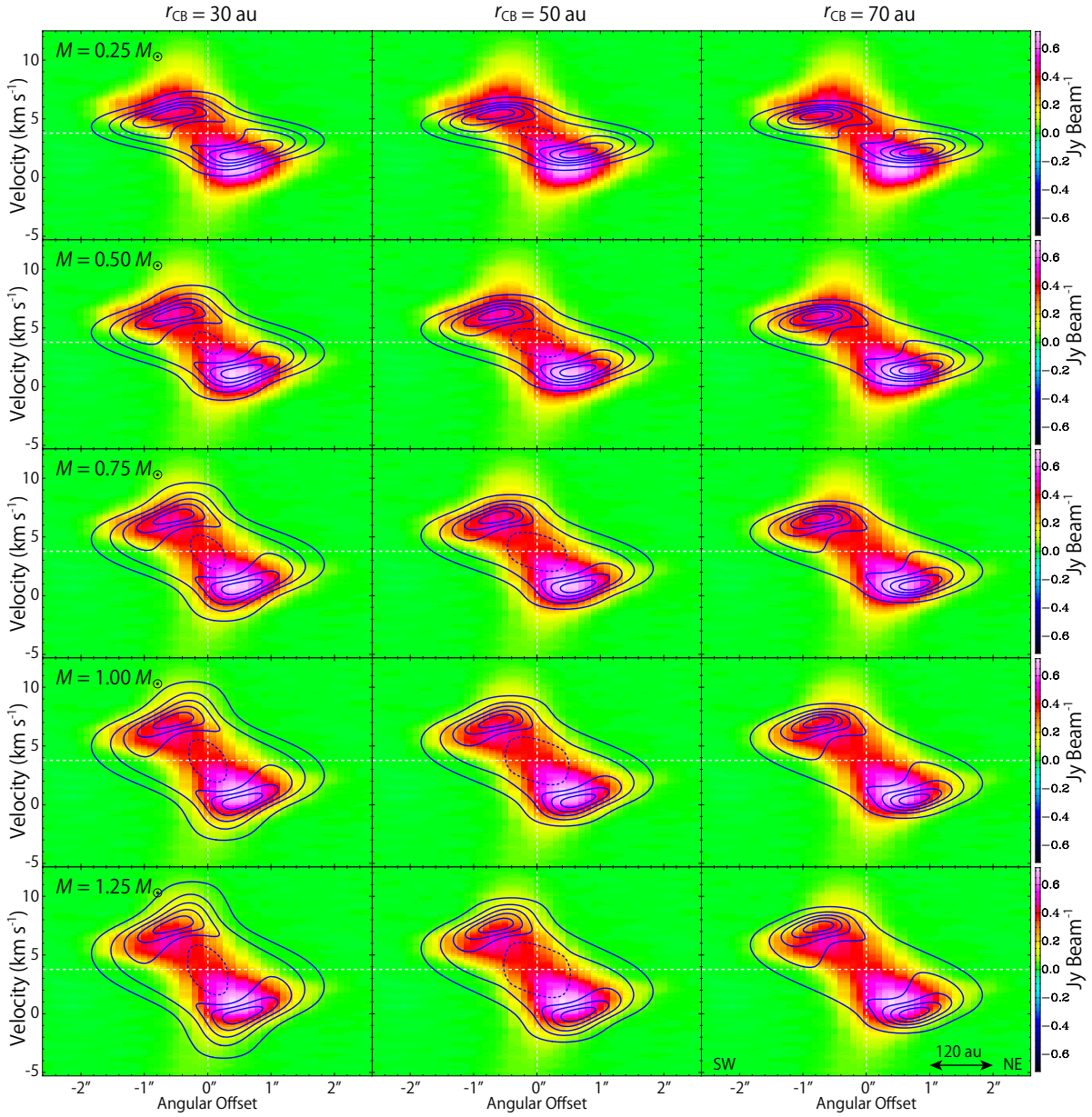

Figure 6.6: Results of the model simulations (blue contours) with various sets of the radius of the centrifugal barrier ($r_{\rm CB}$) and the protostellar mass (M) superposed on the PV diagram of OCS (color) along the envelope direction (P.A. 65°). The other physical parameters for the models are set as follows; $i = 60°$ and $R = 180$ au. The intrinsic line width is assumed to be 1 km s^{-1}. The contour levels are every 20% from 5% of each peak intensity. The dashed contours around the central position in the panels for $r_{\rm CB}$ of 30 and 50 au represent the dip toward the center.

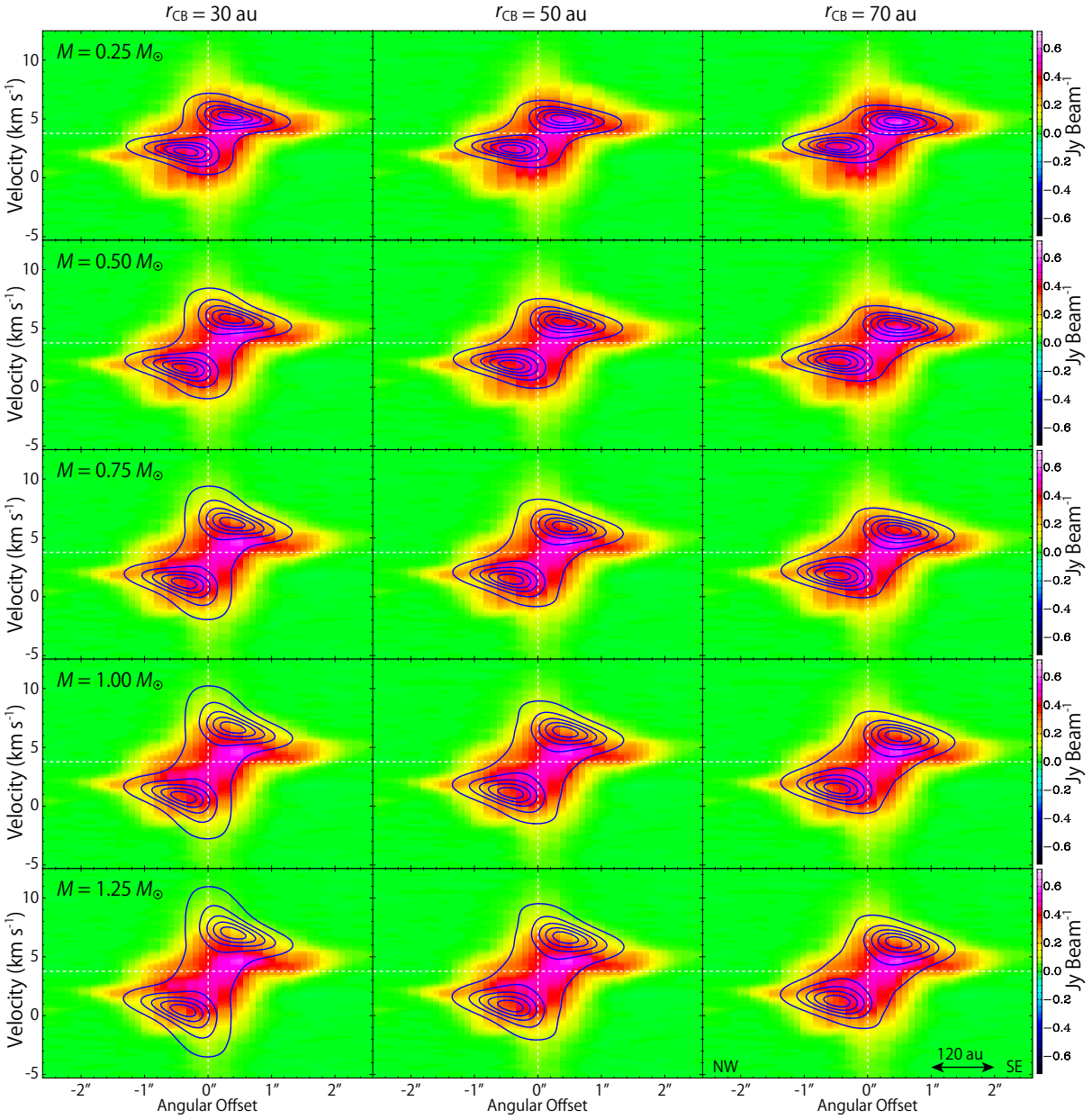

Figure 6.7: Results of the model simulations (blue contours) with various sets of the radius of the centrifugal barrier ($r_{\rm CB}$) and the protostellar mass (M) superposed on the PV diagram of OCS (color) along the outflow direction (P.A. 155°). The other physical parameters and the contour levels are the same as those in Figure 6.6.

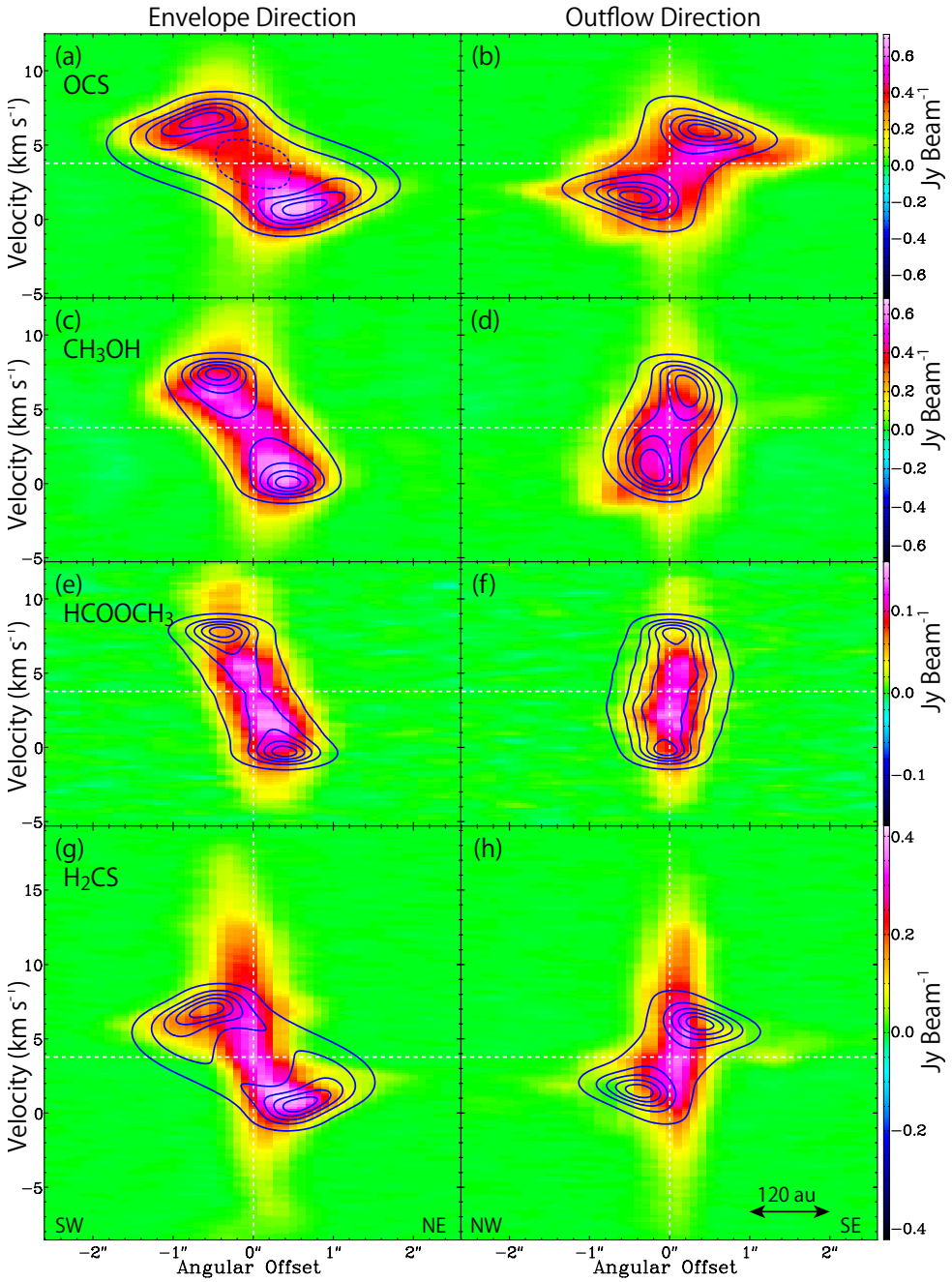

Figure 6.8: Color maps are the same as those in Figure 6.3. Blue contours represent the results of the infalling-rotating envelope models, where $M = 0.75\ M_{\odot}$, $r_{\rm CB} = 50$ au, and $i = 60°$. The outer radii of the envelope R in the models for OCS, CH_3OH, $HCOOCH_3$, and H_2CS are 180, 80, 55, and 150 au, respectively. The contour levels are every 20% from 5% of each peak intensity. Meaning of the dashed contour in panel (a) is denoted in footnotes of Figure 6.6.

Table 6.2: Root Mean Squares of the Intensity Difference between the Observed and Calculated Position-Velocity Diagrams of OCS[a]

	Radius of the Centrifugal Barrier		
Protostellar Mass	30 au	50 au	70 au
0.25 $M_\odot$	100	105	112
0.50 $M_\odot$	88	91	98
0.75 $M_\odot$	86	86	92
1.00 $M_\odot$	90	88	92
1.25 $M_\odot$	96	93	96

[a] In mJy beam^{-1}.

nation angle of the envelope, while the radius of the centrifugal barrier is not. Indeed, an acceptable agreement between the observation and the model result is obtained for an inclination angle ranging between 30° and 70°. For a given radius of the centrifugal barrier ($r_{\rm CB}$), the protostellar mass (M) which reproduces the maximum velocity-shift due to the rotation (4.5 km s^{-1}) depends on the inclination angle (i) as:

$$\frac{M}{M_\odot} = 0.57 \left(\frac{r_{\rm CB}}{50\ {\rm au}}\right) \sin^{-2} i. \tag{6.1}$$

For instance, the protostellar mass is 0.97 $M_\odot$ and 0.64 $M_\odot$ for an inclination angle of 50° and 70°, respectively, for $r_{\rm CB}$ of 50 au. The protostellar mass is estimated by Bottinelli et al. (2004a) and Caux et al. (2011) to be $\sim 1\ M_\odot$ from the difference in the $v_{\rm lsr}$ between Source A and Source B and the velocity width of the observed lines, respectively, with which our result is almost consistent. The distance of the source from the Sun (d) also affects the derived physical parameters. With the apparent size of the centrifugal barrier ($\sim$0.″42 in radius) and the maximum rotation velocity at the centrifugal barrier (4.5 km s^{-1}), the protostellar mass and the radius of the centrifugal barrier have relations to d as:

$$\frac{r_{\rm CB}}{50\ {\rm au}} = \frac{d}{120\ {\rm pc}}, \tag{6.2}$$

$$\frac{M}{M_\odot} = 0.57 \left(\frac{d}{120\ {\rm pc}}\right) \sin^{-2} i. \tag{6.3}$$

If d of 137 pc (Ortiz-León et al., 2017) is employed, $r_{\rm CB}$ and M are recalculated to be 57 au and 0.65 $M_\odot$.

The PV diagrams of OCS along the lines passing through the protostellar position for every 10° of the position angle are shown in Figure 6.9. Starting from the outflow direction (P.A. 155°), features of the PV diagrams do not change symmetrically between clockwise rotation and counter-clockwise rotation of the position angles. This behavior cannot be explained by the Keplerian motion, but requires both rotation and infall motions. The model basically reproduces the trend of the PV diagrams for the various position angles, although we can still find some discrepancies in detailed distributions. The discrepancies seem to originate from asymmetry of the molecular distribution in the infalling-rotating envelope around the protostar, as seen in the moment 0 map (Figure 6.1a). For instance,

the extension of the gas is narrowest along the 125° (P.A.) line instead of 155° (P.A.; outflow direction). This asymmetry makes the discrepancy between the observation and the simulation larger around that position angle (Figure 6.9). Another reason for this discrepancy would be the relative contribution of the rotation and infall motions. Since these two motions have almost opposite directions along the line of sight for the position angle from 75° to 145°, the PV diagram is sensitive to a small difference of their relative contribution. This situation makes difficult to reproduce the observed PV diagrams for these position angles.

It should be stressed that the observed PV diagrams for OCS cannot be explained only by the Keplerian motion, as mentioned above. Figure 6.10 shows the simulation of the PV diagrams along the envelope and outflow directions assuming the Keplerian motion. While the PV diagram along the envelope direction can be explained to some extent, the velocity gradient along the outflow direction cannot be reproduced. Nevertheless, we cannot rule out the possibility that OCS may also reside in the Keplerian disk to some extent in addition to the infalling-rotating envelope, which contributes to the shape of the PV diagrams. Neglecting this contribution may cause additional systematic errors in the above analysis.

In this model, we assume an $r^{-1.5}$ density profile and a constant abundance of molecules for simplicity. The peak intensity of the OCS line is ~ 0.7 Jy beam^{-1} for the blue-shifted velocity component. This intensity corresponds to the brightness temperature of 50 K, which is lower enough than the gas kinetic temperature about 100 K derived below (see Section 6.6.2 and Table 6.3). Since the excitation temperature is close to the gas kinetic temperature in the hot and dense part, this line can be assumed to be optically thin. In these observations, the OCS line is intensest, and hence, the other molecular lines are most likely to be optically thin. In order to assess how this assumption affects the results, we also conducted the simulations by using density profiles of r^0 and $r^{-2.5}$. These may partly account for the effect of the optical depth, the excitation effect, and the temperature gradient effect in an effective way. However, we found that the simulation results of the PV diagrams do not change significantly.

Finally, we note that the PV diagrams of the infalling-rotating envelope model can also explain the essential part of the observed PV diagrams of $C^{34}S$ along the envelope observed with SMA and eSMA (Favre et al., 2014), by using M and r_{CB} derived for OCS.

6.5.2 CH_3OH and $HCOOCH_3$

We also compare the PV diagrams of CH_3OH and $HCOOCH_3$ along the envelope and outflow directions with the model results in Figures 6.8(c–f). The model parameters are set to be the same as those derived from the analysis of OCS ($M = 0.75\ M_\odot$, $r_{CB} = 50$ au, and $i = 60°$), except for the outer radius, and the model images are convolved by an intrinsic line width of 1 km s^{-1} and the synthesized beam for each line listed in Table 6.1. As mentioned in Section 6.3, the distributions of CH_3OH and $HCOOCH_3$ are compact and their two-dimensional Gaussian-fitted sizes deconvolved by the beam are (130 au × 100 au) and (90 au × 40 au) in FWHM, respectively, assuming a distance of 120 pc (Knude & Hog, 1998). Hence, the outer radii of the infalling-rotating envelope model for CH_3OH and $HCOOCH_3$ are set to be 80 au and 55 au, respectively. The latter value just assumes that $HCOOCH_3$ is mostly distributed in a ring-like structure at the centrifugal barrier.

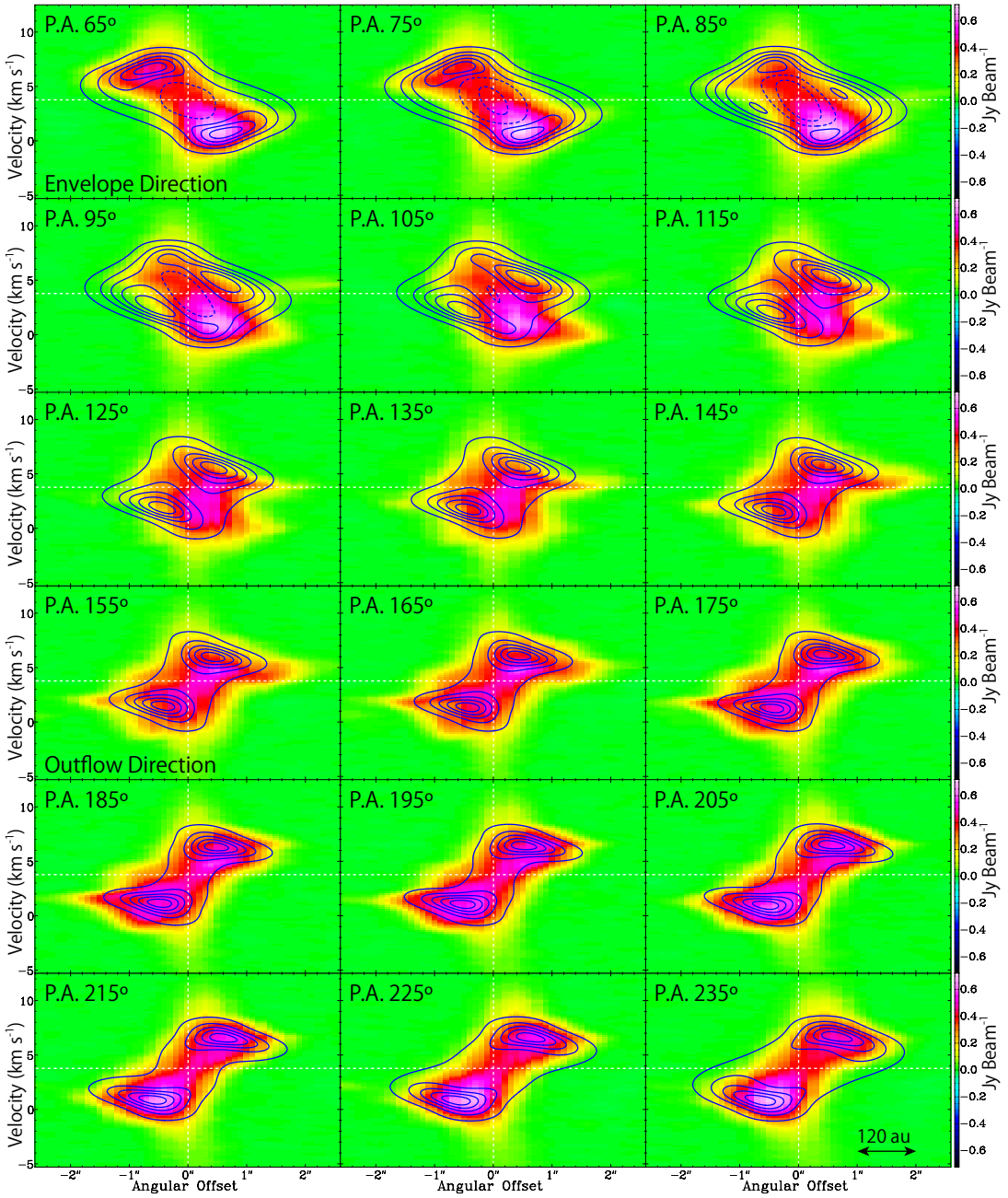

Figure 6.9: PV diagrams of OCS (color) for the 18 lines passing through the protostellar position with various position angles. The position angles of the lines along which the PV diagrams are prepared are every 10° from the envelope direction (P.A. 65°). Blue contours represent the results of the infalling-rotating envelope model, where $M = 0.75\ M_{\odot}$, $r_{\rm CB} = 50$ au, $i = 60°$, and $R = 180$ au. The intrinsic line width is assumed to be 1 km s^{-1}. The contour levels are every 20% from 5% of each peak intensity. Meaning of the dashed contours in panels 'P.A. 65°', 'P.A. 75°', 'P.A. 85°', 'P.A. 95°', and 'P.A. 105°' is denoted in footnotes of Figure 6.6.

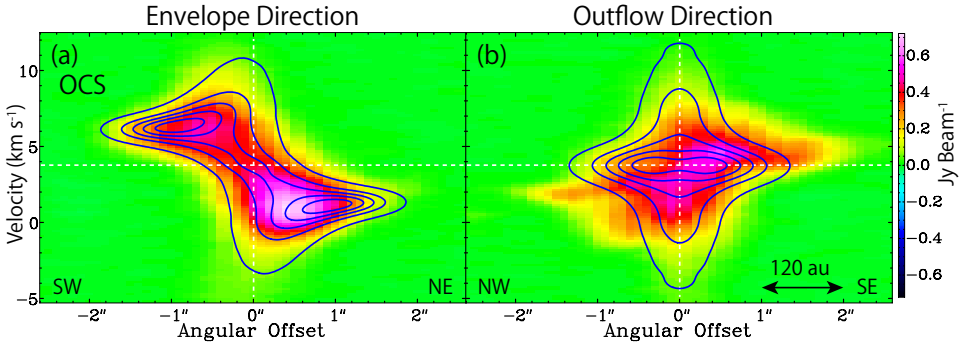

Figure 6.10: PV diagrams of OCS (color) along the envelope direction (P.A. 65°) and the outflow direction (P.A. 155°). Blue contours represent the results of the Keplerian motion with a protostellar mass of 1.5 $M_\odot$, where the outer radius of the model is set to be 180 au and the inclination angle is assumed to be 60°. The contour levels are every 20% from 5% of each peak intensity.

The PV diagrams simulated with the small outer radii show a good agreement with the observations (Figures 6.8c–f). Figures 6.11 and 6.12 show a more detailed comparison using the PV diagrams for every 10° of the position angle. Although there are some discrepancies between the observations and the model results, such as the missing of high velocity-shift components in $HCOOCH_3$, the model reasonably reproduces the observed PV diagrams. Hence, the emitting regions of CH_3OH and $HCOOCH_3$ seem to essentially have a ring-like structure around the centrifugal barrier. Such distributions of CH_3OH and $HCOOCH_3$ are similar to the SO ring around the protostar in L1527 (Sakai et al., 2014a,b). Note that the outer radius employed above for CH_3OH ($R = 80$ au) is close to the centrifugal radius (twice the radius of the centrifugal barrier) by chance, where the centrifugal force balances with the gravitational force.

6.5.3 H_2CS

In Figure 6.13, we overlay the results of the model simulation on the observed PV diagrams of the three lines of H_2CS ($7_{0,7} - 6_{0,6}$; $7_{2,5} - 6_{2,4}$; $7_{4,4} - 6_{4,3}/7_{4,3} - 6_{4,2}$). In this simulation, we used the same parameters as those used for OCS ($M = 0.75\ M_\odot$, $r_{\rm CB} = 50$ au, and $i = 60°$) except for a smaller outer radius of the envelope ($R = 150$ au). The model images are convolved by an intrinsic line width of 1 km s^{-1} and the synthesized beam for H_2CS ($7_{0,7} - 6_{0,6}$) shown in Table 6.1. The simulation result reproduces the observed PV diagrams for the envelope part, although the distribution of the $7_{4,4} - 6_{4,3}/7_{4,3} - 6_{4,2}$ line tends to be less extended to the envelope than the other two lines as in the case of CH_3OH and $HCOOCH_3$.

On the other hand, the components observed near the protostar apparently show broader velocity widths than the results of the infalling-rotating envelope model. These broader velocity components seem to trace the Keplerian disk component in the vicinity of the protostar. Hence, we made a simulation of the PV diagram for the Keplerian disk assuming the protostellar mass determined from the above analysis of the infalling-rotating envelope in Section 6.5.1 (0.75 $M_\odot$). Here, we also assume that the outer radius

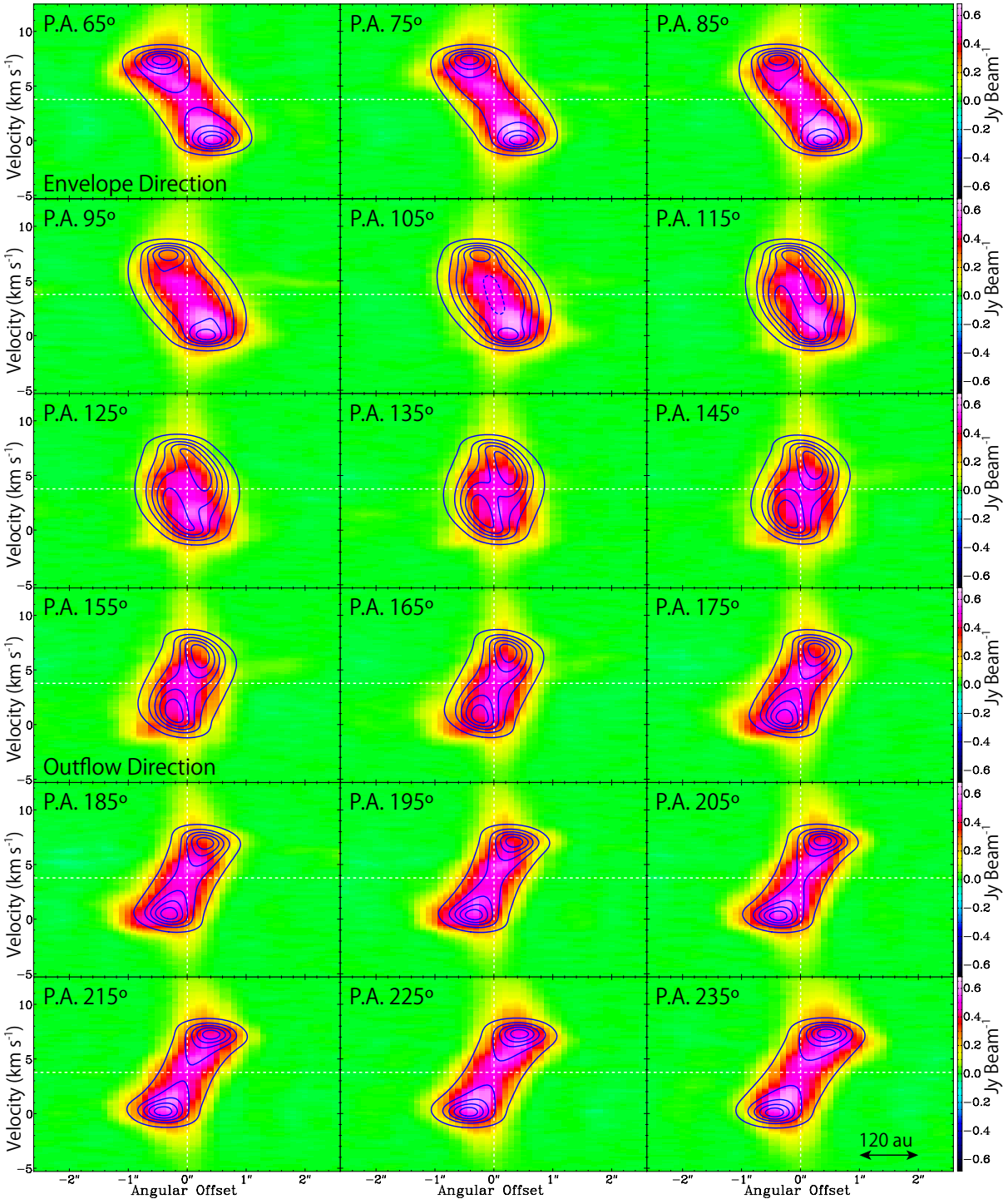

Figure 6.11: PV diagrams of CH_3OH (color) for the 18 lines passing through the protostellar position with various position angles. The position axes are the same as those in Figure 6.9. Blue contours represent the results of the infalling-rotating envelope model, where $M = 0.75\ M_\odot$, $r_{\rm CB} = 50$ au, $i = 60°$, and $R = 80$ au. The intrinsic line width is assumed to be 1 km s^{-1}. The contour levels are every 20% from 5% of each peak intensity. Meaning of the dashed contour in panel 'P.A. 105°' is denoted in footnotes of Figure 6.6.

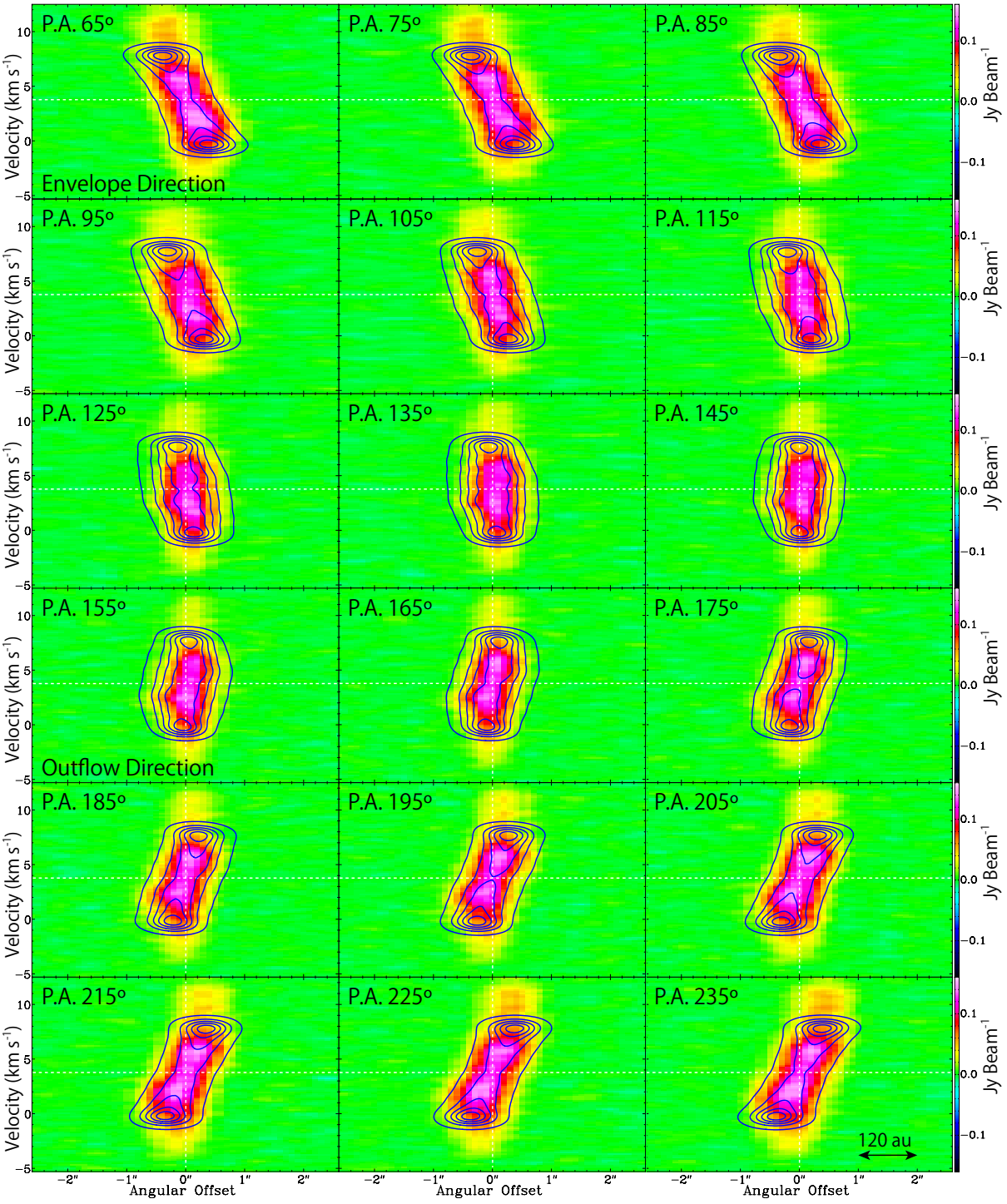

Figure 6.12: PV diagrams of $HCOOCH_3$ (color) for the 18 lines passing through the protostellar position with various position angles. The position axes are the same as those in Figure 6.9. Blue contours represent the results of the infalling-rotating envelope model, where $M = 0.75\ M_\odot$, $r_{\rm CB} = 50$ au, $i = 60°$, and $R = 55$ au. The intrinsic line width is assumed to be 1 km s^{-1}. The contour levels are every 20% from 5% of each peak intensity.

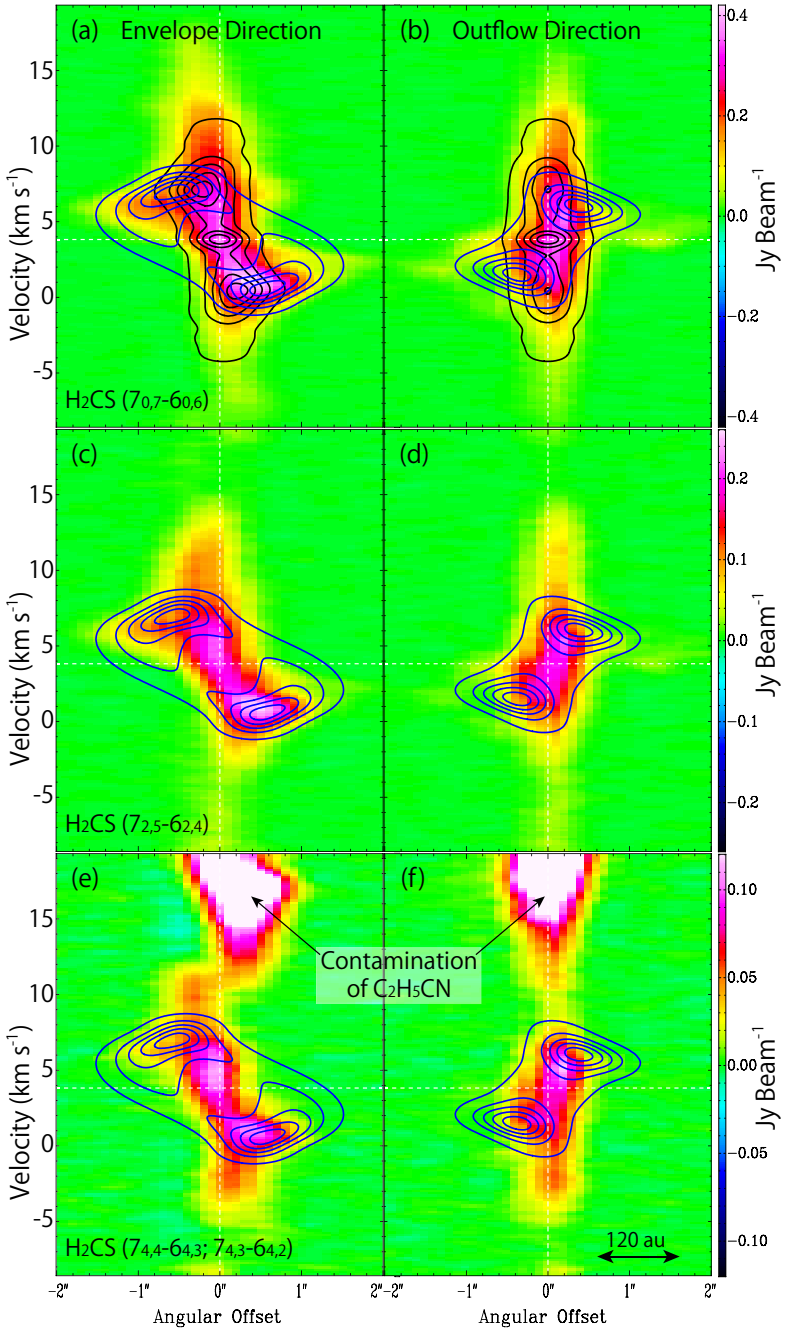

Figure 6.13: PV diagrams of H_2CS ($7_{0,7} - 6_{0,6}$; $7_{2,5} - 6_{2,4}$; $7_{4,4} - 6_{4,3}/7_{4,3} - 6_{4,2}$) along the envelope direction (P.A. 65°) and the outflow direction (P.A. 155°). Blue contours represent the results of the infalling-rotating envelope model, where $M = 0.75\ M_\odot$, $r_{\rm CB} = 50$ au, $i = 60°$, and $R = 150$ au. The line width is assumed to be 1 km s^{-1}. Black contours in panels (a) and (b) represent the results of the simulation for the Keplerian motion inside the centrifugal barrier, where $M = 0.75\ M_\odot$ and $i = 60°$. The contour levels for the two models are every 20% from 5% of each peak intensity. The H_2CS ($7_{4,4} - 6_{4,3}$ and $7_{4,3} - 6_{4,2}$) line is contaminated by the C_2H_5CN ($28_{1,28} - 27_{1,27}$; 240.3193373 GHz) line in panels (e) and (f).

of the Keplerian disk is equal to the radius of the centrifugal barrier (50 au) for simplicity. The result of this disk model is also overlaid on the observed PV diagrams for H_2CS ($7_{0,7}-6_{0,6}$) in Figures 6.13(a) and 6.13(b). It well explains the broader-velocity components, which strongly suggests the existence of the Keplerian disk structure within the centrifugal barrier.

6.6 Discussion

6.6.1 infalling-rotating envelope and Its Centrifugal Barrier

The results presented above most likely show the existence of the infalling-rotating envelope and the indication of its centrifugal barrier in the prototypical hot corino source IRAS 16293–2422 Source A. The observed PV diagrams are reasonably explained by the simple ballistic model of the infalling-rotating envelope (Figures 6.8, 6.9, 6.11–6.13). The existence of the centrifugal barrier is not shown as clearly as in the case of L1527 (Chapter 3; Sakai et al., 2014a) because of the contamination by the Keplerian disk component in this source. Nevertheless, we can estimate its radius by using the ballistic model. For the identification of the centrifugal barrier in the hot corino source, the emission of OCS is found to be useful. L1527 and IRAS 16293–2422 are quite different from each other in the chemical composition, but their physical structures are found to be similar. Hence, the infalling-rotating envelope and its centrifugal barrier would exist in protostellar sources regardless of their chemical characteristics.

On the other hand, the radius of the centrifugal barrier is different from source to source (Chapters 3–5; Sakai et al., 2016). The range of the centrifugal barrier is from a few tens of au to 100 au in radius. We discuss on this variation of the radius of the centrifugal barrier in Chapter 10. Statistical studies of the radius of the centrifugal barrier for a number of young protostellar sources are therefore interesting, and will provide us with rich information regarding the formation process of protoplanetary disks and their diversity.

6.6.2 Origin of the Chemical Change around the Centrifugal Barrier

The present analyses demonstrate chemical differentiation in the closest vicinity of the protostar in the hot corino source. A chemical change seems to be occurring in the region around the centrifugal barrier, probably between the centrifugal radius and the centrifugal barrier, as in the case of the WCCC sources L1527 and TMC-1A (Chapter 4; Sakai et al., 2016). In IRAS 16293–2422 Source A, the OCS emission is mainly distributed in the infalling-rotating envelope up to the radius of 180 au, while the CH_3OH and $HCOOCH_3$ emission is mainly concentrated around the centrifugal barrier. On the other hand, H_2CS resides from the envelope to the Keplerian disk.

So far, OCS has been detected in hot cores and hot corinos (Blake et al., 1987, 1994; Caux et al., 2011). It is known to be abundant in IRAS 16293–2422, because high-excitation lines of the isotopologues, $OC^{34}S$ and $O^{13}CS$, are detected by single-dish observations (Blake et al., 1994; Caux et al., 2011). According to the jump-model analysis

by Schöier et al. (2002), its fractional abundance relative to H_2 is as high as 10^{-7}. However, production processes of OCS are not well understood. The gas phase production (CS + OH, SO + CH) as well as the solid phase production are proposed (Wakelam et al., 2011; Loison et al., 2012). The evaporation temperature of OCS is evaluated to be ∼50 K from the surface binding energy of 2888 K (UMIST database for astrochemistry; McElroy et al., 2013, http://udfa.ajmarkwick.net/index.php), and is lower than the gas temperature of the infalling-rotating envelope derived below from the multiple line analysis of H_2CS. See also Appendix A for the derivation of the evaporation temperature. Hence the liberation of OCS from dust grains cannot be ruled out for the distribution in the infalling-rotating envelope.

On the other hand, the CH_3OH and $HCOOCH_3$ emission is distributed in a narrow region (possibly a ring-like structure) around the centrifugal barrier. Concentration of these molecules around the centrifugal barrier suggests that they would be liberated from ice mantles to the gas phase due to weak accretion shocks expected in front of the centrifugal barrier. This situation is similar to the SO distribution in the WCCC sources L1527 and TMC-1A (Sakai et al., 2014a,b, 2016). Alternatively, they would be thermally evaporated by protostellar heating within a certain radius from the protostar. If this evaporation radius is just outside the radius of the centrifugal barrier by chance, the observed distributions of CH_3OH and $HCOOCH_3$ can be explained. Since the luminosity of IRAS 16293–2422 is as high as 22 $L_\odot$ (Crimier et al., 2010), the CH_3OH evaporation region would be able to extend outward of the centrifugal barrier. According to the spherical model by Crimier et al. (2010), the gas kinetic temperature at the radius of 50 au is estimated to be as high as 130 K, and the outer radius of the infalling-rotating envelope model of 80 au for CH_3OH coincides with the water sublimation radius ($\gtrsim$ 100 K). Hence thermal evaporation by the protostellar heating can cause such an enhancement of CH_3OH and $HCOOCH_3$.

In order to assess these two possibilities, we derived the gas kinetic temperature by using the $7_{0,7} - 6_{0,6}$, $7_{2,5} - 6_{2,4}$, $7_{4,4} - 6_{4,3}/7_{4,3} - 6_{4,2}$ lines of H_2CS. These three transitions can be used as a good thermometer, as shown below, because the cross K-ladder radiative transitions (i.e. $K_a = 2 \rightarrow 0$) are very slow. Since H_2CS is distributed from the infalling-rotating envelope to the Keplerian disk component, we derived the gas kinetic temperatures of the infalling-rotating envelope component, the centrifugal barrier, and the Keplerian disk (Table 6.3). These temperatures are derived from the integrated intensity ratios of the $7_{2,5} - 6_{2,4}$ and $7_{4,4} - 6_{4,3}/7_{4,3} - 6_{4,2}$ lines to the $7_{0,7} - 6_{0,6}$ line. The integrated intensities are calculated for a circular area of the moment 0 maps with a diameter of 0.″5, which is centered at the distance of 1.″0, 0.″5, and 0.″0 from the continuum peak along the envelope direction (Figure 6.1a) for the envelope component, the centrifugal barrier, and the Keplerian disk component, respectively. This diameter is comparable to the size of the synthesized beam. The velocity-shift range for the integration is from 1.0 to 4.0 km s^{-1}, from 2.0 to 5.0 km s^{-1}, and from 5.0 to 7.3 km s^{-1}, for the blue-shifted and red-shifted parts of the envelope component, the centrifugal barrier, and the Keplerian disk component, respectively. Here the systemic velocity component is excluded, because it can be affected by self-absorption. For the Keplerian disk component, only the velocity-shift range higher than the maximum rotation velocity of the infalling-rotating envelope is used so as to exclude the contamination by the envelope component.

Table 6.3: Gas Kinetic Temperature Derived from the H_2CS Lines[a]

	Red-Shifted Component			Blue-Shifted Component		
Transitions	Envelope[b]	CB[c]	Disk[d]	Envelope[b]	CB[c]	Disk[d]
$7_{0,7} - 6_{0,6}$ and $7_{2,5} - 6_{2,4}$	$70 - 110$	$110 - 140$	$70 - 90$	$70 - 110$	$100 - 130$	$70 - 120$
$7_{0,7} - 6_{0,6}$ and $7_{4,4} - 6_{4,3}/7_{4,3} - 6_{4,2}$	$90 - 120$	$130 - 160$	$120 - 140$	$80 - 110$	$130 - 150$	> 190

[a] In K. The gas kinetic temperatures are derived by using RADEX code (van der Tak et al., 2007). The assumed ranges for the H_2 density and the column density of H_2CS are from 10^7 to 10^9 cm^{-3} and from 10^{13} to 10^{15} cm^{-2}, respectively. The error estimation is denoted in footnotes of Figure 6.14.

[b] The infalling-rotating envelope component. The absolute value of the velocity-shift ranges from 1.0 to 4.0 km s^{-1}.

[c] The centrifugal barrier. The absolute value of the velocity-shift ranges from 2.0 to 5.0 km s^{-1}.

[d] The Keplerian disk component. The absolute value of the velocity-shift ranges from 5.0 to 7.3 km s^{-1}.

The intensity ratios are compared with those calculated by using RADEX code (van der Tak et al., 2007), as shown in Figure 6.14. The H_2 density and the column density of H_2CS are assumed to be from 10^7 to 10^9 cm^{-3} and from 10^{13} to 10^{15} cm^{-2}, respectively, the latter of which can be compared with the previously reported value of the column density (3.7×10^{13} cm^{-2}; Blake et al., 1994) considering the beam filling factor. The solid and dashed lines in Figure 6.14 show the gas kinetic temperatures calculated for the various intensity ratios as a function of the H_2 densities (Figure 6.14a) and the column densities of H_2CS (Figure 6.14b). The gas kinetic temperatures barely depend on the H_2 density and the column density of H_2CS. Hence, they can be well evaluated from the observed intensity ratios regardless of the other parameters. The gas kinetic temperatures thus evaluated are listed in Table 6.3.

The gas kinetic temperatures derived above are almost consistent with the temperature at the 50 au scale in the spherical model by Crimier et al. (2010). They are higher than the rotation temperatures of H_2CS and SO_2 derived from the single-dish data, 60 K and 95 K, respectively (Blake et al., 1994). Moreover, the gas kinetic temperatures derived from the $7_{0,7} - 6_{0,6}$ and $7_{2,5} - 6_{2,4}$ lines of H_2CS seem to be higher at the centrifugal barrier than the other areas. As for the gas kinetic temperatures derived from the $7_{0,7} - 6_{0,6}$ and $7_{4,4} - 6_{4,3}/7_{4,3} - 6_{4,2}$ lines of H_2CS, a similar trend of the enhanced temperature at the centrifugal barrier is seen for the red-shifted component, although the gas kinetic temperature derived for the Keplerian disk are higher than that derived for the centrifugal barrier for the blue-shifted component. These results suggest a higher gas kinetic temperature at the centrifugal barrier. If the dust temperature is similarly higher, the abundance enhancement of CH_3OH and $HCOOCH_3$ near the centrifugal barrier would be expected. If the mid-plane temperature of the Keplerian disk component is as low as $70 - 90$ K, these species will be depleted onto dust grains there. This mechanism may be the reason why the CH_3OH and $HCOOCH_3$ emissions in the Keplerian disk component are not as bright as around the centrifugal barrier (i.e. they come from a ring-like structure around the centrifugal barrier). On the other hand, the deficiency of OCS and CS in the Keplerian disk component is puzzling in this context, because the binding energy of OCS (2888 K) and CS (1900 K) are comparable to that of H_2CS (2700 K) (UMIST database for astrochemistry; McElroy et al., 2013, http://udfa.ajmarkwick.net/index.php). Hence, the gas-phase destruction mechanisms of OCS and CS in the disk component have to be considered carefully.

While the above temperature analysis supports the idea of the accretion shock for liberation of organic molecules at the centrifugal barrier, the temperature raise may also originate from the protostellar heating combined with the geometrical effect. If the infall gas is stagnated in front of the centrifugal barrier, the envelope is more extended toward the direction perpendicular to the mid-plane of the envelope and becomes broader around the centrifugal barrier. Then, this part will be directly heated by the protostar without shielding by the mid-plane of the Keplerian disk, resulting in a higher gas kinetic temperature at the centrifugal barrier. Since the spatial resolution of the currently available data is not enough to resolve the vertical structure of the envelope, discrimination of the two possibilities is left for future studies.

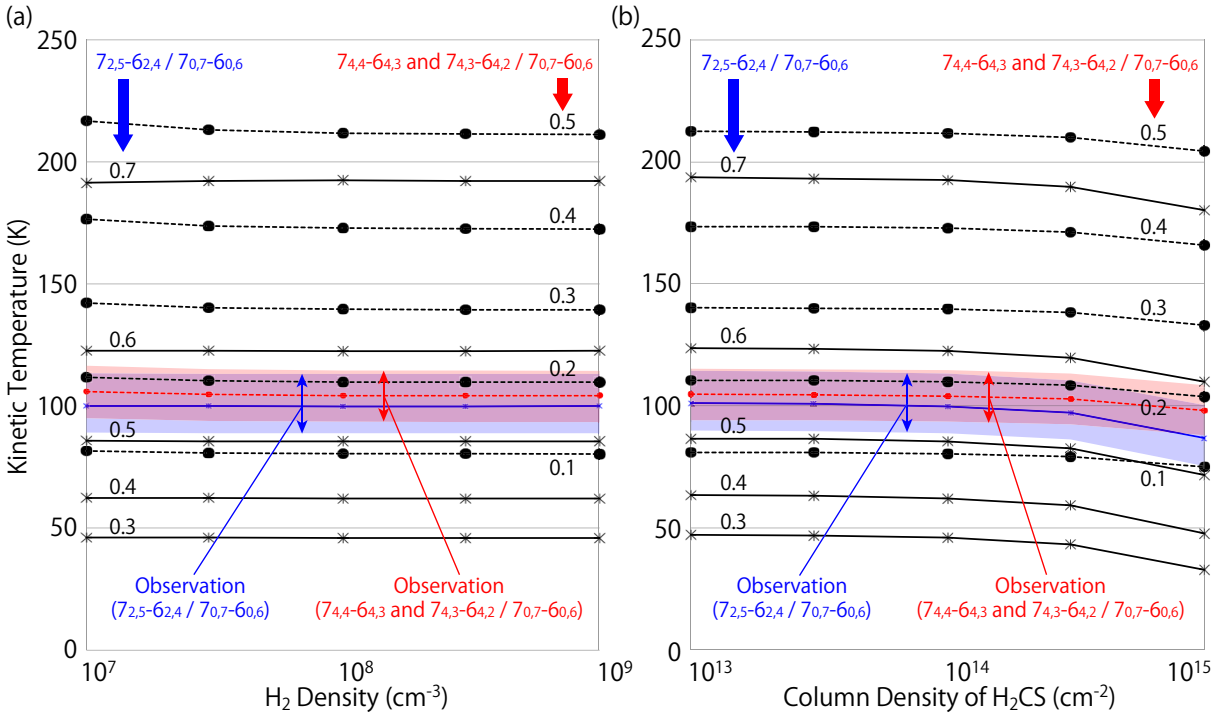

Figure 6.14: An example of determination of the gas kinetic temperature by using the intensity ratios of the H_2CS ($7_{2,5} - 6_{2,4}$; $7_{4,4} - 6_{4,3}$ and $7_{4,3} - 6_{4,2}$) lines relative to the H_2CS ($7_{0,7} - 6_{0,6}$) line. Solid and dashed lines represent the gas kinetic temperature for a given ratio of $7_{2,5} - 6_{2,4}/7_{0,7} - 6_{0,6}$ and $(7_{4,4} - 6_{4,3}$ and $7_{4,3} - 6_{4,2})/7_{0,7} - 6_{0,6}$, respectively, as a function of the H_2 density (a) and the H_2CS column density (b) calculated by using RADEX code (van der Tak et al., 2007). The column density of H_2CS is fixed to be 10^{14} cm^{-2} in panel (a), while the H_2 density is fixed to be 10^8 cm^{-3} in panel (b). The solid blue and dashed red lines represent the observed results of the $7_{2,5} - 6_{2,4}/7_{0,7} - 6_{0,6}$ and $(7_{4,4} - 6_{4,3}$ and $7_{4,3} - 6_{4,2})/7_{0,7} - 6_{0,6}$ ratios in the red-shifted envelope component, respectively, and the blue colored and red colored areas represent their error ranges (3σ). The derived ranges of the gas kinetic temperature for the other components are listed in Table 6.3. The error is estimated only from the statistical error and does not contain the calibration error, because it will be almost canceled in the intensity ratios.

Table 6.4: $HCOOCH_3/CH_3OH$ Column Density Ratios[a]

	Red-Shifted Component			Blue-Shifted Component		
	Envelope[b]	CB[c]	Disk[d]	Envelope[b]	CB[c]	Disk[d]
Ratio	0.8 ± 0.5	4.2 ± 0.3	8.7 ± 1.3	2.7 ± 1.2	4.9 ± 0.3	8.9 ± 1.2

[a] The quoted errors represent 3σ, where the rms noise level is derived from the statistical error.

[b] The infalling-rotating envelope. The absolute value of the velocity-shift ranges from 1.0 to 4.0 km s^{-1}. The rotational temperature is assumed to be 100 K.

[c] The centrifugal barrier. The absolute value of the velocity-shift ranges from 2.0 to 5.0 km s^{-1}. The rotational temperature is assumed to be 130 K.

[d] The Keplerian disk component. The absolute value of the velocity-shift ranges from 5.0 to 7.3 km s^{-1}. The rotational temperature is assumed to be 100 K.

6.6.3 Abundance of $HCOOCH_3$ Relative to CH_3OH

The column densities of CH_3OH and $HCOOCH_3$ are derived for the envelope component, the centrifugal barrier, and the Keplerian disk component. Although these two molecules mainly reside in the envelope component and/or around the centrifugal barrier, they partly exist in the Keplerian disk (Figures 6.8c–f). In order to evaluate the contribution from each component securely, the velocity range for integration is limited to a certain range for each component, as in the case of H_2CS (Section 6.6.2). Hence, the derived column densities do not mean the total ones, and do not have quantitative meanings by themselves. However, the abundance ratios $HCOOCH_3/CH_3OH$ are meaningful for mutual comparison. In the evaluation of the column densities of CH_3OH and $HCOOCH_3$, we employed the LTE approximation. The rotation temperatures for the envelope component, the centrifugal barrier, and the Keplerian disk component are assumed to be 100 K, 130 K, and 100 K, respectively, by referring the gas kinetic temperatures derived from the $7_{0,7} - 6_{0,6}$ and $7_{2,5} - 6_{2,4}$ lines of H_2CS (Table 6.3). The derived $HCOOCH_3/CH_3OH$ abundance ratios are shown in Table 6.4.

If the CH_3OH line is assumed to be optically thin, the $HCOOCH_3/CH_3OH$ abundance ratio is found to be higher than unity, except for the red-shifted envelope component. Such a high ratio is consistent with previous reports (Bottinelli et al., 2007). More importantly, it is lowest for the envelope component, and highest for the Keplerian disk component. This trend can be seen both in the red-shifted and blue-shifted components. It cannot simply be explained by the evaporation process, because the surface binding energy is almost comparable for CH_3OH (4930 K) and $HCOOCH_3$ (4000 K) (UMIST database for astrochemistry; McElroy et al., 2013, http://udfa.ajmarkwick.net/index.php). This may suggest that the chemical composition of grain mantles is processed to enhance $HCOOCH_3$ as grains pass across the centrifugal barrier. Alternatively, $HCOOCH_3$ may be formed in the gas phase around the centrifugal barrier and inside it (Balucani et al., 2015).

6.7 Summary of This Chapter

We analyzed the OCS, CH_3OH, $HCOOCH_3$, and H_2CS data observed toward IRAS 16293–2422 Source A with ALMA Cycle 1 at a sub-arcsecond resolution ($\sim 0''.6 \times 0''.5$). Major findings are as follows:

(1) The molecular distributions are different from molecule to molecule (Figure 6.3). OCS resides in the envelope, while CH_3OH and $HCOOCH_3$ have more compact distributions. On the other hand, H_2CS resides both in the envelope and Keplerian disk components.

(2) The simple infalling-rotating envelope model successfully explains the OCS distribution (Figure 6.9). The kinematic structure of OCS in the envelope is reproduced by the model with the protostellar mass of 0.75 $M_\odot$ and the radius of the centrifugal barrier of 50 au, assuming the inclination angle of 60° and the distance of 120 pc (Knude & Hog, 1998).

(3) The distributions of CH_3OH and $HCOOCH_3$ are concentrated around the centrifugal barrier (Figures 6.11 and 6.12). They may be liberated by weak accretion shocks in front of the centrifugal barrier and/or by protostellar heating.

(4) H_2CS has high-velocity components concentrated toward the protostellar position in addition to the infalling-rotating envelope component (Figure 6.5). These components seem to trace the Keplerian disk component. Their kinematic structures can be explained by the Keplerian motion with a protostellar mass of 0.75 $M_\odot$ (Figure 6.13), which is used to explain the kinematic structure of OCS. Based on the intensities of the $7_{0,7} - 6_{0,6}$, $7_{2,5} - 6_{2,4}$, and $7_{4,4} - 6_{4,3}/7_{4,3} - 6_{4,2}$ lines of H_2CS, the gas kinetic temperatures in the infalling-rotating envelope, the centrifugal barrier, and the Keplerian disk component are evaluated to be $70 - 120$, $100 - 160$, and $70 - 140$ K, respectively (Table 6.3).

(5) The $HCOOCH_3/CH_3OH$ abundance ratios are found to be $0.8 - 2.7$, $4.2 - 4.9$, and $8.7 - 8.9$ in the infalling-rotating envelope, the centrifugal barrier, and the Keplerian disk component, respectively (Table 6.4). The ratio tends to increase from the envelope to the Keplerian disk.

(6) A drastic chemical change is thus found to be occurring around the centrifugal barrier.

The present results indicate that the centrifugal barrier plays a crucial role in hot corino chemistry. Recently, the existence of the centrifugal barrier has been reported for the WCCC sources (Chapter 4; Sakai et al., 2014a,b, 2016), and therefore, it seems to be a common occurrence in low-mass protostellar sources regardless of their chemical characteristics.

Appendix: ALMA Data

The ALMA observations of IRAS 16293–2422 were carried out in the Cycle 1 operations (Jørgensen et al., 2016) on 22 May 2014 with the frequency setting in $230 - 250$ GHz, on 14 June 2014 with the frequency setting in $220 - 240$ GHz, and on 25 April 2014 with both of the frequency settings. Spectral lines of OCS, CH_3OH, $HCOOCH_3$ and H_2CS were observed with the Band 6 receiver at a frequency of 230, 250, 230, and 240 GHz, respectively. $42 - 44$ antennas were used in the observations, where the baseline length ranged from 17.14 to 636.53 m and from 19.58 to 628.65 m for the frequency settings in $230 - 250$ GHz and $220 - 240$ GHz, respectively. The field center of the observations was $(\alpha_{2000}, \delta_{2000}) = (16^{\rm h}32^{\rm m}22\overset{\rm s}{.}72, -24°28'34\overset{''}{.}3)$. The primary beams (half-power beam width) are $24\overset{''}{.}26$ and $25\overset{''}{.}06$ for the observations with the frequency settings in $230 - 250$ GHz and $220 - 240$ GHz, respectively. The total on-source time were 51 minutes and 50 minutes for the $230 - 250$ GHz and $220 - 240$ GHz observations with typical system temperatures of $200 - 300$ K and $50 - 100$ K, respectively. The backend correlator was tuned to a resolution of 122 kHz, which corresponds to the velocity resolution of 0.15 km s^{-1} at 240 GHz, and a bandwidth of 468.750 MHz. J1626-2951, J1700-2610 or J1625-2527 was used for the phase calibration every 8 minutes. The bandpass calibration was done on the following quasars; J1733-1304, J1700-2610, and J1517-2422. The absolute flux density scale was derived from Titan. The data calibration was performed in the antenna-based manner and uncertainties are less than 10% (ALMA Cycle 1 Technical Handbook; Lundgren, 2012). The Brigg's weighting with the robustness parameter of 0.5 was employed to obtain the images of the continuum and the spectral lines. In this analysis, we did not apply the self-calibration for simplicity.

Chapter 7

IRAS 16293–2422 Source B

We have analyzed the OCS, H_2CS, CH_3OH, and $HCOOCH_3$ data observed toward the low-mass protostar IRAS 16293–2422 Source B at a subarcsecond resolution with ALMA. A clear chemical differentiation is seen; OCS and H_2CS show an extended distribution with a slight rotation signature, while CH_3OH and $HCOOCH_3$ are concentrated near the protostar. The extended component is interpreted by the infalling-rotating envelope model with a nearly face-on configuration. The OCS, H_2CS, and CH_3OH lines show the inverse P-Cygni profile, indicating the infall motion in the vicinity of the protostar. Since we find the nearly pole-on outflow lobes in the SiO line, the infalling and outflowing motions should coexist along the line-of-sight to the protostar. A possible mechanism for the coexistence is discussed.

7.1 Introduction

We have confirmed the existence of the infalling-rotating envelope and its centrifugal barrier in a prototypical hot corino source IRAS 16293–2422 Source A by analyzing its kinematic structure in the vicinity of the protostar (Chapter 6). Moreover, we found a drastic chemical change across the centrifugal barrier in this source; different molecular species trace different parts of the disk/envelope system. In Chapters 4–6, we investigated sources with nearly edge-on configurations. Such chemical diagnostics will be a powerful tool to disentangle the infalling-rotating envelope and the Keplerian disk component even for sources with a face-on configuration, where the kinematic structure is difficult to be detected. We therefore conduct a similar analysis to the face-on source IRAS 16293–2422 Source B in this chapter. We demonstrate the usability of the chemical diagnostics, and confirm whether the chemical change found in IRAS 16293–2422 Source A is seen in another hot corino source IRAS 16293–2422 Source B.

IRAS 16293–2422 Source B is a component of the binary system of IRAS 16293–2422 (d = 120 pc; Knude & Hog, 1998) as well as IRAS 16293–2422 Source A, which we have investigated in Chapter 6. It is known to be rich in COMs as well as Source A (e.g. Bottinelli et al., 2004a; Kuan et al., 2004; Jørgensen et al., 2011, 2012, 2016; Pineda et al., 2012). Its disk/envelope system is reported to have a nearly face-on geometry in contrast to the edge-on geometry of Source A (Chapter 6; e.g. Pineda et al., 2012; Zapata et al., 2013) Thus the molecular line emission shows a narrower line width toward Source B than toward Source A. Furthermore, an inverse P-Cygni profile is reported toward Source B

(e.g. Pineda et al., 2012; Jørgensen et al., 2012), which implies the existence of the infalling gas in front of the protostar along the line-of-sight. In this chapter, we analyze molecular distributions and the kinematic structure of this source at a subarcsecond resolution, and compare the results with those of Source A.

7.2 Observation

We used the ALMA Cycle 1 archival data of IRAS 16293–2422, which is used also in Chapter 6 (See Appendix in Chapter 6 for the details). Spectral lines of OCS ($J = 19-18$), CH_3OH ($5_{1,5} - 4_{1,4}$; A^+), $HCOOCH_3$ ($20_{3,17} - 19_{3,16}$; A), and H_2CS ($7_{0,7} - 6_{0,6}$; $7_{2,5} - 6_{2,4}$; $7_{4,4} - 6_{4,3}$, $7_{4,3} - 6_{4,2}$) in the frequency range of $230 - 250$ GHz were observed with the Band 6 receiver. We also analyzed the ALMA Cycle 3 data, which were carried out on 5 March 2016. The spectral line of SiO ($J = 6 - 5$; 260.518 GHz) was observed with the Band 6 receiver. 41 antennas were used in this observation, where the baseline length ranged from 17 to 636 m. The phase center of the observation was (α_{2000}, δ_{2000}) = ($16^h32^m22\overset{s}{.}87$, $-24°28'36\overset{''}{.}3$), and the primary beam is $25''$. The total on-source time was 16.38 minutes with typical system temperature of $60 - 140$ K. The backend correlator was tuned to a resolution of 122 kHz, which corresponds to the velocity resolution of 0.14 km s^{-1} at 260 GHz, and a bandwidth of 58.6 MHz. J1625-2527 was used for the phase calibration every 7 minutes. The bandpass calibration was done on the quasar J1427-4206, and the absolute flux density scale was derived from Titan. The data calibration was performed in the antenna-based manner and uncertainties are less than 10% (ALMA Cycle 3 Technical Handbook; Remijan et al., 2015).

We analyzed the following molecular lines: OCS ($J = 19 - 18$), CH_3OH ($5_{1,5} - 4_{1,4}$; A^+), $HCOOCH_3$ ($20_{3,17} - 19_{3,16}$; A), H_2CS ($7_{0,7} - 6_{0,6}$; $7_{2,5} - 6_{2,4}$; $7_{4,4} - 6_{4,3}$, $7_{4,3} - 6_{4,2}$), and SiO ($J = 6 - 5$). Their rest frequencies, upper state energies, and intrinsic line strengths are summarized in Table 7.1. The Brigg's weighting with the robustness parameter of 0.5 was employed to obtain the images of the continuum and the spectral lines. Self-calibration using the continuum emission was applied to the ALMA Cycle 1 data (the continuum, OCS, CH_3OH, $HCOOCH_3$, and H_2CS). On the other hand, it was not applied to the ALMA Cycle 3 data (SiO), because the continuum sensitivity is not enough for self-calibration due to a limited number of line-free channels.

7.3 Distribution

Figure 7.1 shows the 1.2 mm continuum map. There are two intensity peaks corresponding to the two components of the binary, Source A and Source B. A weak emission bridging between the two peaks can also be seen. These features are consistent with the previous report (Jørgensen et al., 2016). While the distribution around Source A is slightly elongated along the NE-SW direction, that around Source B has an almost round shape. The disk/envelope systems of Source A and B are reported to have nearly edge-on and face-on, respectively (e.g. Rodríguez et al., 2005; Chandler et al., 2005), to which the above distributions are consistent. The sizes of the continuum emission deconvolved by the beam are evaluated to be $(1\overset{''}{.}138 \pm 0\overset{''}{.}007) \times (0\overset{''}{.}583 \pm 0\overset{''}{.}004)$ (P.A. $36\overset{\circ}{.}1 \pm 0\overset{\circ}{.}35$) and

Table 7.1: Parameters of the Observed Lines

Molecule	Transition	Frequency (GHz)	E_u (K)	$S\mu^2$ (Debye^2)[a]	Synthesized Beam
OCS[b]	$J = 19 - 18$	231.0609934	111	9.72	$0\farcs65 \times 0\farcs52$ (P.A. $84\fdg49$)
CH_3OH[b,c]	$5_{1,5} - 4_{1,4}$; A$^+$	239.746253	49	3.89	$0\farcs53 \times 0\farcs46$ (P.A. $71\fdg45$)
$HCOOCH_3$[c,d]	$20_{3,17} - 19_{3,16}$; A	250.25837	134	51.1	$0\farcs61 \times 0\farcs46$ (P.A. $79\fdg40$)
H_2CS[b,c]	$7_{0,7} - 6_{0,6}$	240.2668724	46	19.0	$0\farcs53 \times 0\farcs46$ (P.A. $73\fdg50$)
H_2CS[b,c]	$7_{2,5} - 6_{2,4}$	240.5490662	99	17.5	$0\farcs53 \times 0\farcs46$ (P.A. $73\fdg67$)
H_2CS[b,c]	$7_{4,4} - 6_{4,3}$, $7_{4,3} - 6_{4,2}$	240.3321897	257	12.8, 12.8	$0\farcs53 \times 0\farcs46$ (P.A. $73\fdg58$)
SiO[b,e]	$J = 6 - 5$	260.5180090	43.8	57.6	$0\farcs74 \times 0\farcs59$ (P.A. $89\fdg09$)

[a] Nuclear spin degeneracy is not included.
[b] Taken from CDMS (Müller et al., 2005).
[c] The ALMA Cycle 1 archival data. The self-calibration is employed.
[d] Taken from JPL (Pickett et al., 1998).
[e] The ALMA Cycle 3 data. The self-calibration is not employed.

($0''.429 \pm 0''.003$) × ($0''.357 \pm 0''.003$) (P.A. $139°.0 \pm 1°.6$) for Source A and Source B, respectively, by using the two-dimensional Gaussian fit. The peak flux densities are (314.0 ± 1.4) and (899.9 ± 1.5) mJy beam^{-1} for Source A and Source B, respectively.

Figure 7.2 shows the velocity channel maps of the OCS ($J = 19 - 18$) line. Absorption toward the continuum peak position can be seen in the maps of the $v_{\rm LSR}$ range from 3.4 to 4.3 km s^{-1}. Since the systemic velocity is around 3 km s^{-1} (Bottinelli et al., 2004a), this absorption feature is red-shifted. It is most naturally interpreted as the inverse P-Cygni profile, as previously reported (Jørgensen et al., 2012; Pineda et al., 2012; Zapata et al., 2013). At the systemic velocity, the distribution is extended at a $3''$ (∼400 au) scale in diameter around the continuum peak, although it would suffer from the resolving-out effect with the largest recoverable scale of $\sim 14''$ in this observation.

Figures 7.3, 7.4, and 7.5 show the velocity channel maps of the CH_3OH ($5_{1,5} - 4_{1,4}$; A^+), $HCOOCH_3$ ($20_{3,17} - 19_{3,16}$; A), and H_2CS ($7_{0,7} - 6_{0,6}$) lines, respectively. For all the three lines, the red-shifted components of the emission ($v_{\rm LSR} = 3 - 5$ km s^{-1}) show absorption features toward the continuum peak as in the OCS case. The distributions of

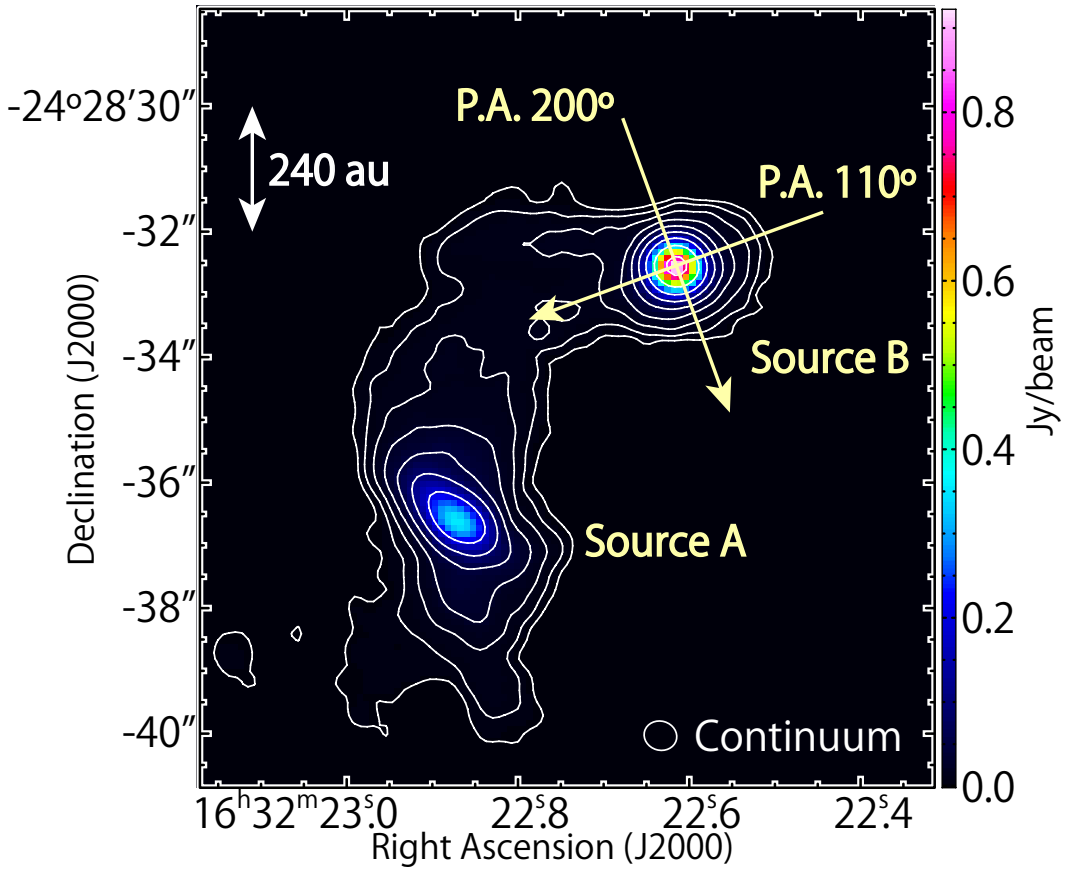

Figure 7.1: The map of the continuum emission at the 1.2 mm band. The contour levels are 10, 20, 40, 80, 160, 320, 640, 1280, and 2560σ, where the rms noise level is 0.3 mJy beam^{-1}. The intensity peak positions are shown by the black crosses. The synthesized is depicted in the bottom-right corner.

CH_3OH and $HCOOCH_3$ are more compact than that of OCS. Although the distribution of H_2CS is also smaller than that of OCS, it is larger than those of CH_3OH and $HCOOCH_3$. The H_2CS emission is slightly extended toward the western side of the continuum peak.

These results for OCS, CH_3OH, $HCOOCH_3$, and H_2CS show small-scale chemical differentiation in the vicinity of the protostar in Source B. A similar chemical differentiation is also seen in Source A; the distributions of CH_3OH and $HCOOCH_3$ are concentrated around the centrifugal barrier with the radius of 50 au, while the OCS and H_2CS distributions are more extended (Chapter 6).

The integrated intensity maps of the six molecular lines of the above four molecular species are shown in Figure 7.6. The intensity distributions, except for that of $HCOOCH_3$, show a ring-like structure around the protostar; the molecular line intensities are weaker toward the continuum peak position with a radius of 0.″25 (∼30 au) than the surrounding

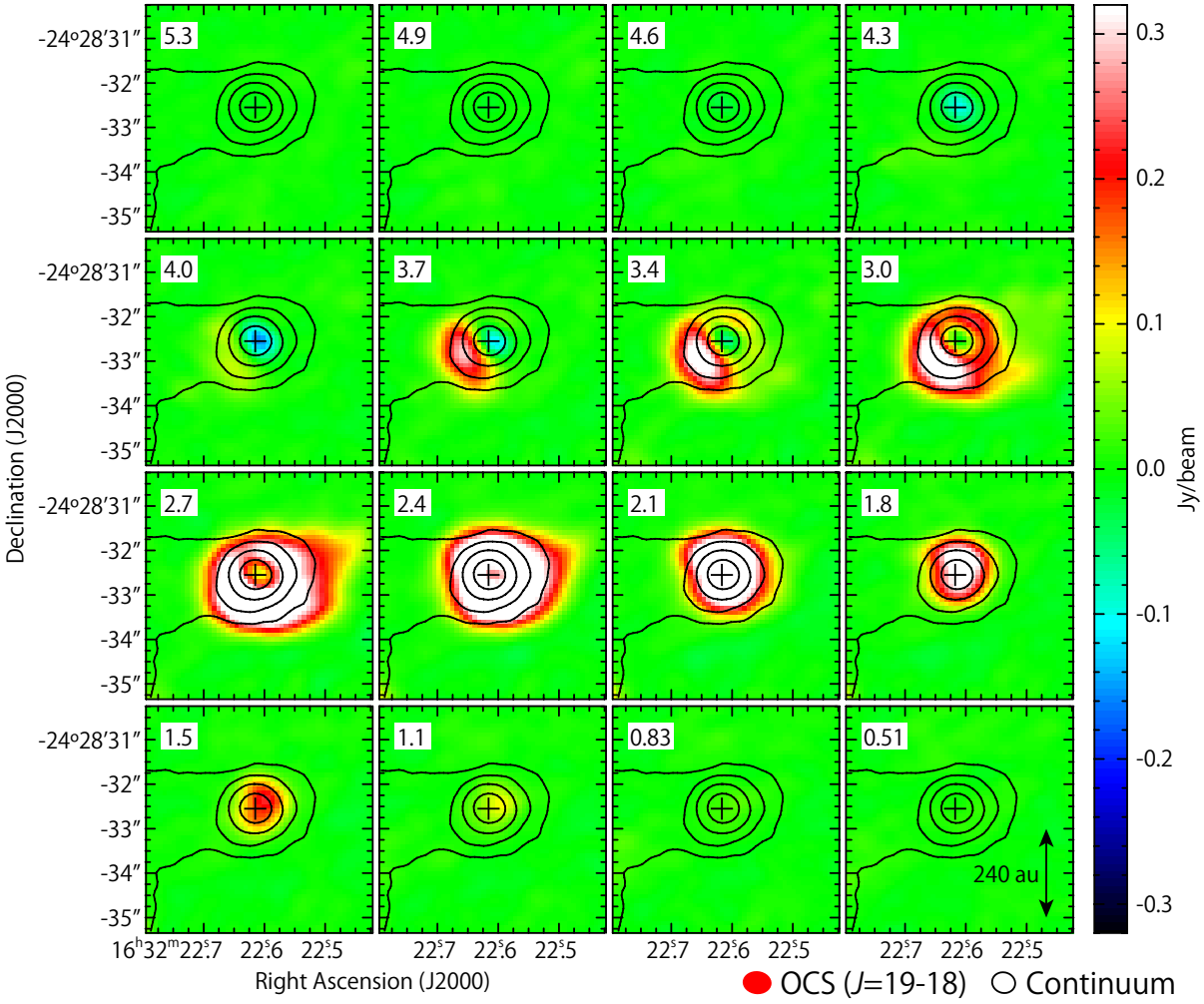

Figure 7.2: The velocity channel maps of the OCS ($J = 19 - 18$) line. The $v_{\rm LSR}$ is shown in the left-upper corner of each panel. The contours represent the continuum map, whose intensity peak position is shown by the black crosses. The contour levels are 20, 80, 320, and 1280σ, where the rms noise level is 0.3 mJy beam^{-1}.

positions. This is due to the contribution of the inverse P-Cygni profile toward the continuum peak position, as shown in the channel maps (Figures 7.2, 7.3, and 7.5).

The different sizes of the molecular distributions seen in the channel maps can also be confirmed in the integrated intensity maps. The OCS distribution is clearly extended over 1″ (∼120 au) around the protostar. The distributions of CH_3OH and $HCOOCH_3$ are concentrated around the protostar with a radius of 0.″6 (∼70 au). The H_2CS ($7_{0,7} - 6_{0,6}$) distribution is slightly more extended than the distributions of CH_3OH and $HCOOCH_3$, but is not so extended as the OCS emission. The distributions of the higher excitation lines of H_2CS ($7_{2,5} - 6_{2,4}$; $7_{4,4} - 6_{4,3}$, $7_{4,3} - 6_{4,2}$) tend to be as compact as those of the CH_3OH and $HCOOCH_3$.

The velocity widths (FWHM) of these line emissions toward Source B are as narrow as 3 km s^{-1}. They are narrower than those toward Source A, which are typically wider than 5 km s^{-1}. The narrow velocity widths likely originate from the nearly face-on

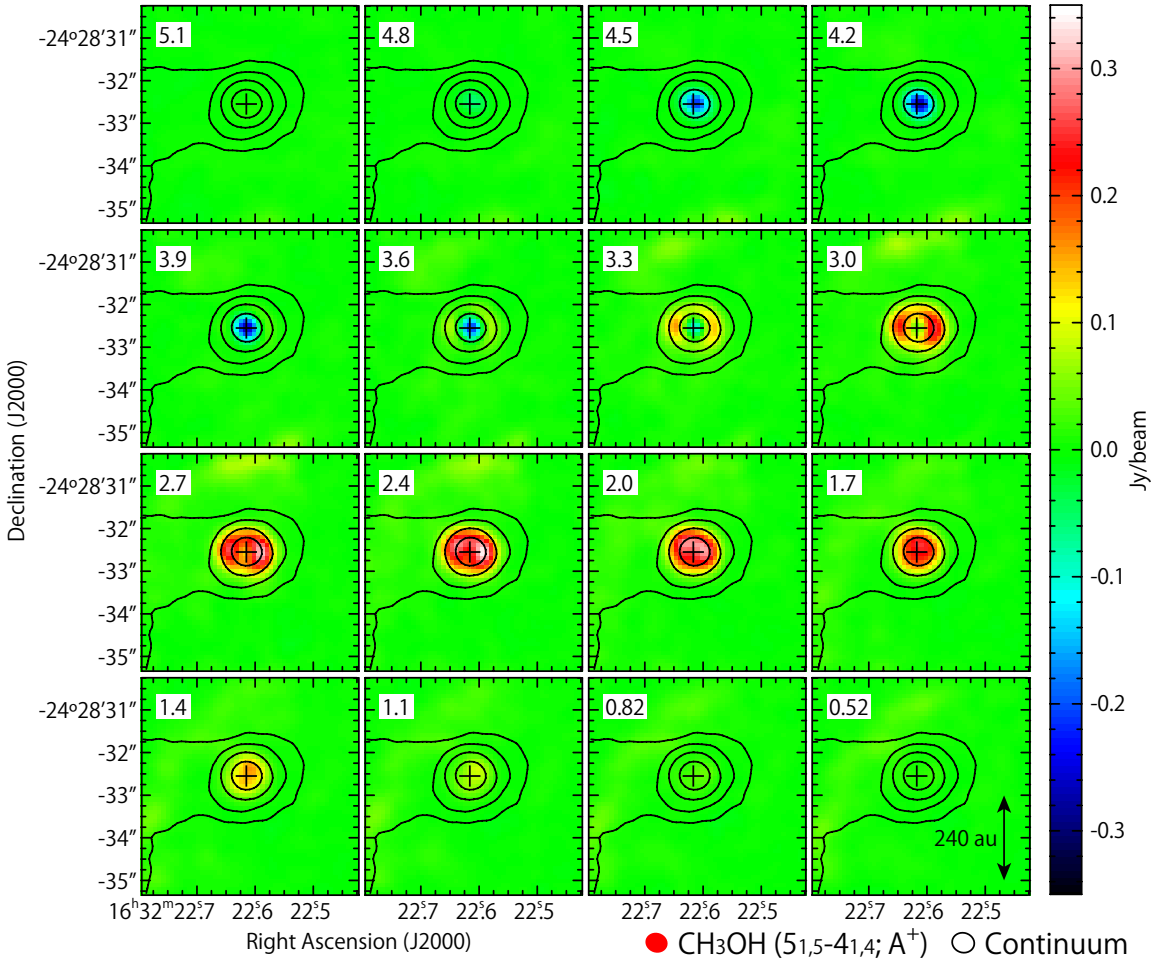

Figure 7.3: The velocity channel maps of the CH_3OH ($5_{1,5} - 4_{1,4}$; A^+) line. The v_{LSR} is shown in the left-upper corner of each panel. The contours represent the continuum map, whose intensity peak position is shown by the black crosses. The contour levels are the same as those in Figure 7.2.

geometry of the disk/envelope system of Source B. Nevertheless, we can recognize small velocity gradient in the channel maps of OCS. At the blue-shifted velocity ($v_{\rm LSR}$ ~1.5 km s^{-1}), the OCS distribution shows a slight offset from the continuum peak position toward the northwestern direction, while at the red-shifted velocity ($v_{\rm LSR}$ ~4 km s^{-1}), it tends to have a slight offset toward the southeastern direction (Figure 7.2). This trend can be confirmed in the integrated intensity maps of the high velocity-shifted components (Figure 7.7). Although the integrated intensity of the red-shifted component is affected by the absorption toward the continuum peak, the red-shifted component of the OCS line, the continuum peak position, and the blue-shifted component of the OCS line seem to be aligned on a straight line along the SE-NW direction with a position angle (P.A.) of about 110°. This velocity gradient suggests rotation motion of the disk/envelope system, slightly inclined from the face-on geometry.

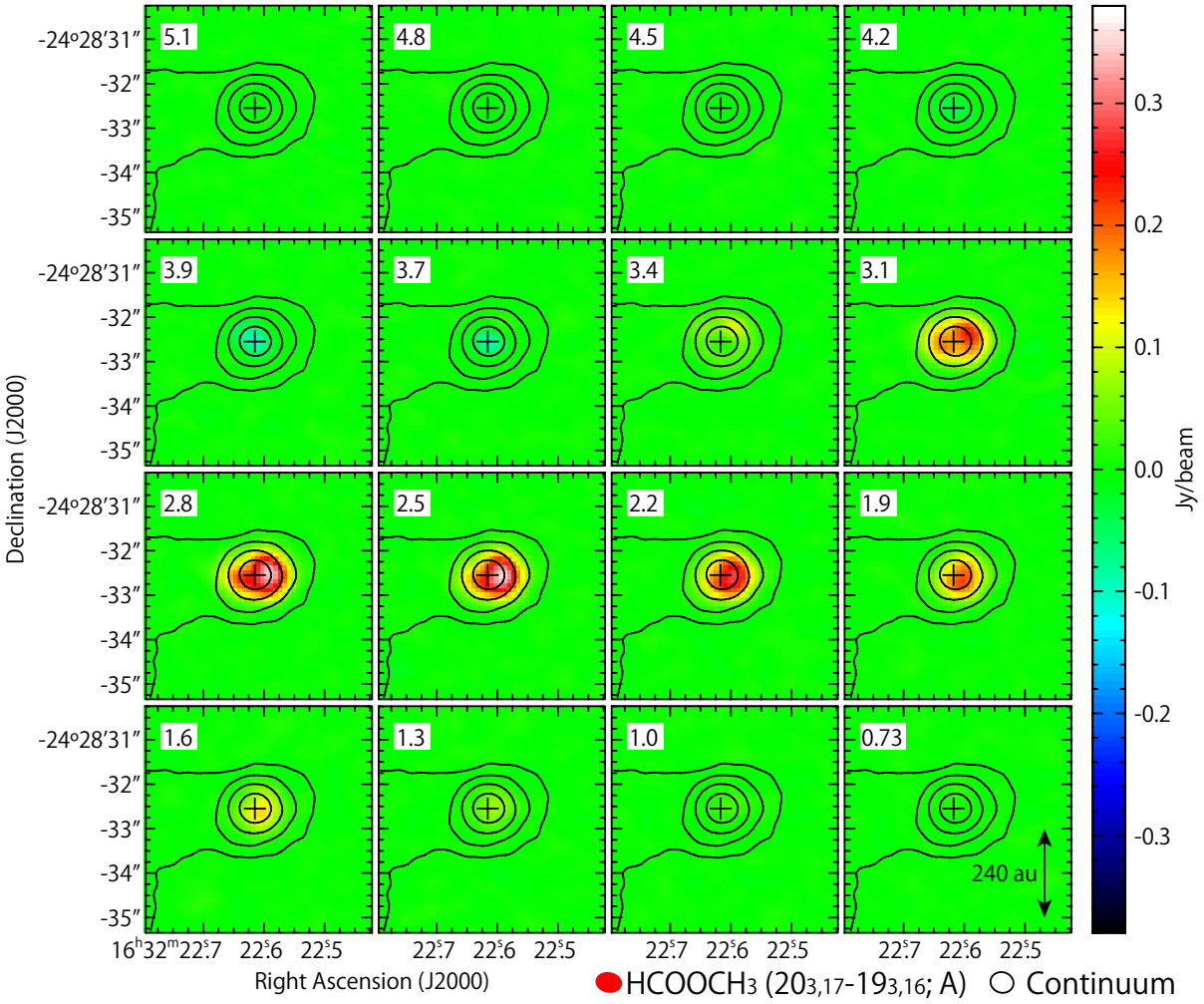

Figure 7.4: The velocity channel maps of the HCOOCH$_3$ ($20_{3,17} - 19_{3,16}$; A) line. The $v_{\rm LSR}$ is shown in the left-upper corner of each panel. The contours represent the continuum map, whose intensity peak position is shown by the black crosses. The contour levels are the same as those in Figure 7.2.

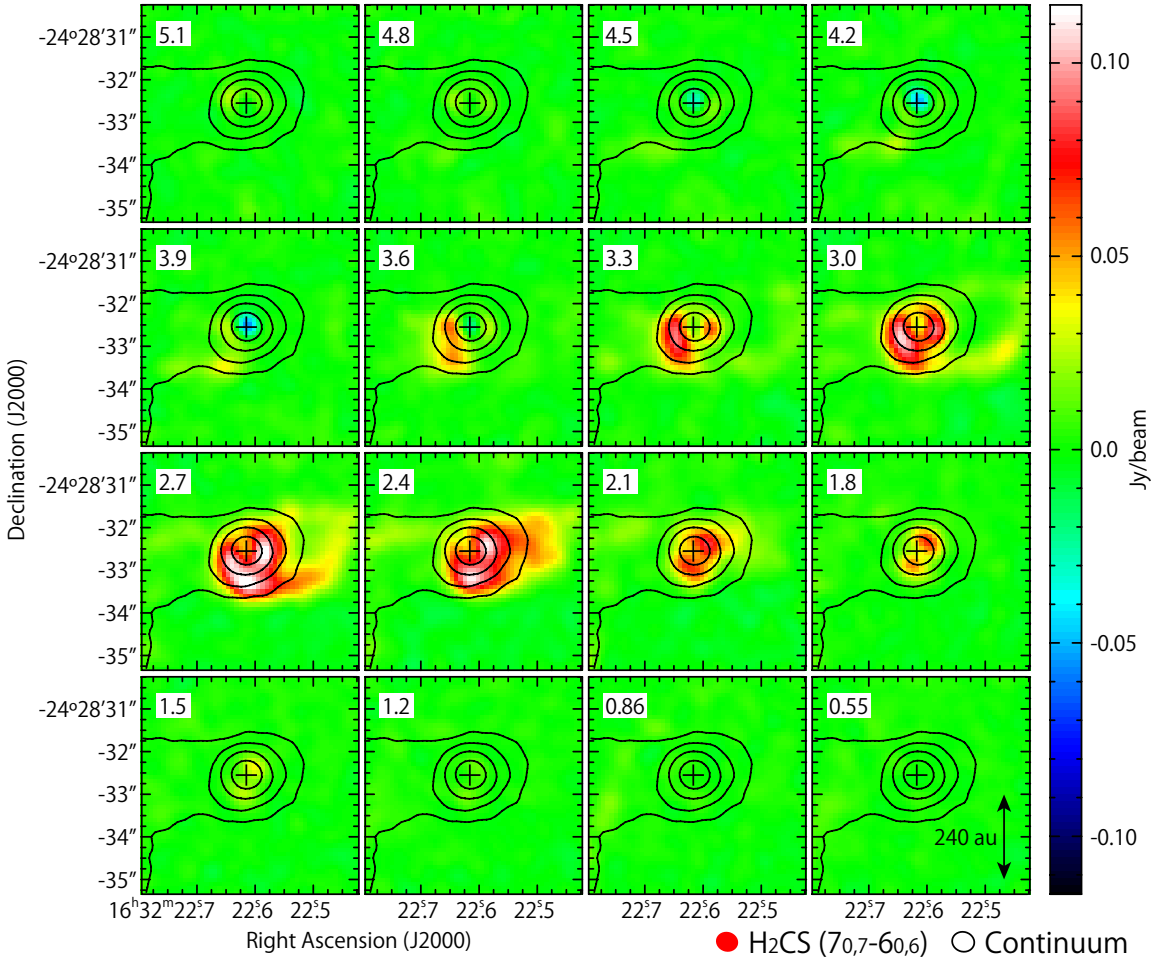

Figure 7.5: The velocity channel maps of the H_2CS ($7_{0,7} - 6_{0,6}$) line. The $v_{\rm LSR}$ is shown in the left-upper corner of each panel. The contours represent the continuum map, whose intensity peak position is shown by the black crosses. The contour levels are the same as those in Figure 7.2.

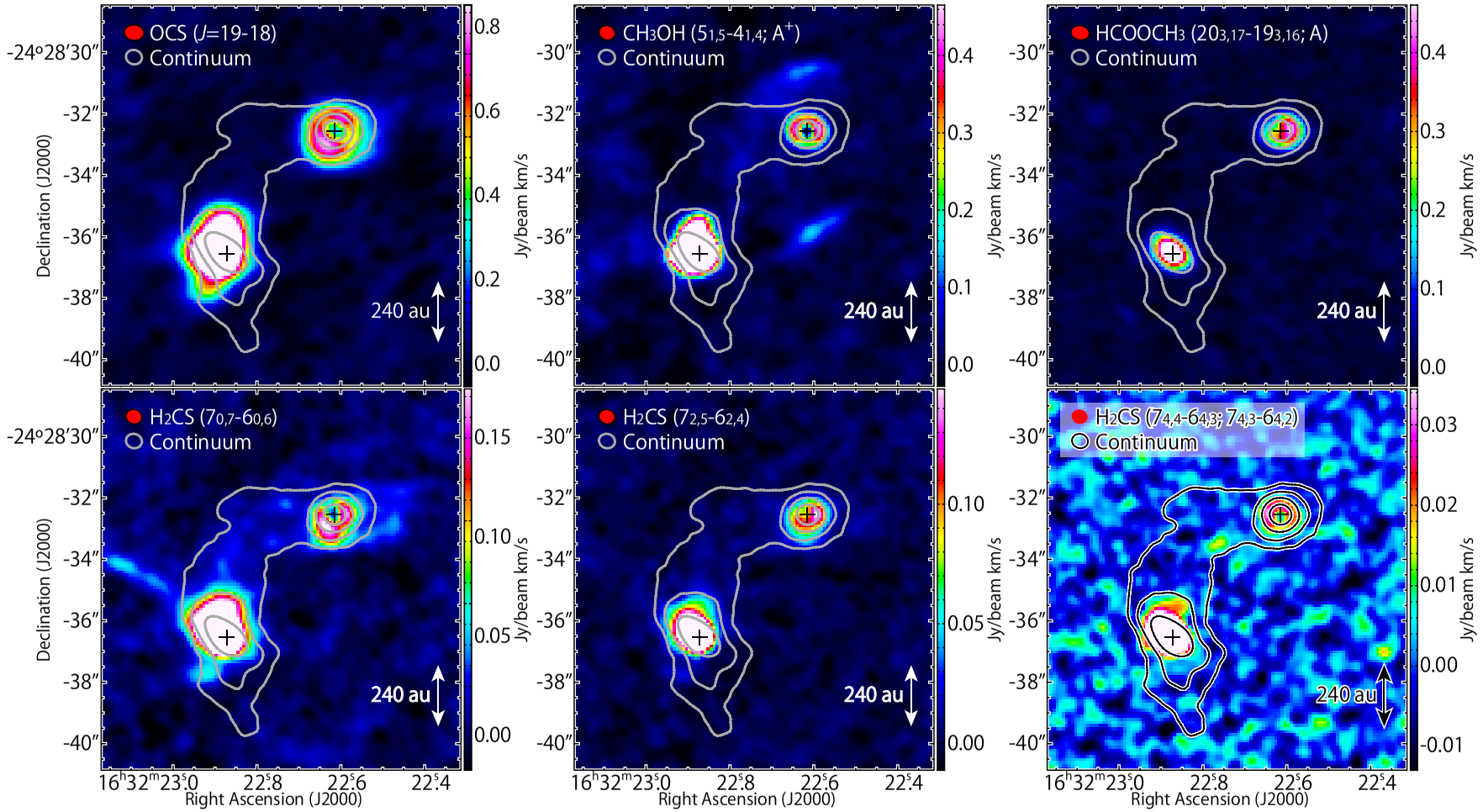

Figure 7.6: The integrated intensity maps of the OCS ($J = 19 - 18$), CH_3OH ($5_{1,5} - 4_{1,4}$; A^+), $HCOOCH_3$ ($20_{3,17} - 19_{3,16}$; A), and H_2CS ($7_{0,7} - 6_{0,6}$; $7_{2,5} - 6_{2,4}$; $7_{4,4} - 6_{4,3}$, $7_{4,3} - 6_{4,2}$) lines associated with Source B (color). The velocity-shift range for the integration is ± 2 km s^{-1}. The contours represent the continuum map, where the contour levels are the same as those in Figure 7.1. The continuum peak positions are shown by the black crosses.

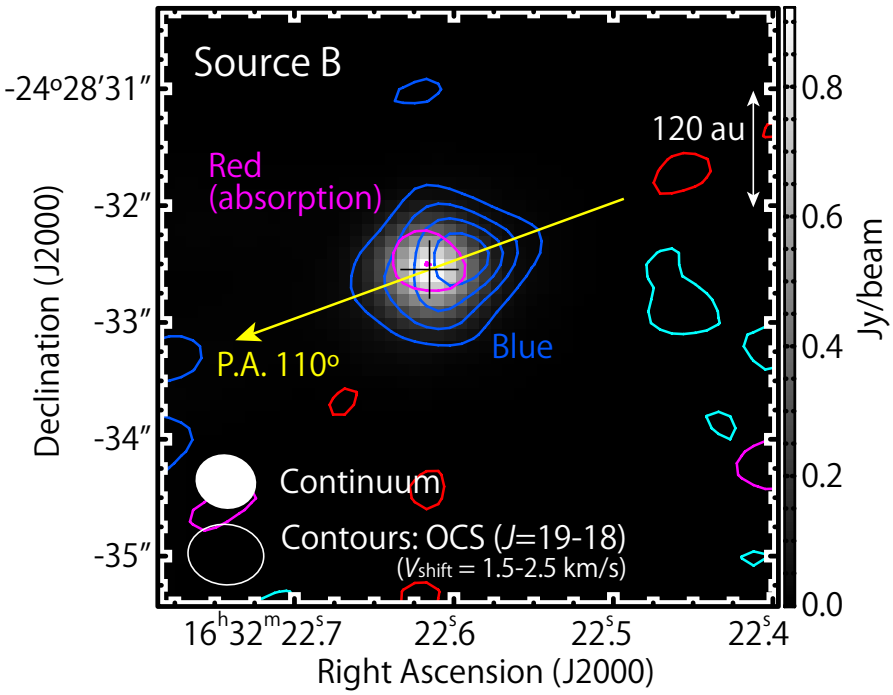

Figure 7.7: The integrated intensity maps of high velocity components of the OCS ($J = 19 - 18$; contours) line. The red and magenta contours represent the integrated intensity map of OCS with the velocity range from 4.4 to 5.4 km s^{-1}. while the blue and cyan contours with the velocity range from 0.4 to 1.4 km s^{-1}. The magenta and cyan contours represent the negative values. The contour levels are every 3σ, where the rms noise level is 5 mJy beam^{-1} km s^{-1}. The grey scale map represent the continuum map, and the intensity peak position in Source B is shown by the black cross.

7.4 Kinematic Structure

7.4.1 Observed Features

The disk/envelope system of IRAS 16293–2422 Source B is thought to have a nearly face-on geometry. Since a hint of a rotation motion can be seen (Section 7.3), the disk/envelope system is slightly inclined. Figures 7.8 to 7.11 show the position-velocity (PV) diagrams of OCS, H_2CS, CH_3OH, and $HCOOCH_3$ that allow us to investigate the velocity structure around the protostar.

In the PV diagrams, the inverse P-Cygni profile is confirmed toward the protostar. Along the P.A. of 110°, a slight velocity gradient can be seen in the OCS line (Figure 7.8), although it is heavily contaminated with the absorption feature toward the protostar position. The velocity in the northwestern side tends to be lower than that in the south-eastern side. In this diagram, the position of the intensity peak has a slight offset from the protostar position. The PV diagrams along the lines with various P.A. also show the absorption feature toward the protostar position. Moreover, the PV diagrams along the lines with the P.A. of 140°, 170°, 200°, and 230° show two intensity peaks with an offset

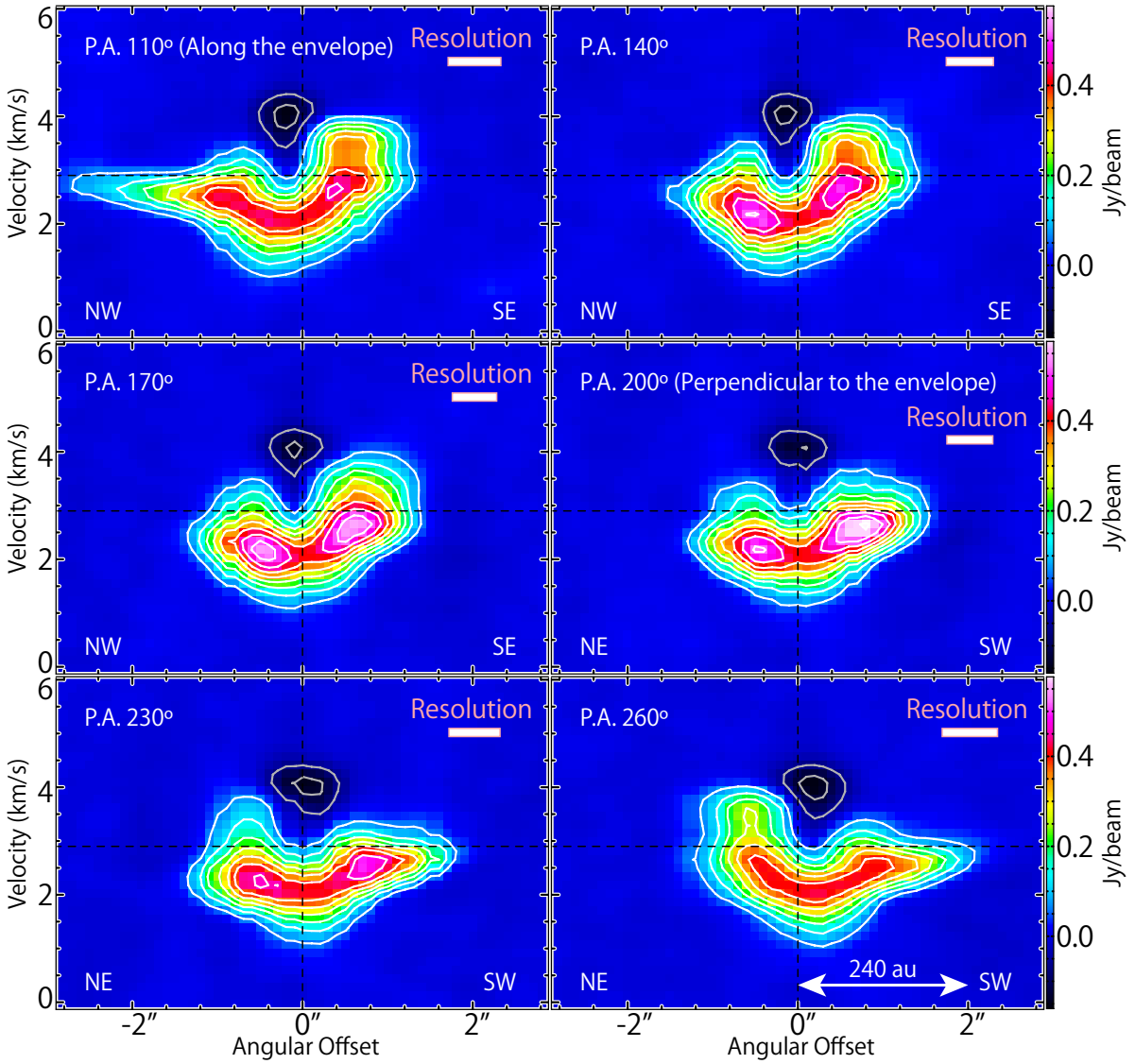

Figure 7.8: The position-velocity diagram of the OCS ($J = 19 - 18$) line. The position axes are centered at the protostar position and their position angles are every 30° from 110°. The contour levels are from -40σ and every 20σ, except for 0σ, where the rms noise level is 3.2 mJy beam^{-1}. The rectangle in each panel represent the spatial and velocity resolutions.

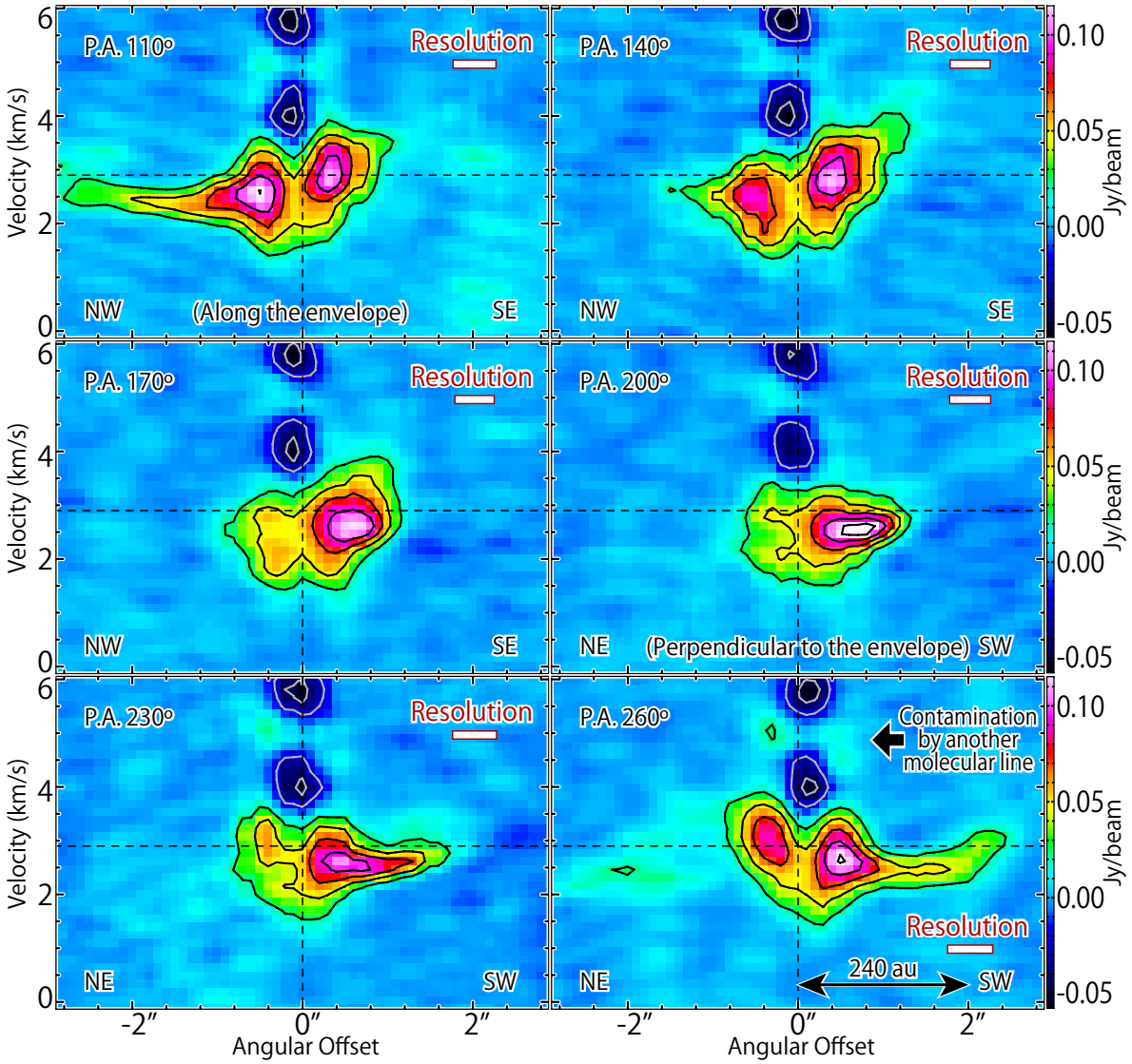

Figure 7.9: The position-velocity diagram of the H_2CS ($7_{0,7} - 6_{0,6}$) line. The position axes are the same as those in Figure 7.8. The contour levels are from -20σ and every 10σ, except for 0σ, where the rms noise level is 2.3 mJy beam^{-1}. There is a contamination by another molecular line with a velocity offset of 2 km s^{-1}.

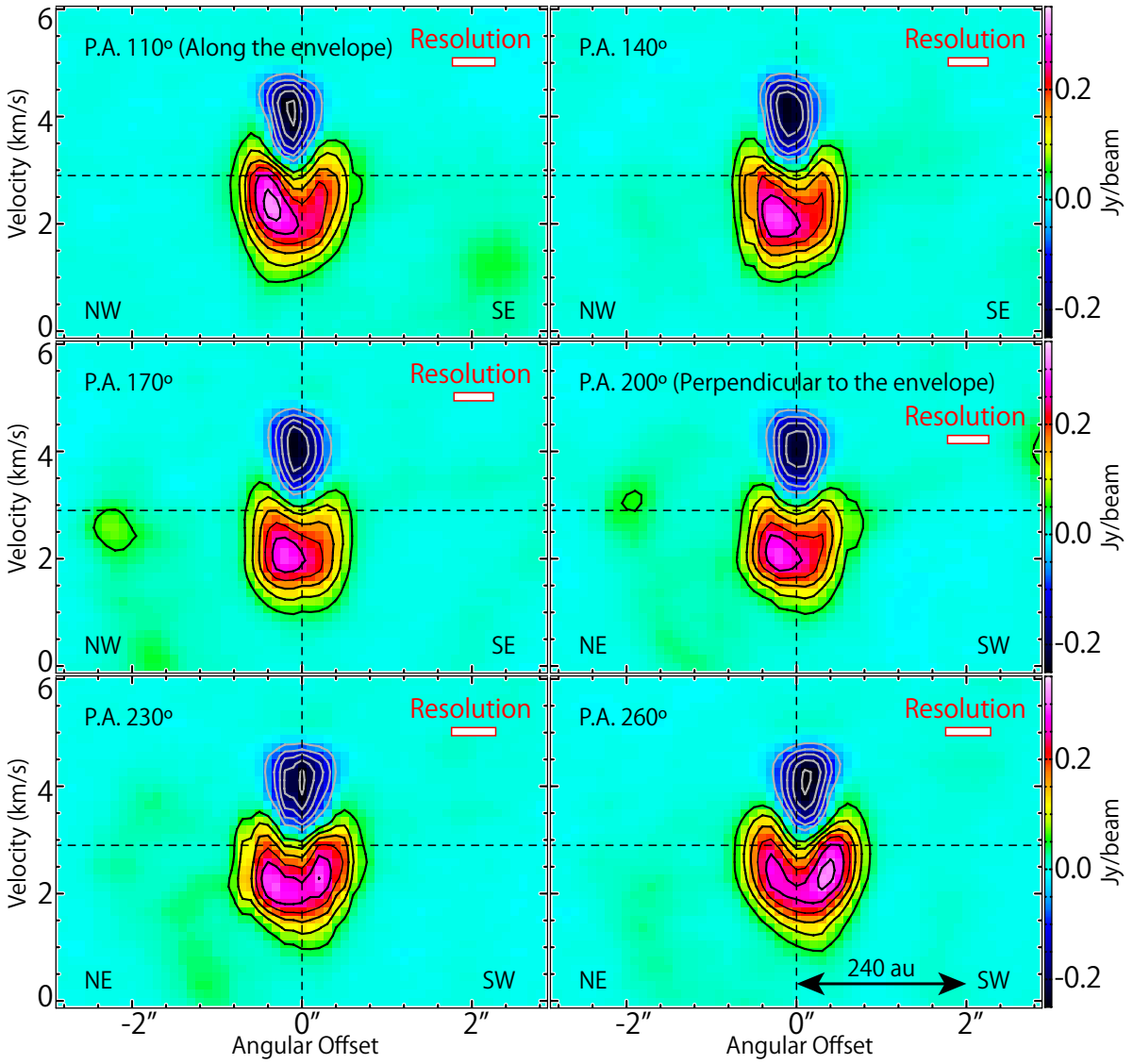

Figure 7.10: The position-velocity diagram of the CH_3OH ($5_{1,5} - 4_{1,4}$; A^+) line. The position axes are the same as those in Figure 7.8. The contour levels are from -100σ and every 20σ, except for 0σ, where the rms noise level is 2.5 mJy beam^{-1}.

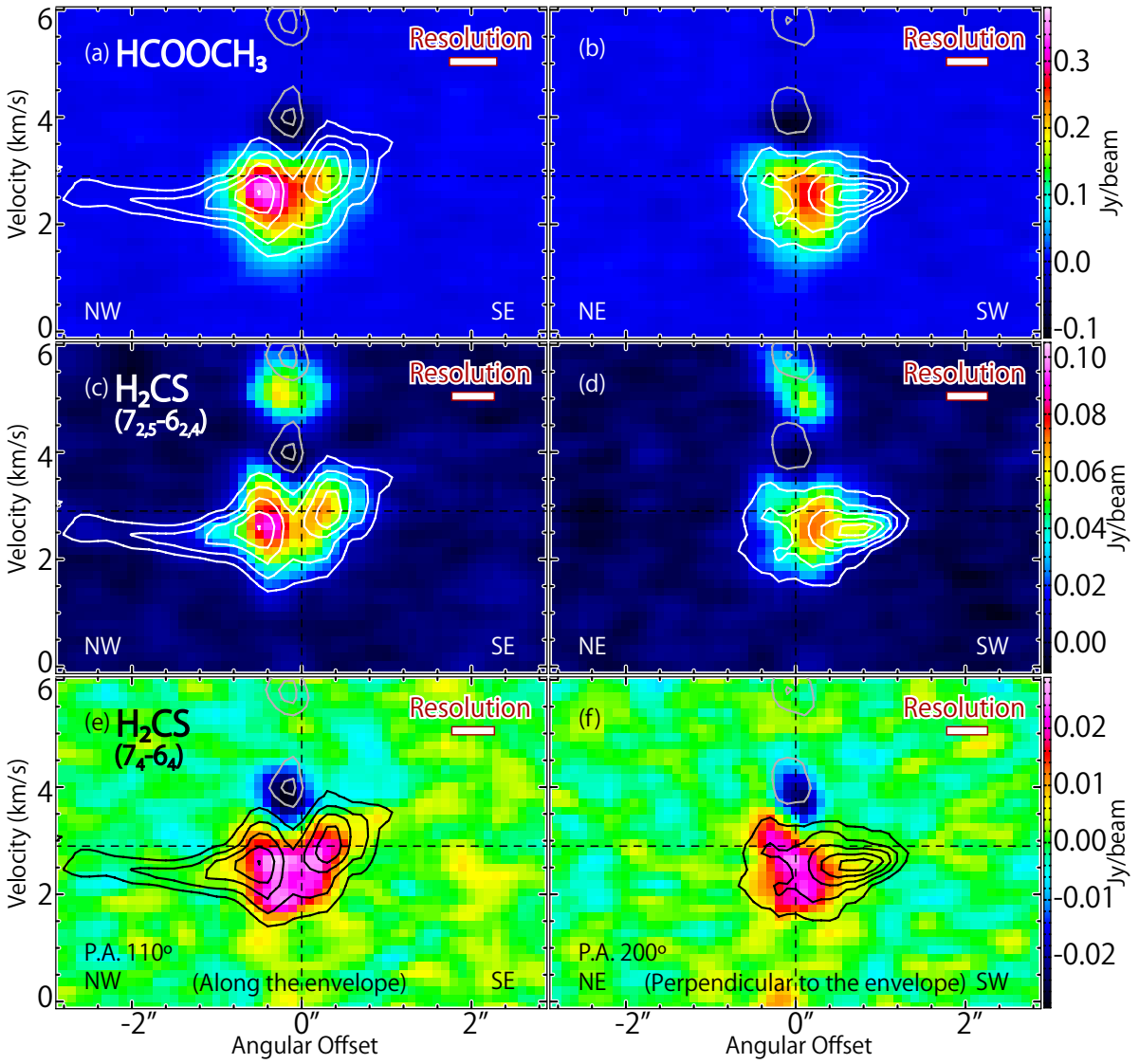

Figure 7.11: The position-velocity diagram of the $HCOOCH_3$ ($20_{3,17} - 19_{3,16}$; A) and two H_2CS ($7_{2,5} - 6_{2,4}$; $7_{4,4} - 6_{4,3}$, $7_{4,3} - 6_{4,2}$) lines. The position axes are the same as those in the panels of P.A.s of 110° and 200° in Figure 7.8. The contours in each panel represent the PV diagram of H_2CS ($7_{0,7} - 6_{0,6}$), which are as the same as those in Figure 7.9.

from the protostar position. For instance, the peak intensity ($\sim$0.6 Jy beam^{-1}) is about 1.5 times higher than the intensity toward the protostar position ($\sim$0.4 Jy beam^{-1}) in the PV diagram along the line with the P.A. of 200°.

The PV diagrams of the H_2CS ($7_{0,7} - 6_{0,6}$) line show a slight velocity gradient along the P.A. of 110° similar to the OCS case (Figure 7.9). The absorption in the red-shifted components toward the continuum peak can be confirmed. There is another absorption feature with the velocity higher than 5 km s^{-1}, which is likely to be a contamination by an unidentified line. As in the case of OCS, the H_2CS line also shows two intensity peaks in the PV diagrams except for that along the P.A. of 200°. The intensity dip toward the continuum peak position is clearer in H_2CS than in OCS. In fact, the peak intensity ($\sim$0.12 Jy beam^{-1}) is twice higher than the intensity toward the continuum peak (0.05 mJy beam^{-1}) in the PV diagram along the P.A. of 110°. The peak intensities have asymmetry in the PV diagrams; the peak intensity at the southern side of the protostar is higher than at the northern side, except for the PV diagram along the P.A. of 110°. This may be caused by the asymmetric distribution of the gas.

On the other hand, the PV diagrams of the CH_3OH line do not show such a velocity gradient (Figure 7.10). In the PV diagram along the P.A. of 110°, the size of the distribution is as compact as 1.″5. The maximum velocity-shift from the systemic velocity is 2 km s^{-1}, which is comparable to that for OCS. The absorption in the red-shifted component is confirmed toward the continuum peak position. The size of the absorption is less than 1″, which is slightly smaller than that of the size of the distribution of the CH_3OH emission. Although all the six PV diagrams of CH_3OH show some asymmetry with respect to the continuum peak position, they are essentially similar to one another in the sizes of the absorption and the distribution of the emission. This asymmetry in the intensities seems to be anti-correlated to that seen in the H_2CS line for the PV diagrams along the P.A. of $(140 - 200)$°. The PV diagrams of the $HCOOCH_3$ line is shown in Figure 7.11. As well as the CH_3OH case, they show a compact distribution without a clear velocity gradient.

7.4.2 Comparison of Molecular Distribution with the Source A Case

Since the rotation motion around Source B is marginally revealed in the OCS and H_2CS lines, we investigate its kinematic structure in more detail. As for Source A, we successfully explained the kinematic structure of the infalling-rotating envelope at a 100 au scale by a ballistic model (Chapter 6). Hence, we take the advantage of this knowledge in the analysis of the Source B data.

In Source A, OCS traces the infalling-rotating envelope, while the COMs highlight the centrifugal barrier, as mentioned in Section 7.1. This is exactly the case in Source B. Hence, the physical structure of the gas around Source B can be explored in a similar way by using the chemical differentiation. By assuming that the OCS line traces the infalling-rotating envelope, the velocity gradient shown in Figure 7.8 can be interpreted as a combination of the infall and rotation motions in the envelope. Since CH_3OH and $HCOOCH_3$ seem to be evaporated from dust grains inside the centrifugal barrier in Source A, their distributions in Source B would be comparable to the size of the centrifugal barrier.

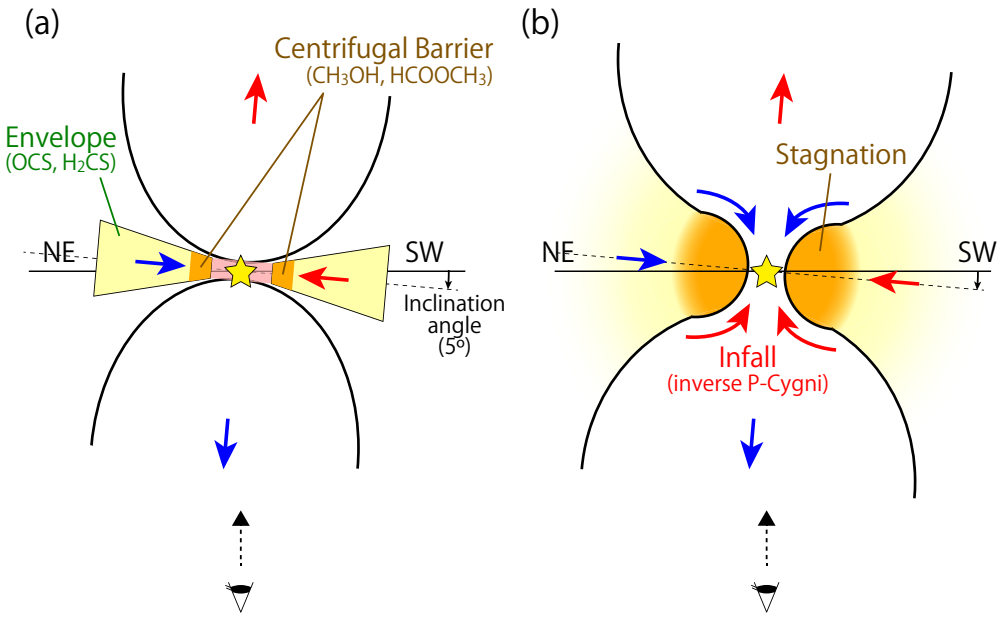

Figure 7.12: The schematic illustration of the disk/envelope system in Source B. The disk/envelope system has a thin structure in panel (a), while it has an infalling gas around the protostar in panel (b).

On the other hand, the distribution of H_2CS in Source B inside the centrifugal barrier seems different from that in Source A. In Source A, high velocity-shift components tracing the disk component inside the centrifugal barrier are observed. In contrast, such components are not apparently seen in Source B. The PV diagram shows a double-peaked structure having an intensity dip at the protostar position (Figure 7.9). This dip structure does not originate from the high dust opacity, because the emission, particularly at the blue-shifted one, is indeed observed toward the protostar position in other molecular lines: the PV diagrams of the CH_3OH, $HCOOCH_3$, and H_2CS ($7_{2,5} - 6_{2,4}$; $7_{4,4} - 6_{4,3}$, $7_{4,3} - 6_{4,2}$) lines show a compact emission in Figures 7.10 and 7.11. The dip is not due to the absorption by the foreground gas either, because the dip is seen at the velocity shift of as high as -1 km s^{-1} from the systemic velocity. Hence, the intensity dip means that H_2CS would be deficient in the closest vicinity of the protostar. The two intensity peaks in the PV diagram just correspond to the position within which CH_3OH and $HCOOCH_3$ appear (Figures 7.11a, b). Considering that CH_3OH and $HCOOCH_3$ are concentrated around the centrifugal barrier in Source A, we think that these two intensity peaks of H_2CS would represent the centrifugal barrier. Although the double-peaked structure is not clearly seen in OCS, the intensity peak of OCS seems to be shifted from the protostar position and almost coincide one of the intensity peaks of H_2CS. Hence, it is most likely that the two intensity peaks in the PV diagram of H_2CS represent the positions of the centrifugal barrier in Source B.

Figure 7.12(a) shows a schematic illustration of the above configuration of the disk/envelope system. The structure of the outflow further supports the configuration, as described later (Section 7.6).

7.5 Modelling

7.5.1 Infalling-Rotating Envelope Model

We investigate the velocity gradient observed in the OCS ($J = 19 - 18$) and H_2CS ($7_{0,7} - 6_{0,6}$) lines, using the infalling-rotating envelope model (Chapter 3). Since the velocity gradient is clearly seen as the double-peaked structure in the PV diagram of H_2CS ($7_{0,7} - 6_{0,6}$) along the disk/envelope direction (P.A. 110°), as mentioned above, we evaluate the physical parameters by comparing the model with this PV diagram.

Figures 7.13 and 7.14 show examples of the infalling-rotating envelope models superposed on the PV diagram of the H_2CS ($7_{0,7} - 6_{0,6}$) line along the disk/envelope direction and the direction perpendicular to it, respectively. We here assumed the systemic velocity ($v_{\rm sys}$) of 2.9 km s^{-1}. In the infalling-rotating envelope model, the main physical parameters are the protostellar mass (M) and the radius of the centrifugal barrier ($r_{\rm CB}$). To see how the PV diagrams of the infalling-rotating envelope model depend on these parameters, we conducted the simulations for various sets of the parameters. We assumed an envelope with a constant thickness of 50 au and the outer radius of 300 au with the inclination angle of 5° (0° for a face-on configuration). We also assumed the intrinsic line width of 0.5 km s^{-1}. The model image is convolved with the synthesized beam. In this model, we assume the $r^{-1.5}$ density profile and the constant abundance of molecules for simplicity, where the effects of the optical depth, excitation, and the temperature gradient are not taken into account. The peak intensity of the OCS line is ~ 0.6 Jy beam^{-1}, which corresponds to the brightness temperature of 40 K. Thus the OCS line seems to be optically thin with the comparison with the gas kinetic temperature derived below (see Section 7.7 and Table 7.2). In these observations, the other molecular lines are weaker than the OCS line, and hence, they can also be assumed to be optically thin.

Needless to say, the absorption feature in the red-shifted component toward the protostar cannot be explained by this simple infalling-rotating envelope model, because it does not consider any radiative transfer effect (Chapter 3). However, the velocity gradient along the disk/envelope direction seems to be reasonably explained by the rotating motion in the infalling-rotating envelope model (Figure 7.13). Especially, the models with $r_{\rm CB}$ of 40 au well reproduce the observation except for the absorption feature. The model is not very sensitive to the protostellar mass (M), and hence, it is weakly constrained around 0.4 $M_\odot$ within a factor of 2 assuming the inclination angle of the disk/envelope system is 5°. On the other hand, the model result strongly depends on $r_{\rm CB}$. In the models with $r_{\rm CB}$ of 60 au, the distance between the two intensity peaks is larger than that observed, because the positions of the two peaks in the model correspond to those of the centrifugal barrier. In the models with $r_{\rm CB}$ of 20 au, the emission seems to be concentrated toward the protostar. This is because that the emission at the centrifugal barrier is not resolved with the synthesized beam for H_2CS ($7_{0,7} - 6_{0,6}$) in the model, and thus the observed double-peaked structure cannot be reproduced. Hence, the $r_{\rm CB}$ can be evaluated to be $(30 - 50)$ au. In the PV diagram along the line perpendicular to the disk/envelope direction (P.A. 200°; Figure 7.14), the models with $r_{\rm CB}$ of 40 au show a better agreement with the observation than those with $r_{\rm CB}$ of 20 or 60 au, although the observation shows asymmetry.

The comparison between the infalling-rotating envelope model and the OCS ($J =$

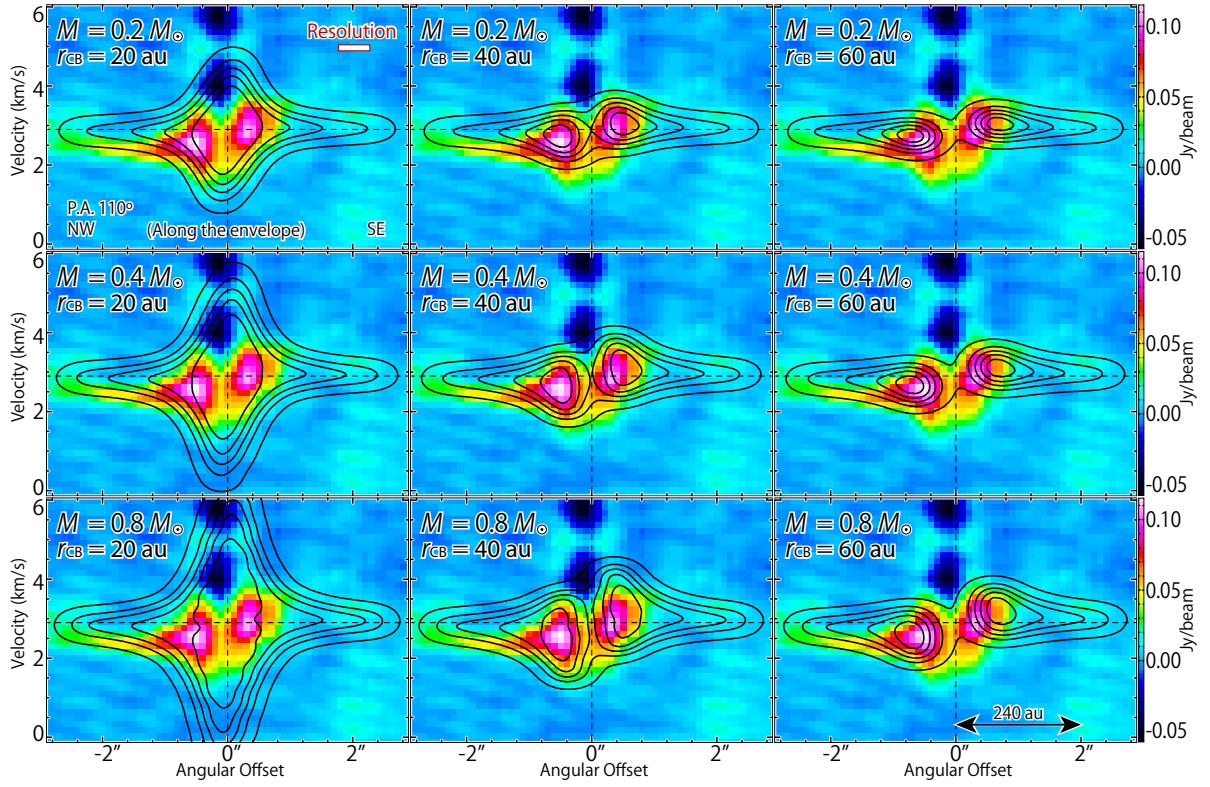

Figure 7.13: The position-velocity diagram of the H_2CS ($7_{0,7} - 6_{0,6}$; color) along the disk/envelope direction (P.A. 110°), where the color maps are the same as the panel (a) in Figure 7.9. The black contours represent the results of infalling-rotating envelope models. The physical parameters for the models are: M = 0.2, 0.4, and 0.8 $M_\odot$; $r_{\rm CB}$ = 20, 40, and 60 au; and i = 5°. The contour levels are every 20% from 5% of each peak intensity.

$19-18$) and CH_3OH ($5_{1,5} - 4_{1,4}$; A^+) lines are also shown in Figure 7.15. Here the model with M of 0.4 $M_\odot$ and $r_{\rm CB}$ of 40 au is employed as a representative. Strictly speaking, the OCS ($J = 19-18$) line does not show a clear double-peaked feature unlike the H_2CS ($7_{0,7}-6_{0,6}$). Nevertheless, the model seems to explain the basic feature of the PV diagram of the OCS ($J = 19-18$) line, except for the absorption feature. On the other hand, the kinematic structure traced by the CH_3OH ($5_{1,5}-4_{1,4}$; A^+) line cannot be explained by the infalling-rotating envelope model obtained from the above analysis. The emitting region of the CH_3OH ($5_{1,5}-4_{1,4}$; A^+) line seems to be concentrated around the centrifugal barrier and/or inside it. This is consistent with the IRAS 16293–2422 Source A case, where the CH_3OH ($11_{0,11} - 10_{1,10}$; A^+) line mainly highlights the centrifugal barrier and/or inside it (Chapter 6).

7.5.2 Origin of the inverse P-Cygni Profile

Although the basic feature of the kinematic structure traced by the molecular lines is reasonably explained by the infalling-rotating envelope model (Figure 7.15) as discussed above, there remains an important problem: *how can we interpret the inverse P-Cygni*

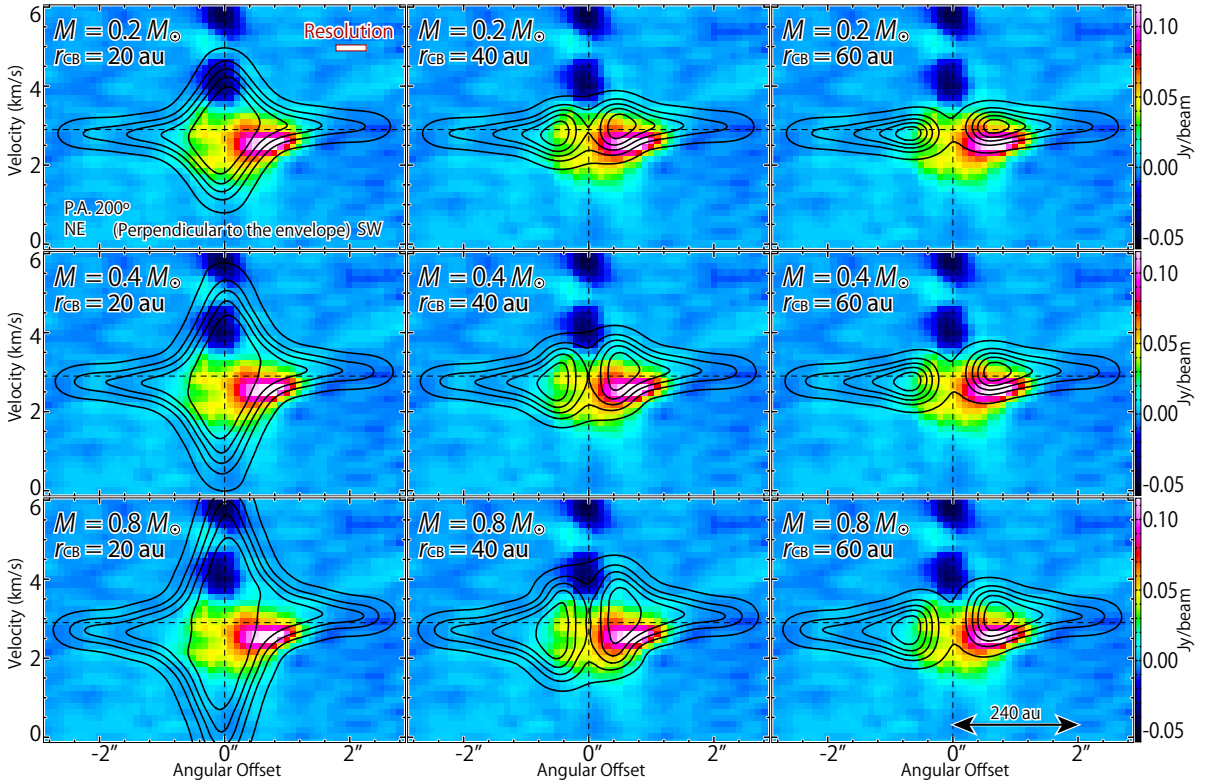

Figure 7.14: The position-velocity diagram of the H_2CS ($7_{0,7} - 6_{0,6}$; color) line along the line perpendicular to the disk/envelope direction (P.A. 200°), where the color maps are the same as the panel (d) in Figure 7.9. The black contours represent the results of infalling-rotating envelope models. The physical parameters for the models are: $M = 0.2$, 0.4, and 0.8 $M_\odot$; $r_{CB} = 20$, 40, and 60 au; and $i = 5°$. The contour levels are every 20% from 5% of each peak intensity.

profile? The inverse P-Cygni profile means an infall motion along the line of sight toward the protostar. Since the disk/envelope system is nearly face-on, the outflow motion also exists along the line of sight as shown in Section 7.6. This situation, namely the coexistence of the infall motion and the outflow motion along the line-of-sight in the vicinity of the protostar, is hardly possible, as far as we consider the thin disk structure such as Figure 7.12(a). At least, a thick disk/envelope structure would be necessary so as that substantial amount of the infalling gas exists near the protostar. In fact, such an infall component perpendicular to the mid-plane near the launching point of the outflow is seen in the simulation of the outflow (Machida & Hosokawa, 2013). Even in this case, there remains the following difficulty. Since the velocity shift of the absorption feature from the systemic velocity is at most 2 km s^{-1} (Figure 7.10), the infalling gas at this velocity-shift has to be located at 180 au, assuming the free-fall with the protostellar mass of 0.4 $M_\odot$. This distance is larger than the size of the COM emission (∼50 au) around the protostar, which accompanies the inverse P-Cygni profile.

Recently, an important hint to solve this problem is found in the other protostellar source L1527. On the basis of the high-resolution molecular line observation with ALMA,

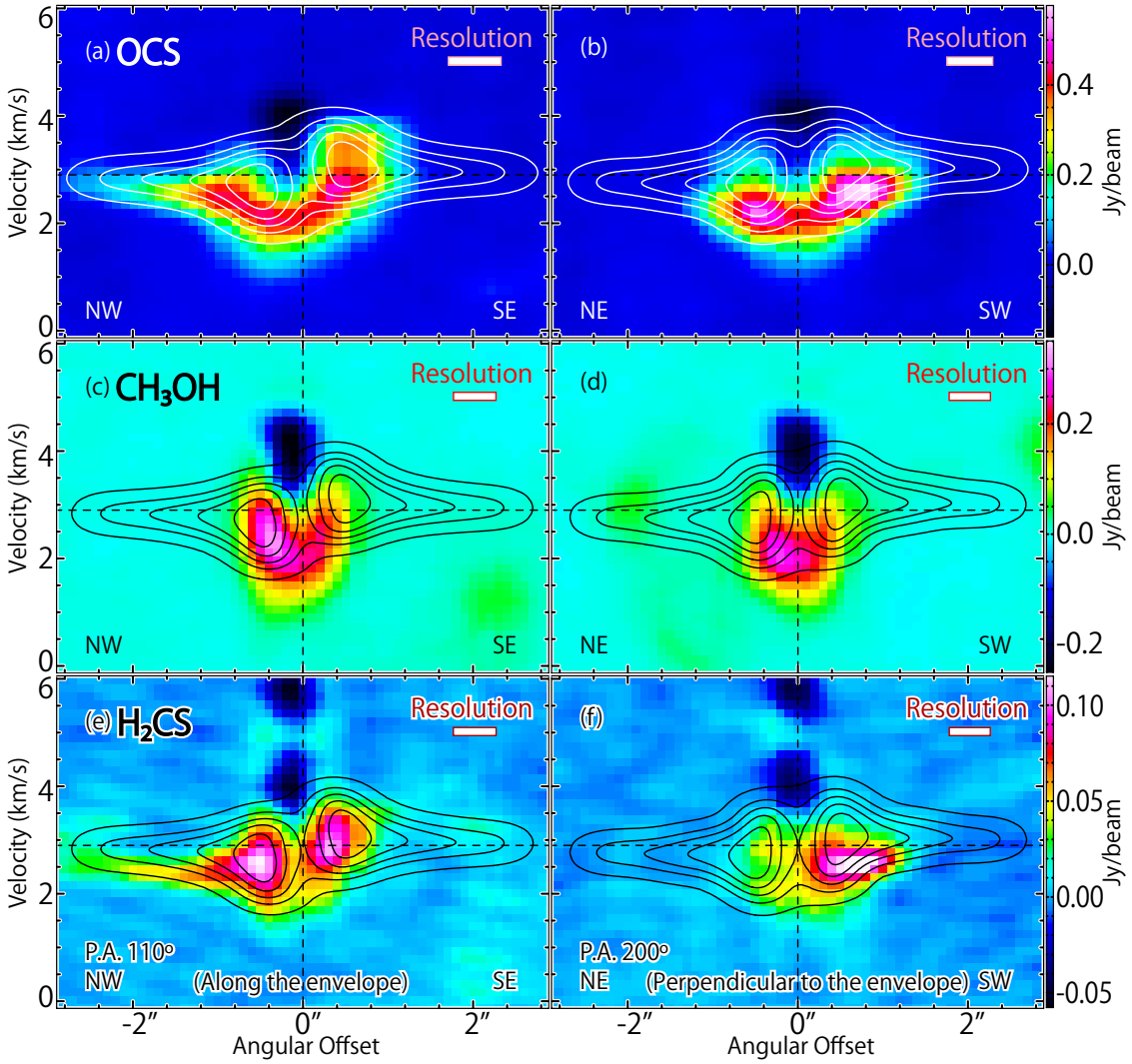

Figure 7.15: The position-velocity diagrams of the OCS ($J = 19 - 18$; a, b), CH_3OH ($5_{1,5} - 4_{1,4}$; A^+; c, d), and H_2CS ($7_{0,7} - 6_{0,6}$; e, f) lines along the disk/envelope direction (P.A. 200°) and the direction perpendicular to it (P.A. 110°), where the color maps are the same as the panels (a, d) in Figures 7.8–7.9. The black and white contours represent the results of the infalling-rotating envelope model, where the physical parameters are $M = 0.4\ M_\odot$, $r_{CB} = 40$ au, and $i = 5°$. The contour levels are every 20% from 5% of each peak intensity.

Sakai et al. (2017) reported that the thickness of the disk/envelope system is broadened at the centrifugal barrier and inward of it due to the stagnation of the accreting gas. A part of the stagnant gas at the centrifugal barrier once moves toward the out-of-plane direction, and falls toward the protostar, if its angular momentum is extracted by some mechanisms (i.e. disk winds and/or low-velocity outflows). Such an infalling gas may cause the inverse P-Cygni profile. This situation is illustrated in Figure 7.12(b). It has previously been thought that the infalling gas in the ambient envelope causes the inverse P-Cygni profile (Pineda et al., 2012). However, the velocity shift of the absorbing gas (∼2

km s^{-1}) seems to be too high for the ambient component.

Hence, we incorporated the free-fall motion in the vicinity of the protostar in the model. We approximated the gas distribution around the protostar as a spherical clump with a radius of the centrifugal barrier for simplicity. Figure 7.16 shows the results of the free-fall from the centrifugal barrier to the protostar. This model simulates the situation that the gas is once stagnated at the distance of 40 au ($r_{\rm CB}$) from the protostar to make a spherical clump, and then it falls to the protostar by the gravity without the initial speed. This very simplified picture can explain the kinematic structure at a 40 au scale around the protostar, including the inverse P-Cygni profile. In this case, the gas having the infall velocity of 2 km s^{-1} (the absorption gas for the inverse P-Cygni profile) is located at 33 au from the protostar. However, it should be stressed that this hypothetical model is just simplified one representing the above hypothetical physical picture. We need to resolve the structure of the vicinity of the protostar to verify its validity.

7.6 Outflow

We also analyzed the SiO ($J = 6 - 5$) data. Figure 7.17 shows the integrated intensity maps of the high velocity-shift components traced by SiO. This molecule is often employed as a shock tracer. Both the blue-shifted and red-shifted components show a shell-like feature surrounding the continuum peak, which are spatially overlapped with each other even at a 300 au scale. This feature implies a nearly pole-on geometry of the outflow. Namely, we are looking at the outflow cavities as a shell like feature. Nevertheless, the blue-shifted components are slightly extended toward the northeastern direction from the continuum peak. On the other hand, the red-shifted emission is stronger than the blue-shifted one in the southwestern side of the continuum peak. Hence, the outflow axis might be inclined slightly, as shown in Figure 7.12. Thus, the blue-shifted outflow lobe seems to be overlapped on the protostar in the line of sight.

In the OCS, CH_3OH, $HCOOCH_3$, and H_2CS lines, the inverse P-Cygni profile is seen toward the protostar. As discussed in Section 7.5.2, the picture shown in Figure 7.12(b) allows the coexistence of the blue-shifted outflow lobe and the infalling gas toward the protostar. In this case, the outflow responsible for the above SiO distribution is not launched directly from the protostar, but could be from the inner part of the disk/envelope system possibly around the centrifugal barrier. In fact, there is a hint for such a situation in the kinematic structure of the SiO emission. The SiO emission shows the bipolar outflow lobes along the P.A. of 200° (Figure 7.18). The blue-shifted and red-shifted lobes are seen in both the northeastern and southwestern sides of the continuum peak, which is consistent with the configuration shown in Figure 7.12(b). If the outflow is accelerated as it propagates away from the protostar (Chapter 3; e.g. Lee et al., 2000), the systemic velocity component likely corresponds to the outflow component at its launching point. At the systemic velocity, the SiO emission is seen at the position with an offset of $\sim 0\farcs5$ from the continuum peak, but not toward the protostar. This implies that the launching point of the outflow has an offset from the protostar (Figure 7.12b). Moreover, the SiO emission at the systemic velocity seems to appear close to the intensity peak of the OCS and H_2CS emission. This feature may suggest that the launching point of the outflow could be around the centrifugal barrier traced by OCS and H_2CS.

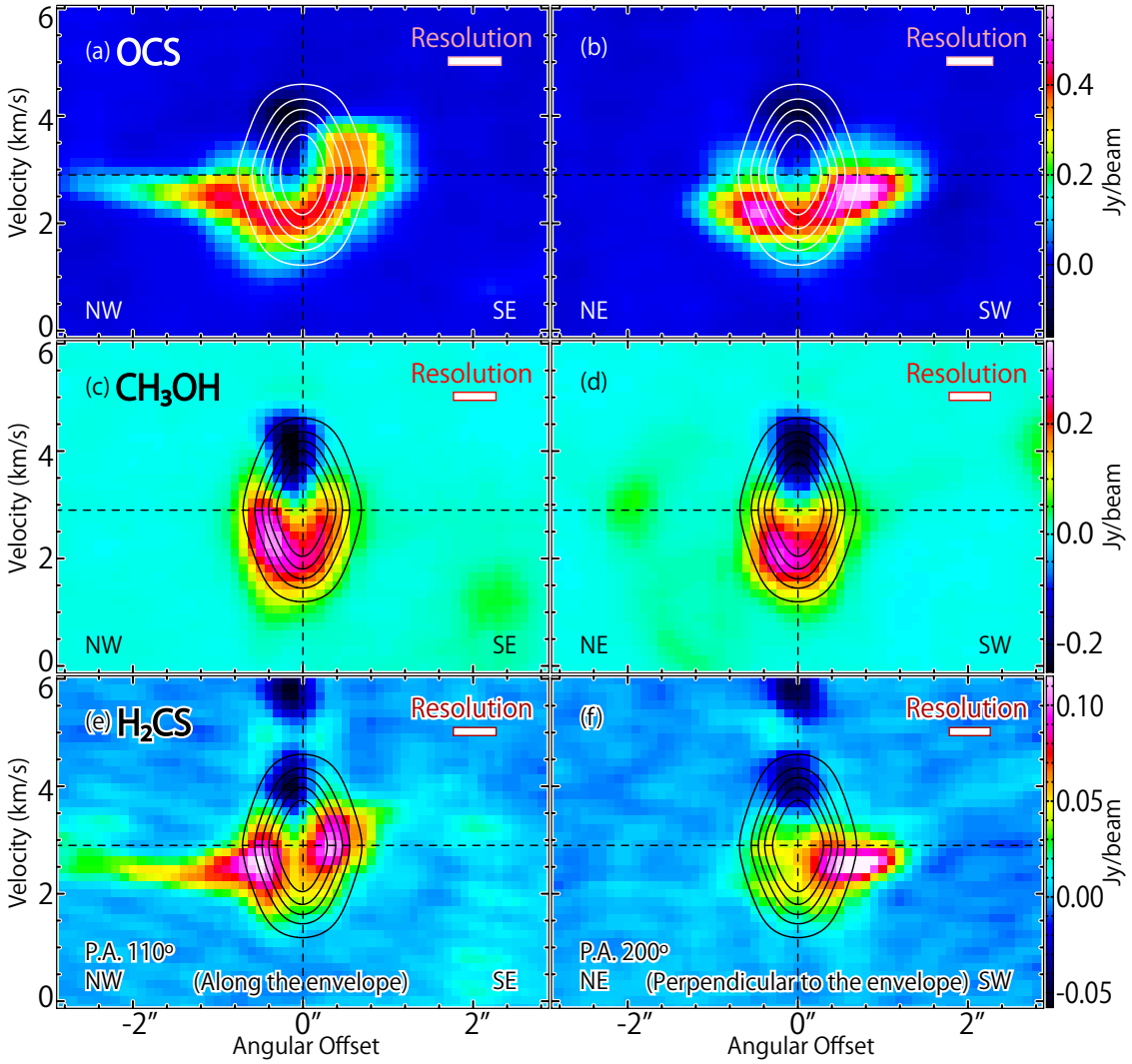

Figure 7.16: The position-velocity diagrams of the OCS ($J = 19 - 18$; a, b), CH_3OH ($5_{1,5} - 4_{1,4}$; A^+; c, d), and H_2CS ($7_{0,7} - 6_{0,6}$; e, f) lines along the disk/envelope direction (P.A. 200°) and the direction perpendicular to it (P.A. 110°), where the color maps are the same as those in Figures 7.15. The black and white contours represent the results of the model for the infall motion from the centrifugal barrier. The physical parameters are $M = 0.4\ M_\odot$, $r_{CB} = 40$ au, and $i = 5°$. The molecular line emission is assumed to be in the region with the distance from the protostar of $(35 - 40)$ au. The contour levels are every 20% from 5% of each peak intensity.

Large-scale outflows blowing out from this binary system have extensively been studied (e.g. Mizuno et al., 1990; Hirano et al., 2001). Their directions are different from that found in this chapter. This contradiction may be due to the complexity of the binary system. The dynamical timescale of the outflow lobes at a larger scale $(10^4 - 10^5)$ au is estimated to be $(10^4 - 10^5)$ years (Mizuno et al., 1990; Hirano et al., 2001). On the other hand, it is reported that Source A and Source B are rotating around each other with the period of $\sim 2 \times 10^4$ years (Bottinelli et al., 2004a). Thus the directions of the two

outflow can be modulated in a complex way. Hence, the small-scale outflow structure in the vicinity of a protostar has to be studied in order to explore the relation between the outflow and the disk/envelope system.

7.7 Gas Kinetic Temperature

In Chapter 6, we evaluated the gas kinetic temperature from the intensities of the two lines ($7_{0,7} - 6_{0,6}$; $7_{2,5} - 6_{2,4}$) of H_2CS in IRAS 16293–2422 Source A. The lines of H_2CS with different K_a can be used as a good tracer of the gas kinetic temperature. As a result, we found that the gas kinetic temperature around Source A once rises from the infalling-rotating envelope to the centrifugal barrier, and then drops in the disk component inside the centrifugal barrier.

Here, we also evaluate the gas kinetic temperature around Source B from the H_2CS line intensities. Figure 7.11 show the PV diagrams of the high excitation lines of H_2CS ($7_{2,5} - 6_{2,4}$; $7_{4,4} - 6_{4,3}$, $7_{4,3} - 6_{4,2}$) on which those of the H_2CS line ($7_{0,7} - 6_{0,6}$) is superposed. The distributions of the higher excitation lines of H_2CS seem to have more concentrated to the protostar position than the H_2CS line ($7_{0,7} - 6_{0,6}$). Thus the intensity ratio of a higher excitation line relative to a lower excitation line becomes higher toward the protostar. This

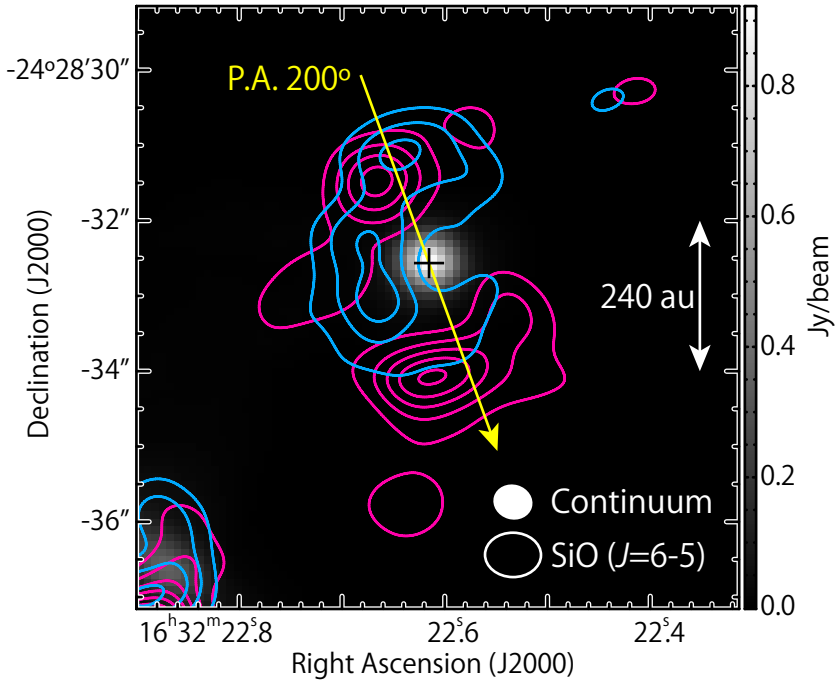

Figure 7.17: The integrated intensity maps of high velocity components of the SiO ($J = 6 - 5$) line. The magenta contours represent the integrated intensity map of SiO with the velocity range from 3.8 to 5.8 km s^{-1}, while the cyan contours with the velocity range from -0.2 to 1.7 km s^{-1}. The contour levels are every 10σ, where the rms noise level is 20 mJy beam^{-1} km s^{-1}. The grey scale map represent the continuum map, and the intensity peak position in Source B is shown by the black cross.

implies that the gas kinetic temperature is raised as approaching to the protostar position. The gas kinetic temperature is evaluated by using the non-LTE code RADEX (van der Tak et al., 2007), as shown in Table 7.2. Temperatures are calculated for the positions with the radii of 0, 40, and 80 au from the continuum peak along the disk/envelope direction (P.A. 110°). For this calculation, we prepare the integrated intensity maps of the three H_2CS lines ($7_{0,7}-6_{0,6}$; $7_{2,5}-6_{2,4}$; 7_4-6_4) with the velocity width of 1 km s^{-1}. The velocity-shift range for the continuum peak position is from -2 to -1 km s^{-1} in order to extract the high velocity-shift component excluding the absorption effect. The velocity-shift range for the

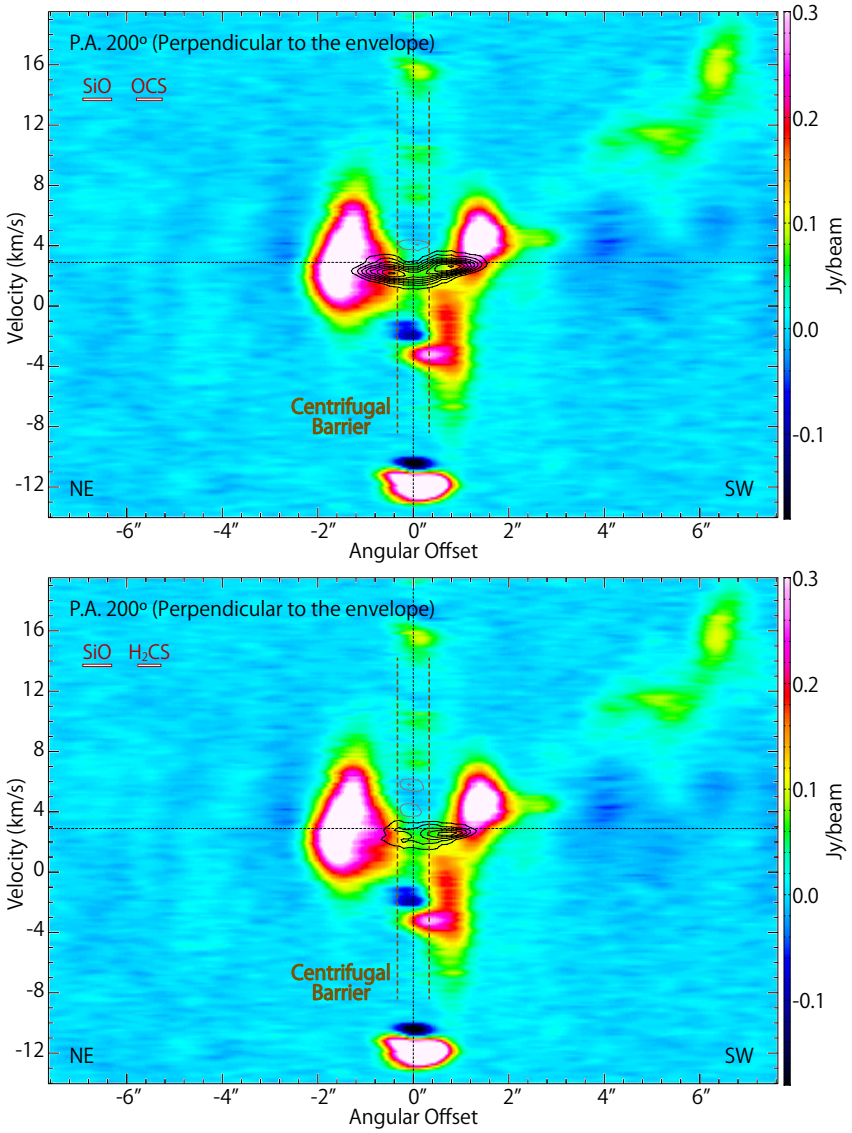

Figure 7.18: The position-velocity diagram of the SiO ($J = 6-5$; color), OCS ($J = 19-18$; black contours in the top panel), and H_2CS ($7_{0,7}-6_{0,6}$; black contours in the bottom panel) along the line centered at the continuum peak with the P.A. of 200°. The absorption features at the velocity of 2 and 10 km s^{-1} in the color map seem to be the contamination by other molecular lines.

Table 7.2: Gas Kinetic Temperature Derived from the H_2CS Lines[a]

Transitions	Offset from the protostar[b]				
	−80 au[c]	−40 au[d]	0 au[e]	+40 au[f]	+80 au[c]
$7_{2,5} - 6_{2,4}$ / $7_{0,7} - 6_{0,6}$[g]	$120 - 171$	> 306	> 167	> 228	$85 - 109$
$7_4 - 6_4$/ $7_{2,5} - 6_{2,4}$[h]	$55 - 118$	$85 - 118$	$73 - 400$	< 85	$63 - 120$

[a] In K. The gas kinetic temperatures are derived by using the RADEX code (van der Tak et al., 2007). The assumed ranges for the H_2 density and the column density of H_2CS are from 10^7 to 3×10^9 cm^{-3} and from 10^{13} to 10^{15} cm^{-2}, respectively. The quoted errors represent 1σ. σ is estimated from the statistical error and does not contain the calibration error, because it will be almost canceled in the intensity ratios.

[b] The positive and negative values represent the offset from the continuum peak position toward the southeastern and northwestern direction, respectively.

[c–f] The velocity-shift range for the integrated intensities is (c) from −0.5 to +0.5, (d) from −1.0 to 0.0, (e) from −2.0 to −1.0, and (f) from 0.0 to +1.0 km s^{-1}.

[g] The gas kinetic temperature derived from the intensity ratio of the H_2CS ($7_{0,7} - 6_{0,6}$; $7_{2,5} - 6_{2,4}$) lines.

[h] The gas kinetic temperature derived from the intensity ratio of the H_2CS ($7_{2,5} - 6_{2,4}$; $7_{4,4} - 6_{4,3}$, $7_{4,3} - 6_{4,2}$) lines. Note that the $7_{4,4} - 6_{4,3}$ and $7_{4,3} - 6_{4,2}$ lines have the same rest frequency.

positions at the radius of 40 au from the continuum peak position is from ±1 to 0 km s^{-1}, which corresponds to the rotating velocity at the centrifugal barrier. The velocity-shift range for the positions with the distance of 80 au from the continuum peak position is from −0.5 to +0.5 km s^{-1}. The above velocity-ranges and the positions are shown in the PV diagram of H_2CS ($7_{0,7} - 6_{0,6}$) (Figure 7.19). It should be noted that the H_2CS ($7_{0,7} - 6_{0,6}$) line may possibly be optically thick toward the continuum peak. Hence, the intensity of the H_2CS ($7_{0,7} - 6_{0,6}$) line may be attenuated, which would overestimate the gas kinetic temperature. Although no systematic dependence on the radius from the protostar can be found, the gas kinetic temperature is generally as high as ∼100 K within ∼80 au. If the dust temperature is similarly as high as the derived gas kinetic temperature, COMs can be evaporated from the dust surfaces, which will result in the hot corino chemistry of IRAS 16293–2422 Source B. We do not find any particular enhancement of the gas kinetic temperature at the centrifugal barrier in Source B in contrast to the Source A case, probably because of the limited resolution of the observations. Higher angular resolution observations are required for further investigation.

7.8 Abundance of $HCOOCH_3$ Relative to CH_3OH

The column densities of CH_3OH and $HCOOCH_3$ are derived for the five regions along the disk/envelope direction, where the gas kinetic temperature is derived with H_2CS lines. The velocity width for integration is the same as the H_2CS case for the evaluation of the gas kinetic temperature (Section 7.7). Hence, the derived column densities do not

represent the total ones, and hence, they do not have quantitative meanings by themselves. However, the abundance ratios $HCOOCH_3/CH_3OH$ are meaningful for comparison from position to position. In IRAS 16293–2422 Source A, we found that the abundance ratio shows a systematic increase as approaching to the protostar position (Chapter 6). This may suggest that the chemical composition is processed to enhance $HCOOCH_3$ in the vicinity of the protostar in Source A.

The derived abundance ratios in Source B are listed in Table 7.3. Our analysis relies on the LTE assumption. In addition, the rotation temperatures are assumed to be 50, 100, and 150 K, based on the range of the gas kinetic temperature derived from the above H_2CS analysis (Section 7.7). If the CH_3OH line is assumed to be optically thin, the $HCOOCH_3/CH_3OH$ abundance ratio is found to be almost equal to or higher than unity. Such a high ratio is consistent with previous reports (e.g. Bottinelli et al., 2007). Optical depths of the CH_3OH and $HCOOCH_3$ lines are estimated to be 0.61 and 0.48, respectively, for the region offset from the protostellar position by -40 au, where their integrated intensities take their highest values, for the rotation temperature of 50 K. Thus the optically thin assumptions is appropriate. In contrast to the Source A case (Chapter 6), the ratio seems lower in the central part than those in the outer part. The ratios are generally lower than those of the disk component in Source A ($8.7 \sim 8.9$).

7.9 Summary of This Chapter

We analyzed the OCS, CH_3OH, $HCOOCH_3$, H_2CS, and SiO data observed toward IRAS 16293–2422 Source B at a sub-arcsecond resolution with ALMA. Major findings are as follows:

(1) The chemical differentiation observed for the above molecules are similar to that found in Source A (Chapter 6); OCS and H_2CS have more extended distributions than CH_3OH and $HCOOCH_3$.

(2) Although the disk/envelope system of Source B has a nearly face-on configuration, a marginal rotation feature is observed in the extended component of the H_2CS and OCS lines. It is reasonably interpreted in terms of the infalling-rotating envelope model assuming the ballistic motion. On the other hand, the CH_3OH and $HCOOCH_3$ lines do not show a rotation motion.

(3) The bipolar outflow lobes near the protostar are detected by SiO, where the blue and red lobes are largely overlapped. This suggests a nearly pole-on geometry with a slight inclination.

(4) The molecular lines, except for $HCOOCH_3$, show absorption features toward the protostar. It is interpreted as the inverse P-Cygni profile by the infalling gas along the line of sight, as previously reported. The infall motion is reasonably explained by the free-fall motion of the gas stagnated around the centrifugal barrier.

(5) The coexistence of the outflow and the infall motion toward the protostar may suggest that the current launching point of the outflow responsible for the SiO emission has an offset from the protostar.

(6) The gas kinetic temperature is evaluated by using the H_2CS lines. The gas kinetic temperature is found to be as high as ∼100 K, which is consistent to the hot corino character of IRAS 16293–2422 Source B.

(7) The abundance ratio of $HCOOCH_3$ relative to CH_3OH is evaluated around the protostar. The abundance ratio is higher than unity but is slightly lower than the Source A case.

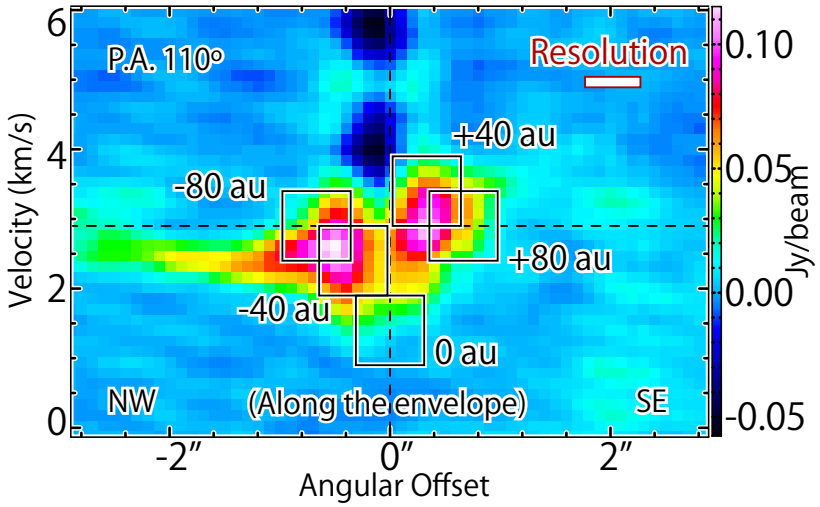

Figure 7.19: The position-velocity diagram of the H_2CS ($7_{0,7} - 6_{0,6}$) line along the disk/envelope direction (P.A. 110°). The vertical edges of the black rectangles represent the velocity ranges which are integrated to derive the gas kinetic temperature in Section 7.7. The horizontal edges of them are centered at the positions at the distance of 0, ±40, and ±80 au from the continuum peak position along the disk/envelope direction (P.A. 110°), where the gas kinetic temperature is derived. The lengths of the horizontal edges of them correspond to the spatial resolution for the H_2CS ($7_{0,7} - 6_{0,6}$) line.

Table 7.3: Abundance of $HCOOCH_3$ Relative to CH_3OH[a]

	Offset from the protostar[b]				
T_{rot}[c]	−80 au[d]	−40 au[e]	0 au[f]	+40 au[g]	+80 au[d]
50 K	5.2 ± 0.5	3.2 ± 0.1	2.0 ± 0.2	5.3 ± 1.2	2.7 ± 0.3
100 K	2.5 ± 0.2	1.54 ± 0.06	0.98 ± 0.09	2.5 ± 0.6	1.3 ± 0.2
150 K	2.1 ± 0.2	1.29 ± 0.05	0.82 ± 0.08	2.1 ± 0.5	1.1 ± 0.1

[a] The quoted errors represent 3σ, where σ is derived from the statistical error. The velocity ranges from 0.9 km s^{-1} to 2.9 km s^{-1}.

[b] The positive and negative values represent the offset from the continuum peak position toward the southeastern and northwestern direction, respectively.

[c] Assumed rotational temperature.

[d–g] The velocity-shift range for the integrated intensities is (d) from −0.5 to +0.5, (e) from −1.0 to 0.0, (f) from −2.0 to −1.0, and (g) from 0.0 to +1.0 km s^{-1}.

Chapter 8

L483

The Class 0 protostar, L483, has been observed in various molecular lines in the 1.2 mm band at a sub-arcsecond resolution with ALMA. An infalling-rotating envelope is traced by the CS line, while a very compact component with a broad velocity width is observed for the CS, SO, HNCO, NH_2CHO, and $HCOOCH_3$ lines. Although this source is regarded as the warm carbon-chain chemistry (WCCC) candidate source at a 1000 au scale, complex organic molecules characteristic of hot corinos such as NH_2CHO and $HCOOCH_3$ are detected in the vicinity of the protostar. Thus, both hot corino chemistry and WCCC are seen in L483. Although such a mixed chemical character source has been recognized as an intermediate source in previous single-dish observations, we here report the first spatially-resolved detection. A kinematic structure of the infalling-rotating envelope is roughly explained by a simple ballistic model with the protostellar mass of $0.1 - 0.2\ M_\odot$ and the radius of the centrifugal barrier (a half of the centrifugal radius) of $30 - 200$ au, with the assumption of the inclination angle of 80° (0° for a face-on configuration). The broad line emission observed in the above molecules most likely comes from the disk component inside the centrifugal barrier. Thus, a drastic chemical change is seen around the centrifugal barrier. The CS line also traces the outflow cavity wall in L483. Its kinematic structure is explained by a parabolic outflow model.

8.1 Introduction

So far, we demonstrated that the infalling-rotating envelope and its centrifugal barrier will exist in low-mass protostellar sources regardless of their chemical characteristics. However, the chemical change occurring across the centrifugal barrier was confirmed with different molecular species depending on the chemical composition of the source. In the previous chapters, we dealt with sources with peculiar chemical compositions; WCCC and hot corino sources. They show the exclusive chemical compositions with each other. Thus more general understandings of the chemical change requires such chemical diagnostics in other sources with different chemical characteristics. We here confirm an intermediate chemical composition of L483, and investigate its kinematic structure.

Chemical composition in the vicinity of the protostar is of fundamental importance, because it will define interstellar chemical heritage to protoplanetary disks. However, a few sources, including three WCCC sources (L1527, IRAS 15398–3359, TMC-1A; Chapters 4,

This chapter has been published in Oya et al., 2017, ApJ, 837, 174

5; Sakai et al., 2014a,b, 2016) and four hot corinos (IRAS 16293–2422 Source A, Source B, IRAS 2A, B335; Chapters 6, 7; Maury et al., 2014; Imai et al., 2016), have been studied so far for chemical characterization at a 100 au scale. Hence, observations of other protostellar sources including the sources with intermediate chemical compositions are still awaited. In this study, we focus on the well-studied Class 0 protostar in L483.

The L483 dark cloud is located in the Aquila Rift ($d = 200$ pc; Jørgensen et al., 2002; Rice et al., 2006), which harbors the Class 0 protostar IRAS 18148–0440 (Fuller et al., 1995; Chapman et al., 2013). Its bolometric luminosity is 13 $L_{\odot}$ (Shirley et al., 2000). We here adopt the systemic velocity of 5.5 km s^{-1} for this source based on previous single-dish observations (Hirota et al., 2009). In this source, the C_4H abundance is relatively high, and it is regarded as a possible candidate for the WCCC source (Sakai et al., 2009a; Hirota et al., 2009, 2010; Sakai & Yamamoto, 2013). Recent detection of the novel carbon-chain radical HCCO further supports the carbon-chain-molecule rich nature of this source (Agúndez et al., 2015). The outflow of L483 has extensively been studied (Fuller et al., 1995; Hatchell et al., 1999; Park et al., 2000; Tafalla et al., 2000; Jørgensen, 2004; Takakuwa et al., 2007a; Leung et al., 2016). It is extended along the east-west axis, where the eastern and western components are red-shifted and blue-shifted, respectively. The position angle of the outflow axis is reported to be 95° by Park et al. (2000) based on the HCO^+ ($J = 1 - 0$) observation and 105° by Chapman et al. (2013) based on the shocked H_2 emission reported by Fuller et al. (1995). The inclination angle of the outflow axis is reported to be ∼50° with respect to the plane of the sky (0° for a face-on configuration) (Fuller et al., 1995). Along the line perpendicular to the outflow, the northern part is blue-shifted, while the southern part is red-shifted, according to the CS ($J = 2 - 1$, $7 - 6$) and HCN ($J = 4 - 3$) observations (Jørgensen, 2004; Takakuwa et al., 2007a). This suggests a rotating motion of the envelope. Chapman et al. (2013) reported the position angle of a pseudo-disk to be 36° based on their *Spitzer* 4.5 μm observation.

In these previous studies, the disk/envelope system is not well resolved, and little is known about a chemical composition in the closest vicinity of the protostar. In the present study, we investigate the physical and chemical structures around the protostar at a 100 au scale with ALMA.

8.2 Observation

The ALMA observations of L483 were carried out in the Cycle 2 operation on 12 June 2014. Spectral lines of CCH, CS, SO, HNCO, t-HCOOH, CH_3CHO, NH_2CHO, $HCOOCH_3$, $(CH_3)_2O$, and SiO were observed with the Band 6 receiver in the frequency range from 244 to 264 GHz (Table 8.1). Thirty-four antennas were used in the observation, where the baseline length ranged from 18.5 to 644 m. The field center of the observations was (α_{2000}, δ_{2000}) = ($18^h17^m29\overset{s}{.}910$, $-04°39'39\overset{''}{.}60$). The primary beam size (FWHM) is $23\overset{''}{.}03$. The total on-source time was 25.85 minutes, where a typical system temperature was $60 - 100$ K. A backend correlator was tuned to a resolution of 61.030 kHz and a bandwidth of each chunk of 58.5892 MHz. The resolution corresponds to the velocity resolution of 0.073 km s^{-1} at 250 GHz. J1733–1304 was used for the bandpass calibration and for the phase calibration every 7 minutes. An absolute flux density scale was derived from Titan. The data calibration was performed in the antenna-based manner, and uncertainties are less than 9%.

Table 8.1: Parameters of the Observed Lines[a]

Molecule	Transition	Frequency (GHz)	E_u (K)	$S\mu^2$ (Debye^2)[b]	A_{ij} (s^{-1})	Synthesized Beam
CS	$J = 5 - 4$	244.9355565	35.3	19	2.98×10^{-4}	$0\farcs51 \times 0\farcs46$ (P.A. $-177\fdg24$)
NH_2CHO[c]	$12_{0,12} - 11_{0,11}$	247.390719	78.1	156	1.10×10^{-3}	$0\farcs56 \times 0\farcs49$ (P.A. $16\fdg44$)
$HCOOCH_3$[c]	$20_{5,16,0} - 19_{5,15,0}$	249.0474280	141.6	50	1.46×10^{-3}	$0\farcs52 \times 0\farcs45$ (P.A. $-177\fdg18$)
SiO[c]	$J = 6 - 5$	260.5180090	43.8	58	9.12×10^{-4}	$0\farcs46 \times 0\farcs42$ (P.A. $-177\fdg78$)
CH_3CHO[c]	$14_{1,14} - 13_{1,13}$; A	260.5440195	96.4	82	6.25×10^{-4}	$0\farcs46 \times 0\farcs42$ (P.A. $-177\fdg81$)
SO	$J_N = 6_7 - 5_6$	261.8437210	47.6	16	2.28×10^{-4}	$0\farcs46 \times 0\farcs42$ (P.A. $3\fdg09$)
CCH[d]	$N = 3 - 2, J = 7/2 - 5/2,$	262.0042600	25.1	2.3	5.32×10^{-5}	$0\farcs98 \times 0\farcs92$ (P.A. $-78\fdg06$)
	$F = 4 - 3$ and $F = 3 - 2$	262.0064820		1.7	5.12×10^{-5}	$0\farcs98 \times 0\farcs92$ (P.A. $-78\fdg06$)
t-HCOOH[c]	$12_{0,12} - 11_{0,11}$	262.103481	82.8	24	2.03×10^{-4}	$0\farcs46 \times 0\farcs42$ (P.A. $2\fdg98$)
$(CH_3)_2O$[c]	$13_{5,8,1} - 13_{4,9,1}$	262.393513	118.0	148	7.18×10^{-5}	$0\farcs46 \times 0\farcs41$ (P.A. $1\fdg69$)
HNCO[c]	$12_{0,12} - 11_{0,11}$	263.7486250	82.3	30	2.56×10^{-4}	$0\farcs48 \times 0\farcs41$ (P.A. $3\fdg87$)

[a] Taken from CDMS (Müller et al., 2005) and JPL (Pickett et al., 1998).

[b] Nuclear spin degeneracy is not included.

[c] 4 channel bind. The spectral profile of the t-HCOOH line (Figure 8.10) is obtained with binding 16 channels.

[d] An outer taper of $1''$ is applied.

Images were obtained by using the CLEAN algorithm, where the Brigg's weighting with the robustness parameter of 0.5 was employed. We applied self-calibration for better imaging. A continuum image was prepared by averaging line-free channels, and the line maps were obtained after subtracting the continuum component directly from the visibilities. Synthesized-beam sizes for the spectral lines are listed in Table 8.1. An rms noise level for the continuum is 0.13 mJy beam^{-1}, while those for CCH, CS, SO, HNCO, NH_2CHO, $HCOOCH_3$, and SiO maps are derived from the nearby line-free channels to be 8.2, 7.6, 6.1, 6.5, 4.4, 5.8, and 3.5 mJy beam^{-1}, respectively, for the channel width of 61.030 kHz.

8.3 Distribution

Figure 8.1 shows the map of the 1.2 mm dust continuum, where the synthesized beam size is $0''.46 \times 0''.42$ (P.A. $11^\circ.76$). Its peak position is determined by the two-dimensional Gaussian fit to be: $(\alpha_{2000}, \delta_{2000}) = (18^h17^m29^s.947, -04^\circ39'39''.55)$. The deconvolved size of the continuum emission is $0''.23 \times 0''.16$ (P.A. 158°), and hence, the image is not resolved. The total flux of the continuum is 28 mJy.

In these observations, we detected the lines of CCH, CS, SO, HNCO, NH_2CHO, $HCOOCH_3$, and SiO. these observations toward L483 is a part of a larger project to delineate physical and chemical structures of the disk forming regions in several protostellar sources with ALMA (#2013.1.01102.S; P.I. N. Sakai), and the above lines are all detected in the other sources (B335 and NGC 1333 IRAS 4A) with the same frequency setup (Imai et al., 2016; López-Sepulcre, 2017). Hence, their detections are secure, although only one line was detected for each of these species except for CCH. As mentioned

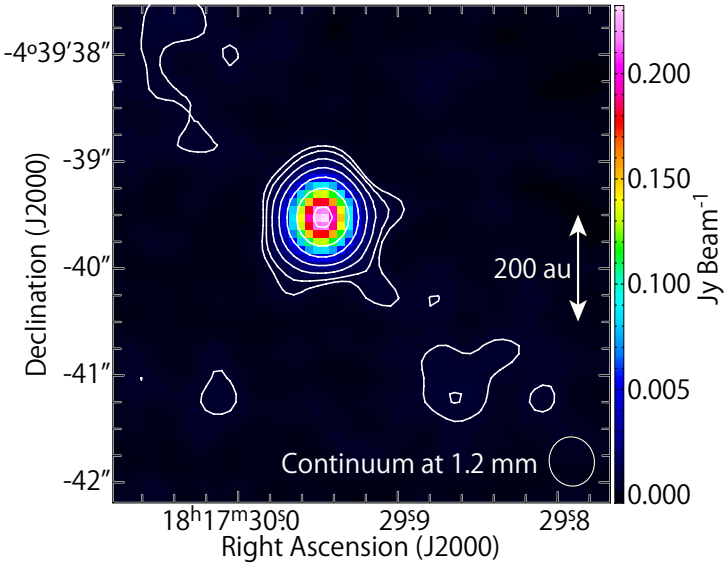

Figure 8.1: A map of the dust continuum at 1.2 mm. The contour levels are 3, 5, 10, 20, 40, 80, and 160σ, where the rms noise level is 0.13 mJy beam^{-1}. The synthesized beam size is $0''.46 \times 0''.42$ (P.A. $11^\circ.76$).

in Section 8.1, this source is regarded as a WCCC candidate source (Sakai et al., 2009a; Hirota et al., 2009, 2010; Sakai & Yamamoto, 2013). Hence, detections of complex organic molecules (COMs) such as NH_2CHO and $HCOOCH_3$, which are characteristic of hot corinos, are notable (e.g., Sakai & Yamamoto, 2013). The integrated intensity maps of CCH, CS, SO, HNCO, NH_2CHO, $HCOOCH_3$, and SiO are shown in Figures 8.2–8.4.

The CCH ($N = 3 - 2, J = 7/2 - 5/2, F = 4 - 3$ and $3 - 2$) emission is extended over a $10''$ scale, and hence, the outer taper of $1''$ is applied to improve a signal-to-noise ratio of the image (Figure 8.2a). The existence of the carbon-chain molecule CCH around the protostar at a few 100 au scale confirms the WCCC nature of this source. The CCH distribution has a hole with a radius of $\sim 0''.5$ around the continuum peak. This feature is similar to that found in the WCCC sources L1527 and IRAS 15398–3359 (Chapter 5; Sakai et al., 2014a,b), which would originate from the gas-phase destruction and/or depletion onto dust grains. The hole of the distribution seems to have a slight offset from the continuum peak to the western side, which implies an asymmetric distribution of the gas in the vicinity of the protostar. This asymmetry may be related to inhomogeneities of the initial gas distribution. In addition to the envelope component, a part of the CCH emission seems to trace an outflow cavity wall. The direction of the outflow axis looks consistent with the previous reports (P.A. $95° - 105°$; e.g., Park et al., 2000; Tafalla et al., 2000; Chapman et al., 2013).

The CS ($J = 5 - 4$) emission also traces the component extended over a $10''$ (Figure 8.2b). In addition, it shows a compact component concentrated to the continuum peak. The deconvolved size of this compact component is $1''.26 \times 0''.88$, and is slightly more extended than the 1.2 mm dust continuum. This slightly extended component will be

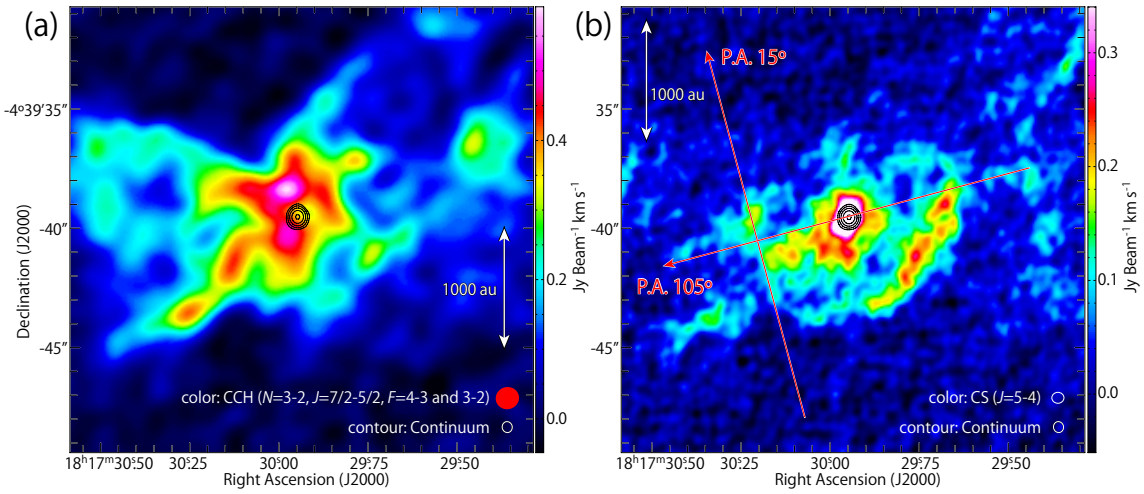

Figure 8.2: Integrated intensity maps of CCH ($N = 3 - 2, J = 7/2 - 5/2, F = 4 - 3$ and $3 - 2$; a) and CS ($J = 5 - 4$; b). The black contours represent the 1.2 mm continuum map, where the contour levels are 10, 20, 40, 80, and 160σ, where the rms noise level is 0.13 mJy beam^{-1}. The outflow axis is along the red arrow with a P.A. of 105° in panel (b). The PV diagram in Figure 8.8(b) is prepared along the red arrow with a P.A. of 15° in panel (b), which is centered at the position with an offset of $4''$ to the southeast from the continuum peak along a P.A. of 105°.

discussed in Section 8.4. On the other hand, the SO ($J_N = 6_7 - 5_6$), HNCO ($12_{0,12} - 11_{0,11}$), NH_2CHO ($12_{0,12} - 11_{0,11}$), and $HCOOCH_3$ ($20_{5,16,0} - 19_{5,15,0}$) distributions are highly concentrated to the continuum peak (Figure 8.3). The sizes of the distributions deconvolved by the synthesized beam are $0''.56 \times 0''.39$, and $0''.26 \times 0''.16$ for SO and HNCO, respectively. The HNCO distribution is almost point-like. Similarly, the distributions of NH_2CHO and $HCOOCH_3$ are also point-like at the resolution of these observations. In addition to these COMs, we tentatively detected the t-HCOOH emission concentrated near the protostar.

The distribution of SiO ($J = 6 - 5$) is different from those of the above molecular species. It has a slight extension toward the northeastern direction from the continuum peak, as shown in Figure 8.4. The extension is significant, considering the synthesized beam of these observations ($\sim 0''.5$). The size of the SiO distribution deconvolved by the synthesized beam is $0''.70 \times 0''.43$ (P.A. 35°).

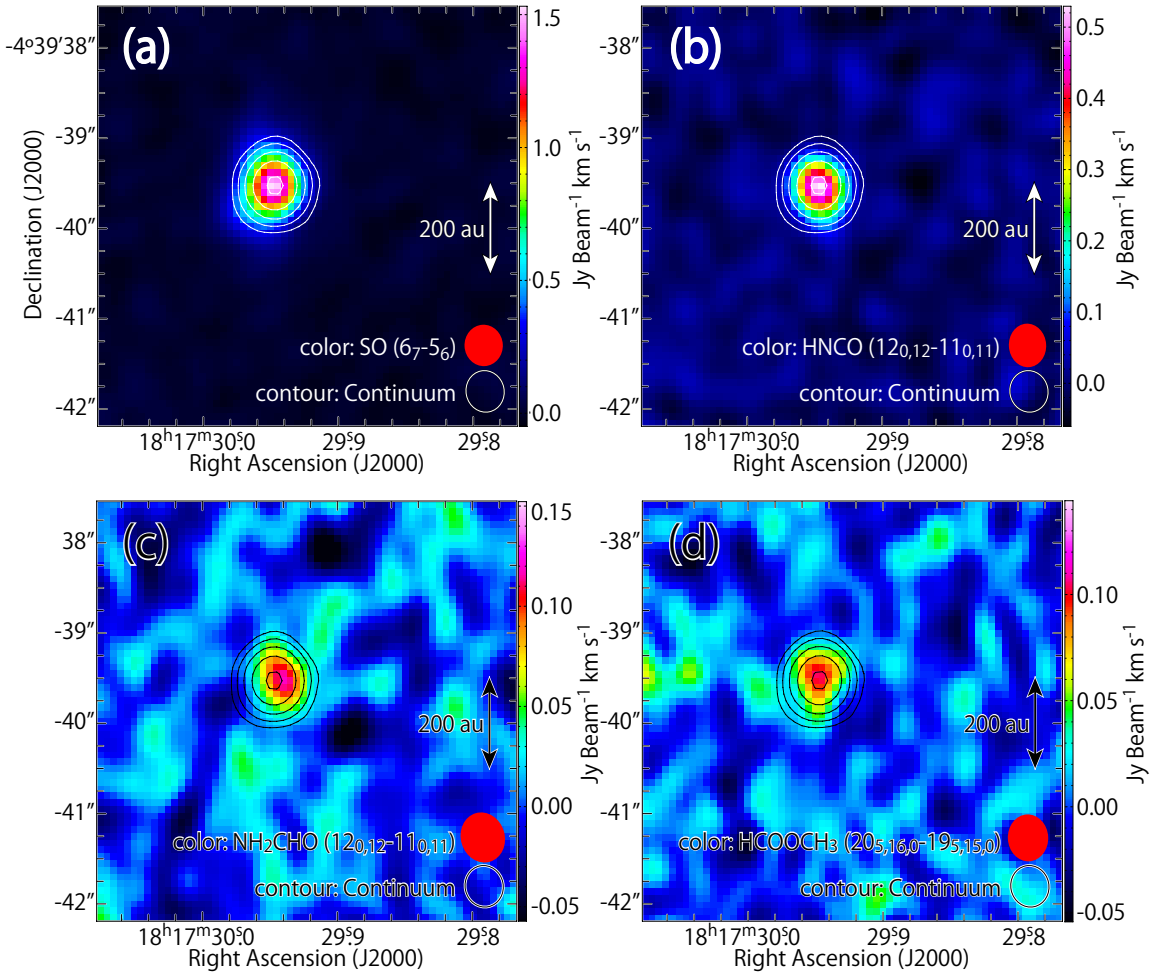

Figure 8.3: Integrated intensity maps of SO ($J_N = 6_7 - 5_6$; a), HNCO ($12_{0,12} - 11_{0,11}$; b), NH_2CHO ($12_{0,12} - 11_{0,11}$; c), and $HCOOCH_3$ ($20_{5,16,0} - 19_{5,15,0}$; d). The contours represent the 1.2 mm continuum map, where the contour levels are the same as those in Figure 8.2.

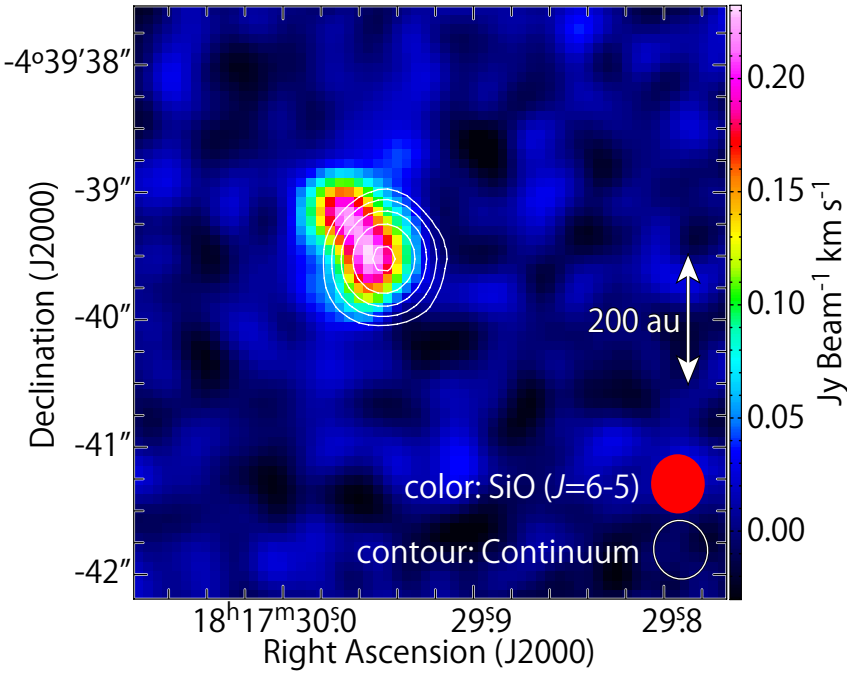

Figure 8.4: An integrated intensity map of SiO ($J = 6-5$). The white contours represent the 1.2 mm continuum map, where the contour levels are the same as those in Figure 8.2.

8.4 Velocity Structure

8.4.1 Geometrical Configuration of the Disk/Envelope System and the Outflow

Here, we focus on the kinematic structure of the gas concentrated around the protostar. In the moment 1 maps of SO and HNCO (Figure 8.5), we see a velocity gradient perpendicular to the outflow axis (P.A. 95° − 105°; e.g., Park et al., 2000; Tafalla et al., 2000; Chapman et al., 2013), which strongly suggests a rotating motion; a component in the northern side of the continuum peak is blue-shifted, while a component in the southern side is red-shifted. The direction of the gradient is qualitatively consistent with the CS ($J = 7 - 6$) and HCN ($J = 4 - 3$) observations reported by Takakuwa et al. (2007a) at a 20″ scale. In this chapter, we employ the position angle of the outflow axis of 105° reported by Chapman et al. (2013), and assume that the disk/envelope system is extended along the position angle of 15°. Since the eastern and western lobes of the outflow are reported to be red-shifted and blue-shifted, respectively (e.g., Fuller et al., 1995; Hatchell et al., 1999; Park et al., 2000; Tafalla et al., 2000; Jørgensen, 2004; Takakuwa et al., 2007a; Leung et al., 2016), the northwestern side of the disk/envelope system is thought to face the observer, as illustrated in Figure 8.6. In the following subsections, the kinematic structures of the observed molecular distributions are described, where CCH is excluded from this analysis due to heavy blending of the hyperfine components and a poor S/N ratio.

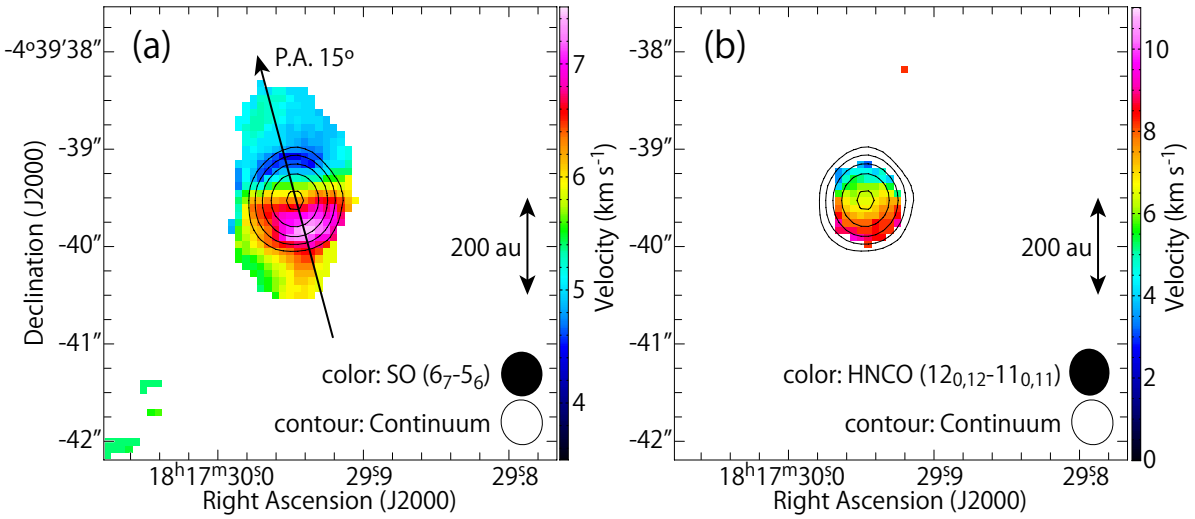

Figure 8.5: Moment 1 maps of SO ($J_N = 6_7 - 5_6$; a) and HNCO ($12_{0,12} - 11_{0,11}$; b). The black contours represent the 1.2 continuum map, where the contour levels are the same as those in Figure 8.2. The PV diagrams in Figures 8.7, 8.9, 8.11, and 8.14 are prepared along the black arrow in panel (a) (P.A. 15°) and along the direction perpendicular to it centered at the continuum peak.

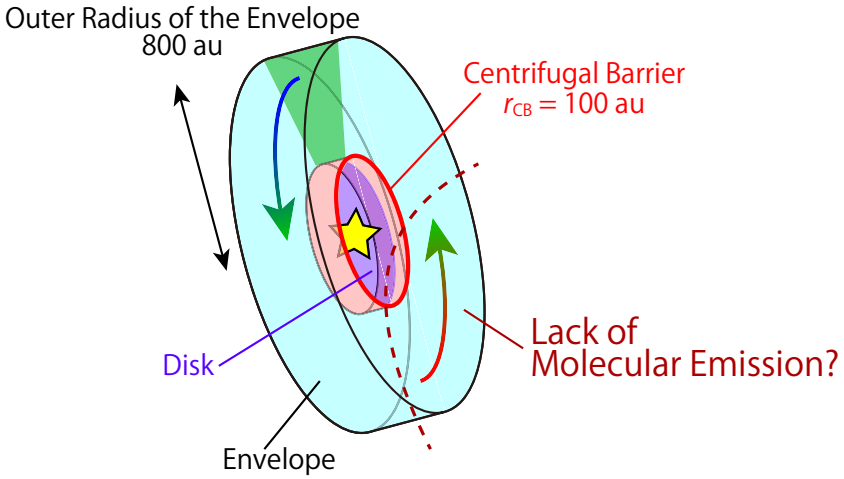

Figure 8.6: Schematic illustration of the disk/envelope system in L483. The mid-plane of the disk/envelope is extended along a P.A. of 15°, and its western side faces the observer. The line emission in the western side of the protostar seems to be missing, according to the observation (See Section 8.3).

8.4.2 CS

Figure 8.7 shows the position-velocity (PV) diagrams of CS ($J = 5 - 4$) along the disk/envelope direction (P.A. 15°). It shows a spin-up feature to the protostar along the disk/envelope direction at an 8″ scale (Figures 8.7a, c). Namely, the southwestern and northeastern sides of the protostar are red-shifted and blue-shifted, respectively. At the same time, a weak feature of the counter velocity component, which is blue-shifted at the southwestern side and red-shifted at the northeastern side, can be seen, although the component at the southwestern side is marginal. This feature is specific to the infalling-rotating envelope, as demonstrated in the previous chapters (e.g. Chapters 3 and 4). Hence, CS likely exists in the infalling-rotating envelope. In addition, CS shows a compact high velocity-shift component concentrated toward the protostar, whose maximum velocity shift is as high as about 6 km s^{-1}.

Along the line perpendicular to the disk/envelope direction (P.A. 105°), a component extended over a 20″ scale is observed (Figure 8.7b). Although this component looks complicated in the velocity structure, it likely traces a part of the outflow cavity. Figure 8.8 shows the PV diagrams along the outflow axis and the line across the outflow lobe in the southeastern side of the protostar, which is indicated by an arrow in Figure 8.2(b). In Figure 8.8(a), we can confirm that the northwestern and southeastern lobes are blue- and red-shifted, respectively. Figure 8.8(a) also shows that the velocity of the outflow component accelerates as the distance from the protostar. In Figure 8.8(b), the elliptic feature of the PV diagram characteristic of the outflow cavity wall is clearly observed. Although both the red-shifted and blue-shifted components with respect to the systemic velocity (5.5 km s^{-1}; Hirota et al., 2009) are seen, the center velocity of the elliptic feature is slightly red-shifted. This elliptic feature is consistent with the configuration illustrated in Figure 8.6. It is quite similar to those observed in the nearly edge-on outflow system of IRAS 15398–3359 (Chapter 5), where both the red-shifted and blue-shifted components can be seen in each outflow lobe. Hence, it is most likely that the outflow of L483 blows nearly on the plane of the sky at least in the vicinity of the protostar in contrast to the previous reports (e.g., Fuller et al., 1995). Hence, the disk/envelope system likely has a nearly edge-on geometry ($i \sim 80°$). The more detailed structure of the outflow is described in Section 8.6.1.

When the outflow axis is perpendicular to the mid-plane of the disk/envelope system, the northwestern side of the disk/envelope system will face the observer. If there is an infall motion in the envelope component, the southeastern and northwestern sides of the protostar would be blue-shifted and red-shifted, respectively, in the PV diagram along the P.A. of 105° (Figure 8.7d). However, this feature is not clearly recognized, because of overwhelming contributions from the outflow component and the missing of the blue-shifted component. The velocity gradient due to the infall motion will be verified with the aid of the kinematic model in Section 8.5. On the other hand, the high velocity-shift component does not show any velocity gradient along the P.A. of 105° around the protostellar position.

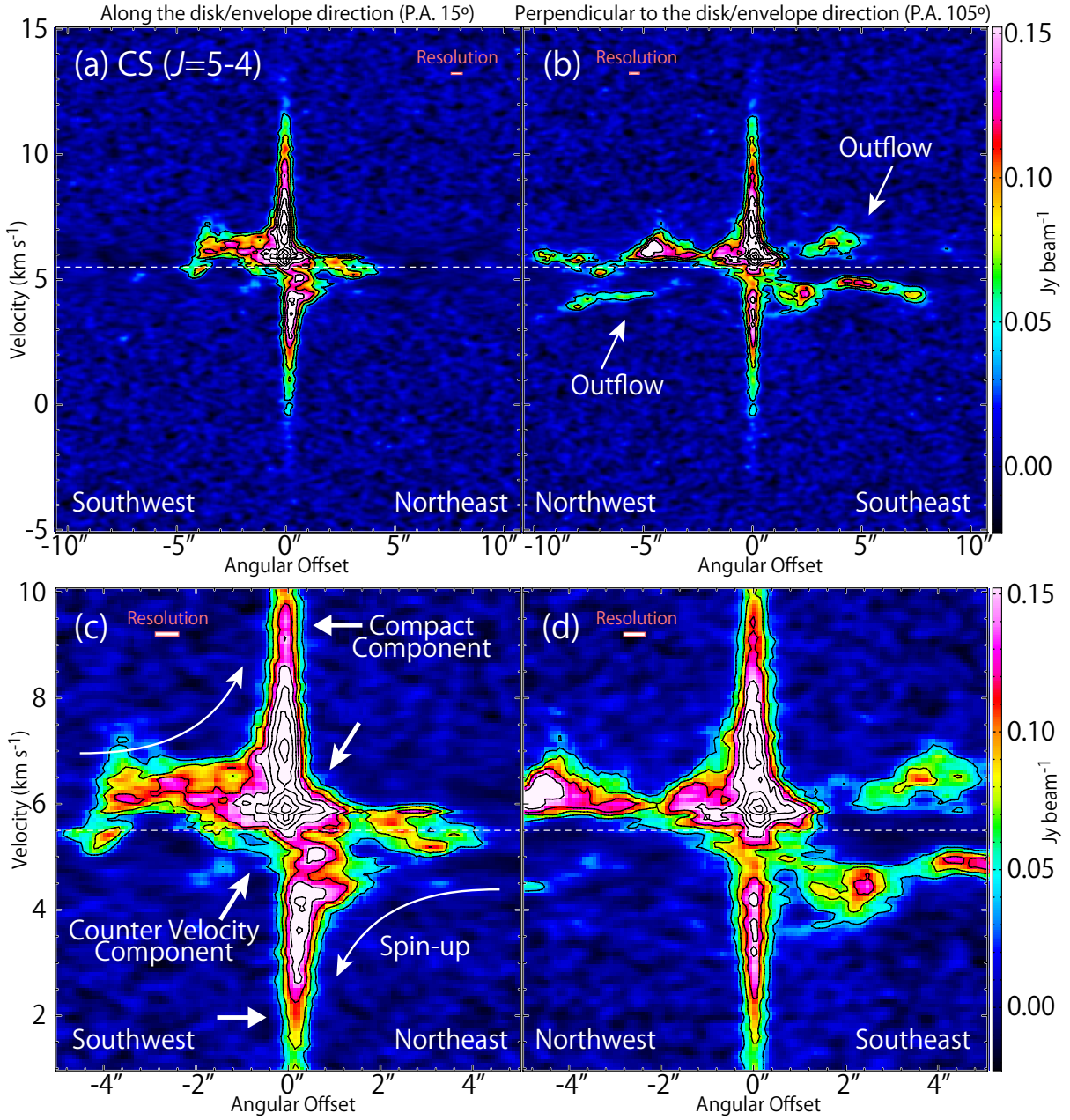

Figure 8.7: Position-velocity diagrams of CS ($J = 5-4$) along the disk/envelope direction (P.A. 15°; a, c) indicated in Figure 8.5, and the direction perpendicular to it (P.A. 105°; b, d). Panels (c, d) are the blow-ups of the central parts of panels (a, c). The contour levels are every 5σ, where the rms noise level is 7.6 mJy beam^{-1}. The white dashed lines represent the systemic velocity (5.5 km s^{-1}). The rectangle in the top-left corner of each panel represents the spatial and velocity resolutions.

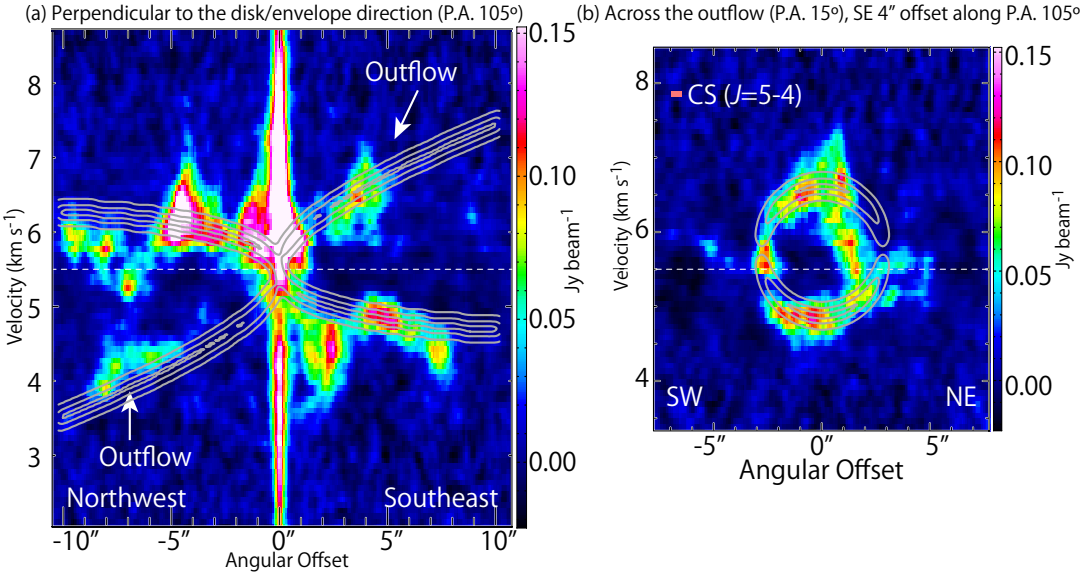

Figure 8.8: Position-velocity diagrams of CS ($J = 5 - 4$) along the outflow axis (a; P.A. 105°) and the line across the outflow (b; P.A. 15°) shown in Figure 8.2(b). The position axis in panel (b) is centered at the distance of 4″ from the protostellar position toward the southeastern direction. The contour levels are every 5σ, where the rms noise level is 7.6 mJy beam^{-1}. Gray contours represent the results of the outflow model, where the physical parameters are as follows; $i = 80°$, $C = 0.0025$ au^{-1}, and $v_0 = 0.0015$ km s^{-1} au^{-1}. The contour levels for the outflow model is every 40% from the 10% to the peak intensity.

8.4.3 SO and HNCO

The PV diagrams of SO ($J_N = 6_7 - 5_6$) and HNCO ($12_{0,12} - 11_{0,11}$) are shown in Figure 8.9. Along the disk/envelope direction, a slight velocity gradient is seen for SO (Figure 8.9a), while it is scarcely recognized for HNCO (Figure 8.9c). This velocity gradient in SO is consistent with that found in CS, and hence, it seems to originate from the rotating motion in the inner part of the disk/envelope system. No definitive velocity gradient along the line perpendicular to the disk/envelope direction can be seen for SO and HNCO in Figures 8.9(b, d). Hence, the SO and HNCO emission reveals no significant infall motion in the vicinity of the protostar.

The high velocity-shift components of SO and HNCO near the protostellar position correspond to that found in the CS emission (Figure 8.7). Figure 8.10 shows the line profiles of CS, SO, and HNCO in a circular region with a diameter of 0.″5 centered at the continuum peak. The line profile of SO shows a profile similar to that of CS, except for the self-absorption in CS. Their broad line widths reflect the high velocity-shift component concentrated around the protostar shown in Figures 8.7, 8.9(a), and 8.9(b). HNCO also shows a component whose velocity shift from the systemic velocity is larger than 5 km s^{-1}. However, the red-shifted component is brighter than the blue-shifted component. This feature is also seen in its PV diagrams (Figures 8.9c, d). This implies that the HNCO distribution is asymmetric in the vicinity of the protostar.

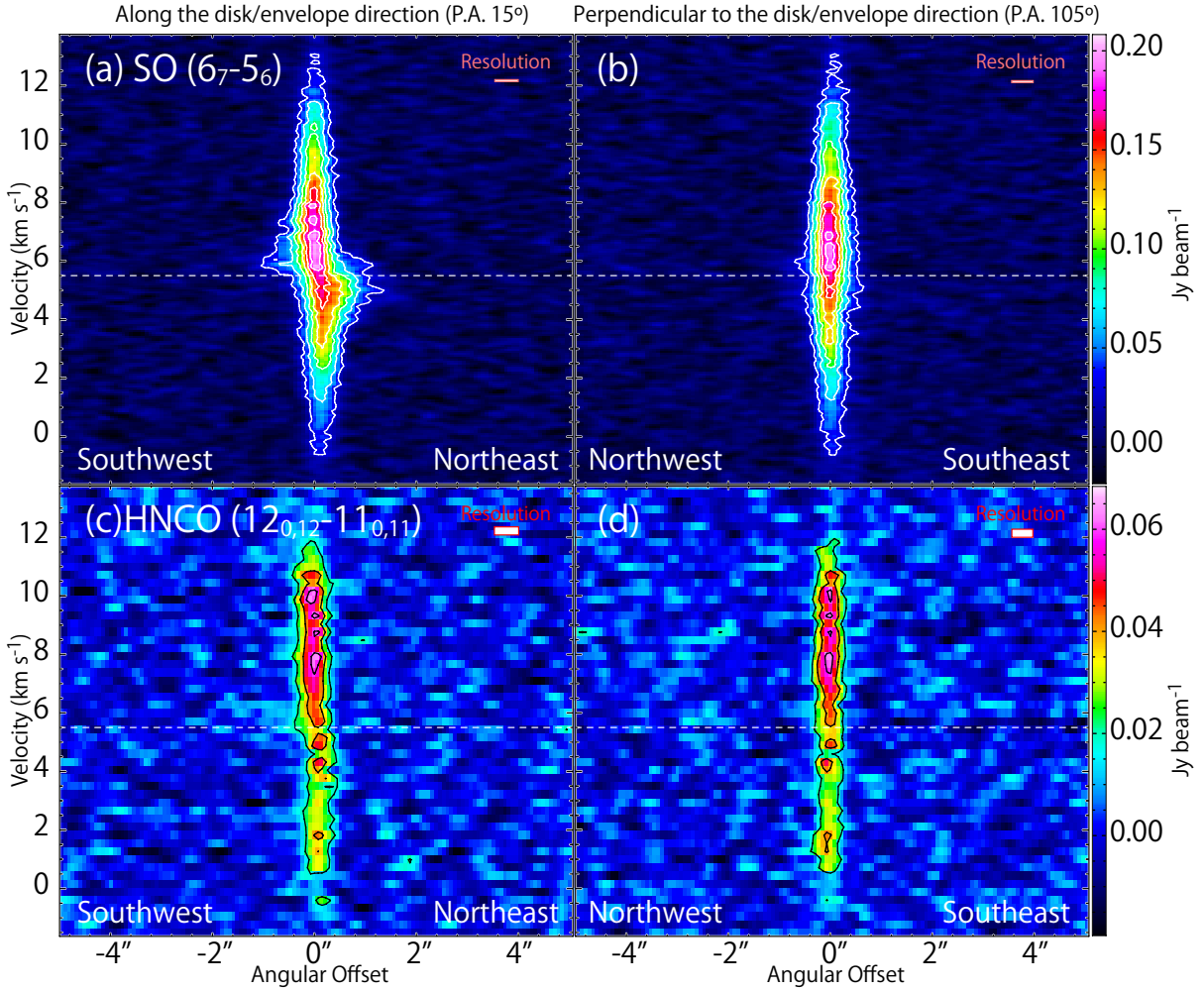

Figure 8.9: Position-velocity diagrams of SO ($J_N = 6_7{-}5_6$; a, b) and HNCO ($12_{0,12}{-}11_{0,11}$; c, d) along the disk/envelope direction (P.A. 15°; a, c) indicated in Figure 8.5, and the direction perpendicular to it (P.A. 105°; b, d). The contour levels are every 5 and 3σ, where the rms noise levels are 6.1 and 6.5 mJy beam^{-1}, for SO and HNCO, respectively.

8.4.4 NH_2CHO and $HCOOCH_3$

The most notable result in this study is detections of the COMs, NH_2CHO and $HCOOCH_3$. These two species are concentrated around the protostar, as shown in the moment 0 maps (Figures 8.3c, d). The spectral line profiles of NH_2CHO and $HCOOCH_3$ toward the protostellar position are dominated by a red-shifted component (Figure 8.10), which is similar to the HNCO spectrum. Since the red-shifted component is enhanced for all the HNCO, NH_2CHO, and $HCOOCH_3$ spectra consistently, their detections are secure; i.e. they do not correspond to other species/transitions. The red-shifted line profile implies an asymmetric distribution of those molecules in the vicinity of the protostar, as mentioned in Section 8.4.3. However, an origin of the asymmetry is puzzling, and is left for future high angular-resolution observations.

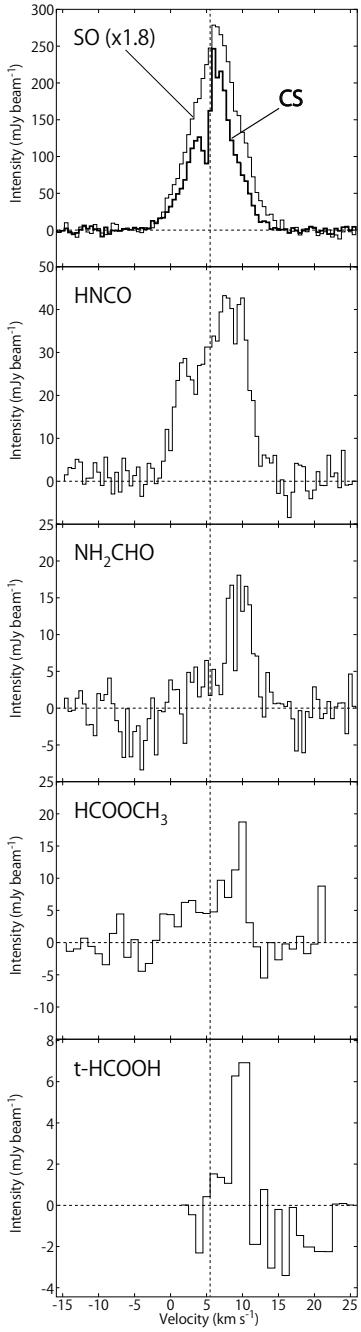

Figure 8.10: Spectral line profiles of CS ($J = 5 - 4$), SO ($J_N = 6_7 - 5_6$), HNCO ($12_{0,12} - 11_{0,11}$), NH_2CHO ($12_{0,12} - 11_{0,11}$), $HCOOCH_3$ ($20_{5,16,0} - 19_{5,15,0}$), and t-HCOOH ($12_{0,12} - 11_{0,11}$) toward the protostellar position. The line intensities are averaged in a circular region with a diameter of $0''.5$ centered at the continuum peak. The original spectra are smoothed to improve the signal-to-noise ratio, so as that the velocity resolution is 0.5 km s^{-1} for CS, SO, HNCO, and NH_2CHO, and 1 km s^{-1} for $HCOOCH_3$ and t-HCOOH.

8.5 Analysis with the Infalling-Rotating Envelope Model

In order to understand the chemical differentiation observed above in terms of the physical structure around the protostar, we analyze the kinematic structure of the disk/envelope system. In previous chapters, the kinematic structures of the infalling-rotating envelopes are successfully explained by a simple ballistic model in several sources. Hence, we apply the same model to the CS data in L483. However, we cannot reproduce the overall velocity structure with the infalling-rotating envelope model. As explained below, we need to consider the two physical components; the infalling-rotating envelope and the centrally concentrated component.

We employ the infalling-rotating envelope model described in Chapter 3. Here, we assume the flattened envelope with a constant thickness (30 au), and employ the inclination angle (i) of 80° (See Section 8.6). Unfortunately, the key parameters can loosely be constrained from these observations because of the contamination of the overwhelming centrally-concentrated component. Hence, we calculate the models with various parameters to find the reasonable set of the parameters by eye. Figures 8.11(a) and 8.11(b) shows an example of the simulation of the infalling-rotating envelope which reproduces the observed PV diagrams as much as possible except for the central high-velocity components. The model parameters are the protostellar mass (M) of 0.15 $M_{\odot}$ and the radius of the centrifugal barrier ($r_{\rm CB}$) of 100 au. The infall motion along the direction perpendicular to the disk/envelope system can marginally be recognized in the PV diagram with the aid of the model (Figure 8.11b). Its blue-shifted part is missing probably due to the asymmetric gas distribution mentioned above (Figure 8.6).

To see how the model PV diagram depends on the radius of the centrifugal barrier ($r_{\rm CB}$) and the protostellar mass (M), we also conducted the simulations of the PV diagrams along the disk/envelope direction and along the direction perpendicular to it by using the infalling-rotating envelope model with various sets of these two parameters, as shown in Figures 8.12 and 8.13, respectively. For the case of no rotation ($r_{\rm CB} = 0$ au), the positions of the most blue-shifted component and the most red-shifted component coincide in the model, which apparently contradict with the observation (Figure 8.12). On the other hand, the velocity of the counter-velocity component, which represents the infall motion of the infalling-rotating envelope, is underestimated for the $r_{\rm CB} = 300$ au case. As for the mass of the protostar, 0.05 $M_{\odot}$ and 0.5 $M_{\odot}$ do not reproduce the PV diagram. Above all, a reasonable agreement is obtained, except for the central high-velocity components, for the range of $r_{\rm CB}$ from 30 au to 200 au and the range of the protostellar mass from 0.1 $M_{\odot}$ to 0.2 $M_{\odot}$. Hence, the $r_{\rm CB}$ of 100 au and the protostellar mass of 0.15 $M_{\odot}$ are chosen as the representative values, as mentioned above (Figure 8.11). For more stringent constraints, further detailed analysis with a high angular-resolution observation is needed. The infall motion has a higher velocity-shift than the observation if the model parameters are set to explain the high velocity-shift component centrally concentrated near the protostar. This justifies the two-component model consisting of the infalling-rotating envelope and the centrally concentrated component described above. Although we can see some excess red-shifted emission in the southwestern part of the PV diagram (Figure 8.11a), the model can roughly reproduce the infalling-rotating envelope part of the PV diagrams. We analyze the high-velocity component in a separate way, as described below.

The most likely candidate for the centrally-concentrated high-velocity component

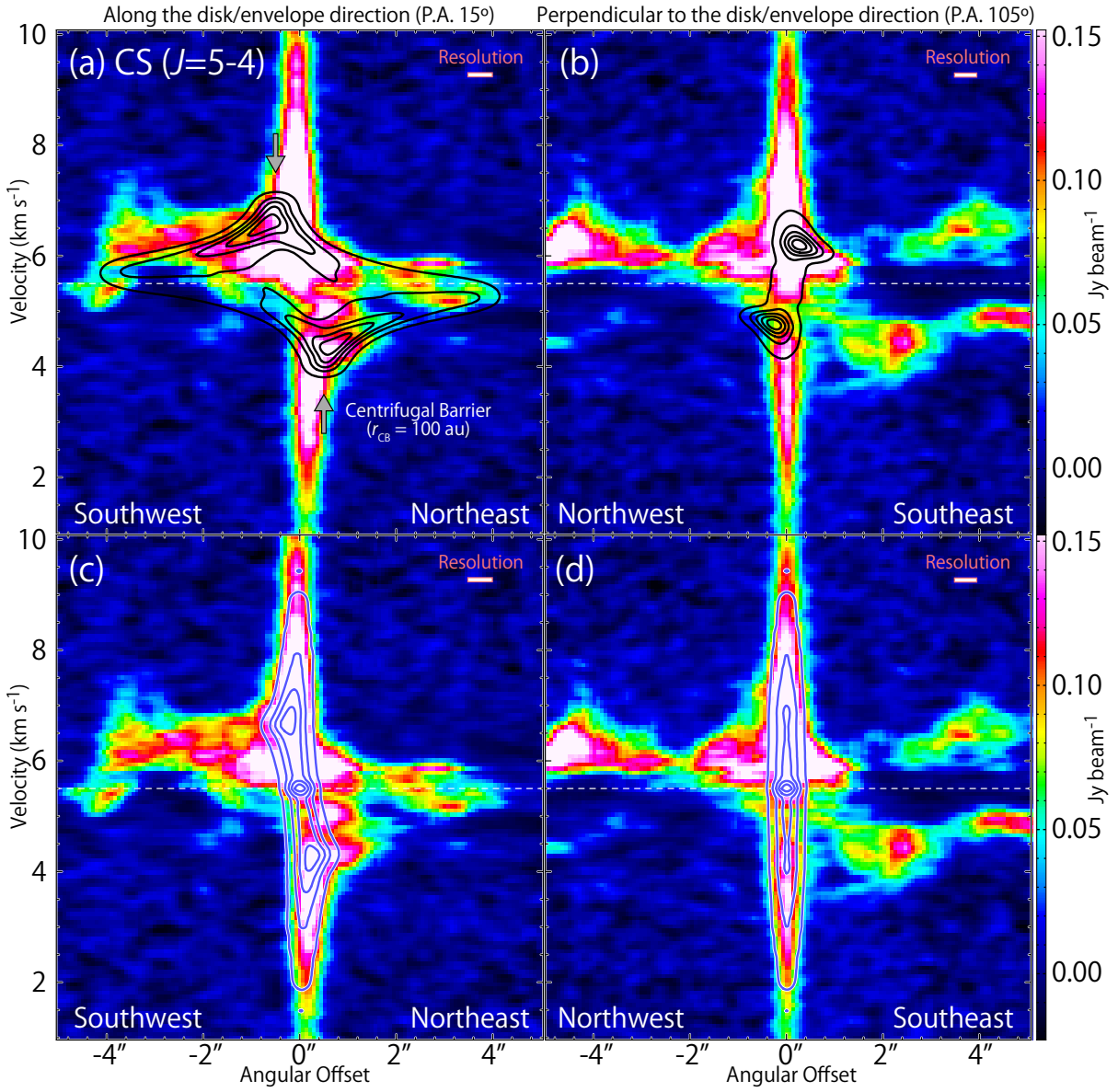

Figure 8.11: Position-velocity diagrams of CS ($J = 5 - 4$), where the color maps are the same as the panels (c, d) in Figure 8.7. The black contours in panels (a, b) represent the results of the infalling-rotating envelope models, where $M = 0.15\ M_{\odot}$, $r_{\rm CB} = 100$ au, and $i = 80°$. The blue contours in panels (c, d) represent the results of the Keplerian model with the above M and i values, where the emission is simply assumed to come from the inside of the centrifugal barrier. In panels (a–d), the intrinsic line width is assumed to be 0.2 km s^{-1}, and the model image is convolved with the synthesized beam. The contour levels are every 20% from 5% of each peak intensity.

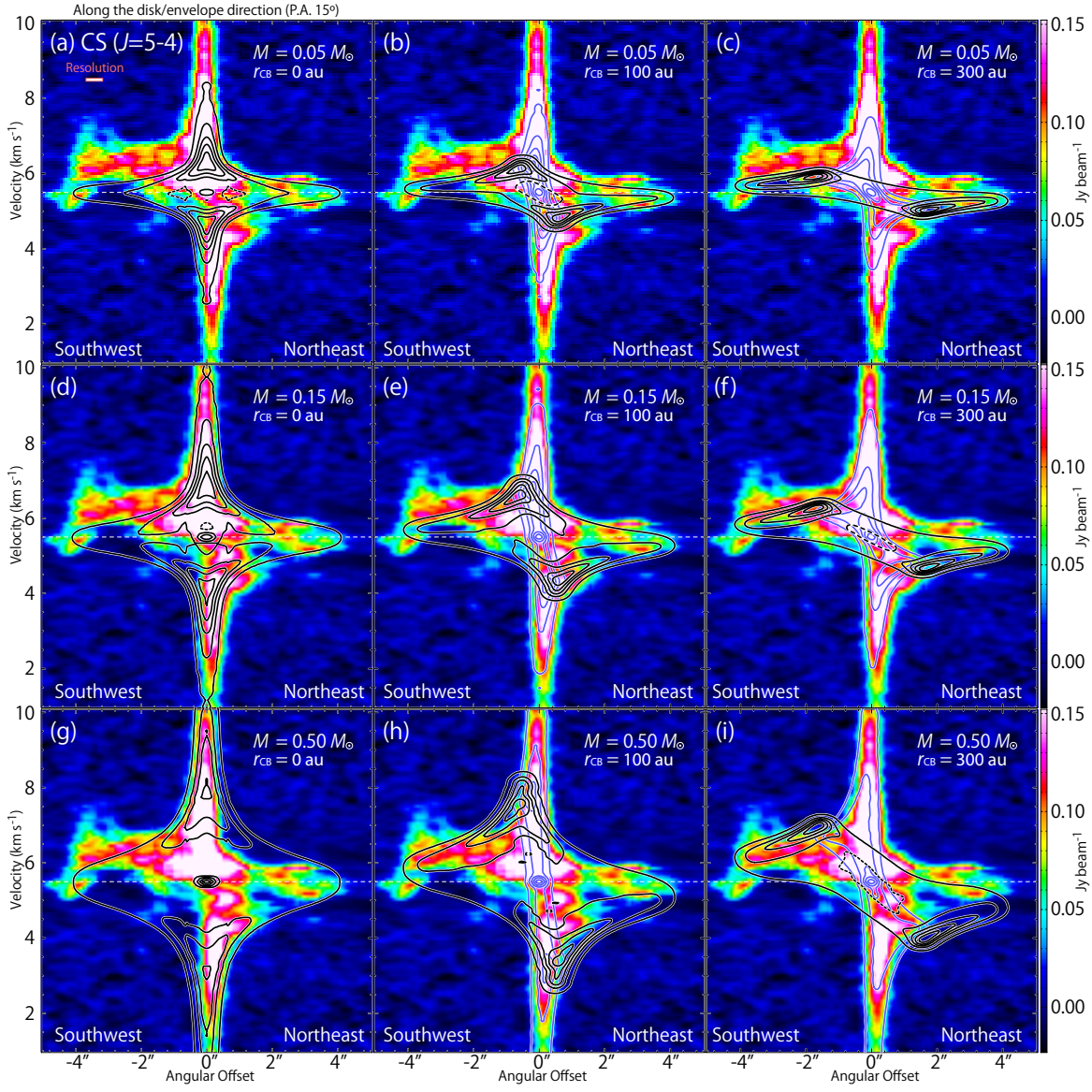

Figure 8.12: Position-velocity diagram of CS ($J = 5-4$) along the disk/envelope direction (P.A. 15°), where the color maps are the same as the panel (c) in Figure 8.7. The black contours represent the results of the infalling-rotating envelope models. The parameters are: $M = 0.05$, 0.15, and 0.5 $M_\odot$; $r_{\rm CB} = 0$, 100, and 300 au; $i = 80°$. The blue contours represent the results of the Keplerian model with the same physical parameters as those for the infalling-rotating envelope model in each panel. In the Keplerian model, the emission is simply assumed to come from the inside of the centrifugal barrier. The contour levels are every 20% from 5% of the peak intensity of each model. The dashed contours around the central position in the (a, b, d, f, h, i) panels represent the dip toward the center.

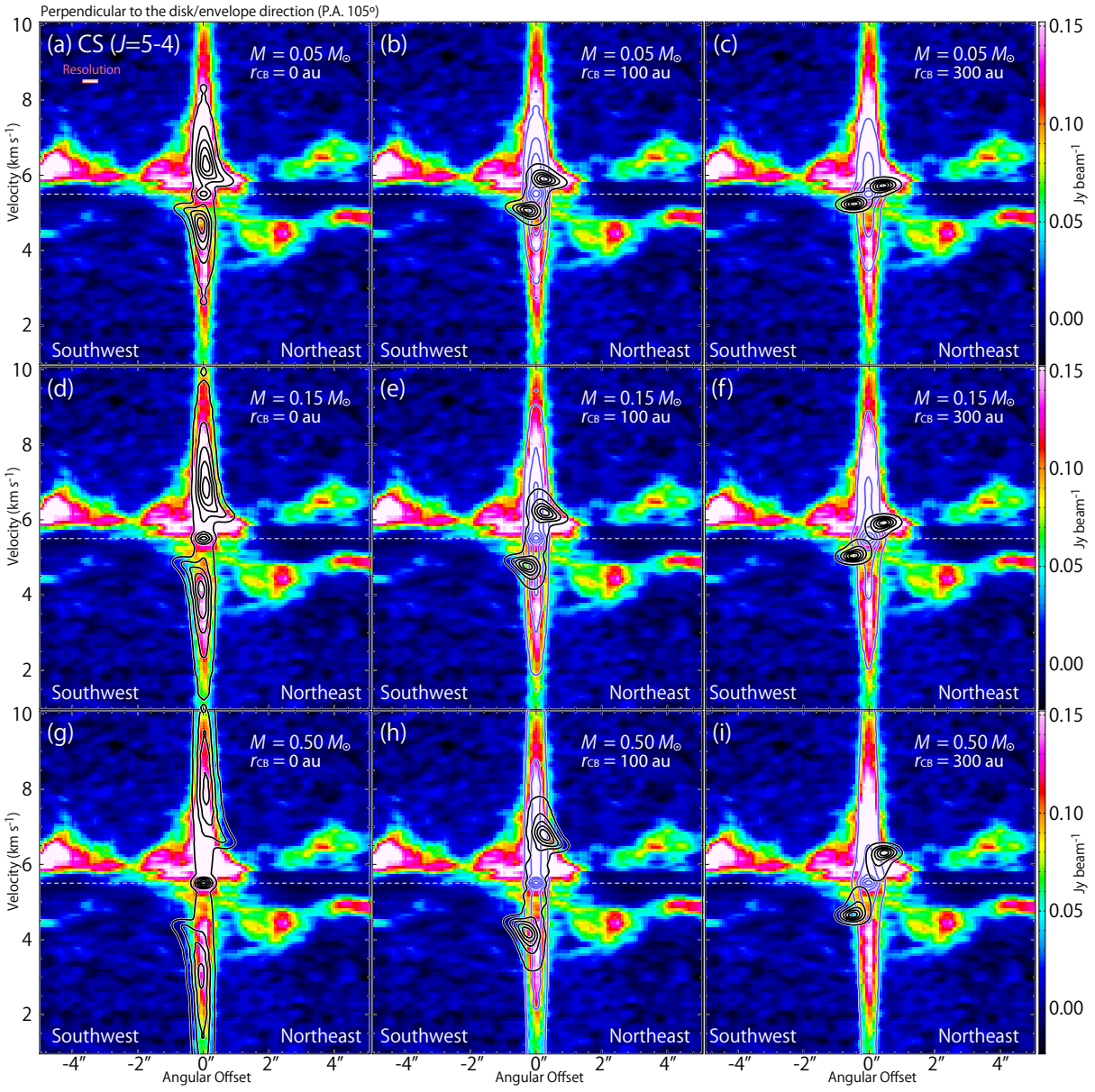

Figure 8.13: Position-velocity diagram of CS ($J = 5-4$) along the direction perpendicular to the disk/envelope direction (P.A. 105°), where the color maps are the same as the panel (d) in Figure 8.7. The black contours represent the results of the infalling-rotating envelope models. The parameters are: $M = 0.05$, 0.15, and 0.5 $M_{\odot}$; $r_{\rm CB} = 0$, 100, and 300 au; $i = 80°$. The blue contours represent the results of the Keplerian model with the same physical parameters as those for the infalling-rotating envelope model in each panel. In the Keplerian model, the emission is simply assumed to come from the inside of the centrifugal barrier. The contour levels are every 20% from 5% of the peak intensity of each model.

traced by CS, SO, HNCO, NH_2CHO, and $HCOOCH_3$ is the Keplerian disk inside the centrifugal barrier, although the rotation curve is not resolved. Assuming M of 0.15 $M_\odot$ and i of 80°, which are roughly estimated from the above analysis of the infalling-rotating envelope and the below analysis of the outflow, we can reproduce the high velocity-shift part of the PV diagrams of CS and SO by the Keplerian disk model (Figures 8.11 and 8.14). A radius of the emitting region of the maximum velocity component (∼6 km s^{-1}) in the disk is estimated to be as small as 4 au. We also show the results of the Keplerian disk model combined with the infalling-rotating envelope model in Figure 8.15. In addition, the results of the Keplerian disk model are overlaid on those of the infalling-rotating envelope model in Figures 8.12 and 8.13 for reference.

In the infalling-rotating envelope model and the Keplerian model, we assume the $r^{-1.5}$ density profile and the constant abundance of molecules for simplicity, where the effects of the optical depth, excitation, and the temperature gradient are not taken into account. At the distance of 100 au (r_{CB}) or larger from the protostar, the intensity of the observed CS line is less than 0.2 Jy $beam^{-1}$, which corresponds to the brightness temperature of less than 17 K. This temperature is lower than the gas kinetic temperature in the emitting region of the CS line, which is roughly expected to be higher than the desorption temperature of CS (∼ 35 K; Appendix A), by a factor of 2 or larger. Therefore, the CS line can be assumed to be optically thin in the envelope component outside the centrifugal barrier. On the other hand, the peak intensity of the CS line is ∼ 0.35 Jy $beam^{-1}$ inside the centrifugal barrier, which corresponds to the brightness temperature of 30 K for the beam size of $0''.51 \times 0''.46$. With the luminosity L of 13 $L_\odot$ (Shirley et al., 2000), the gas temperature T is roughly estimated to be 75 K at the distance r of 100 au from the protostar by use of the following equation: $\frac{L}{4\pi r^2} = \sigma T^4$, where σ denotes the Stefan-Boltzmann constant. Since the peak CS intensity is lower than the expected gas kinetic temperature, the above analysis of the velocity structure does not seriously suffer from the optical depth effect. Nevertheless, the excitation effect and the temperature gradient may affect the intensity distribution in reality. These effects may contribute the much higher intensity of the high-velocity component near the protostar ($< r_{CB}$) than the low-velocity component outer the centrifugal barrier. However, they will not seriously affect the above analysis, because we mainly focus on only the velocity structure but not on the intensity profile.

In L483, the kinematic structure of the gas traced by CS around the protostar is similar to those of H_2CO in L1527 and H_2CS in IRAS 16293–2422 A, which are explained by a combination of the infalling-rotating envelope component and the (possible) Keplerian disk component inside the centrifugal barrier (Chapter 6; Sakai et al., 2014b). Hence, the CS distribution in L483 is different from those in L1527 and TMC-1A (Chapter 4; Sakai et al., 2014b, 2016), where CS resides only in the infalling-rotating envelope. Such a distribution of CS in L483 seems to resemble the IRAS 16293–2422 A case. In IRAS 16293–2422 A, the emission of the normal isotopic species of CS seems to come from the disk as well as the infalling-rotating envelope (Y. Oya et al. in preparation), although the $C^{34}S$ emission traces the envelope outside the centrifugal barrier (Favre et al., 2014). The difference of the behavior of CS would originate from the higher bolometric luminosity of L483 (13 $L_\odot$; Shirley et al., 2000) and IRAS 16293–2422 Source A (22 $L_\odot$; Crimier et al., 2010) than L1527 (1.7 $L_\odot$; Green et al., 2013) and TMC-1A (2.5 $L_\odot$; Green et al.,

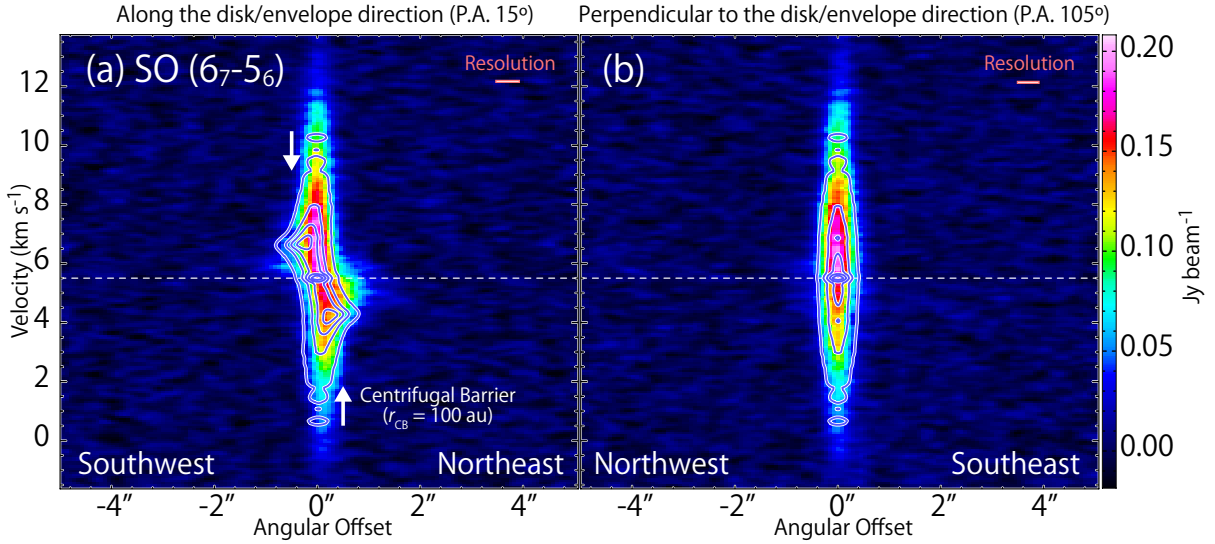

Figure 8.14: Position-velocity diagrams of SO ($J_N = 6_7 - 5_6$), where the color maps are the same as those in Figures 8.9(a, b). The blue contours represent the results of the Keplerian model, where $M = 0.15\ M_\odot$ and $i = 80°$, and the emission is simply assumed to be only inside the centrifugal barrier (100 au). The contour levels are every 20% from 3% of each peak intensity.

2013). The higher bolometric luminosity would cause the higher temperature of the disk component inside the centrifugal barrier, which prevents the CS depletion in this region. Since the binding energy of CS is 1900 K (UMIST Database for Astrochemistry; McElroy et al., 2013, http://udfa.ajmarkwick.net/index.php), the evaporation temperature is about 40 K (Appendix A; Yamamoto, 2017). This is just above the mid-plane temperature of the disk just inside the centrifugal barrier in L1527 (30 K; Sakai et al., 2014b). If the mid-plane temperature inside the centrifugal barrier is higher in L483 due to the higher bolometric luminosity, CS does not freeze out.

On the other hand, the rotation feature of the SO emission revealed in the PV diagrams (Figure 8.9a) looks similar to that in L1527 (Sakai et al., 2014a), where SO mainly highlights the centrifugal barrier. However, the high velocity-shift components concentrated toward the protostar are much brighter in L483 than in L1527, and hence, the rotating motion traced by SO in L483 is expected to come mainly from the disk component inside the centrifugal barrier (Figure 8.14). The relatively high bolometric luminosity in L483 could again help in escaping SO from depletion onto dust grains in the disk component.

Assuming that the SO emission appears inside of the centrifugal barrier, we can directly estimate its radius. The doconvolved size (FWHM) is 0.″5 (100 au) along the disk/envelope direction (P.A. 15°), and hence, the radius of the centrifugal barrier is estimated to be ∼50 au. Since this size will be affected by the strong emission from the vicinity of the protostar, it can be regarded as the lower limit. On the other hand, the 5σ contour in the PV diagram of SO (Figure 8.9a) is extended to 2.″4 (= 480 au), where the radius deconvolved with the beam size along the position angle of 15° is ∼1″ (∼ 200 au). Since the SO line may trace the envelope component just outside the centrifugal barrier (Sakai et al., 2017), this size can be regarded as the upper limit for the radius of the

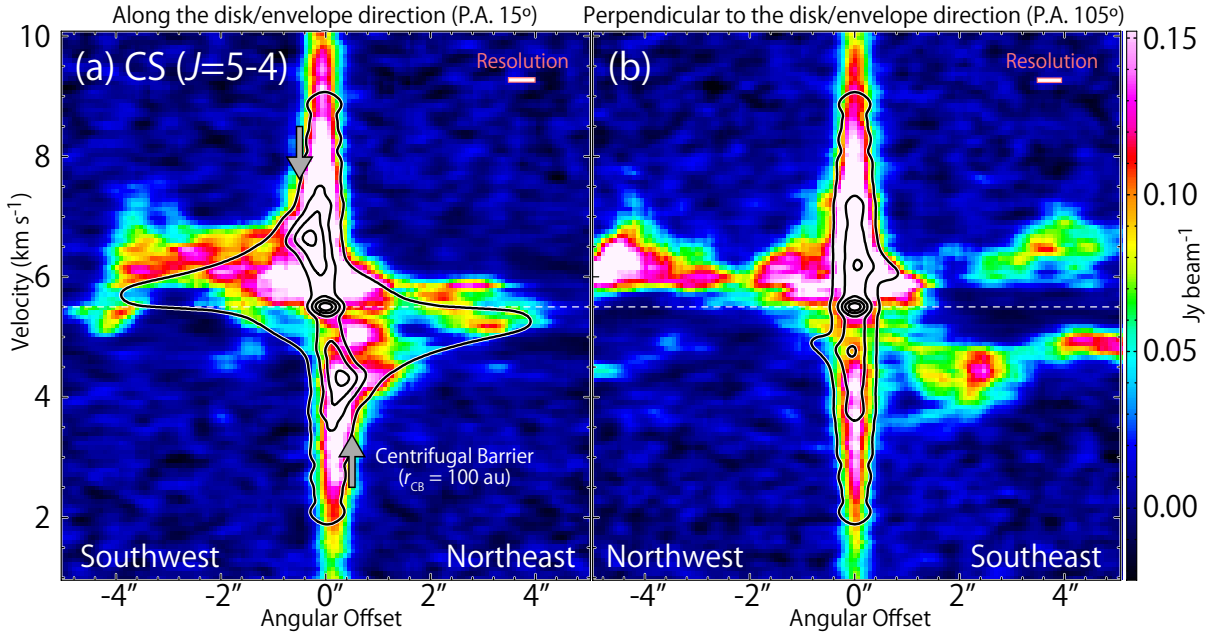

Figure 8.15: Position-velocity diagrams of CS ($J = 5-4$) along the disk/envelope direction (P.A. 15°; a) and the direction perpendicular to it (P.A. 105°; b), where the color maps are the same as the panels (c, d) in Figure 8.7. The black contours represent the results of an infalling-rotating envelope model combined with the Keplerian model, where the physical parameters are the same as those for the models for Figure 8.11. The contour levels are every 20% from 3% of each peak intensity.

centrifugal barrier. Although it is difficult to derive the radius of the centrifugal barrier from the SO emission because of the contamination by the disk component in L483, these sizes will directly give rough estimates for the size of the centrifugal barrier. They are consistent with the estimate from the analysis of the PV diagrams of CS in Section 8.5.

8.6 Outflow Structure

8.6.1 Outflow Cavity Wall Traced by CS

In the above analysis of the infalling-rotating envelope, we assumed that the disk/envelope system of L483 has a nearly edge-on configuration with the inclination angle (i) of 80° (0° for a face-on configuration). The inclination angle is derived from the outflow structure traced by CS (Section 8.4.2). Here, we investigate the outflow structure in detail. As shown in Figure 8.8(a), the outflow component is accelerated as an increasing distance from the protostar along the outflow axis. In Figure 8.8(b), an elliptic feature across the outflow axis is evident. Since an extended component is often resolved out in interferometric observations, the elliptic feature likely corresponds to the outflow cavity wall. These features are quite similar to those found in a low-mass Class 0 source IRAS 15398–3359 (Chapter 5), where the kinematic structure of the outflow cavity wall was well explained by a standard outflow model (Lee et al., 2000), as presented in Chapter 5. Thus, we

conduct a similar analysis for L483. The details of the outflow model are described in Chapter 3.

8.6.2 Comparison with the Outflow Model

The white contours in Figure 8.8 represent an example of the outflow model results. In this model, the intensity of the emission is assumed to be proportional to the column density, where the molecular density is simply assumed to be constant. Although these assumptions may not be realistic, they do not affect the following analysis seriously, where we only focus on the velocity structure but not on the intensity profile. They seem to well explain the observed kinematic structure of the CS line. The model assumes that the outflow cavity wall has a parabolic feature, and the velocity on the cavity wall is proportional to the distance from the protostar. The physical parameters for the model are as follows; $i = 80°$, $C = 0.0025$ au^{-1}, and $v_0 = 0.0015$ km s^{-1} au^{-1}. Here, the emission from the cavity wall is convolved by the synthesized beam for the CS line and the intrinsic line width of 0.2 km s^{-1}. In this model, the abundance of the molecular gas is assumed to be constant on the cavity wall and zero for the other positions for simplicity. Thus the contours in Figure 8.8 just show the velocity structure on the cavity wall, and the intensity itself does not have quantitative meanings. Based on this simulation, we employed i of 80° for the envelope analysis in Section 8.5.

Figure 8.16 shows the PV diagrams of CS ($J = 5 - 4$), where the position axes are taken along the line with the position angle of 15°. They are perpendicular to the outflow axis (P.A. 105°) with the offset of ($0'' - 10''$) from the protostellar position toward the southeastern direction. The origin of each position axis is taken on the outflow axis. Figure 8.17 is similar to Figure 8.16 except that the offset is taken toward the northwestern direction. The diagrams are prepared to be centered at the positions on the outflow axis and across it from southwest to northeast. Although the diagrams seem to be heavily contaminated by the disk/envelope components in the panels with the offsets of ($0'' - 1''$) from the protostar, the elliptic feature of the outflow component can be confirmed in the panels with larger offsets. The results of the above outflow model are represented by the white contours in these figures, and they seem to reasonably explain the observed outflow components in all the panels.

With the physical parameters estimated in the above analysis, the dynamical time scale ($t_{\rm dyn}$) of the outflow lobes can be evaluated to be $\sim 3 \times 10^3$ yr. Hatchell et al. (1999) previously reported model calculations with $t_{\rm dyn}$ of $(2 - 6) \times 10^3$ yr for the CO observations. Although Fuller et al. (1995) evaluated it to be 13×10^3 yr based on the CO observations, they also mentioned that it was inconsistent with the young age of IRAS 18148–0440 less than 4.2×10^3 yr evaluated from its low bolometric temperature. Since they assumed i of 50°, $t_{\rm dyn}$ is recalculated to be 2×10^3 yr with the correction of the inclination angle to be 80°. Thus, these values of $t_{\rm dyn}$ are consistent with each other, and the most plausible value of $t_{\rm dyn}$ is as low as a few 10^3 yr.

8.6.3 Rotation Motion in the Outflow

Outflow launching is thought to be a potential mechanism to extract the angular momentum of the envelope gas at the centrifugal barriers. If this is the case, outflows are

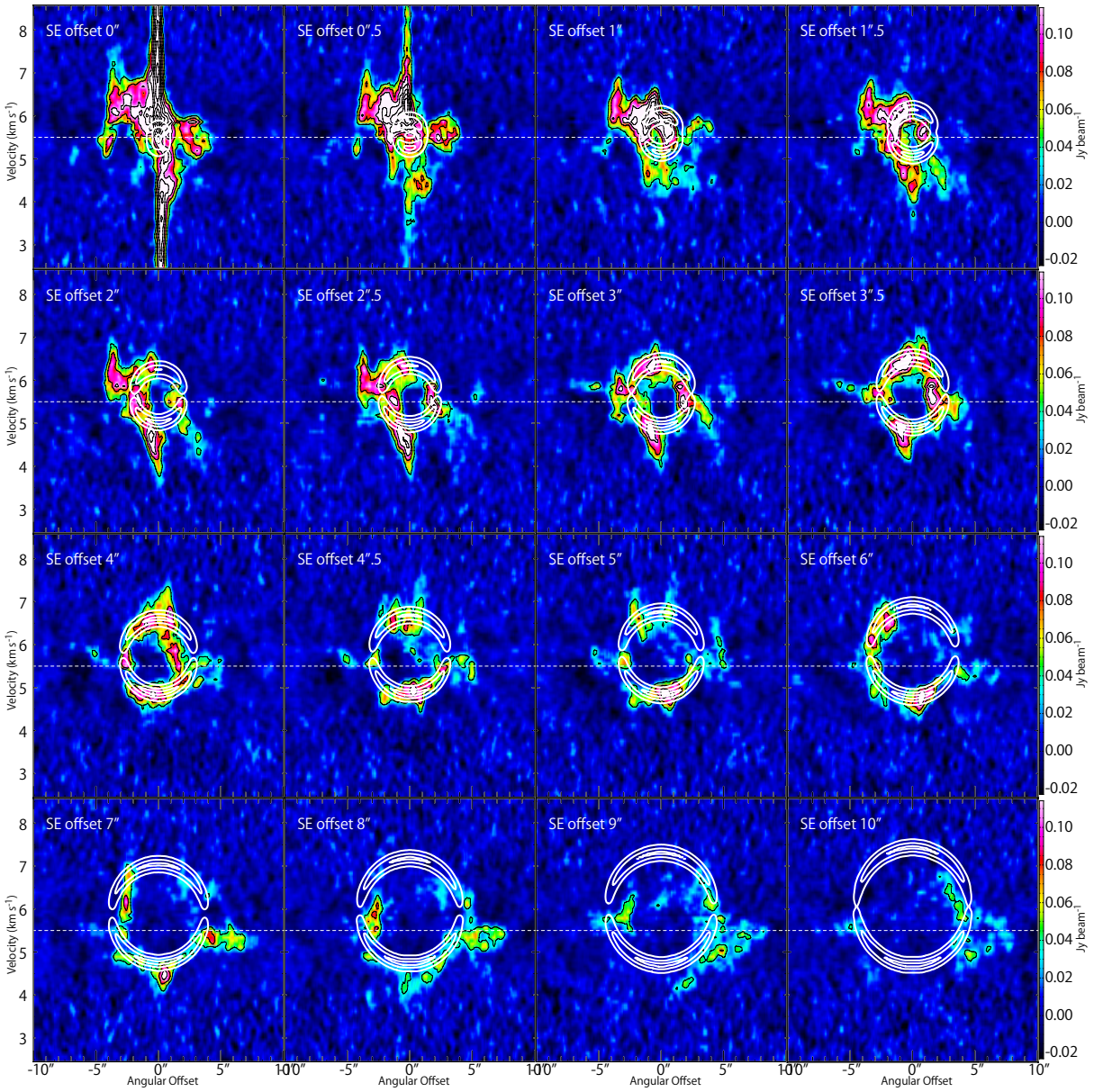

Figure 8.16: Position-velocity diagrams of CS ($J = 5 - 4$) across the outflow axis. The position axes are along the position angle of 15°, which are perpendicular to the outflow axis (P.A. 105°). Their central positions (angular offset of 0″) are on the outflow axis with an offset of the distance of (0″ − 10″) from the protostellar position toward the southeastern direction. The color map in the panel labeled as 'SE offset 4″' is the same as that in Figure 8.8(b). The contour levels for CS are every 5σ, where the rms noise level is 7.6 mJy beam^{-1}. White contours represent the results of the outflow model, where the physical parameters are as follows; $i = 80°$, $C = 0.0025$ au^{-1}, and $v_0 = 0.0015$ km s^{-1} au^{-1}. No rotating motion is taken into account. The contour levels for the outflow model are every 40% from the 10% to the peak intensity in each panel.

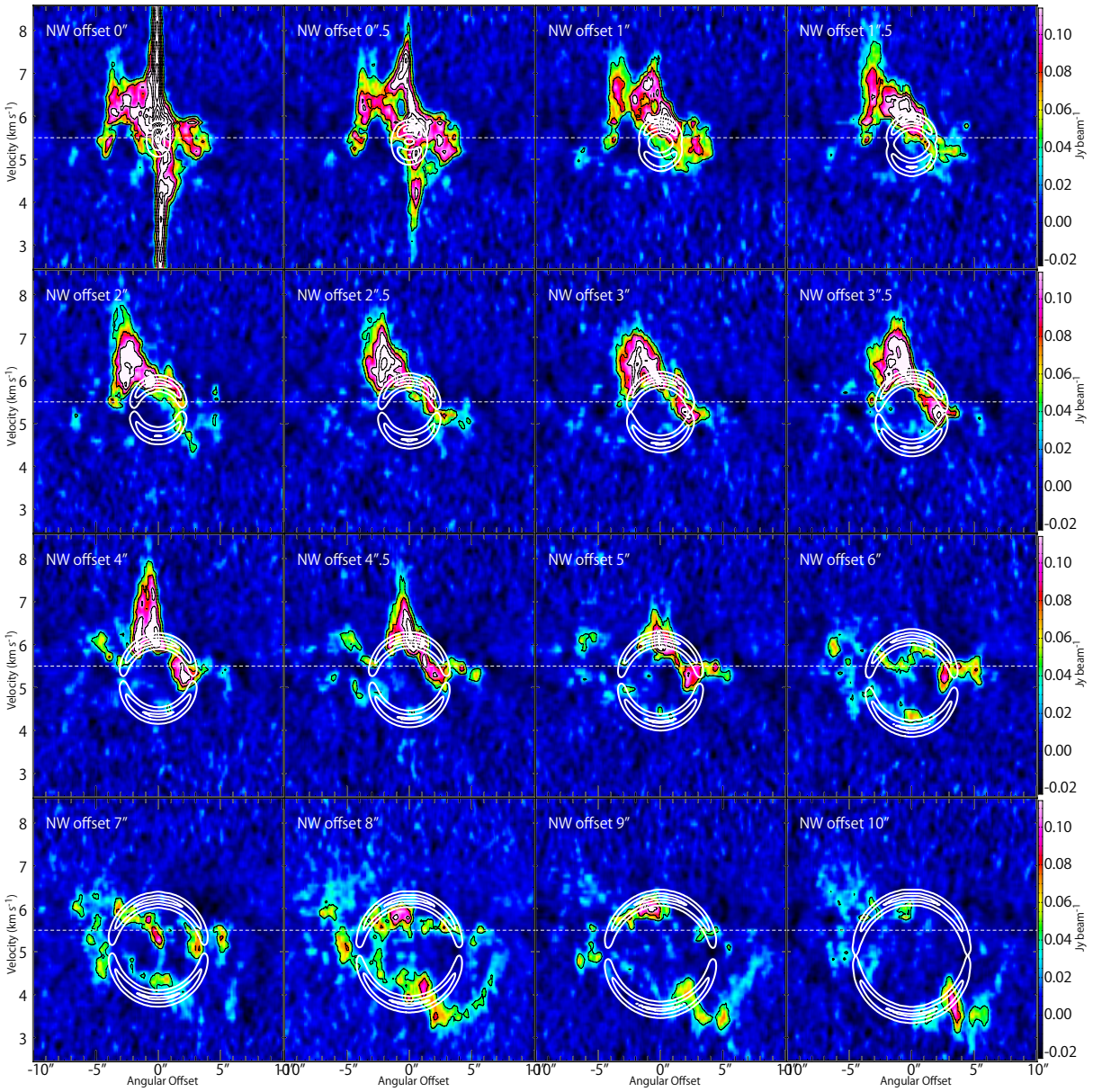

Figure 8.17: Position-velocity diagrams of CS ($J = 5 - 4$) across the outflow axis. The position axes are along the position angle of 15°, which are perpendicular to the outflow axis (P.A. 105°). Their central positions (angular offset of 0″) are on the outflow axis with an offset of the distance of (0″ − 10″) from the protostellar position toward the northwestern direction. The contour levels for CS are every 5σ, where the rms noise level is 7.6 mJy beam^{-1}. White contours represent the results of the same outflow model shown in Figure 8.16. The contour levels for the outflow model are every 40% from the 10% to the peak intensity in each panel.

expected to have a rotating motion. We examined the rotating motion of the outflow cavity wall in L1527 (Chapter 4) based on this prediction without success due to the insufficient S/N ratio. Here, we conduct such an analysis for L483, where the S/N ratio is much better than that in the L1527 case. Figures 8.18–8.21 show the model results (white contours) superposed on the PV diagrams of CS, where the rotating motion of the outflow is taken into account. The rotation velocity on the outflow cavity wall is simply calculated by assuming the angular momentum conservation. The amount of the specific angular momentum of the outflowing gas is assumed to be as the same (Figures 8.18, 8.19) or twice (Figures 8.20, 8.21) as that in the representative infalling-rotating envelope model with M of 0.15 $M_{\odot}$ and $r_{\rm CB}$ of 100 au described in Section 8.5 (7.9×10^{-4} km s^{-1} pc). In the panels with a smaller offset from the protostar, the model results are different from those without the rotating motion (Figures 8.16, 8.17). This is because the rotating motion is more prominent for a smaller radial size under the angular momentum conservation. We compare the model results with the observations, and find a hint that the models with rotating motions would better reproduce the observations than those without the rotating motion in the panels with the smaller offsets (e.g. an offset of $1'' - 4''$).

If the outflow plays a role in extraction of the specific angular momentum from the envelope gas at the centrifugal barrier, the outflow should have a specific angular momentum larger than that of the envelope. If it is the case, the outflow would have a larger rotation velocity than the model in Figures 8.18 and 8.19. Although we find a hint of the outflow rotation, it is still early to say that the outflow is launched from the centrifugal barrier. As shown in these figures, the rotating motion of the outflow, even if it exists, is difficult to be detected definitively. We thus need to observe the kinematic structure in the vicinity of its launching point much more carefully at a higher angular-resolution.

8.6.4 SiO Emission

The distribution of SiO extends to the northeastern direction from the continuum peak, as mentioned in Section 8.3. The position angle of the direction of this extension is $\sim$35° (Figure 8.4). Figure 8.22 shows the velocity channel maps of SiO. The blue-shifted component of SiO ($v_{\rm LSR} < 3.8$ km s^{-1}) is offset from the protostar by $\sim 0\farcs5$ ($\sim$ 100 au), while the weak red-shifted component appears at the protostellar position. The position of the blue-shifted component of SiO is close to the expected position of the centrifugal barrier ($r_{\rm CB} = 100$ au) or inside it. Since its velocity is faster than that of CS, it does not seem to come from a part of the infalling-rotating envelope. It is most likely that this component represents the shock caused by the outflow. The existence of such a shocked gas near the centrifugal barrier is puzzling. It might be related to the launching mechanism of the outflow, although the association of the shocked gas with the centrifugal barrier has to be explored at a higher angular-resolution.

8.7 Chemical Composition

L483 is proposed to have the WCCC character on the basis of the single-dish observations (Sakai et al., 2009a; Hirota et al., 2009, 2010; Sakai & Yamamoto, 2013). It is confirmed by detection of CCH in the vicinity of the protostar at a 1000 au scale. Nevertheless,

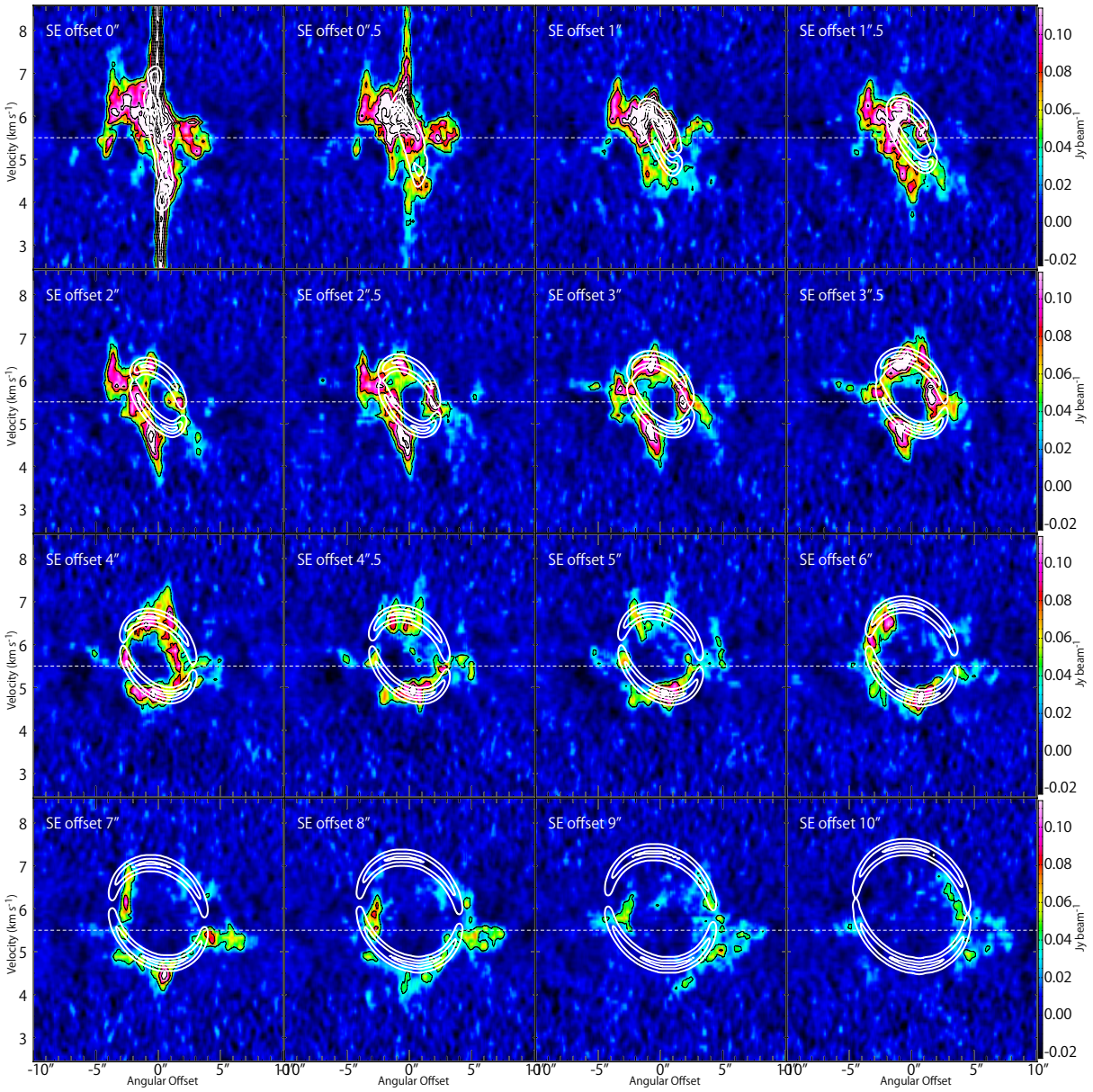

Figure 8.18: Position-velocity diagrams of CS ($J = 5 - 4$) across the outflow axis. The color maps and the black contours are the same as those in Figure 8.16. White contours represent the results of the outflow model, where the physical parameters are as follows; $i = 80°$, $C = 0.0025$ au^{-1}, and $v_0 = 0.0015$ km s^{-1} au^{-1}. A rotating motion is taken into account. The specific angular momentum of the gas is assumed to be conserved to be 7.9×10^{-4} km s^{-1} pc, which corresponds to that of the infalling-rotating envelope model with M of 0.15 $M_\odot$ and $r_{\rm CB}$ of 100 au. The contour levels for the outflow model are every 40% from the 10% to the peak intensity in each panel.

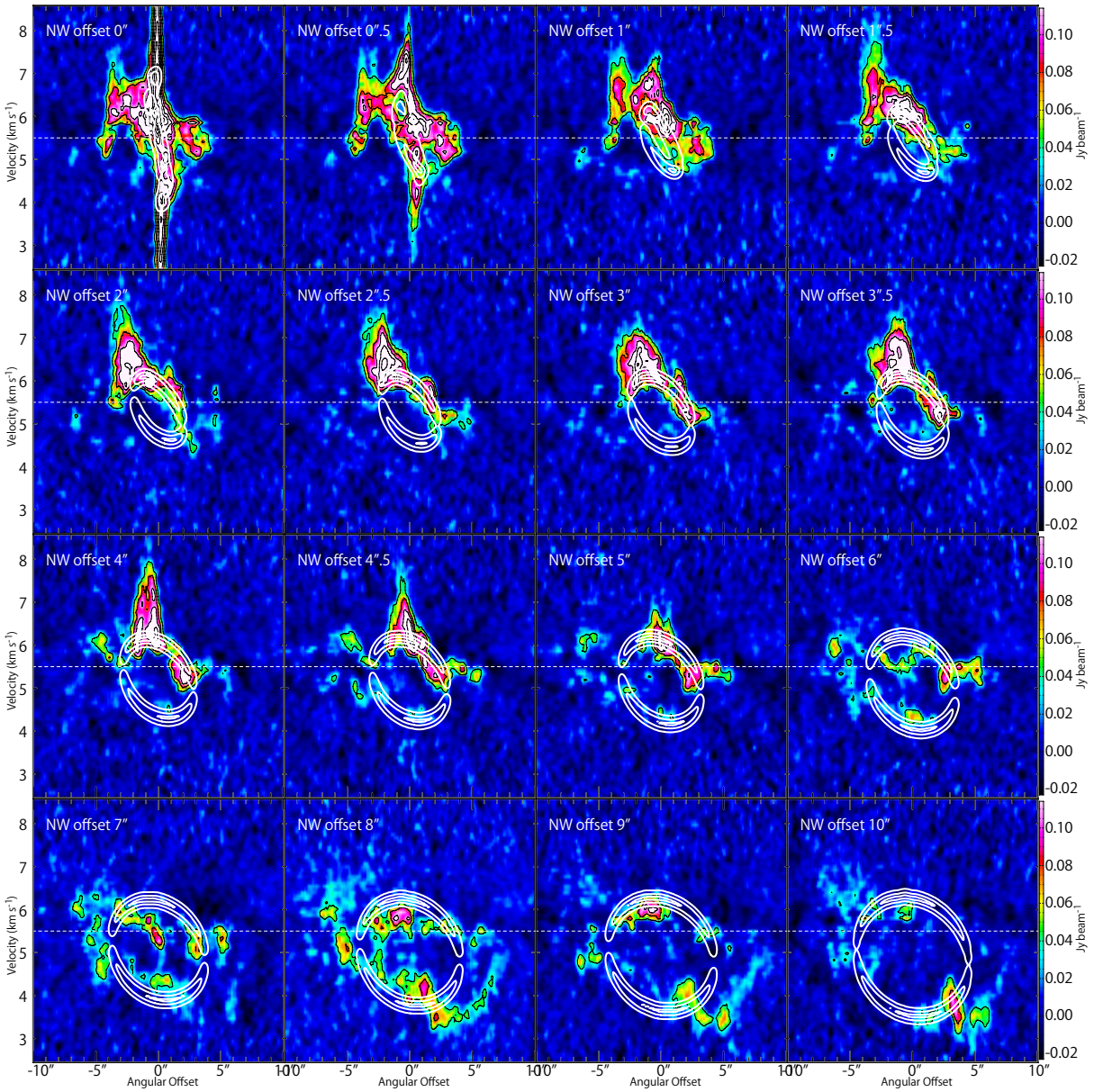

Figure 8.19: Position-velocity diagrams of CS ($J = 5 - 4$) across the outflow axis. The color maps and the black contours are the same as those in Figure 8.17. White contours represent the results of the same outflow model shown in Figure 8.18. The contour levels for the outflow model are every 40% from the 10% to the peak intensity in each panel.

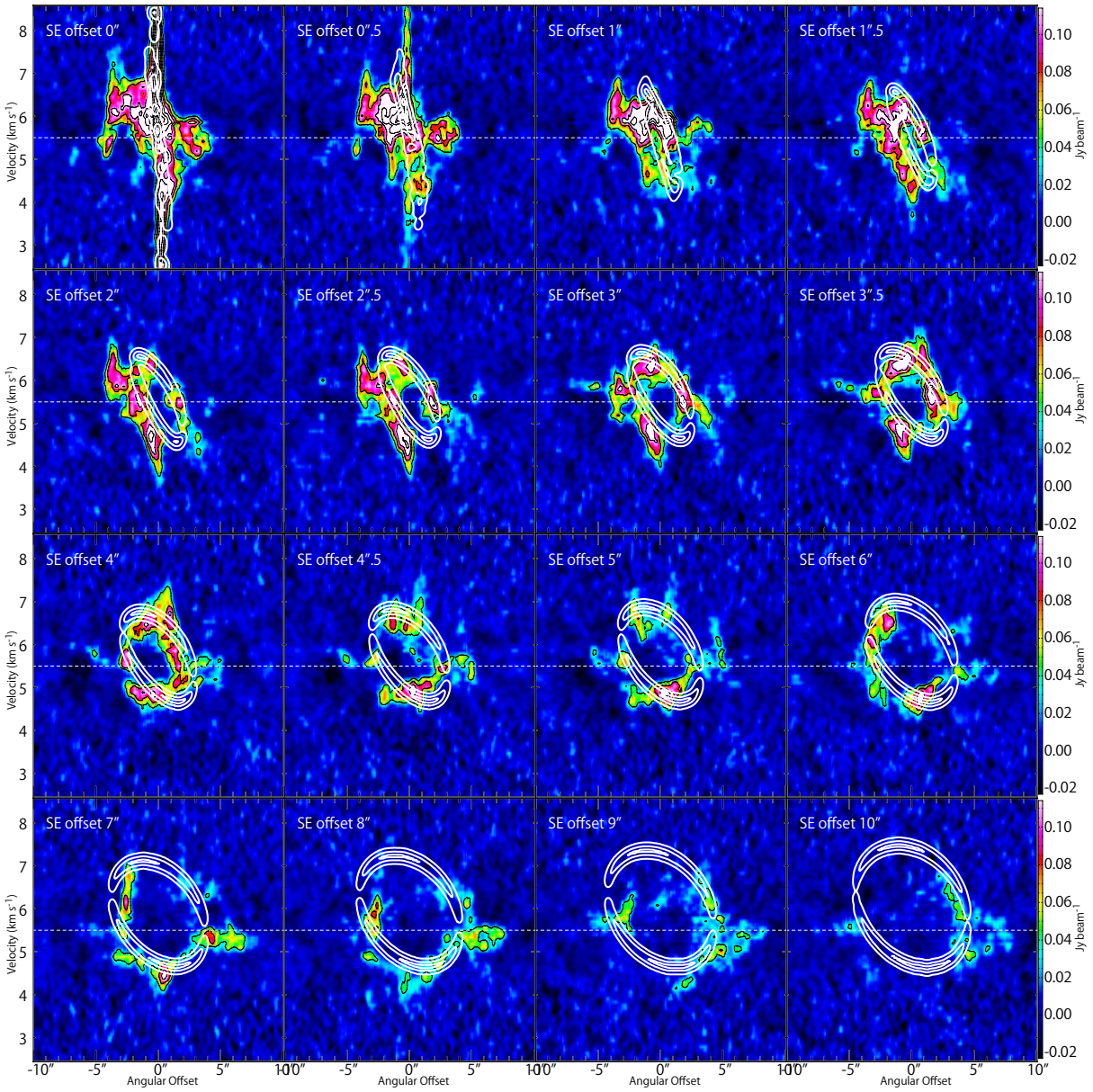

Figure 8.20: Position-velocity diagrams of CS ($J = 5 - 4$) across the outflow axis. The color maps and the black contours are the same as those in Figure 8.16. White contours represent the results of the outflow model, where the physical parameters are as follows: $i = 80°$, $C = 0.0025$ au^{-1}, and $v_0 = 0.0015$ km s^{-1} au^{-1}. A rotating motion is taken into account. The specific angular momentum of the gas is assumed to be conserved to be 15.8×10^{-4} km s^{-1} pc, which corresponds to twice that of the infalling-rotating envelope model with M of 0.15 $M_\odot$ and $r_{\rm CB}$ of 100 au. The contour levels for the outflow model are every 40% from the 10% to the peak intensity in each panel.

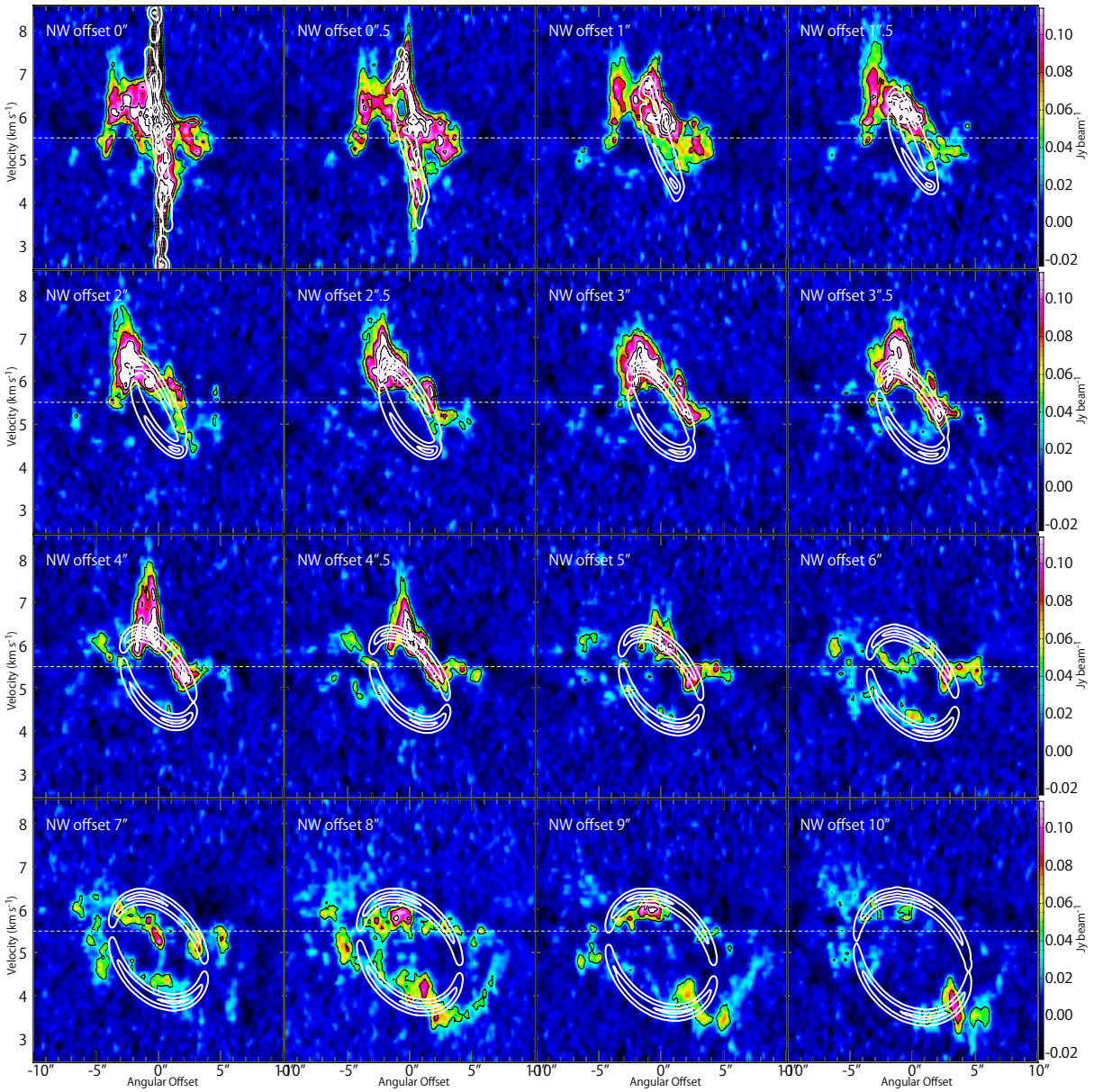

Figure 8.21: Position-velocity diagrams of CS ($J = 5 - 4$) across the outflow axis. The color maps and the black contours are the same as those in Figure 8.17. White contours represent the results of the same outflow model shown in Figure 8.20. The contour levels for the outflow model are every 40% from the 10% to the peak intensity in each panel.

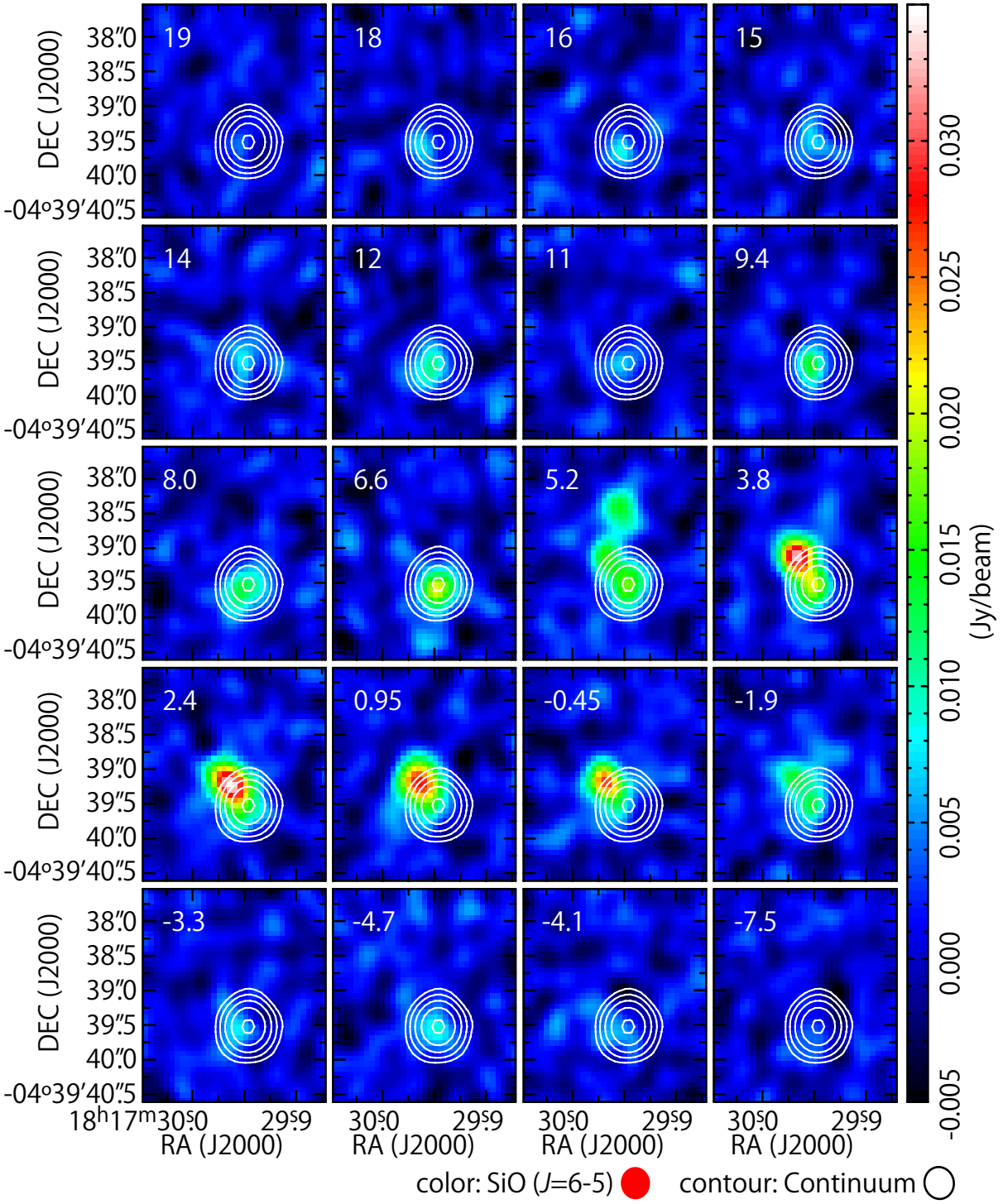

Figure 8.22: Velocity channel maps of SiO ($J = 6 - 5$; color). Each map represents the averaged intensity with the velocity width of 1.4 km s^{-1}. The white contours represent the 1.2 mm continuum map, where the contour levels are the same as those in Figure 8.2. The value in the top left corner of each panel is the averaged velocity (km s^{-1}).

NH_2CHO and $HCOOCH_3$, which are related to hot corino chemistry, are also detected. Furthermore, we tentatively detected the weak lines of t-HCOOH and CH_3CHO. This is the first spatially-resolved detection of saturated COMs in the WCCC source. Although such a mixed chemical character source has been recognized as an intermediate source in previous studies (Sakai et al., 2009a), the present observation confirms its definitive existence of such a source at a high angular-resolution.

The beam averaged column densities of NH_2CHO and $HCOOCH_3$ toward the protostellar position are evaluated by assuming local thermodynamic equilibrium at 70, 100, and 130 K (Table 8.2). This range of the temperature is typical of hot corinos (e.g. Chapter 6). The beam-averaged column densities of NH_2CHO and $HCOOCH_3$ are calculated to be $(1.5 \pm 0.7) \times 10^{14}$ cm^{-2} and $(7 \pm 4) \times 10^{15}$ cm^{-2}, respectively, at 100 K. The column densities change by 30% and 14% for the change in the assumed temperature by $\pm$30 K for NH_2CHO and $HCOOCH_3$, respectively. The column density of the tentatively detected species (t-HCOOH) and the upper limits to the column densities of CH_3CHO and $(CH_3)_2O$ are also calculated, as shown in Table 8.2.

To derive their fractional abundances relative to H_2, the beam-averaged H_2 column density is derived from the dust continuum to be 6.5×10^{23} cm^{-2} by using the following relation (Ward-Thompson et al., 2000):

$$N(\mathrm{H_2}) = \frac{2 \ln 2 \cdot c^2}{\pi h \kappa_\nu m} \times \frac{F(\nu)}{\nu^3 \theta_{\mathrm{major}} \theta_{\mathrm{minor}}} \times \left(\exp\left(\frac{h\nu}{kT}\right) - 1 \right), \tag{8.1}$$

where M is the gas mas, κ_ν is the mass absorption coefficient with respect to the gas mass, m is the averaged mass of a particle in the gas (3.83×10^{-24} g), ν is the frequency, $F(\nu)$ is the peak flux, θ_{major} and θ_{minor} are the major and minor beam size, respectively, c is the speed of light, h is the Planck's constant, and T is the dust temperature. We here assume the dust temperature of 100 K. κ_ν is evaluated to be 0.008 cm^2 g^{-1} at 1.2 mm with $\beta = 1.8$ (Shirley et al., 2011) under the assumption that κ_ν depends on the wavelength λ with the equation: $\kappa_\nu = 0.1 \times (0.3 \text{ mm}/\lambda)^\beta$ cm^2 g^{-1} (Beckwith et al., 1990). If the dust temperature is 70 K and 130 K, the H_2 column density is 9.5×10^{23} and 4.9×10^{23} cm^{-2}, respectively. The fractional abundances relative to H_2 are then evaluated to be $(1.3 - 3.9) \times 10^{-10}$ and $(7.3 - 16.2) \times 10^{-9}$ for NH_2CHO and $HCOOCH_3$, respectively, by assuming that the gas temperature is the same as the dust temperature (Table 8.2). These fractional abundances of NH_2CHO and $HCOOCH_3$ are comparable with those reported for the hot corinos, IRAS 16293–2422 (6×10^{-10} and 9×10^{-9}; Jaber et al., 2014) and B335 ($(1 - 9) \times 10^{-10}$ and $(2 - 8) \times 10^{-9}$; Imai et al., 2016). Therefore, L483 indeed harbors a hot corino activity in the closest vicinity of the protostar.

As mentioned in Section 8.4, different molecules trace different parts in this source. The infalling-rotating envelope is traced by CS (and possibly CCH), while the compact component concentrated in the vicinity of the protostar, which is likely to be a disk component inside the centrifugal barrier, is traced by CS, SO, HNCO, NH_2CHO, and $HCOOCH_3$. As described in the previous chapters, such a chemical change around the centrifugal barrier is reported for some other sources; L1527, TMC-1A, IRAS 16293–2422 Source A, and Source B (Chapters 4, 6, 7; Sakai et al., 2014b, 2016). However, CS and SO are found to be quite abundant in the compact component concentrated in the vicinity of the protostar in this source in contrast to the L1527 and TMC-1A cases. The situation similar to L483 is also seen in IRAS 16293–2422 A (Section 8.4.2). Thus, the chemical

change would be highly dependent on sources. Hence, it is still essential to investigate chemical structures of various protostellar sources at a sub-arcsecond resolution.

8.8 Summary of This Chapter

We observed the Class 0 protostar L483 with ALMA in various molecular lines. The major results are as follows:

(1) A chemical differentiation at a 100 au scale is found in L483. The CCH emission has a central hole of $0''.5$ (100 au) in radius. The CS emission traces the compact component concentrated near the protostar, the extended envelope component, and a part of the outflow cavity. In contrast, the SO and HNCO emission only shows the compact component.

(2) In spite of the WCCC character of this source, the saturated COMs, NH_2CHO and $HCOOCH_3$, are detected. Their emission is highly concentrated near the protostar. This result is the first spatially-resolved example of the mixed character source of WCCC and hot corino chemistry.

(3) The kinematic structures of the envelope and the disk components traced by CS are analyzed by simple models of the infalling-rotating envelope and the Keplerian disk in order to understand the observed chemical differentiation in terms of the physical structure. The protostellar mass of $0.1 - 0.2\ M_\odot$ and the radius of the centrifugal barrier of $30 - 200$ au roughly explain the infalling-rotating envelope part of the observed PV diagrams of CS. The compact component likely traces the Keplerian disk component inside the centrifugal barrier, although the rotation curve is not resolved. Hence, the above chemical change seems to be occurring around the centrifugal barrier.

(4) In L483, CS, which is thought to be a good tracer of the infalling-rotating envelope, traces the disk component as well as the envelope component. SO, which highlights the ring-like structure around the centrifugal barrier in L1527 and TMC-1A, also traces the disk component in this source. These results would originate from the higher luminosity of L483.

(5) CS also traces the outflow component extending along the southeast-northwest direction. It is recognized as the outflow cavity wall and its kinematic structure is well explained by a parabolic outflow model.

(6) The SiO distribution has an extension from the protostellar position. It may trace the local outflow-shock near the centrifugal barrier.

Table 8.2: Column Densities and Fractional Abundances of the Molecules Observed toward the Protostar Position[a,b]

	Column Density (10^{14} cm^{-2})			Fractional Abundance Relative to H_2 (10^{-10})		
Dust Temperature	70 K	100 K	130 K	70 K	100 K	130 K
CS	5.1 ± 0.2	6.2 ± 0.2	7.5 ± 0.2	5.3 ± 0.2	9.6 ± 0.3	15.2 ± 0.5
HNCO	9.6 ± 1.1	11.5 ± 1.3	14.1 ± 1.6	10.0 ± 1.1	17.7 ± 2.0	28.6 ± 3.2
NH_2CHO	1.2 ± 0.6	1.5 ± 0.7	1.9 ± 0.9	1.3 ± 0.6	2.4 ± 1.1	3.9 ± 1.9
$HCOOCH_3$	69.8 ± 35.9	69.9 ± 36.0	80.0 ± 41.2	73 ± 38	107 ± 55	162 ± 84
			Tentative-detection			
t-HCOOH	2.0 ± 1.9	2.4 ± 2.2	2.9 ± 2.7	2.1 ± 1.9	3.6 ± 3.4	5.8 ± 5.5
			Upper Limit			
CH_3CHO	< 0.62	< 0.75	< 0.95	< 0.65	< 1.2	< 1.9
$(CH_3)_2O$	< 116.1	< 119.6	< 135.0	< 121.6	< 183.8	< 273.6

[a] Derived under the assumption of local thermodynamic equilibrium at the temperature of 100K. N(H_2) is derived from the 1.2 mm dust continuum emission (See Section 8.7).

[b] Errors are derived from three times the root mean square noise of the integrated intensity.

Chapter 9

Chemical Differentiation

In this thesis, we have investigated the emission of various molecular lines toward the five young low-mass protostellar sources. We have confirmed the chemical difference of the disk-forming region between the sources showing the WCCC and the hot corino chemistry. We have also found a drastic chemical change across the centrifugal barrier in each source; some molecular lines preferentially trace the infalling-rotating envelope component, while others highlight its centrifugal barrier. Moreover, some molecular lines trace disk components even inside the centrifugal barrier. We here discuss chemical processes which cause the chemical diversity and the chemical differentiation.

9.1 Chemical Diversity

9.1.1 Chemical Diversity in a Disk Forming Region

As described in Chapter 1, it is well known that the chemical composition of the protostellar envelopes shows significant diversity at a 1000 au scale (Sakai & Yamamoto, 2013). The two distinct cases are the warm carbon-chain chemistry (WCCC) and the hot corino chemistry. In this thesis, the chemical composition and its distribution in the vicinity of a protostar were investigated toward the five representative sources revealing the WCCC and the hot corino chemistry. We confirmed that the chemical diversity recognized at a few 1000 au scale resolution by single-dish observations can also be seen at a 100 au scale by high angular resolution observations with ALMA (Table 9.1); WCCC sources, L1527 and IRAS 15398–3359 (Chapter 4 and 5), are rich in unsaturated carbon-chain and related molecules (e.g. CCH and c-C_3H_2) at a few 100 au scale, while they are confirmed to be deficient in saturated complex organic molecules (COMs; e.g. CH_3OH) even with the high angular resolution and high sensitivity of ALMA. On the other hand, hot corino sources, IRAS 16293–2422 Source A and Source B (Chapters 6 and 7), are confirmed to be rich in COMs, such as CH_3OH and $HCOOCH_3$, and their distributions are highly concentrated in the vicinity of the protostar at a 100 au scale or smaller. These results suggest that the chemical diversity seen at a few 1000 au scale resolution is indeed seen in a more compact region at a 100 au scale for the above sources as it is.

Table 9.1: Chemical Differentiation in Low-Mass Protostellar Sources

Source Name	Chemistry	Luminosity ($L_\odot$)	Envelope	Centrifugal Barrier	Disk
L1527[a]	WCCC	1.7	CCH, c-C_3H_2, CS, H_2CO	SO	H_2CO (, CS?)
IRAS 15398–3359[b]	WCCC	1.8	CCH, H_2CO		(H_2CO?)
TMC-1A[c]	WCCC	2.5	CS	SO	
IRAS 16293–2422 Source A[d]	HC[e]	22	OCS, H_2CS	CH_3OH, $HCOOCH_3$	H_2CS (, COMs?)
IRAS 16293–2422 Source B[f]	HC[e]		OCS, H_2CS	CH_3OH, $HCOOCH_3$	(OCS?)
L483[g]	Intermediate	13	CCH, CS	SO	CS, SO, COMs[h]
B335[i]	Intermediate	0.72	CCH, CS	(Not resolved: CS, SO, COMs[h])[j]	

[a] This work (Chapter 4) and Sakai et al. (2014a,b). The bolometric luminosity is taken from Green et al. (2013).
[b] This work (Chapter 5). The bolometric luminosity is taken from Jørgensen et al. (2013).
[c] Taken from Sakai et al. (2016). The bolometric luminosity is taken from Green et al. (2013).
[d] This work (Chapter Chapter 6). The bolometric luminosity is taken from Crimier et al. (2010). It is a sum for Sources A and B.
[e] Hot corino chemistry.
[f] This work (Chapter Chapter 7). The bolometric luminosity is taken from Crimier et al. (2010). It is a sum for Sources A and B.
[g] This work (Chapter Chapter 8). The bolometric luminosity is taken from Shirley et al. (2000).
[h] e.g., NH_2CHO and $HCOOCH_3$.
[i] Taken from Imai et al. (2016). The bolometric luminosity is taken from Evans et al. (2015).
[j] The centrifugal barrier and the disk component are not resolved.

On the other hand, L483 (Chapter 8), which was recognized as a WCCC candidate source based on single-dish observations (Hirota et al., 2009, 2010) shows a different feature. In this source, CCH is indeed abundant at a few 100 au scale with the ALMA observations, which is consistent with its WCCC characteristics. However, some COM lines (HNCO, NH_2CHO, and $HCOOCH_3$), which are specific to the hot corino chemistry, are also detected in the vicinity of the protostar at a 100 au scale or smaller. Since COMs are generally expected to be deficient in WCCC sources as shown in the above L1527 and IRAS 15398–3359 cases, the detection of the COM emission in L483 was completely unexpected. Hence, L483 shows the WCCC characteristics at the envelope scale ($\sim$ a few 100 au), while it shows the hot corino activity at the disk formation scale ($\sim$ 100 au). Such a mixed character source was first identified definitively, although its existence was suggested by single-dish observations of carbon-chain molecules (CCH, C_4H, etc.) and CH_3OH (Sakai et al., 2009a, Higuchi et al. in prep.).

In this regard, Imai et al. (2016) recently reported that the low-mass Class 0 source B335 reveals the hot corino chemistry. B335 is a representative Bok globule (Keene et al., 1980) and is regarded as one of the best test-bed source for the star formation studies (e.g., Yen et al., 2015; Evans et al., 2015). They conducted the ALMA observation toward B335, and detected a number of COM lines (CH_3CHO, NH_2CHO, and $HCOOCH_3$) concentrated within a few 10 au around the protostar. Thus, B335 apparently harbors a hot corino. Nevertheless, they also found that this source shows extended distributions of CCH and c-C_3H_2 over a scale of a few 100 au. Based on these results, B335 can be interpreted as the mixed character source, as in the case of L483.

In any case, a 100 au scale is just a scale of protoplanetary disks. Thus, all the above results imply that the initial condition in chemical evolution from protoplanetary disks to planets already has diversity at the earliest evolutionary stages.

9.1.2 Which Kind of the Chemical Characteristics is Common?

WCCC and the hot corino chemistry are distinct cases of the chemical diversity of protostellar sources, and have often been thought to be exclusive to each other. The difference in the duration time of the starless core is suggested to be the cause of the difference of the chemical composition (Sakai et al., 2009a; Sakai & Yamamoto, 2013). In this picture, the chemical evolution of starless cores from the time when the external UV radiation is shielded to the time of the birth of a protostar is considered. In the initial stage of the chemical evolution, the carbon mostly exists in the ionized form (C^+) or the atomic form (C), and they are gradually converted to CO through gas-phase chemical reactions. The time scale of the conversion ($\tau_{\rm chem}$) is estimated to be a few 10^5 yr. The time scale is determined by the H_3^+ density, which is roughly independent of the H_2 density (Suzuki et al., 1992; Yamamoto, 2017)[#]. The chemical time scale is comparable to the dynamical

[#] The chemical time scale is determined by formation time scale of molecules. Molecular formation is initiated by the reaction with H_3^+, and hence, the time scale is given by $\frac{1}{k[H_3^+]}$, where k is the Langevin rate coefficient (10^{-9} cm^3 s^{-1}; Yamamoto, 2017). Since $[H_3^+]$ is 10^{-4} cm^{-3} independent of the H_2 density, the chemical time scale is about 3×10^5 yr.

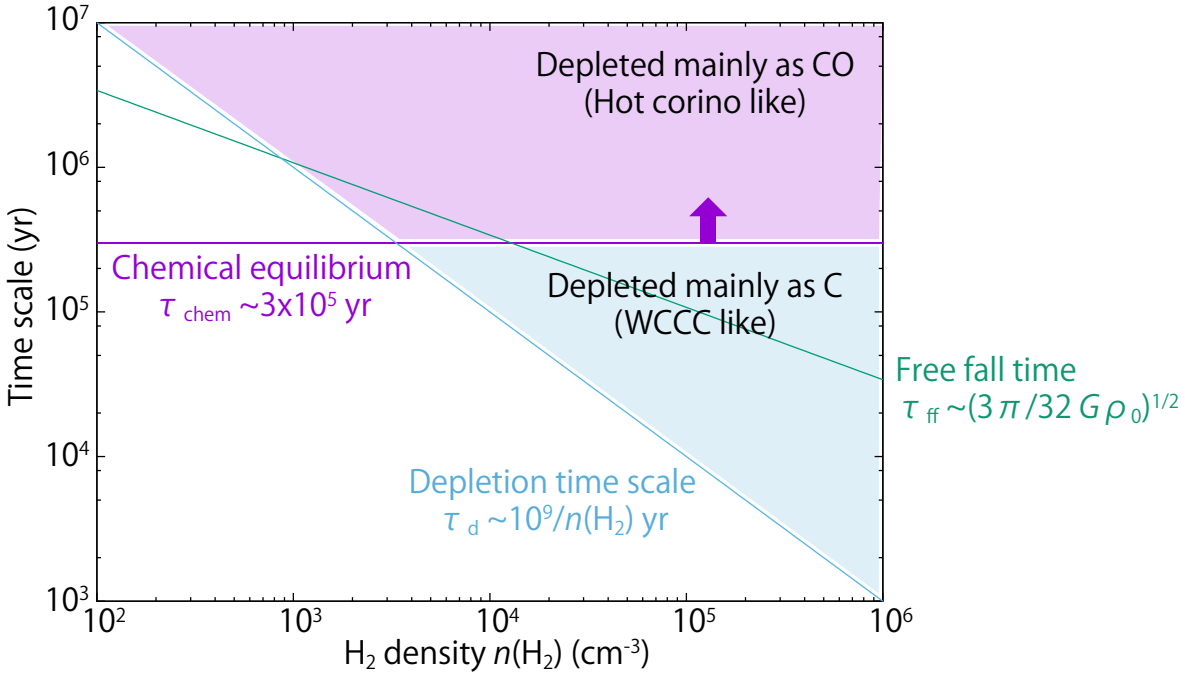

Figure 9.1: Various time scales as functions of H_2 density. If the depletion time scale is longer than the time scale of the chemical equilibrium, the atomic C is converted to CO, and then CO is adsorbed onto the dust grains. If the depletion time scale is shorter than the time scale of the chemical equilibrium, the atomic C is adsorbed onto the dust grains as it is. This mechanism causes the diversity of the chemical composition of grain mantle, and thereby that of protostellar cores.

time scale; the free fall time is represented as follows:

$$\tau_{\rm ff} = \sqrt{\frac{3\pi}{32 G \rho_0}} \tag{9.1}$$

$$\propto n({\rm H_2})^{-\frac{1}{2}}, \tag{9.2}$$

where G denotes the gravitational constant, and ρ_0 the initial mass density. The time scale of the molecular adsorption onto the dust surface (the depletion time scale) is roughly estimated to be as follows (e.g., Yamamoto, 2017):

$$\tau_{\rm d} = \frac{10^9}{n({\rm H_2})} {\rm yr} \tag{9.3}$$

$$\propto n({\rm H_2})^{-1}. \tag{9.4}$$

Figure 9.1 shows the relation between the above time scales and the H_2 density. These time scales ($\sim 10^5$ yr) are comparable to that of the starless-core stage (a few 10^5 yr; Chapter 1).

If the duration time of such a starless core phase is long, the core stays in a moderately dense condition for a long time. Then the gas-phase carbon is mostly converted to CO,

and then CO is depleted onto dust grains, as the density increases (Figure 9.2a). The CO molecules on dust grains are subject to hydrogenation reactions with the H atom to form CH_3OH and probably COMs such as CH_3CHO, $HCOOCH_3$, and $(CH_3)_2O$. After the onset of star formation, dust grains are heated up, and COMs are evaporated. This is the hot corino chemistry. If the duration time is, in contrast, short, the C atom is mainly depleted onto dust grains before it is converted to CO in the gas phase (Figure 9.2b). The C atoms on dust grains are hydrogenated to form CH_4. After the onset of star formation, CH_4 comes out of dust grains, and produces various carbon-chain molecules in the gas phase as:

$$C^+ + CH_4 \rightarrow C_2H_3^+ + H, \tag{9.5}$$

$$C_2H_3^+ + e^- \rightarrow C_2H_2 + H, C_2H + H + H. \tag{9.6}$$

This is the WCCC. The basic picture of these processes are confirmed by the chemical model calculations (Aikawa et al., 2008; Hassel et al., 2008). The exclusive nature of WCCC and hot corino chemistry can thus be explained. At the same time, the existence of a source with an intermediate (or mixed) chemical characteristics is also expected in this scheme, because the depletion of the mixture of C and CO can occur for an appropriate duration time.

Both the WCCC and the hot corino chemistry are triggered by evaporation of molecular species from dust grains. However, the temperature necessary for these two processes are different. The WCCC is triggered by evaporation of CH_4, which occurs in a warm region above $25-30$ K. On the other hand, the hot corino chemistry is triggered by evaporation of COMs or disruption of ice mantle of dust grains, which occurs in a hot region above 100 K. Hence, the WCCC region is generally larger than the hot corino. Before the ALMA era, the both regions are sufficiently smaller than the observation beams, and hence, they are just regarded as the chemical feature of protostellar cores. However, these two regions are now resolved at a high angular resolution with ALMA. In fact, the above L483 case seems to be a good example of a source with the mixed characteristics.

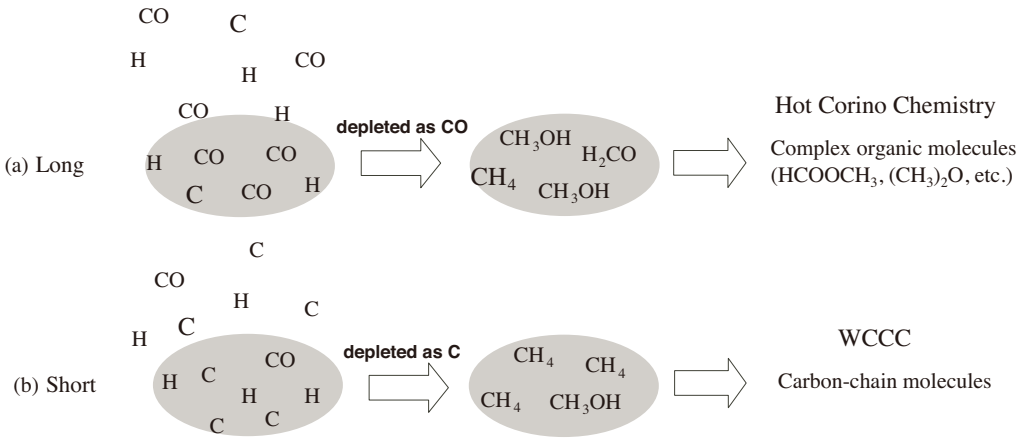

Figure 9.2: Schematic illustration of the depletion of CO and atomic C onto dust grains and their conversion into COMs and CH_4. (a) Long and (b) short duration times favor the hot corino chemistry and WCCC, respectively. Taken from Sakai et al. (2009a).

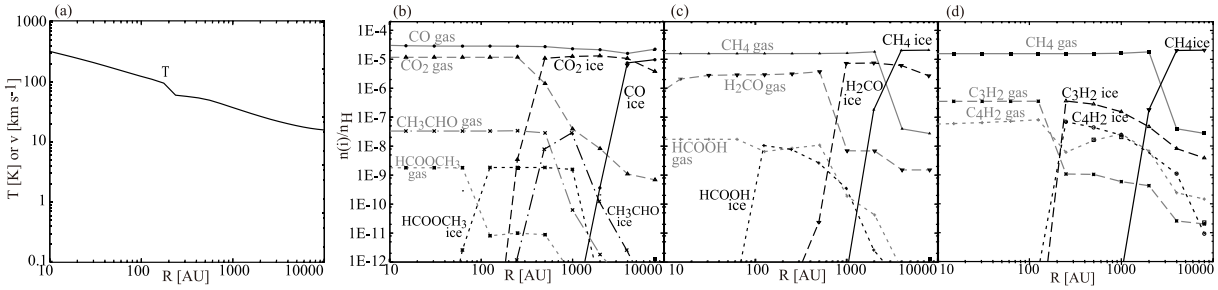

Figure 9.3: Radial distribution of (a) the gas temperature and (b–d) those of molecules in the protostellar core at the final stage of the chemical model of the contracting cloud. Black lines represent ice-mantle species, while gray lines represent gas-phase species. Taken from Aikawa et al. (2008).

In fact, the chemical model calculations predict the mixed chemical characteristics. Figure 9.3 shows the result of the chemical model calculation for a contracting protostellar core (Aikawa et al., 2008). In this model, CH_4 is evaporated at the radius of 1000 au from the protostar, and triggers the WCCC. Indeed, the abundances of carbon-chain molecules start to be enhanced inward of the evaporation radius of CH_4. On the other hand, COMs appears in the inner region (< 100 au), whose temperature is higher than 100 K. Hence, the mixed chemical character source, which is identified in L483 with ALMA, may represent a 'standard' case of the chemical composition of protostellar cores. The recent result for B335 also supports this idea. So far, the representative WCCC sources, L1527 and IRAS 15398–3359, and the representative hot corino source, IRAS 16293–2422, have extensively been studied because of their peculiar chemical nature. However, they should be regarded as the distinct cases, and the intermediate (or mixed) character sources, such as L483 and B335, would be more common. In order to assess this possibility, statistical studies are required. Such studies will also provide us an important clue to understanding the 'environmental factor' responsible for the appearance of the distinct cases.

9.2 Chemical Change

9.2.1 Drastic Chemical Change around the Centrifugal Barrier

In this thesis, we have found chemical changes across the centrifugal barrier in all the observed protostellar sources. As shown in Figure 9.4, different molecules trace different physical components around the protostar.

In general, the chemical composition of the gas is changed by gas-phase reactions and/or gas-grain interactions (i.e., evaporation of molecules from dust grains as well as depletion of molecules onto dust grains). For instance, CCH is thought to be broken up by the gas-phase reaction, such as:

$$\mathrm{CCH + O \rightarrow CH + CO}, \tag{9.7}$$

$$\mathrm{He^+ + CCH \rightarrow C^+ + CH + He}, \tag{9.8}$$

$$\mathrm{H^+ + CCH \rightarrow C_2^+ + H_2}. \tag{9.9}$$

Alternatively, CCH would be depleted onto dust grains in the mid-plane just inside the centrifugal barrier, if the dust temperature is lower than its desorption temperature of about 40 K. The time scale of the depletion of molecules onto dust grains is given as: $t_{\rm dep} \sim 10^9/n({\rm H_2})$ yr. Since the mid-plane density just inside the centrifugal barrier is $10^7 - 10^8$ cm^{-3} and the temperature is about 30 K for L1527 (Sakai et al., 2014a), the depletion time scale is shorter than the rotation period at the centrifugal barrier ($\sim 10^3$ yr). Thus, CCH is lost in the gas-phase while it goes around the protostar at the centrifugal barrier, and it would not be delivered into the gas phase of the disk component inside the centrifugal barrier. In fact, CCH traces the envelope component, but not the disk component in WCCC sources in Table 9.1. Note that CCH may be delivered to the disk component in the solid phase. However, it will readily be polymerized, and never appears in the gas phase.

A similar situation may occur for CS. CS is generally abundant in the gas phase of dense molecular clouds (e.g., Tatematsu et al., 1993), and hence, they also exist in the infalling-rotating envelope. If the mid-plane temperature is lower than the desorption temperature of CS (35 K; See Appendix A), the gas-phase CS molecules falling from the envelope will be depleted onto dust grains while they are rotating (or stagnated) around the centrifugal barrier. CS is also destroyed by the ionic species like He^+ and H^+. Note that, in contrast to the CCH case, the CS + O reaction has the activation energy of 783 K, so that it is only effective at higher temperature. As a result, CS mainly traces the infalling-rotating envelope in L1527. If the mid-plane temperature is higher than the desorption temperature of CS, CS is not frozen out onto dust grains and can survive in the gas phase. This situation seems to be seen in L483, because the luminosity of L483 (13 $L_\odot$; Crimier et al., 2010) is higher than that of L1527 (1.7 $L_\odot$; Green et al., 2013), as discussed in Chapter 8.

The chemical composition can also be changed by evaporation of molecules from dust grains. There are two mechanisms that liberate surface molecules into the gas phase;

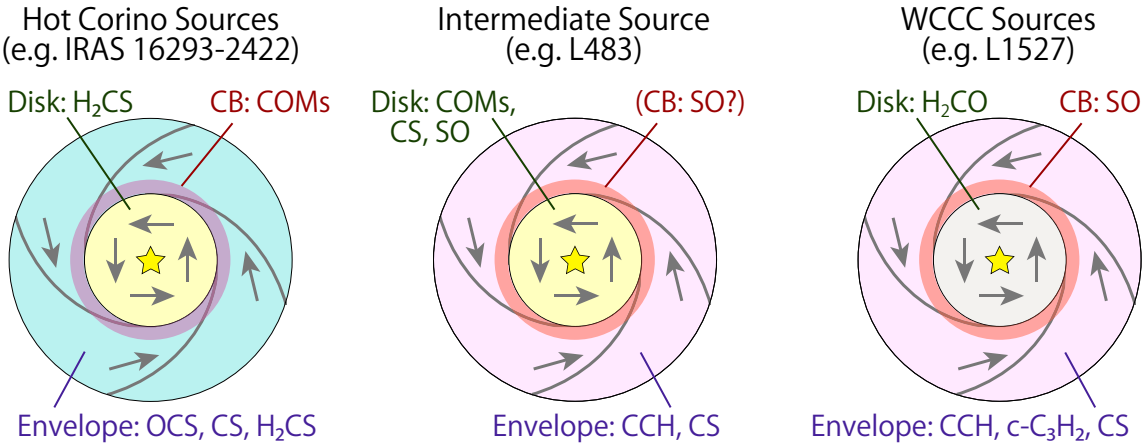

Figure 9.4: Schematic illustration of the major tracers of the envelope component, the centrifugal barrier, and the disk component in hot corino sources (left), WCCC sources (right), and the hybrid case of them (center).

those are shock heating and protostellar heating. In the infalling-rotating envelope, the gas is stagnated in front of the centrifugal barrier, and the accreting gas with the infall velocity of a few km s^{-1} causes a weak accretion shock (Aota et al., 2015; Sakai et al., 2017). Then the temperature is raised near the shock front, which evaporates the surface molecules. The SO molecules in L1527 seem to be evaporated from dust grains in this mechanism in front of the centrifugal barrier. Indeed, the temperature is found to be raised up to 60 K or higher around the centrifugal barrier (Sakai et al., 2014b, 2017). In IRAS 16293–2422 Source A, a similar enhancement of the temperature around the centrifugal barrier is observed, as described in Chapter 6. This will cause the evaporation of COMs there, which would be the origin of the hot corino chemistry.

Another mechanism responsible for desorption of molecules is the protostellar heating. Generally, the dust temperature becomes higher as approaching to the protostar due to the illumination by the protostar (Masunaga et al., 1998; Jørgensen et al., 2002). Since the desorption temperature is different from molecule to molecule, as described in Appendix A, one may expect that this causes chemical differentiation as a function of the radius from the protostar. However, the actual distribution of molecules is not as simple as expected. The different distributions of OCS and H_2CS in IRAS 16293–2422 Source A, which have similar desorption temperature, are not explained in this way. On the other hand, the contribution of this mechanism seems important for CS in L483, as mentioned above. In addition, the protostellar heating in combination with the geometrical effect of the centrifugal barrier may also play an important role of the distribution of COMs in IRAS 16293–2422 Source A, as discussed in Chapter 6. Although we cannot rule out the contribution of the protostellar heating to desorption of molecules, the physical changes around the centrifugal barrier plays an important role in the chemical differentiation.

9.2.2 Tracers in WCCC and Hot Corino Sources

As demonstrated in Chapters 4–8, the chemical compositions are useful to disentangle the physical components in the disk-forming regions. For such chemical diagnostics, it is essential to understand what kind of molecular species trace which part of the disk/envelope system.

As shown in Table 9.1 and Figure 9.4, the chemical changes are seen in different molecules in different sources. The envelope components are traced by unsaturated organic molecules (i.e. carbon-chain and related molecules) in the WCCC sources (L1527, IRAS 15398–3359, and TMC-1A), while it is traced by OCS and H_2CS in the hot corino sources (IRAS 16293–2422 Source A and Source B). The centrifugal barriers are highlighted by SO in the WCCC sources and by COMs in hot corino sources. The disk components inside the centrifugal barrier is traced by various molecules, such as H_2CO, H_2CS, SO, and COMs, depending on sources. It should be noted that the emitting region of one molecule is also different from source to source, as shown in the CS case.

Based on the above results, useful tracers of the disk/envelope system seem to depend on the chemical characteristics of sources, although some trends can be recognized. Thus, confirmation of the applicabilities of the molecules listed in Table 9.1 as the tracers of the physical components in various sources is essential to the establishment of chemical diagnostics for the disk-forming regions. Moreover, characterizing the chemical behavior of more molecular species is also awaited.

Chapter 10

Physical Diversity

In Chapters 4–8, the physical parameters have been characterized for the five sources with the aid of the infalling-rotating envelope, Keplerian disk, and outflow models described in Chapter 3. The physical parameters, such as the protostllar mass, the radius of the centrifugal barrier, and the inclination angle have been derived. In these analyses, the common existence of a centrifugal barrier in the protostellar sources is confirmed. Its physical role is an interesting issue in studies of the protostellar evolution. We here discuss it in relation to the disk formation and the mechanism of the outflow launch.

10.1 Evolution from Envelopes to Disks

The existence of the centrifugal barrier of the infalling-rotating envelope was first reported by Sakai et al. (2014a). An existence of the centrifugal barrier is naturally derived from simple assumptions of the energy and angular momentum conservation. Thus, it is expected that the centrifugal barrier of the infalling-rotating envelope commonly exists in protostellar sources. In fact, its existence or hint was observationally confirmed in the five young low-mass protostellar sources in this thesis. Moreover, disk structures seem to be formed inside the centrifugal barriers even at early evolutionary stages. The centrifugal barrier seems to be a boundary between the infalling-rotating envelope outside it and the disk component inside it. Hence, the centrifugal barrier will have an important role in the physical mechanism of the disk formation as well as in the chemical evolution described in Chapter 9.

Generally, the size of a rotationally-supported disk, or a Keplerian disk, is thought to correspond to the *'centrifugal radius'* (Hartmann, 2009b). It is the radius where the centrifugal force of the gas and the gravity under the protostellar mass are balanced, and is twice the radius of the centrifugal barrier (Chapter 3). Thus the gas can stably continue rotating around the protostar at the centrifugal radius. As mentioned later, the angular momentum of the gas infalling at a later time tends to be larger, which makes the centrifugal radius larger. This results in the smooth growth of the disk. However, this is a rather static picture. In an infalling-rotating envelope, the rotation speed and the infall speed are the same at the centrifugal radius. Since the rotation speed is the same as the Keplerian speed, the rotation motion can be continuous from the infalling-rotating envelope to the Keplerian disk at the centrifugal radius. On the other hand, there remains the infall motion, and the infalling gas tends to go further inward of the centrifugal radius.

Indeed, our observational results indicate that the gas apparently keeps falling beyond the centrifugal radius toward the centrifugal barrier.

In more realistic cases, the infall motion of the gas will be suppressed due to the gas pressure. But this effect is not effective near the centrifugal radius, as discussed below. The static ($P_{\rm stat}$) and dynamic ($P_{\rm dyn}$) pressures of the gas are represented as follows:

$$P_{\rm stat} = \rho c_s^2, \tag{10.1}$$

$$P_{\rm dyn} = \frac{1}{2}\rho v_{\rm fall}^2, \tag{10.2}$$

where ρ, c_s, and $v_{\rm fall}$ denote the density, the sound speed, and the radial velocity of the gas, respectively. Thus, if ρ can be assumed to be locally constant, the dynamic pressure is larger than the static pressure where $v_{\rm fall}$ is larger than $\sqrt{2}c_s$. Therefore the gas cannot be supported by the static pressure and keeps falling toward the centrifugal barrier.

As for the L1527 case, such a condition is expected until the gas reaches near the centrifugal barrier, as shown in Figure 10.1. In fact, the static and dynamic pressures are evaluated to be (0.5 and 1.6) $\times 10^{-6}$ dyn cm^{-2} at the centrifugal radius, where the $v_{\rm fall}$ is 0.9 km s^{-1}, with the assumptions of the gas density of 10^8 cm^{-3} and c_s of 0.35 km s^{-1}. (Note that c_s is proportional to $\sqrt{T}$, where T is the gas temperature. c_s is calculated to be $\sim$0.35 km s^{-1} with the gas temperature of 30 K in the infalling-rotating envelope of L1527.)

The magnetic pressure is represented as:

$$P_M = \frac{B^2}{2\mu_0}, \tag{10.3}$$

where B is the magnetic field and μ_0 the magnetic permeability. Then, we obtain the following practical expression:

$$P_M = 3.98 \times 10^{-14}\ B(\mu G)^2 \text{ dyn cm}^{-2}. \tag{10.4}$$

Hence, the magnetic pressure can be comparable to the dynamic pressure, only when the magnetic field is of the order of mG. According to the previous magnetic field measurements using the Zeeman effect, such a strong magnetic field can only be seen in maser spots (Crutcher, 2012), and is unlikely for the infalling-rotating envelope of the low-mass star forming regions. Furthermore, the ratio of the magnetic pressure to the static gas pressure is assumed to be unity or less in the MHD calculations (e.g. Machida et al., 2011). Otherwise the disk/envelope structure is unstable (Machida et al., 2000; Shibata et al., 1990). Therefore, the magnetic breaking is not expected to be effective around the centrifugal radius in the low-mass star forming regions, neither.

Since ρ and c_s will be increased around the centrifugal barrier due to the stagnation of the gas and the relatively high temperature at the centrifugal barrier (60 K in L1527) to the infalling-rotating envelope (30 K in L1527), the static pressure will be enhanced near the centrifugal barrier. Thus the gas may stop falling before it reaches at the centrifugal barrier. This means that the edge of the rotationally supported disk is smaller than the centrifugal radius.

On the other hand, we could expect some cases, where the infalling-rotating envelope model is not appropriate: e.g., sources with a very small or high protostellar mass. With

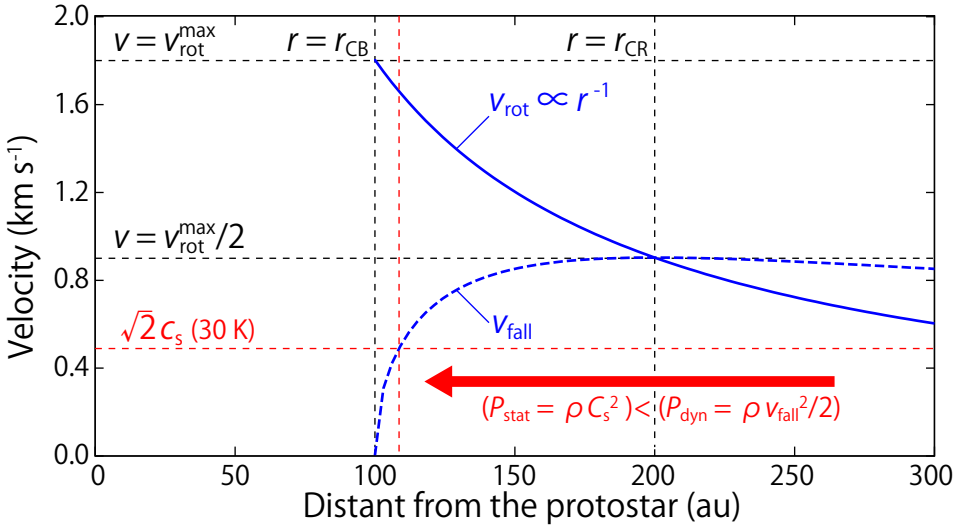

Figure 10.1: The velocity profile in the infalling-rotating envelope model for the L1527 case. In the infalling-rotating envelope model, the infall velocity is maximum ($v_{\rm fall} = 0.9$ km s^{-1}) at the centrifugal radius ($r_{\rm CR} = 200$ au). The sound speed c_s is assumed to be 0.35 km s^{-1}, which corresponds to the value at the temperature of 30 K.

a small protostellar mass, the infall velocity is small and thus the dynamic pressure of the gas is small. This will result in the static pressure around the centrifugal radius higher than the dynamic pressure. With a high protostellar mass, the gas temperature around the centrifugal radius will be high due to the high luminosity. Thus, the static pressure, which is proportional to T through c_s, could be higher than the dynamic pressure. In these situations, the infall gas may be supported by the static gas and cannot fall toward the centrifugal barrier. In addition, as for the more evolved sources, the infalling envelope gas may be exhausted, and thus the dynamic pressure may not be high enough to push the stagnated gas in front of the centrifugal barrier any more. Therefore, the edge of the disk would be extended to the centrifugal radius.

In contrast, the gas can never go inward of the centrifugal barrier unless it loses the angular momentum and the energy, and hence, it will be stagnated in front of the centrifugal barrier by colliding with the gas infalling afterwards. Such gas stagnation has recently been observed by high-resolution observations of L1527 with ALMA (Sakai et al., 2017) (See Chapter 11). The above mechanism will cause a weak accretion shock around the centrifugal barrier, as mentioned in Chapter 9, which is indeed highlighted by the emission of SO and COMs for the WCCC and hot corino sources, respectively. Thus the disk formation, that is the transition from the infalling-rotating envelope to the disk component, is not a straightforward process, but involves discontinuous physical processes.

Although our infalling-rotating envelope model can reasonably explain the basic kinematic structure observed for the five protostellar sources, some caveats need to be mentioned. The infalling-rotating envelope model used in this thesis is a quite simplified one; it does not consider various effects, such as gas pressure, magnetic breaking, self gravity, and time variation of the angular momentum. In reality, these effects will affect *'where the infall motion of the gas practically vanishs'*. These complex situations considered,

it is still unknown *'what is occurring between the centrifugal radius and the centrifugal barrier'*. Thus, more detailed investigations of the physical structure in the disk forming region are needed to understand the detailed physical mechanisms.

10.2 Angular Momentum of the Envelope Gas

As shown in Chapters 4–8, the radius of the centrifugal barrier ($r_{\rm CB}$) varies from source to source; the centrifugal barrier is spatially resolved in some sources (e.g. L1527), while it is not in some other sources in the present study (e.g. IRAS 15398–3359). This suggests that the magnitude ratio of the rotation motion relative to the infall motion depends on sources. Since a disk structure is supported by a rotation motion of the gas around the protostar, characterization the ratio is essential to understanding the disk formation. To discuss it more quantitatively, we derive the specific angular momentum (j) of the envelope gas. In the infalling-rotating envelope model (Chapter 3), the radius of the centrifugal barrier can be represented in terms of j in the following equation:

$$r_{\rm CB} = \frac{j^2}{2GM}, \tag{10.5}$$

where G denotes the gravitational constant, and M the protostellar mass. Since $r_{\rm CB}$ is proportional to the square of j, a small change in j results in a large change in $r_{\rm CB}$. Thus, $r_{\rm CB}$ is a good barometer of j. With the equation (10.5), j can be derived from M and $r_{\rm CB}$, which are determined from the observations with the aid of the infalling-rotating envelope model. The j value derived for each source is summarized in Table 10.1. The table includes the results reported for TMC-1A and B335 (Sakai et al., 2016; Imai et al., 2016). In Table 10.1, j seems to vary by an order of magnitude from source to source.

It is theoretically expected that the specific angular momentum increases along the protostellar evolution for a single source. When we consider a turbulent parent core, the most fundamental rotation motion is the rigid rotation. In this case, the gas more distant from the center possesses a larger specific angular momentum. Along with the evolution of the source, the gas that was originally more distant from the protostar falls toward the protostar, and it brings a larger specific angular momentum into the vicinity of the protostar. Thus, the specific angular momentum of the infalling gas in the vicinity of the protostar is thought to increase gradually. Since the evolution of the specific angular momentum will affect the physical condition of a future disk structure, its characterization is essential in the study of the disk formation. However, such a trend cannot clearly be seen in Table 10.1. For instance, the j value for the Class I source TMC-1A is similar to that of the Class 0 sources. The specific angular momentum can also vary from source to source depending on the initial angular momentum of the parent clouds. This contribution may overwhelm the potential evolution of the specific angular momentum in a single source. Yen et al. (2017) compiled the measurements of j at various size scales for various sources, and indicated a significant variation of j at the small radius. Their result is consistent with ours.

10.3 Relation between the Envelope and the Outflow

The gas at the centrifugal barrier cannot fall into the disk inside it because of the energy and angular momentum conservation. Thus, some mechanisms to extract the angular momentum of the envelope gas are required to form the disk component and also to make the protostar grow further. Outflows are thought to be the most probable candidate for such a mechanism. If this is the case, outflows would be launched from the centrifugal barrier to bring out the angular momentum. In fact, hints of this picture are seen in this thesis; in IRAS 16293–2422 Source B (Chapter 7), the pole-on outflow lobes traced by SiO show a radial offset near the protostar, and their launching point seems to be near the centrifugal barrier traced by OCS and H_2CS (Figure 7.18). In L483 (Chapter 8), the SiO emission shows an intensity peak at the position apart from the protostar by 100 au, which corresponds to the radius of the centrifugal barrier (Figure 8.22). Since SiO is known as a shock tracer (e.g., Mikami et al., 1992), the results for the both sources imply a possible shock between the outflowing gas and the infalling envelope gas near the centrifugal barrier.

Sakai et al. (2017) reported that the envelope gas in L1527 is stagnated at the centrifugal barrier, and that it has a substantial extension perpendicular to the mid-plane. It is likely that a part of the gas is moving away from the mid-plane. Sakai et al. (2017) suggested a possibility that this outflowing motion forms the so-called 'disk winds' or 'low-velocity molecular outflow' launched at the centrifugal barrier. If so, one would expect a rotation motion of the outflow particularly in the vicinity of the centrifugal barrier. However, a definitive evidence of the rotation motion of the outflow has not been seen in L1527 (Chapter 4). Although a hint of the outflow rotation is seen in L483 (Chapter 8), the relation between the outflow launching and the centrifugal barrier is still controversial at this stage.

If the centrifugal barrier is responsible for the outflow launch, there would be some relations between the radius of the centrifugal barrier and the outflow shape. For instance, the outflow launched from the smaller radius of the centrifugal barrier may be more collimated due to less centrifugal motion. To inspect such a possibility, the outflow parameter C is plotted against the specific angular momentum of the infalling-rotating envelope (Figure 10.2). However, a clear relation is not seen between them at the present stage; there is a big difference in C between L1527 and L483, having the similar specific angular momentum. More samples are apparently needed.

10.4 Evolution of Outflows

The C and v_0 values for the several sources are listed in Table 10.2, where the error ranges for L1527, IRAS 15398–3359, and L483 are estimated by eye from the fits with various parameters. Since the observations with ALMA in this thesis are focused on the central region around the protostar, the dynamical time scales cannot be estimated adequately from our data. Therefore, the dynamical time scales for L1527 and IRAS 15398–3359 in Table 10.2 are taken from Yıldız et al. (2015).

Table 10.1: Physical Parameters[a]

Source Name	Evolutional Stage	Chemistry[b]	Inclination Angle (°)[c]	Protostellar Mass ($M_\odot$)	Radius of the CB[d](au)	j (10^{-4} km s^{-1} pc)[e]
L1527[f]	Class 0/I	WCCC	85	0.18 ± 0.05	100 ± 20	8.7 ± 1
IRAS 15398–3359[f]	Class 0/I	WCCC	70	0.02 ± 0.02	<30	<1.6
TMC-1A[g]	Class I	WCCC	70	0.25 ± 0.05	50 ± 10	7.2 ± 1
IRAS 16293–2422 Source A[f]	Class 0	HC	60	0.75 ± 0.25	50 ± 10	12.5 ± 2
IRAS 16293–2422 Source B[f]	Class 0	HC	5	$0.4^{+0.4}_{-0.2}$	40 ± 10	8.2^{+4}_{-2}
L483[f]	Class 0	Intermediate	80	0.15 ± 0.05	100^{+100}_{-70}	7.9^{+4}_{-3}
B335[h]	Class 0	Intermediate	90	>0.13	<10	∼2.9

[a] The protostellar mass and the radius of the centrifugal barrier are derived with the aid of the infalling-rotating envelope model, except for the values for B335. They typically contains uncertainties of about a few 10%. See the analysis sections for each source for more details.

[b] 'WCCC' represents the warm carbon-chain chemistry, while 'HC' represents the hot corino chemistry.

[c] 0° for a face-on configuration. The values for L1527, IRAS 15398–3359, and L483 are derived from the outflow analysis (See Table 10.2).

[d] Centrifugal barrier.

[e] Specific angular momentum of the envelope gas derived from the protostellar mass and the radius of the centrifugal barrier.

[f] This work (Chapters 4–8).

[g] Taken from Sakai et al. (2016).

[h] Taken from Imai et al. (2016). The specific angular momentum is calculated by assuming M of 0.13 $M_\odot$ and $r_{\rm CB}$ of 10 au, just for reference.

10.4.1 Comparison between L1527 and IRAS 15398–3359

Both of L1527 (Chapter 4) and IRAS 15398–3359 (Chapter 5) have a nearly edge-on configuration of the outflow/envelope structure. However, the appearance of their outflows shown in the integrated intensity maps are quite different from each other. The outflow of L1527 shows a butterfly-feature, while that of IRAS 15398–3359 is well collimated. While we assumed an offset between the two lobes in L1527 to explain the outflow structure as suggested by Tobin et al. (2008) (Section 4.2.3), no such offset is seen for the two lobes in IRAS 15398–3359. It should be noted that the outflow component is contaminated with the envelope component within 1″ from the protostar position in IRAS 15398–3359. Apart from the offset, the difference of the opening angles of the outflow cavity is reflected on the difference of the values of C by a factor of 14 (Table 10.2).

10.4.2 Relation to Dynamical Ages

The outflow parameters are reported for the Class 0/I source VLA 05487 in the Orion dark cloud L1617 and the Class II/III source RNO 91 in the L43 molecular cloud by Lee et al. (2000). Moreover, those for the Class 0 source L1448C (L1448 mm) in Perseus are reported by Hirano et al. (2010), and those for the HH 46/47 molecular outflow on the outskirts of the Gum Nebula by Arce et al. (2013). The outflow parameters for these sources are summarized in Table 10.2. Here, it should be noted that the coefficient of proportionality reported for these sources are in the unit of arcsecond:

$$C_{\rm as} = CD, \quad v_{\rm as} = v_0 D, \tag{10.6}$$

where D denotes the distance of the source.

Figure 10.3 shows a semi-log plot of C versus dynamical time scale $t_{\rm dyn}$ for these six sources. The green dashed line in Figure 10.3 represents the best-fit result, where an

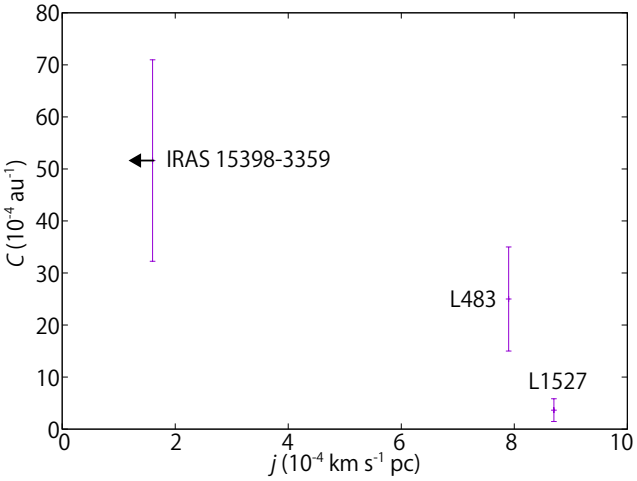

Figure 10.2: Plots of the curvature parameter (C) of the outflow against the specific angular momentum of the infalling-rotating envelope. The value of the specific angular momentum for IRAS 15398–3359 is the upper limit.

equal weight is assumed for all the sources. Although the number of the sources is too small for statistical arguments, the parameter C seems to decrease exponentially with the dynamical time scale of outflows. The correlation coefficient for this plot is -0.95. This feature is consistent with the previous works reporting a relationship between the opening angles of outflows and the source ages (e.g. Arce & Sargent, 2006; Seale & Looney, 2008; Velusamy et al., 2014). The trend of increasing opening angle as increasing age is also revealed by the theoretical simulations (e.g Shang et al., 2006; Offner et al., 2011; Machida & Hosokawa, 2013). However, previous observational studies are based on morphology of outflows. Although the appearance of integrated intensity maps of outflows is affected by the inclination angle, its effect is not considered for some cases. In contrast, the outflow parameters reported in this thesis are derived from both the geometrical and kinematic structures of the outflow by using the parabolic model considering the inclination angle. The results quantitatively supports the trend suggested previously. As described above, the angular momentum of the envelope gas is also expected to increase as the protosetellar evolution. This may contribute to decreasing the C value (Figure 10.2).

Figure 10.4 shows a semi-log plot of v_0 versus dynamical time scale $t_{\rm dyn}$. Although the correlation coefficient of -0.75 is lower than that for the plot in Figure 10.3, the velocity of the gas also seems to decrease exponentially with the dynamical time scale of outflows. There seems to reveal a trend that outflows with shorter dynamical time scales have higher v_0. This trend is derived from the velocity structure of the outflow, which was not considered in the morphological studies. Although the parameters derived in this thesis (L1527, IRAS 15398–3359, and L483) are obtained with an observation focused on a narrow region without the whole structure of the outflow, they are consistent with the values previously reported based on the analysis of the large-scale outflow structures. Therefore, outflows can be characterized with the aid of the parabolic outflow model focused on a narrow region (a few 100 au scale) around the protostar, even if the whole structure is not observed. This strengthens the idea that the acceleration and geometry of the outflow are mostly defined in a very small region near the protostar.

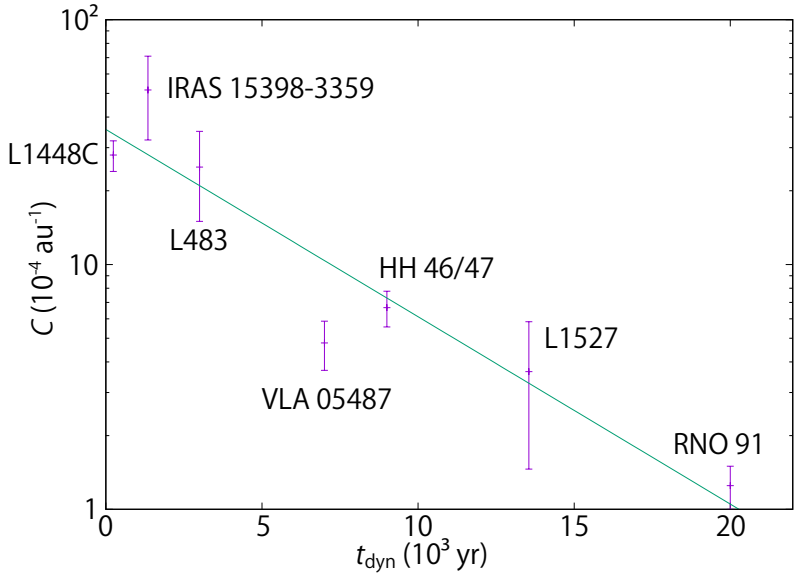

Figure 10.3: Relation between the curvature parameter (C) of an outflow and its dynamical time scale. The dynamical time scales for L1527 and IRAS 15398–3359 are the averaged value of the two lobes. The green dashed line represents the best-fit function: $\log C = (-0.18 \pm 0.03) \times (t_{\rm dyn} \times 10^{-3}) + (-5.6 \pm 0.3)$, where the uniform weights are applied to all the sources. The correlation coefficient for this plot is -0.95.

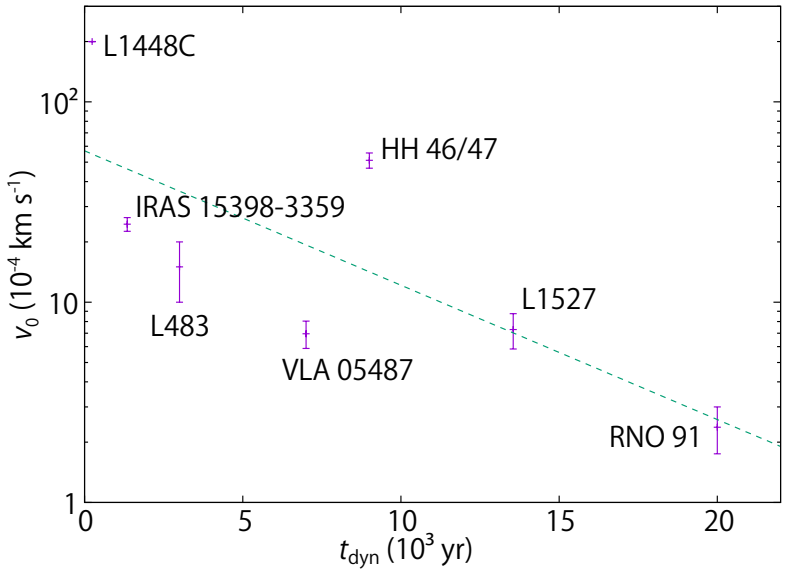

Figure 10.4: Relation between the velocity parameter (v_0) of an outflow and its dynamical time scale. The dynamical time scales for L1527 and IRAS 15398–3359 are the averaged value of the two lobes. The green dashed line represents the best-fit function: $\log v_0 = (-0.15 \pm 0.06) \times (t_{\rm dyn} \times 10^{-3}) + (-5.2 \pm 0.6)$, The correlation coefficient for this plot is -0.75, where the uniform weights are applied to all the sources.

Table 10.2: Best fit parameters for the models of the outflow cavity walls and the dynamical time scales

Source	Distance (pc)	$t_{\rm dyn}$ (10^3 yr)	Inclination Angle[a] (°)	C (10^{-4} au^{-1})	v_0 (10^{-4} km s^{-1})
L1527[b]	137	20.6 (east), 6.5 (west)[c]	85 ± 10	3.6 ± 2.2	7.3 ± 1.5
IRAS 15398–3359[b]	155	0.9 (northeast), 1.8 (southwest)[c]	70 ± 10	52 ± 19	25 ± 2
L483[b]	200	3	80 ± 5	25 ± 10	15 ± 5
VLA 05487[d]	460	∼7	71 ± 3	4.8 ± 1.1	7.0 ± 1.1
RNO 91[d]	160	∼20	70 ± 4	1.3 ± 0.25	2.4 ± 0.6
L1448C[e]	250	∼ 0.24	69	24, 32	200
HH 46/47[f]	450	9	61 ± 1	6.7 ± 1.1	51 ± 4

[a] 0° for a face-on configuration.
[b] This work (Chapters 4, 5, 8).
[c] Determined from the CO ($J = 3 - 2$) emission (Yıldız et al., 2015).
[d] Determined from the CO ($J = 1 - 0$) emission (Lee et al., 2000).
[e] Determined from the CO ($J = 3 - 2$) emission (Hirano et al., 2010).
[f] Determined from the CO ($J = 1 - 0$) emission (Arce et al., 2013).

Chapter 11

Conclusion

In this thesis, the physical and chemical structures of the disk-forming regions (Figure 11.1) in the five low-mass protostellar sources have been characterized with the aid of simple kinematic models of the infalling-rotating envelope, Keplerian disk, and the outflow. We have made some significant contributions to astrochemistry and star-formation studies. The new insights obtained in this thesis also raise new important questions to be addressed in the future.

11.1 Summary of This Thesis

Major outcomes of this thesis are summarized below. We have been able to address the questions raised in Introduction (Chapter 1), at least partly.

(1) The infalling-rotating envelope and its centrifugal barrier are common occurrences in the observed sources. These physical structures are seen regardless of the chemical characteristics (WCCC/hot corino chemistry/mixed character) of the sources. The infalling-rotating envelope model based on the simple physical assumptions (the energy and angular momentum conservation) works well to characterize the observed kinematic structure. Thus, the model seems to capture the basic physics in disk forming regions.

(2) The centrifugal barrier is most likely the transition zone from the infalling-rotating envelope to the disk inside it. The kinematic structure is discontinuously changed across the centrifugal barrier. It is expected that this physical change is also related to the launching mechanism of the outflow as an extraction mechanism of the angular momentum of the gas. Although some hints are found in this thesis, the relation it is not obvious at the present stage.

(3) The fact that the observed kinematic structure is well represented by the infalling-rotating envelope model implies that the magnetic field does not effectively affect the gas motion at least in the infalling-rotating envelope at a few 100 au scale.

(4) The chemical change across the centrifugal barrier is seen in all the observed sources, which is probably caused by the accretion shock in front of the centrifugal barrier as well as the protostellar heating. The molecular species tracing each physical component of the disk forming region (the infalling-rotating envelope, the centrifugal

barrier, and the disk component) is different depending on the chemical characteristics of the sources. This would result in a chemical diversity in protoplanetary disks and eventually in planets.

(5) The chemical processes in the stagnated gas around the centrifugal barrier are expected to determine the chemical heritage passed from the infalling-rotating envelope to the disk component. Thus, the initial condition of the chemical evolution in protoplanetary disks is defined in the transition zone.

(6) Several molecular lines are recognized as good tracers for the physical components The chemical diagnostics will be a powerful tool for star-formation studies in the ALMA era, although it is still infancy.

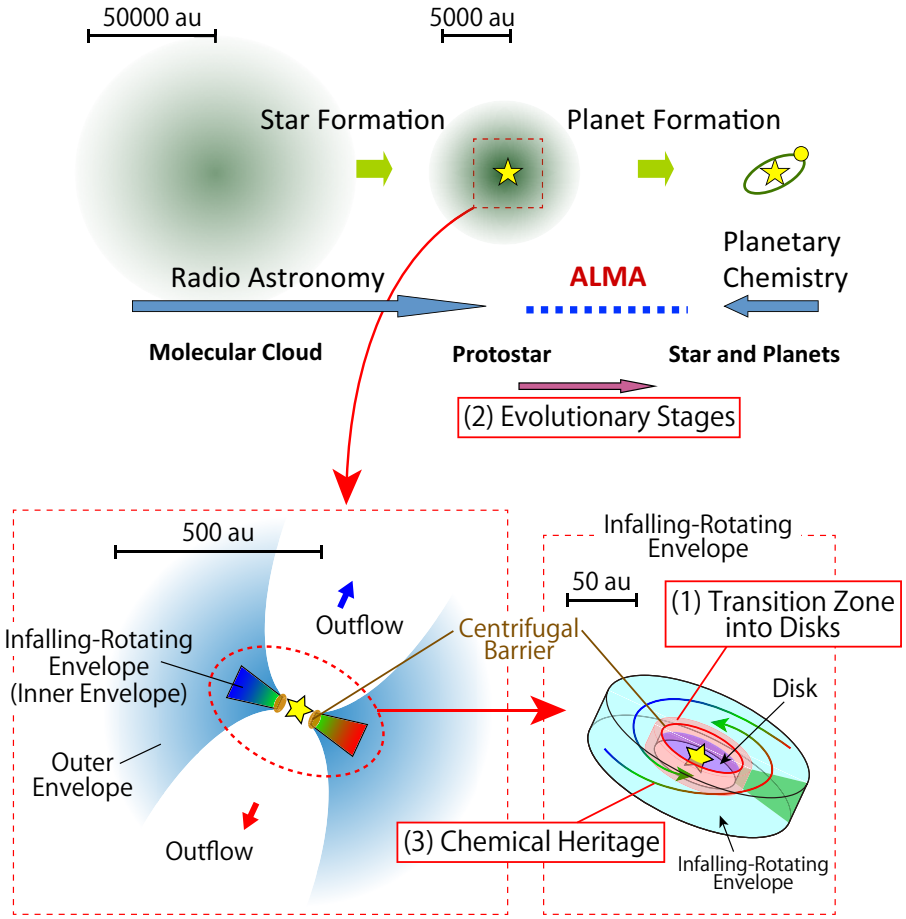

Figure 11.1: Schematic illustration of the protostellar evolution process (top). The bottom illustrations depict the disk/envelope system of young low-mass protostellar sources, whose physical and chemical structures we characterized in this thesis. The focusing points of the future projects mentioned in Section 11.2 are also shown.

11.2 Future Prospects

11.2.1 Transition Zone from the Envelope to the Disk

In this thesis, we have demonstrated that images at a sub-arcsecond resolution unveil unexpected phenomena. However, there are still complex physical components remained to be resolved, for instance, the detailed structure of the transition zone from the infalling-rotating envelope to the disk, the stagnation of the gas at the centrifugal barrier, and the launching points of the outflow. The physical parameters for some sources observed in this thesis are just upper limits. Higher angular resolution observations will allow us to characterize them more accurately.

Based on these motivations, we are going to conduct such higher angular-resolution observations with ALMA. These projects plan to observe the sources with which this thesis has dealt at an angular resolution of up to $0\farcs07$ ($\sim$ 10 au). Some parts of these programs have already been executed in these years. With a high angular-resolution observation ($\sim 0\farcs2$) toward L1527, Sakai et al. (2017) has indeed confirmed the extension of the scale height of the envelope gas at the centrifugal barrier due to the gas stagnation (Figure 11.2), as described in Chapter 10. The higher angular-resolution observations will provide us with new insights into the disk formation study.

11.2.2 How about in More Evolved Sources?

The concept of the infalling-rotating envelope and its centrifugal barrier has been confirmed to be common at the evolutionary stages of Class 0 and I. Moreover, the chemical process occurring around the centrifugal barrier would determine the initial condition for

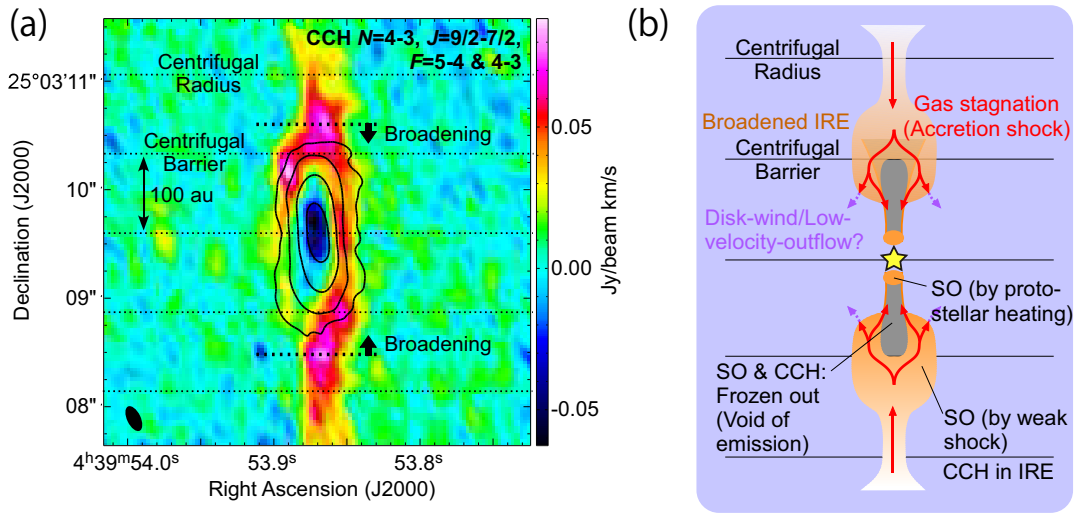

Figure 11.2: (a) Integrated intensity map of CCH ($N = 4-3, J = 9/2-5/2, F = 5-4$ and $4-3$; color). White contours represent the 0.8 mm dust continuum map. The contour levels for the continuum are 10, 40, 160, 320, and 640σ, where the rms noise level is 0.9 mJy beam^{-1}. (b) Schematic illustration of the physical and chemical structures of the disk/envelope system of L1527. Taken from Sakai et al. (2017).

the chemical evolution in the disk formation. This thesis shows that chemical diversity is already seen at its earliest stage. Then, the next question naturally rises: how does it evolve in the future? Thanks to the high sensitivity of ALMA, the weak molecular line emission of various molecular species is being detected in protoplanetary disks (e.g., Huang et al., 2017). For instance, the H_2CS line is detected toward MWC 480 (IAU Symposium 332). This detection is interesting, because H_2CS is detected in the disk component of IRAS 16293–2422 Source A (Chapter 6). The chemical characterization of more sources in the Class II stage is urgent to delineate the whole scenario of the chemical evolution from infalling-rotating envelopes to protoplanetary disks and eventually to planets.

11.2.3 Chemical Heritage: Importance of Sulfur Chemistry

Understandings of the behavior of various molecular species in the disk-forming region are essential to building the sound bases of the chemical diagnostics. The observational results in this thesis suggest that S-bearing molecules, such as CS, SO, OCS, and H_2CS, would be key species in the chemical differentiation in the disk forming region. However, their chemical behaviors are still unknown both observationally and theoretically. Since they will be sensitive to physical changes in disk formation, physical characterization of each source is required in order to understand the chemical behaviors of S-bearing molecules. In IRAS 16293–2422 Source A (Chapter 6), H_2CS traces the disk component while OCS does not in spite of their similar desorption temperature (Chapter 9). It suggests that there are some chemical mechanisms which reduces the OCS abundance and enhance the H_2CS abundance inside the centrifugal barrier. Identification of the specific chemical processes responsible for this trend is highly awaited. Such chemical processes will also affect the chemical heritage delivered into the disk. The detection of H_2CS toward the protoplanetary disk mentioned above may further indicate that it is delivered into the planets. Moreover, a recent study with Rosetta also found various S-bearing species in the coma of comet 67P/Churyumov-Gerasimenko (Calmonte et al., 2016). Hence, the sulfur chemistry is the central issue for astrochemical studies of the disk formation in the next decade.

So far, sulfur chemistry has been studied for molecular clouds and star-forming regions (e.g., Prasad & Huntress, 1982; Millar & Herbst, 1990; Wakelam et al., 2004, 2005, 2011). The most difficult point in the sulfur chemistry is that we do not exactly know the sulfur abundance available for the gas-phase reactions. In the previous models, 99% of sulfur is simply assumed to be depleted onto dust grains. However, this fraction is quite arbitrary. Moreover, we do not exactly know the major form of sulfur on dust grains, although H_2S is thought to be a potential candidate. Hence, the sulfur chemistry seems unpredictable at the present stage in hot regions like the disk forming regions, where extensive gas-grain interaction is occurring. Under such a circumstance, we need to start with understandings of abundances and distributions of various S-bearing molecules in protostellar cores.

Based on this prospect, we have already started a spectral line survey observation of S-bearing species with single-dish telescopes (IRAM 30 m, NRO 45 m). We succeeded to detect the OCS and H_2CS lines at the wavelength of 1.2 mm toward several hot corino sources (Figure 11.3, such as Serpens SMM1, SMM4, NGC 1333 IRAS 2A, and NGC 1333 IRAS 4B. Although these species has not been popular in the observational studies of low-mass protostellar sources, understandings of their detailed distribution in the vicinity of

the protostar will be essential to the establishment of the chemical diagnostics and further exploration of the chemical evolution from molecular clouds to star-forming regions.

The above future projects are schematically illustrated in Figure 11.1. By tackling these projects with a full use of ALMA, we would like to contribute to unveiling the whole picture of the physical and chemical evolution in formation of Solar-type stars.

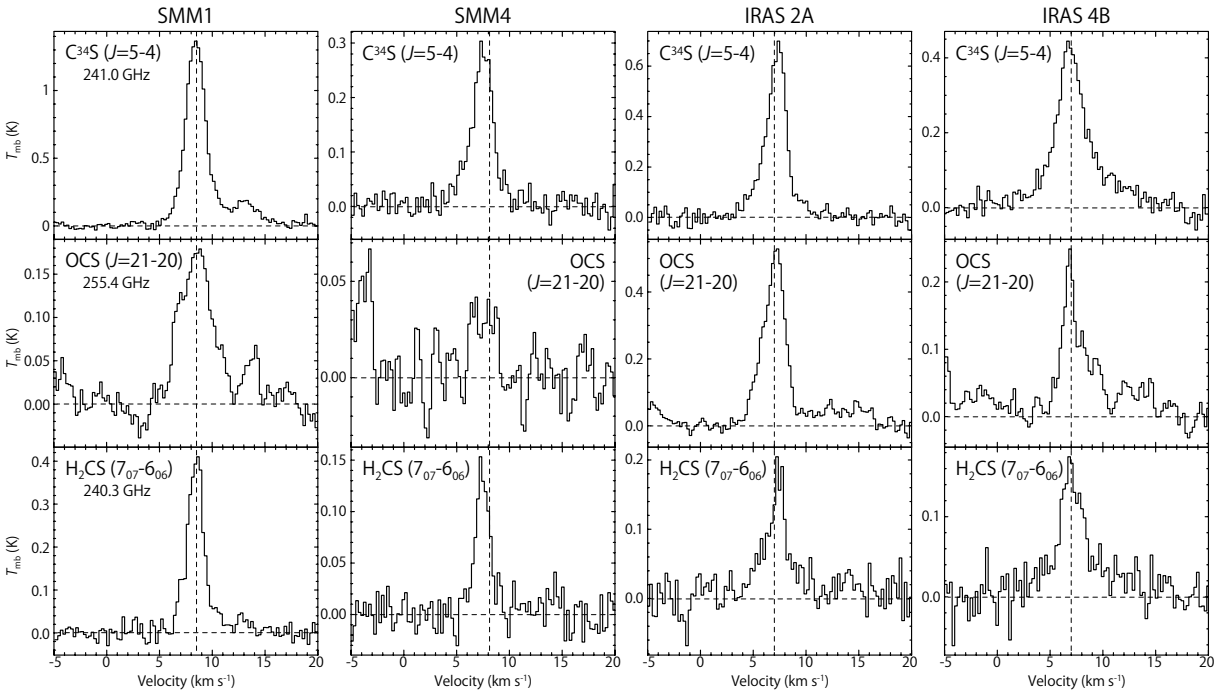

Figure 11.3: Spectra of S-bearing molecules observed toward the four hot corino sources with the IRAM 30 m telescope. The vertical dashed line represents the systemic velocity of each source. Broad OCS lines, which would come from the vicinity of the protostar, are detected.

Acknowledgements

The author is grateful to Professor Satoshi Yamamoto for his invaluable advice and encouragement. The author is indebted to Dr. Nami Sakai for her valuable discussions and for providing the ALMA data used in this thesis. The author acknowledges Dr. Cecilia Ceccarelli for her kind collaboration. The author thanks to Drs. Ewine van Dishoeck, Jes Jørgensen, Bertrand Lefloch, Ana López-Sepulcre, and Cécile Favre for their collaboration. The author is also grateful to Drs. Tomoyuki Hanawa, Yasushi Suto, Masaki Sano, Yuri Aikawa, Masahiro Machida, Tomoya Hirota, Yoshimasa Watanabe, and all the members in Yamamoto Group of Department of Physics, The University of Tokyo, and Sakai Group of RIKEN for their great supports and discussion in various aspects of this research. Finally, the author thanks Profs. Takao Nakagawa, Aya Bamba, Hideko Nomura, Takashi Onaka, Masami Ouchi, and Jun'ichi Yokoyama for their valuable comments and suggestions as reviewers of this thesis. This thesis makes use of the following ALMA data sets: ADS/JAO.ALMA #2011.0.00604.S, ADS/JAO.ALMA #2011.0.00777.S, ADS/JAO.ALMA #2012.1.00712.S, ADS/JAO.ALMA #2013.1.01102.S, ADS/JAO.ALMA #2015.1.01060.S. ALMA is a partnership of the ESO (representing its member states), the NSF (USA) and NINS (Japan), together with the NRC (Canada) and the NSC and ASIAA (Taiwan), in cooperation with the Republic of Chile. The Joint ALMA Observatory is operated by the ESO, the AUI/NRAO and the NAOJ. The author is grateful to the ALMA staff for their excellent support. The author also acknowledges the the Advanced Leading Graduate Course for Photon Science (ALPS) and the JSPS fellowship for financial support. This study is supported by Grant-in-Aid from the Ministry of Education, Culture, Sports, Science, and Technologies of Japan (15J01610).

Appendix A

Desorption Temperature

In radio observational studies, rotational spectral lines are observed in interstellar clouds. The line emission (or absorption) arises from freely rotating molecules only in the gas phase. However, interstellar molecules also exist on the surface of dust grains and in the ice mantles. In disk forming regions, the dust temperature is high enough for various molecular species to evaporate/sublimate from dust grains, and it cause a substantial change in the chemical composition of the gas. In the study of the chemical evolution, we should hence consider the evaporation/sublimation of molecules from dust grains as well as the chemical process. Here, we evaluate the *'desorption temperature'* of some molecular species observed in this thesis. Desorption temperature of a molecular species (or also called as *'adsorption temperature'*) is a typical temperature at which the molecular species desorbs from dust grains.

A.1 Balance of the Adsorption and the Desorption

When a molecule collides with a dust grain, it can be adsorbed on dust surfaces due to attracting forces, such as van der Waals force and/or electrostatic forces. The rate of the adsorption of molecules is represented as follows (Yamamoto, 2017):

$$R_{\rm ads} = n\,({\rm X})\,S\sigma < v >, \tag{A.1}$$

where n(X) denotes the number density of molecule X in the gas phase, σ the geometrical cross section of dust grains, and $< v >$ the average speed of X. S is the sticking probability, with which a molecule is adsorbed in its collision with a dust grain. We here assume S of unity, which means that a molecules is adsorbed in every collision.

Adsorbed molecules are thermally desorbed from dust surfaces into the gas phase. The rate of the thermal desorption depends on the *'desorption energy'* (or *'binding energy'*) $E_{\rm des}$ of each molecular species, and it can be represented as follows (Yamamoto, 2017):

$$R_{\rm des} = N_s\,({\rm X})\,\nu_0 \exp\left(-\frac{E_{\rm des}}{k_{\rm B}T}\right), \tag{A.2}$$

where N_s(X) denotes the number of molecule X on a particular dust grain, $k_{\rm B}$ the Boltzmann constant, T the dust temperature. In a chemical picture, the desorption of a

molecule is caused by the vibration between the molecule and the dust surface. The characteristic frequency of the vibration mode is denoted as ν_0, which is typically 10^{12} Hz (30 cm^{-1}) (Yamamoto, 2017). $N_s(\mathrm{X})$ can be represented as follows:

$$n_s\left(\mathrm{X}\right) = N_s\left(\mathrm{X}\right) n_g, \tag{A.3}$$

where $n_s(\mathrm{X})$ denotes the number density of molecules X on dust grains in a unit volume, and n_g the number density of the dust in a unit volume. Let Σ the effective collision area of dust per H molecule, it is related to n_g as:

$$\Sigma = \frac{n_g \sigma}{n_0}, \tag{A.4}$$

where n_0 denotes the number density of H nuclei: $n_0 = n\left(\mathrm{H}\right) + 2n\left(\mathrm{H_2}\right)$. Thus, the rate of the thermal desorption can be represented as:

$$R_{\mathrm{des}} = \frac{n_s\left(\mathrm{X}\right)\sigma}{n_0 \Sigma} \nu_0 \exp\left(-\frac{E_{\mathrm{des}}}{k_{\mathrm{B}} T}\right). \tag{A.5}$$

In the steady state, the rates of the adsorption and thermal desorption of molecules are balanced. Thus, we obtain the relation:

$$n\left(\mathrm{X}\right) < v > = \frac{n_s\left(\mathrm{X}\right)}{n_0 \Sigma} \nu_0 \exp\left(-\frac{E_{\mathrm{des}}}{k_{\mathrm{B}} T}\right). \tag{A.6}$$

Here, the desorption temperature is the temperature at which the number density of molecules X in the gas phase equals to that on dust grains in unit volume: $n\left(\mathrm{X}\right) = n_s\left(\mathrm{X}\right)$. Under this condition, the desorption temperature (T_{des}) can be represented as:

$$k_{\mathrm{B}} T_{\mathrm{des}} = E_{\mathrm{des}} \left(\log \frac{\nu_0}{n_0 \Sigma < v >}\right)^{-1}. \tag{A.7}$$

Here, the desorption temperature of molecule X is proportional to its desorption energy. A typical value of Σ is 10^{-22} cm^{-2} (Yamamoto, 2017).

Figure A.1 shows the relation between the desorption temperature and the desorption energy with typical values for n_0 and $< v >$. From the plots, the factor of proportionality of T_{des} to E_{des} is approximated to be $50-60$. Assuming the factor to be 55, the desorption temperatures of some molecular species can be roughly estimated as summarized in Table A.1.

Table A.1: Desorption Energies and Desorption Temperatures of Molecular Species

Molecular Species	Desorption Energy[a] $E_{\rm des}/k_B$ (K)	Desorption Temperature[b] $T_{\rm des}$(K)
H	600	11
H_2	430	8
H_2O	4800	87
CCH	2137	39
CO	1150	21
H_2CO	2050	37
CH_3OH	4930	90
H_2S	2743	50
CS	1900	35
SiO	3500	64
NH_2CHO	5556	101
H_2CS	2700	49
HCOOH	5000	91
SO	2600	47
$HCOOCH_3$	4000	73
OCS	2888	53
SO_2	5330	97

[a] Taken from UMIST database for astrochemistry (McElroy et al., 2013, http://udfa.ajmarkwick.net/index.php)

[b] Derived from the desorption energy with using the equation (A.7).

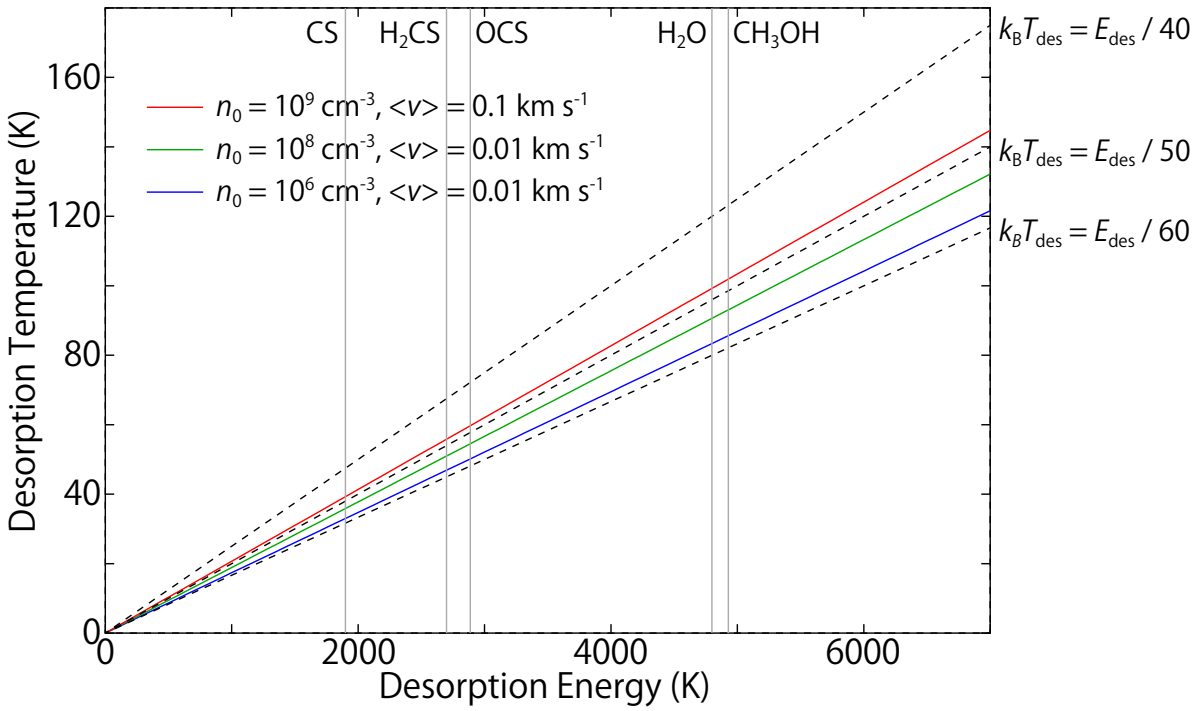

Figure A.1: Relation between the desorption temperature and the desorption energy. Solid lines represent the plots derived from the equation (A.7), where n_0 and $< v >$ are assumed to be $(10^6 - 10^9)$ cm^{-3} and $(0.01 - 0.1)$ km s^{-1}, respectively. Dashed lines represent the plots of the following relation: $k_B T_{\rm des} = C E_{\rm des}$, where C denotes the factor of proportionality of $40 - 60$.

Bibliography

Agúndez, M., Cernicharo, J., & Guélin, M. 2015, A&A, 577, L5

Aikawa, Y., Wakelam, V., Garrod, R. T., & Herbst, E. 2008, ApJ, 674, 984-996

ALMA Partnership, 2017, S. Asayama, A. Biggs, I. de Gregorio, B. Dent, J. Di Francesco, E. Fomalont, A. Hales, J. Hibbard, G. Marconi, S. Kameno, B. Vila Vilaro, E. Villard, F. Stoehr

Andre, P., Ward-Thompson, D., & Barsony, M. 1993, ApJ, 406, 122

André, P., Men'shchikov, A., Bontemps, S., et al. 2010, A&A, 518, L102

Aota, T., Inoue, T., & Aikawa, Y. 2015, ApJ, 799, 141

Arce, H. G., & Sargent, A. I. 2006, ApJ, 646, 1070

Arce, H. G., Mardones, D., Corder, S. A., et al. 2013, ApJ, 774, 39

Bachiller, R. 1996, ARA&A, 34, 111

Balucani, N., Ceccarelli, C., & Taquet, V. 2015, MNRAS, 449, L16

Baraffe, I., & Chabrier, G. 2010, A&A, 521, A44

Beuther, H., Schilke, P., & Gueth, F. 2004, ApJ, 608, 330

Beuther, H., Zhang, Q., Greenhill, L. J., et al. 2005, ApJ, 632, 355

Beckwith, S. V. W., Sargent, A. I., Chini, R. S., & Güsten, R. 1990, AJ, 99, 924

Beichman, C. A., Myers, P. C., Emerson, J. P., et al. 1986, ApJ, 307, 337

Benson, P. J., & Myers, P. C. 1989, ApJS, 71, 89

Blake, G. A., Sutton, E. C., Masson, C. R., & Phillips, T. G. 1987, ApJ, 315, 621

Blake, G. A., van Dishoeck, E. F., Jansen, D. J., Groesbeck, T. D., & Mundy, L. G. 1994, ApJ, 428, 680

Born, M., & Wolf, E., 1959, 'Principles of Optics', Cambridge Univ. Press, p.562

Bottinelli, S., Ceccarelli, C., Neri, R., et al. 2004a, ApJ, 617, L69

Bottinelli, S., Ceccarelli, C., Lefloch, B., et al. 2004b, ApJ, 615, 354

Bottinelli, S., Ceccarelli, C., Williams, J. P., & Lefloch, B. 2007, A&A, 463, 601

Brinch, C., Jørgensen, J. K., & Hogerheijde, M. R. 2009, A&A, 502, 199

Calmonte, U., Altwegg, K., Balsiger, H., et al. 2016, MNRAS, 462, S253

Caux, E., Kahane, C., Castets, A., et al. 2011, A&A, 532, A23

Cazaux, S., Tielens, A. G. G. M., Ceccarelli, C., et al. 2003, ApJ, 593, L51

Ceccarelli, C., Castets, A., Loinard, L., Caux, E., & Tielens, A. G. G. M. 1998, A&A, 338, L43

Ceccarelli, C., Castets, A., Caux, E., et al. 2000a, A&A, 355, 1129

Ceccarelli, C., Loinard, L., Castets, A., Tielens, A. G. G. M., & Caux, E. 2000b, A&A, 357, L9

Ceccarelli, C., Loinard, L., Castets, A., Faure, A., & Lefloch, B. 2000c, A&A, 362, 1122

Ceccarelli, C. 2004, Star Formation in the Interstellar Medium: In Honor of David Hollenbach, 323, 195

Chandler, C. J., Brogan, C. L., Shirley, Y. L., & Loinard, L. 2005, ApJ, 632, 371

Chapman, N. L., Davidson, J. A., Goldsmith, P. F., et al. 2013, ApJ, 770, 151

Cheung, A. C., Rank, D. M., Townes, C. H., Thornton, D. D., & Welch, W. J. 1968, Physical Review Letters, 21, 1701

Cheung, A. C., Rank, D. M., Townes, C. H., Thornton, D. D., & Welch, W. J. 1969, Nature, 221, 626

Choi, M., Kang, M., & Tatematsu, K. 2011, ApJ, 728, L34

Codella, C., Cabrit, S., Gueth, F., et al. 2007, A&A, 462, L53

Coffey, D., Bacciotti, F., Ray, T. P., Eislöffel, J., & Woitas, J. 2007, ApJ, 663, 350

Crimier, N., Ceccarelli, C., Maret, S., et al. 2010, A&A, 519, A65

Crutcher, R. M. 2012, ARA&A, 50, 29

Evans, N. J., II, Dunham, M. M., Jørgensen, J. K., et al. 2009, ApJS, 181, 321-350

Evans, N. J., II, Di Francesco, J., Lee, J.-E., et al. 2015, ApJ, 814, 22

Ewen, H. I., & Purcell, E. M. 1951, Nature, 168, 356

Favre, C., Jørgensen, J. K., Field, D., et al. 2014, ApJ, 790, 55

Feigelson, E. D., & Montmerle, T. 1999, ARA&A, 37, 363

Fuller, G. A., Lada, E. A., Masson, C. R., & Myers, P. C. 1995, ApJ, 453, 754

Green, J. D., Evans, N. J., II, Jørgensen, J. K., et al. 2013, ApJ, 770, 123

Graninger, D. M., Wilkins, O. H., & Öberg, K. I. 2016, ApJ, 819, 140

Gueth, F., Guilloteau, S., & Bachiller, R. 1996, A&A, 307, 891

Hassel, G. E., Herbst, E., & Garrod, R. T. 2008, ApJ, 681, 1385-1395

Hatchell, J., Fuller, G. A., & Ladd, E. F. 1999, A&A, 344, 687

Hara, C., Shimajiri, Y., Tsukagoshi, T., et al. 2013, ApJ, 771, 128

Hartmann, L., Cassen, P., & Kenyon, S. J. 1997, ApJ, 475, 770

Hartmann, L. 2009a, Astrophysics and Space Science Proceedings, 13, 23

Hartmann, L. 2009, Accretion Processes in Star Formation: Second Edition, by Lee Hartmann. ISBN 978-0-521-53199-3. Published by Cambridge University Press, Cambridge, UK, 2009b,

Hartmann, L., Herczeg, G., & Calvet, N. 2016, ARA&A, 54, 135

Harvey, D. W. A., Wilner, D. J., Myers, P. C., Tafalla, M., & Mardones, D. 2003, ApJ, 583, 809

Hayashi, C. 1961, PASJ, 13, 450

Henyey, L. G., Lelevier, R., & Levée, R. D. 1955, PASP, 67, 154

Hey, J. S. 1946, Nature, 157, 47

Hinshaw, G., Larson, D., Komatsu, E., et al. 2013, ApJS, 208, 19

Högbom, J. A. 1974, A&AS, 15, 417

Hogerheijde, M. R. 2001, ApJ, 553, 618

Hogerheijde, M. R., van Dishoeck, E. F., Blake, G. A., & van Langevelde, H. J. 1998, ApJ, 502, 315

Hirano, N., Mikami, H., Umemoto, T., Yamamoto, S., & Taniguchi, Y. 2001, ApJ, 547, 899

Hirano, N., Ho, P. P. T., Liu, S.-Y., et al. 2010, ApJ, 717, 58

Hirota, T., Bushimata, T., Choi, Y. K., et al. 2007, PASJ, 59, 897

Hirota, T., Ohishi, M., & Yamamoto, S. 2009, ApJ, 699, 585

Hirota, T., Sakai, N., & Yamamoto, S. 2010, ApJ, 720, 1370

Huang, J., Öberg, K. I., Qi, C., et al. 2017, ApJ, 835, 231

Imai, M., Sakai, N., Oya, Y., et al. 2016, ApJ, 830, L37

Jaber, A. A., Ceccarelli, C., Kahane, C., & Caux, E. 2014, ApJ, 791, 29

Jansen, D. J., van Dishoeck, E. F., Black, J. H., Spaans, M., & Sosin, C. 1995a, A&A, 302, 223

Jansen, D. J., Spaans, M., Hogerheijde, M. R., & van Dishoeck, E. F. 1995b, A&A, 303, 541

Jansky, K. G. 1933, Nature, 132, 66

Johansson, L. E. B., Andersson, C., Ellder, J., et al. 1984, A&A, 130, 227

Jørgensen, J. K., Schöier, F. L., & van Dishoeck, E. F. 2002, A&A, 389, 908

Jørgensen, J. K. 2004, A&A, 424, 589

Jørgensen, J. K., Bourke, T. L., Myers, P. C., et al. 2005, ApJ, 632, 973

Jørgensen, J. K., Bourke, T. L., Nguyen Luong, Q., & Takakuwa, S. 2011, A&A, 534, A100

Jørgensen, J. K., Favre, C., Bisschop, S. E., et al. 2012, ApJ, 757, L4

Jørgensen, J. K., Visser, R., Sakai, N., et al. 2013, ApJ, 779, L22

Jørgensen, J. K., van der Wiel, M. H. D., Coutens, A., et al. 2016, A&A, 595, A117

Keene, J., Hildebrand, R. H., Whitcomb, S. E., & Harper, D. A. 1980, ApJ, 240, L43

Knude, J., & Hog, E. 1998, A&A, 338, 897

Kristensen, L. E., van Dishoeck, E. F., Bergin, E. A., et al. 2012, A&A, 542, A8

Kristensen, L. E., Klaassen, P. D., Mottram, J. C., Schmalzl, M., & Hogerheijde, M. R. 2013, A&A, 549, L6

Kuan, Y.-J., Huang, H.-C., Charnley, S. B., et al. 2004, ApJ, 616, L27

Lada, C. J., & Wilking, B. A. 1984, ApJ, 287, 610

Larson, R. B. 1969, MNRAS, 145, 271

Launhardt, R., Pavlyuchenkov, Y., Gueth, F., et al. 2009, A&A, 494, 147

Lee, C.-F., Mundy, L. G., Reipurth, B., Ostriker, E. C., & Stone, J. M. 2000, ApJ, 542, 925

Lee, C.-F., Ho, P. T. P., Palau, A., et al. 2007, ApJ, 670, 1188

Lee, C.-F., Ho, P. T. P., Bourke, T. L., et al. 2008, ApJ, 685, 1026-1032

Lee, C.-F., Hirano, N., Palau, A., et al. 2009, ApJ, 699, 1584

Leung, G. Y. C., Lim, J., & Takakuwa, S. 2016, ApJ, 833, 55

Lindberg, J. E., Jørgensen, J. K., Brinch, C., et al. 2014, A&A, 566, A74

Lindberg, J. E., Jørgensen, J. K., Watanabe, Y., et al. 2015, A&A, 584, A28

Loinard, L., Rodríguez, L. F., D'Alessio, P., Wilner, D. J., & Ho, P. T. P. 2002, ApJ, 581, L109

Loison, J.-C., Halvick, P., Bergeat, A., Hickson, K. M., & Wakelam, V. 2012, MNRAS, 421, 1476

Lombardi, M., Lada, C. J., & Alves, J. 2008, A&A, 480, 785

Looney, L. W., Mundy, L. G., & Welch, W. J. 2000, ApJ, 529, 477

López-Sepulcre, A., Sakai, N., Imai, M., 2017, Accepted in A&A

Lumbreras, A. M., & Zapata, L. A. 2014, AJ, 147, 72

Lundgren, A., ALMA Cycle 1 Technical Handbook, Version 1.01, ALMA

Machida, M., Hayashi, M. R., & Matsumoto, R. 2000, ApJ, 532, L67

Machida, M. N., Inutsuka, S.-I., & Matsumoto, T. 2011, PASJ, 63, 555

Machida, M. N., & Hosokawa, T. 2013, MNRAS, 431, 1719

MacLeod, J., Lorne, A., Harris, A., Tacconi, L., & Schuster, K. 1994, JCMT Newsletter, Sep/Oct, 46

Mardones, D., Myers, P. C., Tafalla, M., et al. 1997, ApJ, 489, 719

Maret, S., Belloche, A., Maury, A. J., et al. 2014, A&A, 563, L1

Masson, C. R., & Mundy, L. G. 1988, ApJ, 324, 538

Masunaga, H., Miyama, S. M., & Inutsuka, S.-i. 1998, ApJ, 495, 346

Maury, A. J., Belloche, A., André, Ph., et al. 2014, A&A, 563, L2

Mikami, H., Umemoto, T., Yamamoto, S., & Saito, S. 1992, ApJ, 392, L87

Millar, T. J., & Herbst, E. 1990, A&A, 231, 466

Mizuno, A., Fukui, Y., Iwata, T., Nozawa, S., & Takano, T. 1990, ApJ, 356, 184

McElroy, D., Walsh, C., Markwick, A. J., et al. 2013, A&A, 550, A36

Müller, H. S. P., Schlöder, F., Stutzki, J., & Winnewisser, G. 2005, Journal of Molecular Structure, 742, 215

Mundy, L. G., Wootten, H. A., & Wilking, B. A. 1990, ApJ, 352, 159

Mundy, L. G., Wootten, A., Wilking, B. A., Blake, G. A., & Sargent, A. I. 1992, ApJ, 385, 306

Muller, C. A., & Oort, J. H. 1951, Nature, 168, 357

Murillo, N. M., Lai, S.-P., Bruderer, S., Harsono, D., & van Dishoeck, E. F. 2013, A&A, 560, A103

Myers, P. C., & Ladd, E. F. 1993, ApJ, 413, L47

Öberg, K. I., van der Marel, N., Kristensen, L. E., & van Dishoeck, E. F. 2011, ApJ, 740, 14

Offner, S. S. R., Lee, E. J., Goodman, A. A., & Arce, H. 2011, ApJ, 743, 91

Ohashi, N., Hayashi, M., Ho, P. T. P., & Momose, M. 1997, ApJ, 475, 211

Ohashi, N., Saigo, K., Aso, Y., et al. 2014, ApJ, 796, 131

Onishi, T., Mizuno, A., Kawamura, A., Ogawa, H., & Fukui, Y. 1996, ApJ, 465, 815

Ortiz-León, G. N., Loinard, L., Kounkel, M. A., et al. 2017, ApJ, 834, 141

Oya, Y., Sakai, N., Sakai, T., et al. 2014, ApJ, 795, 152

Oya, Y., Sakai, N., Lefloch, B., et al. 2015, ApJ, 812, 59

Oya, Y., Sakai, N., López-Sepulcre, A., et al. 2016, ApJ, 824, 88

Oya, Y., Sakai, N., López-Sepulcre, A., et al. 2017, ApJ, 837, 174

Palla, F. 1999, NATO Advanced Science Institutes (ASI) Series C, 540, 375

Palla, F., & Stahler, S. W. 1991, ApJ, 375, 288

Park, Y.-S., Panis, J.-F., Ohashi, N., Choi, M., & Minh, Y. C. 2000, ApJ, 542, 344

Pech, G., Zapata, L. A., Loinard, L., & Rodríguez, L. F. 2012, ApJ, 751, 78

Pickett, H. M., Poynter, R. L., Cohen, E. A., et al. 1998, J. Quant. Spec. Radiat. Transf., 60, 883

Pineda, J. E., Maury, A. J., Fuller, G. A., et al. 2012, A&A, 544, L7

Plambeck, R. L., & Wright, M. C. H. 1987, ApJ, 317, L101

Prasad, S. S., & Huntress, W. T., Jr. 1982, ApJ, 260, 590

Rao, R., Girart, J. M., Marrone, D. P., Lai, S.-P., & Schnee, S. 2009, ApJ, 707, 921

Reber, G. 1940, ApJ, 91, 621

Remijan, A., Adams, M., Warmels, R., et al. 2015, ALMA Cycle 3 Technical Handbook Version 1.0, ALMA

Rice, E. L., Prato, L., & McLean, I. S. 2006, ApJ, 647, 432

Rodríguez, L. F., Loinard, L., D'Alessio, P., Wilner, D. J., & Ho, P. T. P. 2005, ApJ, 621, L133

Sakai, N., Sakai, T., & Yamamoto, S. 2006, PASJ, 58, L15

Sakai, N., Sakai, T., Osamura, Y., & Yamamoto, S. 2007, ApJ, 667, L65

Sakai, N., Sakai, T., Hirota, T., & Yamamoto, S. 2008a, ApJ, 672, 371

Sakai, N., Sakai, T., & Yamamoto, S. 2008b, Ap&SS, 313, 153

Sakai, N., Sakai, T., Hirota, T., Burton, M., & Yamamoto, S. 2009a, ApJ, 697, 769

Sakai, N., Sakai, T., Hirota, T., & Yamamoto, S. 2009b, ApJ, 702, 1025

Sakai, N., Sakai, T., Hirota, T., & Yamamoto, S. 2010, ApJ, 722, 1633

Sakai, N., Ceccarelli, C., Bottinelli, S., Sakai, T., & Yamamoto, S. 2012, ApJ, 754, 70

Sakai, N., Sakai, T., Hirota, T., et al. 2014a, Nature, 507, 78

Sakai, N., Oya, Y., Sakai, T., et al. 2014b, ApJ, 791, L38

Sakai, N., Oya, Y., López-Sepulcre, A., et al. 2016, ApJ, 820, L34

Sakai, N., Oya, Y., López-Sepulcre, A., et al. 2017, MNRAS, 467, L76

Sakai, N., & Yamamoto, S. 2013, Chemical Reviews, 113, 8981

Seale, J. P., & Looney, L. W. 2008, ApJ, 675, 427-442

Schilke, P., Groesbeck, T. D., Blake, G. A., Phillips, & T. G. 1997, ApJS, 108, 301

Schöier, F. L., Jørgensen, J. K., van Dishoeck, E. F., & Blake, G. A. 2002, A&A, 390, 1001

Shang, H., Allen, A., Li, Z.-Y., et al. 2006, ApJ, 649, 845

Shibata, K., Tajima, T., & Matsumoto, R. 1990, ApJ, 350, 295

Shirley, Y. L., Evans, N. J., II, Rawlings, J. M. C., & Gregersen, E. M. 2000, ApJS, 131, 249

Shirley, Y. L., Mason, B. S., Mangum, J. G., et al. 2011, AJ, 141, 39

Shu, F. H. 1977, ApJ, 214, 488

Shu, F. H., Adams, F. C., & Lizano, S. 1987, ARA&A, 25, 23

Shu, F., Najita, J., Ostriker, E., et al. 1994a, ApJ, 429, 781

Shu, F. H., Najita, J., Ruden, S. P., & Lizano, S. 1994b, ApJ, 429, 797

Snyder, L. E., Buhl, D., Zuckerman, B., & Palmer, P. 1969, Physical Review Letters, 22, 679

Spezzano, S., Bizzocchi, L., Caselli, P., Harju, J., & Brünken, S. 2016, A&A, 592, L11

Stahler, S. W., Shu, F. H., & Taam, R. E. 1980, ApJ, 241, 637

Sternberg, A., & Dalgarno, A. 1995, ApJS, 99, 565

Sutton, E. C., Blake, G. A., Masson, C. R., & Phillips, T. G. 1985, ApJS, 58, 341

Suzuki, H., Yamamoto, S., Ohishi, M., et al. 1992, ApJ, 392, 551

Tachihara, K., Dobashi, K., Mizuno, A., Ogawa, H., & Fukui, Y. 1996, PASJ, 48, 489

Tafalla, M., Myers, P. C., Mardones, D., & Bachiller, R. 2000, A&A, 359, 967

Takakuwa, S., Kamazaki, T., Saito, M., Yamaguchi, N., & Kohno, K. 2007a, PASJ, 59, 1

Takakuwa, S., Ohashi, N., Bourke, T. L., et al. 2007b, ApJ, 662, 431

Takakuwa, S., Saito, M., Lim, J., et al. 2012, ApJ, 754, 52

Takahashi, S., & Ho, P. T. P. 2012, ApJ, 745, L10

Takahashi, S., Ohashi, N., & Bourke, T. L. 2013, ApJ, 774, 20

Tatematsu, K., Umemoto, T., Kameya, O., et al. 1993, ApJ, 404, 643

Tercero, B., Cernicharo, J., Pardo, J. R., & Goicoechea, J. R. 2010, A&A, 517, A96

Tobin, J. J., Hartmann, L., Calvet, N., & D'Alessio, P. 2008, ApJ, 679, 1364-1384

Tobin, J. J., Hartmann, L., & Loinard, L. 2010, ApJ, 722, L12

Tobin, J. J., Hartmann, L., Chiang, H.-F., et al. 2012, Nature, 492, 83

Tobin, J. J., Hartmann, L., Chiang, H.-F., et al. 2013, ApJ, 771, 48

Tomisaka, K. 2002, ApJ, 575, 306

Torres, R. M., Loinard, L., Mioduszewski, A. J., & Rodríguez, L. F. 2007, ApJ, 671, 1813

Turner, B. E. 1989, ApJS, 70, 539

van der Tak, F. F. S., Black, J. H., Schöier, F. L., Jansen, D. J., & van Dishoeck, E. F. 2007, A&A, 468, 627

van Dishoeck, E. F., Blake, G. A., Jansen, D. J., & Groesbeck, T. D. 1995, ApJ, 447, 760

van Kempen, T. A., van Dishoeck, E. F., Hogerheijde, M. R., & Güsten, R. 2009, A&A, 508, 259

Velusamy, T., Langer, W. D., & Thompson, T. 2014, ApJ, 783, 6

Wakelam, V., Castets, A., Ceccarelli, C., et al. 2004, A&A, 413, 609

Wakelam, V., Ceccarelli, C., Castets, A., et al. 2005, A&A, 437, 149

Wakelam, V., Hersant, F., & Herpin, F. 2011, A&A, 529, A112

Ward-Thompson, D., Zylka, R., Mezger, P. G., & Sievers, A. W. 2000, A&A, 355, 1122

Watanabe, Y., Sakai, N., Lindberg, J. E., et al. 2012, ApJ, 745, 126

Wilson, R. W., Jefferts, K. B., & Penzias, A. A. 1970, ApJ, 161, L43

Wilson, T. L., Johnston, K. J., Henkel, C., & Menten, K. M. 1989, A&A, 214, 321

Wootten, A. 1989, ApJ, 337, 858

Xue, Y., Suto, Y., Taruya, A., et al. 2014, ApJ, 784, 66

Yamamoto, S., 2017, 'Introduction to Astrochemistry: Chemical Evolution from Interstellar Clouds to Star and Planet Formation', Springer, (Berlin, Heidelberg), Chap. 6

Yeh, S. C. C., Hirano, N., Bourke, T. L., et al. 2008, ApJ, 675, 454-463

Yen, H.-W., Takakuwa, S., Ohashi, N., & Ho, P. T. P. 2013, ApJ, 772, 22

Yen, H.-W., Takakuwa, S., Ohashi, N., et al. 2014, ApJ, 793, 1

Yen, H.-W., Takakuwa, S., Koch, P. M., et al. 2015, ApJ, 812, 129

Yen, H.-W., Koch, P. M., Takakuwa, S., et al. 2017, ApJ, 834, 178

Yıldız, U. A., Kristensen, L. E., van Dishoeck, E. F., et al. 2012, A&A, 542, A86

Yıldız, U. A., Kristensen, L. E., van Dishoeck, E. F., et al. 2015, A&A, 576, A109

Zapata, L. A., Schmid-Burgk, J., Muders, D., et al. 2010, A&A, 510, A2

Zapata, L. A., Loinard, L., Rodríguez, L. F., et al. 2013, ApJ, 764, L14

Zapata, L. A., Arce, H. G., Brassfield, E., et al. 2014, MNRAS, 441, 3696

Zhou, S., Wu, Y., Evans, N. J., II, Fuller, G. A., & Myers, P. C. 1989, ApJ, 346, 168